

Novel monolithic stabilized finite element method for fluid-structure interaction

Stéphanie El Feghali

▶ **To cite this version:**

Stéphanie El Feghali. Novel monolithic stabilized finite element method for fluid-structure interaction. Other. Ecole Nationale Supérieure des Mines de Paris, 2012. English. NNT : 2012ENMP0030 . pastel-00743488

HAL Id: pastel-00743488
https://pastel.hal.science/pastel-00743488

Submitted on 19 Oct 2012

HAL is a multi-disciplinary open access archive for the deposit and dissemination of scientific research documents, whether they are published or not. The documents may come from teaching and research institutions in France or abroad, or from public or private research centers.

L'archive ouverte pluridisciplinaire **HAL**, est destinée au dépôt et à la diffusion de documents scientifiques de niveau recherche, publiés ou non, émanant des établissements d'enseignement et de recherche français ou étrangers, des laboratoires publics ou privés.

ParisTech
INSTITUT DES SCIENCES ET TECHNOLOGIES
PARIS INSTITUTE OF TECHNOLOGY

MINES ParisTech

Ecole doctorale n°364 : Sciences Fondamentales et Appliquées

Doctorat ParisTech

T H È S E

pour obtenir le grade de docteur délivré par

l'École nationale supérieure des mines de Paris

Spécialité " Mécanique Numérique"

présentée et soutenue publiquement par

Stephanie EL FEGHALI

le 28 Septembre 2012

Novel monolithic stabilized finite element method for Fluid-Structure Interaction

~ ~ ~

Nouvelle formulation monolithique en éléments finis stabilisés pour l'Interaction Fluide-Structure

Directeur de thèse : **Thierry COUPEZ**
Co-encadrement de la thèse : **Elie HACHEM**

Jury

M. Ramon CODINA, Professeur, CIMNE, Universitat Politècnica de Catalunya,	Rapporteur
M. Wolfgang A. WALL, Professeur, LNM, Technische Universität München	Rapporteur
M. Didier CLAMOND, Professeur, Laboratoire J.A. Dieudonné, Université de Nice Sophia-Antipolis	Examinateur
M. Thierry COUPEZ, Professeur, CEMEF, MINES ParisTech	Examinateur
M. Elie HACHEM, Maître de conférence, CEMEF, MINES ParisTech	Examinateur
M. Michel RAVACHOL, Docteur, Direction de la Prospective , Dassault Aviation	Examinateur

T H E S E

MINES ParisTech
CEMEF UMR CNRS 7635
1, rue Claude Daunesse - CS 10207
06904 Sophia Antipolis Cedex - France

Acknowledgements

First of all, I would like to convey my deepest gratitude to the director of my Ph.D., Thierry Coupez, for recruiting me and giving me the opportunity to achieve this work and also for his brightful and fruitful ideas and for guiding me through the important phases of this thesis. I would like also to thank Elie Hachem. I had a real chance of working with him and I am very grateful for his help and support. I appreciate all his contributions, ideas, and remarks. Moreover, I thank Elie for giving me the first opportunity to come to CEMEF as an intern and helped me during all my stay in France.

I gratefully acknowledge support from EDF, CEA and Technicom, especially from Elisabeth Longatte and Franc Baj.

I want to thank Karim as well who stood by me during my Ph.D. and encouraged and supported me.

I would like to express my gratitude for all my friends in CEMEF, Pamela, Nadine, Fadi, Rebecca, Greg Ghina, Ali, Jeff, Christophe, Emile, Larbi, Greg Puaux...My appreciation goes to Jeff who helped me alot especially during my final Ph.D. year.

I can not forget my brothers and friends outside CEMEF who supported me and gave me good advice during these three years, Rachel, Georges, Elio, Shirely, Patrick, Simon, Moe, Joe and Carine.

A special "thanks" goes to the Ladies of CEMEF who make the working environment joyful, Marie-Françoise, Françoise, Geneviève, Florence, Carole, Murielle and the librarians Brigitte and Sylvie. I would like to thank also all the staff at CEMEF, Group EII and special mention to the directors: Yvan Chastel and Elisabeth Massoni.

I am very grateful to Patrick Coels for his advices, motivation, help and for the fruitful conversations we had.

Thank you God for giving me the power and strength to complete this work.

To my parents I dedicate my thesis.

Abstract

Numerical simulations of fluid-structure interaction (FSI) are of first interest in numerous industrial problems: aeronautics, heat treatments, aerodynamic, bioengineering.... Because of the high complexity of such problems, analytical study is in general not sufficient to understand and solve them. FSI simulations are then nowadays the focus of numerous investigations, and various approaches are proposed to treat them. We propose in this thesis a novel monolithic approach to deal with the interaction between an incompressible fluid flow and rigid/ elastic material. This method consists in considering a single grid and solving one set of equations with different material properties. A distance function enables to define the position and the interface of any objects with complex shapes inside the volume and to provide heterogeneous physical properties for each subdomain. Different anisotropic mesh adaptation algorithms based on the variations of the distance function or on using error estimators are used to ensure an accurate capture of the discontinuities at the fluid-solid interface. The monolithic formulation is insured by adding an extra-stress tensor in the Navier-Stokes equations coming from the presence of the structure in the fluid. The system is then solved using a finite element Variational MultiScale (VMS) method, which consists of a decomposition, for both the velocity and the pressure fields, into coarse/resolved scales and fine/unresolved scales. The distinctive feature of the proposed approach resides in the efficient enrichment of the extra constraint. In the first part of the thesis, we use the proposed approach to assess its accuracy and ability to deal with fluid-rigid interaction. The rigid body is prescribed under the constraint of imposing the nullity of the strain tensor, and its movement is achieved by solving the rigid body motion. Several test case, in 2D and 3D with simple and complex geometries are presented. Results are compared with existing ones in the literature showing good stability and accuracy on unstructured and adapted meshes. In the second part, we present different routes and an extension of the approach to deal with elastic body. In this case, an additional equation is added to the previous system to solve the displacement field. And the rigidity constraint is replaced with the corresponding behaviour law of the material. The elastic deformation and motion are captured using a convected level-set method. We present several 2D numerical tests, which are considered as classical benchmarks in the literature, and discuss their results.

Keywords: Fluid-Structure Interaction, Monolithic Formulation, Stabilized Finite Element Method, Anisotropic Mesh Adaptation, Incompressible flow, Rigid body motion, Elastic behaviour.

Résumé

L'Interaction Fluide-Structure (IFS) décrit une classe très générale de problèmes physiques, ce qui explique la nécessité de développer une méthode numérique capable de simuler le problème IFS. Un solveur IFS qui peut traiter un écoulement de fluide incompressible en interaction avec des structures élastique ou rigide est ainsi développé. Cela permet au solveur de couvrir une large gamme d'applications.

La méthode proposée est développée dans le cadre d'une formulation monolithique eulérien. Cette méthode consiste à considérer un seul maillage et à résoudre un seul système d'équations avec des propriétés matérielles différentes. Une fonction distance permet de définir la position et l'interface de tous les objets à l'intérieur du domaine et de fournir les propriétés physiques pour chaque sous-domaine. L'adaptation de maillage anisotrope basée sur la variation de la fonction distance est ensuite appliquée pour assurer une capture précise des discontinuités à l'interface fluide-solide.

La formulation monolithique est assurée par l'ajout d'un tenseur supplémentaire dans les équations de Navier-Stokes, qui tenseur provient de la présence de la structure dans le fluide. Le système obtenu est résolu par une méthode éléments finis et stabilisé grâce à une formulation variationnelle multi-échelle. Cette formulation consiste à décomposer les champs de vitesse et de pression en grande et petite échelle. La particularité de notre approche réside dans l'enrichissement du tenseur de l'extra contrainte. La première application est une simulation IFS avec un corps rigide. Le corps rigide est décrit en imposant une valeur nulle du tenseur des déformations, et le mouvement est obtenu par la résolution du mouvement de corps rigide. Nous évaluons le comportement et la précision de notre formulation proposée par la simulation dŠexemples $2D$ et $3D$. Les résultats sont comparés avec la littérature et montrent que la méthode est stable et précise.

La seconde application est une simulation IFS avec un corps élastique. Dans ce cas, une équation permettant de résoudre le champ de déplacement est ajoutée au système précédent. La contrainte de rigidité, quant à elle, est remplacée par la loi de comportement du corps élastique. La déformation et le mouvement du corps élastique sont alors obtenus en résolvant l'équation de convection de la level-set. Nous illustrons la flexibilité de la formulation proposée par des exemples $2D$.

Mots clés: Interaction Fluide-Structure, Formulation monolithique, Elément Finis Stabilisés, Remaillage anisotrope, Mouvements de corps rigide, Ecoulement incompressible, Comportement élastique.

Contents

1 General introduction **1**
- 1.1 Introduction to Fluid-Structure Interaction . . . 2
- 1.2 Brief literature review . . . 3
  - 1.2.1 Eulerian Formulation . . . 3
  - 1.2.2 Lagrangian Formulation . . . 3
  - 1.2.3 Arbitrary Lagrangian-Eulerian Formulation . . . 4
  - 1.2.4 Eulerian-Lagrangian Formulation . . . 5
  - 1.2.5 Fictitious Domain . . . 5
  - 1.2.6 Monolithic and partitioned approaches . . . 6
- 1.3 Objective of the thesis . . . 7
  - 1.3.1 Numerical method and applications . . . 8
- 1.4 Framework of the thesis . . . 9
- 1.5 Layout of the thesis . . . 10
- 1.6 Résumé français . . . 12

2 Level-Set Approach and Mesh Adaptation **14**
- 2.1 Introduction . . . 15
- 2.2 The Level-Set approach . . . 16
- 2.3 Mixing laws . . . 17
- 2.4 Construction of an anisotropic mesh . . . 18
  - 2.4.1 Anisotropic local remeshing method . . . 19
  - 2.4.2 An *a posteriori* error estimate method . . . 20
- 2.5 Interface tracking . . . 24
- 2.6 Conclusion . . . 25
- 2.7 Résumé français . . . 25

3 FSI with Rigid Body structure **26**
- 3.1 Introduction . . . 29
- 3.2 Rigid body motion . . . 30
- 3.3 Monolithic SFEM for rigid body motions in the incompressible navier-stokes flow . . . 32
  - 3.3.1 Introduction . . . 32
  - 3.3.2 Immersed volume method . . . 34

3.3.2.1 Level-set approach . . . 34
3.3.2.2 Mixing laws . . . 34
3.3.2.3 Anisotropic mesh adaptation . . . 35
3.3.3 Governing equations . . . 36
3.3.4 Stabilized finite-element method (SFEM) . . . 38
3.3.5 Numerical scheme . . . 41
3.3.6 Validation for 2D cases . . . 43
3.3.6.1 Immersion of solid bodies in fluid . . . 43
3.3.6.2 Several disks in an imposed flow . . . 45
3.3.6.3 Falling disk in a channel . . . 47
3.3.6.4 Tetris benchmark . . . 50
3.3.7 Conclusion . . . 51
3.4 Immersed Stress Method for FSI at high Reynolds number . . . 53
3.4.1 Introduction . . . 54
3.4.2 Immersed Volume Method . . . 56
3.4.2.1 Level-set approach . . . 56
3.4.2.2 Mixing laws . . . 56
3.4.2.3 Anisotropic mesh adaptivity . . . 57
3.4.3 Governing equations . . . 58
3.4.3.1 Rigid body restriction in a stationary Stokes flow . . . 59
3.4.3.2 The Navier-Stokes equations with a rigid body . . . 61
3.4.4 Stabilized Finite-Element Method (SFEM) . . . 64
3.4.5 Numerical experiments . . . 68
3.4.5.1 2D immersion of solid bodies in an incompressible fluid . . . 68
3.4.5.2 Immersion of solid bodies in fluid 3D . . . 70
3.4.5.3 Flow around a fixed circular cylinder (2-D) . . . 71
3.4.5.4 Oscillating circular cylinder in a channel . . . 74
3.4.5.5 Unsteady flow past an immersed helicopter in forward flight 75
3.4.6 Conclusion . . . 77
3.5 Monolithic VMS method for FSI with anisotropic adaptive meshing . . . 78
3.5.1 Introduction . . . 78
3.5.2 Construction of an anisotropic mesh . . . 80
3.5.2.1 Level-set function . . . 80
3.5.2.2 Edge based error estimation . . . 80
3.5.2.3 Gradient Recovery . . . 82
3.5.2.4 Metric construction from the edge distribution tensor . . . 82
3.5.2.5 Error behaviour due to varying the edge length . . . 83
3.5.2.6 Extension to multi-component field . . . 84
3.5.2.7 Mixing laws . . . 85
3.5.3 Governing equations . . . 86
3.5.3.1 The Navier-Stokes equations with a rigid body . . . 86
3.5.3.2 Full Euleurian formulation . . . 87
3.5.3.3 Rigid body kinetics . . . 89

3.5.4 Stabilized Finite-Element Method (SFEM) . . . 89
3.5.5 Numerical experiments . . . 92
3.5.5.1 Falling disk in a channel . . . 92
3.5.5.2 Falling cylinder in an incompressible fluid . . . 94
3.5.5.3 Tetris benchmark . . . 95
3.5.5.4 2D immersion of a NACA0012 airfoil in an incompressible fluid at Reynolds 5000 . . . 98
3.5.5.5 Unsteady flow past a 3D immersed simplified vehicle model 100
3.5.6 Conclusion . . . 101
3.6 Conclusion . . . 102
3.7 Résumé . . . 102

4 Lagrangian and Eulerian description 105
4.1 Introduction . . . 106
4.2 Lagrangian description . . . 106
4.2.1 Elementary Deformation . . . 107
4.2.2 Mass conservation . . . 109
4.2.3 Conservation of momentum . . . 109
4.2.3.1 St. Venant-Kirchhoff material . . . 109
4.2.3.2 Neo-Hookean material . . . 110
4.3 Eulerian description . . . 110
4.3.1 Deformation . . . 111
4.3.2 Mass conservation . . . 112
4.3.3 Conservation of momentum . . . 113
4.3.3.1 Fluid momentum equation . . . 113
4.3.3.2 Structural momentum equation . . . 114
4.4 Conclusion . . . 114
4.5 Résumé français . . . 115

5 FSI with Elastic structure 117
5.1 Introduction . . . 118
5.2 Governing equations . . . 118
5.2.1 Complete Eulerian formulation . . . 120
5.2.1.1 Weak form . . . 121
5.3 Stabilized Finite-Element Method (SFEM) . . . 124
5.3.1 MultiScale approach . . . 125
5.3.2 Coarse scale formulation . . . 126
5.3.3 Stablized formulation . . . 128
5.4 Numerical Results . . . 128
5.4.1 Ealstic flow cavity . . . 129
5.4.2 Oscillating disk . . . 131
5.4.3 Elastic plate in an imposed flow . . . 131
5.5 Conclusion . . . 134

5.6 Resumé français 135

6 General conclusion and perspectives **137**

Appendices

A Simulation of FSI in Nuclear Reactor **145**
A.1 Introduction 145
A.2 Context 147
A.3 Objectives 148
A.4 Immersed Volume Method 149
A.4.1 Level-set approach 149
A.4.2 Mixing laws 150
A.4.3 Anisotropic mesh adaptivity 150
A.5 Governing equations 151
A.6 Numerical experiments 153
A.6.1 Flow around a 2D immersed **fixed** cylinder 154
A.6.1.1 Permanent regime ($5 \leq \mathrm{Re} \leq 49$) 154
A.6.1.2 Periodic vortex shedding regime ($49 \leq \mathrm{Re} \leq 190$) 157
A.6.2 Flow around a 2D immersed **forced** oscillating cylinder 159
A.6.2.1 Locked configurations 160
A.6.2.2 Unlocked configurations 160
A.6.3 Flow around a 2D immersed **flexible** cylinder 163
A.7 Conclusion 166

References **167**

Chapter 1

General introduction

Contents

1.1 Introduction to Fluid-Structure Interaction 2

1.2 Brief literature review 3

1.2.1 Eulerian Formulation 3

1.2.2 Lagrangian Formulation 3

1.2.3 Arbitrary Lagrangian-Eulerian Formulation 4

1.2.4 Eulerian-Lagrangian Formulation 5

1.2.5 Fictitious Domain 5

1.2.6 Monolithic and partitioned approaches 6

1.3 Objective of the thesis 7

1.3.1 Numerical method and applications 8

1.4 Framework of the thesis 9

1.5 Layout of the thesis 10

1.6 Résumé français 12

1.1 Introduction to Fluid-Structure Interaction

Fluid-structure interaction (FSI) is the behaviour study of a system consisting of two different mechanical entities: a mobile structure (rigid or deformable) and a fluid (flowing or at rest) around or inside the structure. The evolution of each entity depends on the evolution of the other, thus a coupling phenomenon appears. More precisely, the aerodynamic forces influence the movement and/or deformation of the structure, on the other hand, the movement and/or deformation of the structure affects the fluid flow and thus the direction and intensity of the aerodynamic loads. FSI describes a wide variety of physical problems arising in engineering [1], technology [2], aerodynamics [3], automotive [4] and biomechanics [5]. The application varies from interaction of air and tissue in a human body to the aviation and shipbuilding in industry. For instance, the study of air flow over an airplane wing, a sail boat or a bridge structure is extremely important in the construction of these objects. Figure 1.1 illustrates the FSI cycle and represents several domain of applications. As noticed, the characteristic scales in time and space vary vastly from one application to another and understanding such coupled problems tend to be difficult.

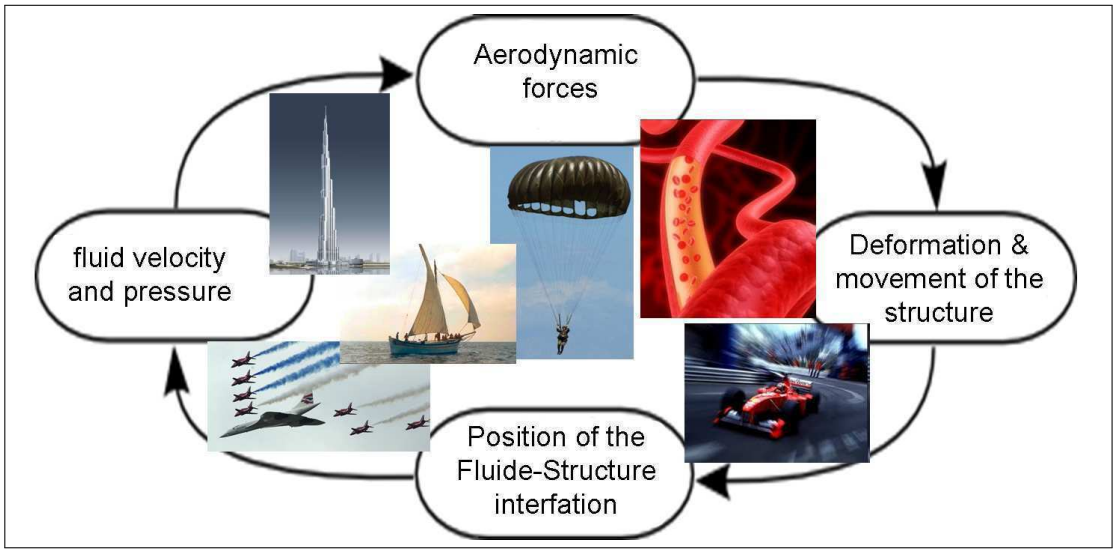


Figure 1.1: The FSI cycle (Wikipedia) with different domain of applications in engineering, aerodynamics, automotive and biomechanics

Because of the complexity of such problems, experimental studies are in general extremely costly and time consuming [6, 7]. Additionally, in spite of the available computers performance and the actual maturity of Computational Fluid Dynamics (CFD) and Computational Structural Dynamics (CSD), several key issues in the domain of computational FSI still prevent simulations from really helping in solving academic and industrial problems. FSI simulations are then nowadays the focus of numerous investigations, and various

approaches are proposed to treat them. Efforts are continuously pushed towards higher performance by seeking new developments that must be able to deal with different situations and regimes. In particularly, they must be able to treat encountered problems ranging from the mesh adaptation issues to the coupling engines between different codes, from small/large deformations to low/high Reynolds numbers flows and on simple to very complicated geometries.

In Centre of Material Forming, the development of advanced numerical methods on the FSI can be used for many applications in materials forming, especially multi-domain calculations, coupling-field tools, the phase change system, thermal control system, and some process such as quenching, drying and heat treatment, hydro forming.

1.2 Brief literature review

First, we present the state of the art and the different methods and models existing in the literature to tackle FSI problems. We begin by shedding light on the different formulations used.

1.2.1 Eulerian Formulation

The Eulerian description studies the evolution of a material quantity through a region of space. The associated reference system is fixed. In a finite element (FE) framework, the Eulerian formulation requires a fixed mesh in space. This mesh defines an invariable volume over time and a given material can migrate from one FE to another. Some material particles can even leave the initially defined area and, in this case any information on these particles is lost. The use of Eulerian formulations showed difficulties in the study of problems with moving boundaries [8]. The boundaries of the material don't generally coincide everywhere and at all times with the edge of an element. As a result, taking into account the physical boundary conditions present a major difficulty. Also the precision of the material boundaries are affected when evolving in time. Thus many elements are needed to cover the space where the material will be located during the simulation. From another part, the Eulerian formulation allows a significant distortion of the material. This explains the use of the Eulerian formulation in fluid mechanics or in the case of forming materials when studying the stationary processes. Additionally, modelling an elastic material in an Eulerian framework is also possible as presented in the works of Cottet et al. [9], where the interaction of an isotropic elastic membrane and a viscous incompressible fluid is simulated.

1.2.2 Lagrangian Formulation

In the Lagrangian description, the particle's motion is considered as a certain quantity moving in space starting from a known reference. The reference system is attached to the particle. This formulation is widely adopted in solid mechanics [10]. In the FE

method, the Lagrangian formulation requires that each node remains in contact with the same material particle throughout the deformation process. This property is interesting from a numerical point of view because, during the integration of constitutive equations, the convective terms do not appear in the equations. Moreover, each node remains in coincidence with the same phase throughout the whole deformation process. In particular, the nodes located at the interface of the solid remain on its boundary during the whole simulation and hence, tracking a moving interface does not present major difficulties. However, in the presence of large deformations, the mesh can be distorted and this leads to inaccurate results if not the end of the simulation. Thus an expensive but necessary mesh adaptation is required.

1.2.3 Arbitrary Lagrangian-Eulerian Formulation

Among the used approaches, the arbitrary Lagrangian-Eulerian (ALE) gained lots of interest [11, 12, 13]. It combines the advantages of the Lagrangian representation (well-defined interface, facility at imposing boundary conditions) and those of the Eulerian formulation (possibility of handling large distortions). The idea of this mixed formulation is the development of a grid moving at an independent rate of the structure. As a result, the structure moves relative to the mesh, as in a pure Eulerian formulation, but the external shape of the elements is controlled by the boundary conditions of the problem, as in a Lagrangian formulation. Note that in FSI, the Navier-Stokes equation would be solved in a moving/deformable domain. As a consequence, a modification of the convective term is required. Moudid [14] uses ALE formulation for the incompressible fluid and a Lagrangian formulation for the structure. The simulation of a fluid flow in a channel with a flexible wall or not in the presence of deformable obstacles is achieved by developing an instantaneous model to control each part the fluid and the structure. At each iteration, the obtained pressure from the fluid numerical model is used as the external solicitation for the solid numerical model.

ALE method works very well for the FSI problem as long as the rotations, translations/deformations of the solid remain within certain limits [15, 16, 17]. However, for problems in which these limits are exceeded, the elements become ill-shaped , and the ALE is not enough. Figure 1.2 shows the distorted ALE meshes due to the thin structural motion. As a solution to this problem, a combination of ALE with some form of remeshing is often used [19]. However, this can be a difficult task. Another effective solution is developed in Wall et al.'s work [20, 21, 22] . A deformable fluid mesh using the ALE formulation is extended over a fixed Eulerian mesh. The mesh is connected to the moving structure and deforms according to the interface deformation. As an advantage of this approach, the ALE domain does not extend on the whole fluid domain. Indeed, it moves and deforms with the structure while the majority of the background mesh remains fixed. The fixed Eulerian mesh and deforming ALE fluid mesh are coupled using the extended finite element method (XFEM) and the Lagrange multipliers. Sternel et al. [23] use the finite volume method for the fluid and the FE method for the solid. They adapt the ALE

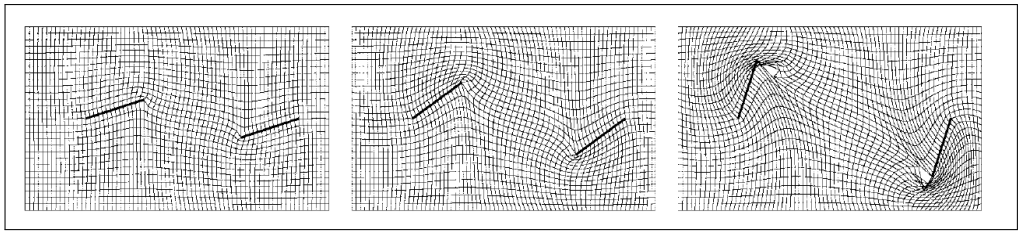


Figure 1.2: Distorted ALE meshes as presented in [18]

method using a nonlinear multigrid technique.

As noticed, the ALE method is not sufficient to model FSI problems; it always requires coupling with other techniques.

1.2.4 Eulerian-Lagrangian Formulation

The Eulerian-Lagrangian method models the fluid in an eulerian description and the structure in the Lagrangian description [24]. The essential difference compared to ALE method maintains in the way the fluid mesh is treated. In this case, it is not affected by the motion of the fluid-structure interface and thus preventing mesh distortion when the structural deformation or rotation is important as depicted in the figure 1.2. The fluid-structure interface is defined by the level-set method. The fluid and structure can be coupled using a Lagrange multiplier methods and penalty methods [18]. Legay and coworkers [25, 26] used the Eulerian-Lagrangian description in order to deal with several thin structures immersed in a fluid. The space-time approximations of the velocity and pressure are enriched using appropriate functions (the extended FE method), to take into account the different discontinuities due to the presence of the structure in the fluid. The enriched domain is the set of all elements cut by the structures.

1.2.5 Fictitious Domain

Fictitious Domain methods are considered as a powerful technique for solving partial differential equations [27, 28]. The basic idea is to extend a problem on a complex geometry domain (possibly time-dependent) to a larger easier domain (the fictitious domain). This framework provides two main advantages for solving the problem:

- The extended domain is a simple geometry; as a result it admits simpler and more regular meshes. This fact allows faster resolution methods such as direct solvers for elliptical problems on rectangular domains.
- The extended domain can be time-independent even if the original domain is time dependant. Thus, the same fixed mesh can be used for the whole resolution, eliminating the need to repeat the remeshing and projection.

Indeed, the boundary conditions on the initial boundary domain must be applied on the extended domain, so that the solution remains the same. This method has been used by Glowinski et al. [28, 29] to solve FSI problems with large rotations and translations of the rigid bodies. Using this method, the sedimentation of rigid bodies in a fluid domain can be calculated. The solids are immersed in the fluid domain and coupled by applying constraints using a Lagrange multiplier. Similar methods were introduced for thin bodies: a fluid mesh is considered and the solid mesh is immersed and both are coupled with the Lagrange multiplier applied on the structural interface [30]. This method is no longer limited to thin bodies by introducing Lagrange multipliers throughout the entire solid body. In fact, using this approach, Yu et al. [31] were able to calculate the pressure drop across the solid body, which is very important in biomechanics. A combination of a fictitious domain method with mesh adaptation is proposed by Lon Van et al. [32, 33] in order to calculate the pressure drop and shear stress on the structural interface. In this article, the pressure drop through a plastic membrane using the fictitious domain with mesh adaptation is presented.

1.2.6 Monolithic and partitioned approaches

Two mainly approaches are presented in the literature to solve the solid and fluid behaviour: the monolithic and the partitioned approaches.

The monolithic method consists in solving, using one single grid, the same system describing the fluid and the structure mechanical equations. The disadvantage of this method is that it does not allow to couple existing fluid and solid solvers, instead a global specific framework is needed. Examples of a monolithic method are presented in the work of Hübner et al. [34] and Walhorn et al. [35], where the linearized equations of the fluid structure and the coupling conditions are solved simultaneously in one system without taking into account the fluid pressure.

The partitioned method allows the use of specific codes for each domain. Smaller and better conditioned subsystems are solved instead of a global problem. The difficulty appears when exchanging information from one code to another. Two coupling algorithms are distinguished in the partitioned approach: strongly and weakly coupled schemes [36, 37, 38, 39].
Loosely coupled schemes require a single solution for each field in each time increments. As a consequence, an accurate achievement of the coupling conditions is not accomplished. These schemes present an intrinsic instability once applied on FSI problems with incompressible flow. The instability depends on the fluid/ structure density ratio and the geometry of the domain [40]. Also, restrictions on the time step are expected. However, studies show that reducing in time step increases the instability. The instability exists in the scheme itself; it is called the artificial added mass effect [41]. In fact, parts of the fluid act as an additional weight on the structural degrees of freedom at the coupling interface. In other terms, the fluid forces depend on the predicted structural displacement at the

interface instead of the real forces and therefore include some incorrect coupling forces. This contribution induces instability. In application, the artificial added mass effect does not occur in aero-elastic problems but much more relevant in biomechanical applications. Strongly coupled schemes and monolithic schemes converge to the same solution and both require sub-iterations. But, when the problem become more complex, the iterations of the strongly coupled schemes are more difficult to resolve. The advantages and disadvantages of the both approaches are summarized in figure 1.3. As presented in the work of Razzaq [42], comparison on their flexibility, stability and robustness of the needed programming is highlighted.

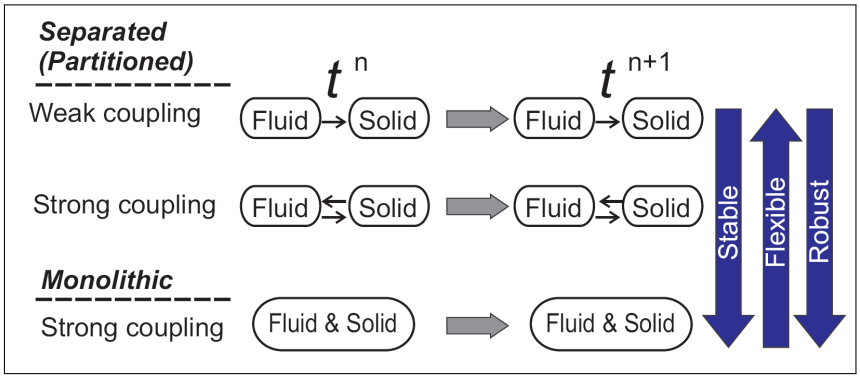


Figure 1.3: Coupling strategies for FSI problem as presented in [42]

Idelsohn et al. [43] have developed a Laplacian matrix at the interface which allows reaching the same convergence results as the monolithic approach. It can be achieved by separating the pressure from the velocity (the velocity is calculated independently of the pressure and the pressure is then calculated using the previous results). This work circumvents the problem of the artificial added mass effect and presents the simulation of an incompressible fluid and an elastic solid for different time steps and different density ratios.
The thesis of Förster [44] is devoted to improve the stabilization methods for the partitioned approach based on an ALE formulation for the flow with a FE and a Lagrangian formulation for the structure using a nonlinear solver. A key to a stable algorithm is the geometric conservation and its effect to a stable simulation of the fluid flow over a deforming domain. This regime is stable when the structural density is much higher than the fluid's. As an example: the interaction of structures with an air flow.

1.3 Objective of the thesis

As explained previously, the more general way for solving FSI problem is the monolithic approach in an Eulerian framework. In fact the difficulty of the remaining approaches is that they require the development of a specific FSI solver, an accurate coupling of the

schemes and mesh adaptation. In the monolithic approach, the former is done naturally but the latter remains applicable. The purpose is to reach a formulation capable of dealing with any structure: elastic or a rigid one. As a consequence, a main objective of this thesis is to propose a monolithic approach for FSI based on the multidisciplinary expertise of CIMLib [45, 46], a FE library, developed in CEMEF. Such expertise is present in the Immersed Volume Method (IVM) which is an effective tool to circumvent problems of meshes overlapping and is widely used in fluid applications [47, 48].

The solid is immersed in the fluid using level-set functions [49, 50]. The deformation/motion of the structure is realised by solving the convection equation of the level-set function. To improve the geometric representation and the numerical results, anisotropic mesh adaptation is used [51, 52, 53, 54]. This technique enables to produce strongly stretched element near the fluid-structure interface. All these numerical tools along with the development of a stable FE solver in the CIMLib library will contribute to achieve a reliable FSI modelling system.

1.3.1 Numerical method and applications

To cover a wide range of FSI applications, we were interested, to start with, the simulation of an immersed elastic/rigid structure in an incompressible fluid flow. Simulating rigid bodies in a flow still a difficult challenge using a monolithic framework. The complexity remains in reaching a global system for the rigid and fluid having such different behaviours.

The seeked global formulation should respond properly to the structural and fluid performance and reaction. Thus the primary variables for each one should be respected and well presented. Mixed FE methods and irreducible methods have been used for the solution of solid mechanics problems. In the former, the displacement and constraints fields are considered to be primary variable. In the latter, only the displacement field is considered as primary variable and then the stress field can be obtained. While irreducible methods lack precision for the behaviour of nonlinear solid, the mixed method has two drawbacks: computational cost and lack of stability. Cerva et al. [55] present the advantage of mixed stabilization methods comparing to the irreducible methods, and provide a stable mixed strain/displacement and stress/displacement FE formulation. The incompressible fluid problem requires the velocity and pressure as primary variables, an irreducible formulation is not applicable.

Tthe first examples on FSI with rigid body were developed in CIMLib [56, 57, 58]. In this case, the rigid body is treated by simply penalizing the strain rate using a very important viscosity in the solid, which can be sometimes sufficient [59, 60, 61]. It is also possible to enforce directly the nullity of the strain by using an Augmented Lagrange Mulptipliers method [29, 62, 63, 59], solved by an iterative Uzawa algorithm. The problem is solved by adding an extra-stress tensor coming from the presence of the structure in the fluid.

In this work, we propose to describe the global behaviour by the classical Navier-Stocks equations, with an extra-stress tensor for the structure. The velocity and pressure are considered as primary variables for the whole system while the extra-stress tensor reflects the behaviour law of the immersed structure. It is worth mentioning, that this stress tensor can be generalized for a rigid or an elastic body. In order to complete the system and the description of the solid behaviour, an additional equation is added which depends on the structural behaviour law. And finally the displacement variable is added when dealing with an elastic body since it is's a primary variable in this case.

The last essential key to model the complete FSI problem is maintaining its stability and thus developing the appropriate stabilized FE method. In fact, in the presence of high discontinuity material properties at the interface between the fluid and solid, numerical oscillations appear at the interface and pollute the global solutions. Additionally, the classical FE approximation for the flow problem alone must verify two criteria: the compatibility condition known by the inf-sup or "Brezzi-Babuska" condition which requires an appropriate pair of the function spaces for the velocity and the pressure [64, 65, 66] and the stability in the convection dominated flows [67, 68]. Therefore, we propose an extension of the multiscale-stabilized Navier-Stokes solver [61, 67] taking into account the solid constraint as an extra-stress tensor. It uses a multiscale stabilized FE method based on the enrichment of the functional spaces for the velocity, the pressure and the stress tensor.

1.4 Framework of the thesis

This thesis was supported by *Carnot* and MINES. The objective is to start and develop a new FSI thematic and activity at CEMEF. During the three year Phd program, several industrial partner were interested in such FSI formulation. We recall three examples:

- **EFD and CEA** : The simulation of Fluid-Structure Interaction in Nuclear Reactor. A master project was financed and a master degree student was recruited to work on this project.
- **Technicom - Thales** : The simulation of an elastic solid structure embedded in a fluid. A Phd program with Nice university is obtained for 2012-2015.
- **Helicoop** : A small study for the simulation of unsteady flow around a helicopter.

All the developments and numerical simulations in this thesis were carried out using CIMLib [46, 45, 69] a FE C++ library developed in CEMEF (www.cemef.mines-paristech.fr) by CIM research group (Calculs Intensifs en Mécanique). CIMLib is the base for different numerical applications developed at CEMEF, in collaboration with other research teams and industrial partners. This scientific library represents an Object Oriented Program and a fully parallel code, written in C++, and gathers the numerical developments of the group (Ph.D. students, researchers, associate professors, etc). It aims

at providing a set of components that can be organized to build numerical softwares, such as REM3D, XIMEX, Forge3 and THOST. It also has the capability of performing mesh adaptation by calculating metrics which are in turn send to MTC, a topological mesher-remesher interfaced in CIMLib and developed by T.Coupez [51, 70]. MTC is based on local mesh topology optimizations and works for all meshing applications, from adaptive remeshing to mesh generation, using a minimal volume principle.

1.5 Layout of the thesis

The manuscript is organized as follows: The second chapter constitutes the core of the monolithic method where all details are given. We begin by explaining the use of level-set functions to define the structure along with the material properties all over the domain. Afterwards, we present the different mesh adaptation techniques used in this work. Furthermore, interface tracking when dealing with a structure in motion or deformation is explained. In the third chapter, the formulation with a rigid body in an incompressible fluid flow is detailed. The monolithic approach is realised by adding an extra stress tensor to the Navier-Stokes equation. This extra stress represents the presence of the structure in the fluid domain. The stabilized FE formulation based on the variational multiscale method is detailed. Several applications are performed in order to prove the efficiency of our algorithms in 2D and 3D. Comparison with the litterature and other approaches are also considered.

The fourth chapter details the Lagrangian and Eulerian approach needed to reach a similar formulation for the fluid and elastic structure. We begin by explaining the Lagrangian formulation along with the momentum and mass conservation equation usually written in this framework when dealing with solid mechanics problems. Then the reformulation of these quantities in an Eulerian approach is described. Furthermore, the balance equation of an incompressible fluid is presented. The fifth chapter is dedicated to the second application performed on FSI problems with an elastic body. A similar system to the one achieved for FSI problems with a rigid body is reached, showing the general phase of the solver. Several examples to illustrate the efficiency of the method are presented at the end. Furthermore, the general conclusion and perspectives are presented in the sixth chapter. Finally, an application on FSI in nuclear reactor for the industrial partner, EDF, is presented in the appendix.

Since there are four papers in this document, some aspects may be revisited for completeness.

The work in this thesis has contributed to the following written publications in international Journals:

- S. El Feghali, E. Hachem, and T. Coupez, Monolithic stabilized finite element method for rigid body motions in the incompressible Navier-Stokes flow, *European Journal of Computational Mechanics* , vol 19. 547−573, 2010.

- E. Hachem, S. Feghali, R. Codina, T. Coupez, Immersed Stress Method for solving Fluid-Structure Interaction at high Reynolds number, *submitted to International Journal for Numerical Methods in Engineering* , April 2012.

- E. Hachem, S. Feghali, T. Coupez, R. Codina, Monolithic Variational Multiscal method for Fluid-Structure Interaction with Anisotropic Adaptive Meshing, *submitted to Computer and Structures*, May 2012.

and the following oral and written communications:

- S. Feghali, E. Hachem, T. Coupez, Stable/Stabilized mixed formulation for fluid structure interaction: theory and application. In *Fluid Structure Interaction Symposium*, UTC, Compiègne, France, June 3−4, 2010.

- E. Hachem, S. Feghali and T. Coupez, Stabilized Finite Element Methods vs LES modeling for fluidstructure interaction with anisotropic adaptive meshing. In *French Research Group in Fluid-Structure Interaction (GDR IFS et Turbulence)* , ESPCI, Paris, France, November 3−5, 2010.

- S. Feghali, E. Hachem, T. Coupez, A full Eulerian stabilized finite element method for fluid structure interaction. In *16th International Conference on Finite Elements in Flow Problems (FEF 2011)* , Munich, Germany, March 23−25, 2011.

- E. Hachem, S. Feghali, H. Shaw, H. Digonnet and T. Coupez, 3D Anisotropic Adaptive Meshing and Stabilised Finite Element Methods for Multiphase Flows at Low and High Reynolds Number. In *Coupled Problems in Science and Engineering (Coupled 2011)*, Island of Kos, Greece, June 20−22, 2011

- S. Feghali, E. Hachem and T. Coupez, The use of Variational Multiscale Method to solve Fluid-Structure Interaction problem. In *French Research Group in Fluid-Structure Interaction (GDR IFS 2011)* , CEMEF, Sophia Antipolis, France, October 8−9, 2012.

- S. Feghali, E. Hachem and T. Coupez, Development of new stabilized three-fields finite element method for fluid-structure interaction. In *The Third Annual Meeting of the Lebanese Society for Mathematical Sciences (LSMS 2012)* , Beirut, Lebanon, April 27−28, 2012.

- E. Hachem, S. Feghali, T. Coupez, Immersed Stress Method for solving Fluid-Structure Interaction with Anisotropic Mesh Adaptation, *11th U.S. National Congress on Computational Mechanics (USNCCM)*, Minnesota, USA, July 25−29, 2011.

1.6 Résumé français

Ce chapitre constitue l'introduction de cette thèse effectuée au Centre de Mise en Forme des matériaux (CEMEF). Premièrement, l'interaction fluide- structure (IFS) est présentée, avec ses différentes applications ainsi que ses limites.

Nous avons ensuite réalisé une brève étude bibliographique sur les différentes méthodes adaptés aux problèmes IFS et notamment les approches monolithique et partitionnés. Nous décrivons ensuite l'objectif de cette thèse qui consiste à modéliser le problème IFS dans un cadre monolithique. Pour y parvenir, des modules numériques déjà présents dans la CIMLib sont utilisés tels que l'immersion de volume et l'adaptation de maillage. Le développement d'un nouveau solveur élément finis stabilisé et son implémentation dans CIMLib sont les premiers objectifs de ce travail. La stabilisation est basée sur l'enrichissement des espaces fonctionnels pour la vitesse, la pression et la contrainte.

Les applications mécaniques sont ensuite introduites. La première application IFS est la simulation de l'interaction fluide-rigide et la deuxième est la simulation de l'interaction fluide-élastique. Ces problèmes sont gouvernés par les équations de Navier-Stokes avec une extra-contrainte régissant la présence de la structure dans le fluide. Concernant l'application fluide-élastique, le champ de déplacement sera aussi calculé. Finalement, l'organisation de ce manuscrit de thèse sera détaillée et les contributions de cette thèse seront énumérées.

Chapter 2

Level-Set Approach and Mesh Adaptation

Contents

2.1 Introduction 15
2.2 The Level-Set approach 16
2.3 Mixing laws 17
2.4 Construction of an anisotropic mesh 18
2.4.1 Anisotropic local remeshing method 19
2.4.2 An *a posteriori* error estimate method 20
2.5 Interface tracking 24
2.6 Conclusion 25
2.7 Résumé français 25

2.1 Introduction

Recall that in the partitioned approaches, often used to simulate FSI problems, the global domain is divided into several subdomains [36, 37, 38] where each one is analyzed separately. The global solution is then constructed by suitably joining local solution from each subdomain. The difficulty remains in coordinating between the meshes. As a result, adapting the mesh becomes a necessity and occasionally extremely costly. Other alternative approaches have been applied to represent the fluid-structure interface such as the Immersed Boundary (IB) methods and the fictitious domain method. The interface is convected in a Lagrangian way using the immersed boundary (IB) methods [27, 71]. The fictitious domain method [27, 28] treats the coupling between the domains by applying a constraint across the rigid body using a Lagrange multiplier. To simulate the interaction of thin and bulky structures the extended finite element method (XFEM) is combined with a Lagrange multiplier [20]. In this case, the Eulerian fluid field and the Lagrangian structural field are partitioned and iteratively coupled using Lagrange multiplier techniques.

In the present work, we are going to use, detail and extend an implicit method to capture the interface, the Immersed Volume Method (IVM) [61]. This method is based on the level-set approach, on mixing laws and on meshing adaptation. Using the level-set approach and the mixing laws the different interface and physical properties would be defined. Consequently, different subdomains are treated as a single fluid with variable material properties. As a result, the coupling at the fluid-structure interface is obtained naturally and no need to enforce it. Moreover, the calculations of the boundary integrals are no longer applicable since the fluid-structure interface is only defined by the zero value of the level-set function.

Furthermore, dealing with fluid-structure problems in a monolithic context undermines the necessity to work with a fine mesh at the interface not only to describe properly the considered structure but also to take into account high discontinuities of physical properties. The proposed mesh generation algorithm allows the creation of anisotropic elements stretched along interface. Definitely, when dealing with moving structures, periodic mesh adaptation is required to follow the interface all along the computations. To track this interface, the level-set function should be convected. Hence, the motion and/or deformation of the structure is naturally taken into consideration.

Note that, this method is coupled with some additional features that could allow the resolution of a single set of equation for both solid and fluid. In our case, the immersion of the extra-stress tensor to take into account the behaviour law of the solid (detailed in chapters 3 and 5).

The outline of the chapter is as follows: first the level-set approach is explained; next a brief review on mixing different physical properties for each sudbomain is prescribed; then different possible mesh adaptation algorithms are highlighted and finally interface tracking is presented.

2.2 The Level-Set approach

A signed distance function of an interface Γ is used to localize the interface of the immersed body Ω_s and initialize the desirable properties on both sides of this interface. At any point $\mathbf{x}$ of the computational domain Ω, the level-set function α corresponds to the signed distance from Γ. In turn, the interface Γ is then given by the iso-zero of the function α:

$$\begin{cases} \alpha(\mathbf{x}) = \pm d(\mathbf{x}, \Gamma), \mathbf{x} \in \Omega, \\ \Gamma = \{\mathbf{x}, \alpha(\mathbf{x}) = 0\} \end{cases} \tag{2.1}$$

In this document, a sign convention is used: $\alpha \geq 0$ inside the immersed body defined by the interface Γ and $\alpha \leq 0$ outside this domain. Figure 2.1 illustrates a level-set function of a circular domain. The values of this function are positive inside the domain, negative outside and null at the interface. Further details about the algorithm used to compute the distance are available in [72].

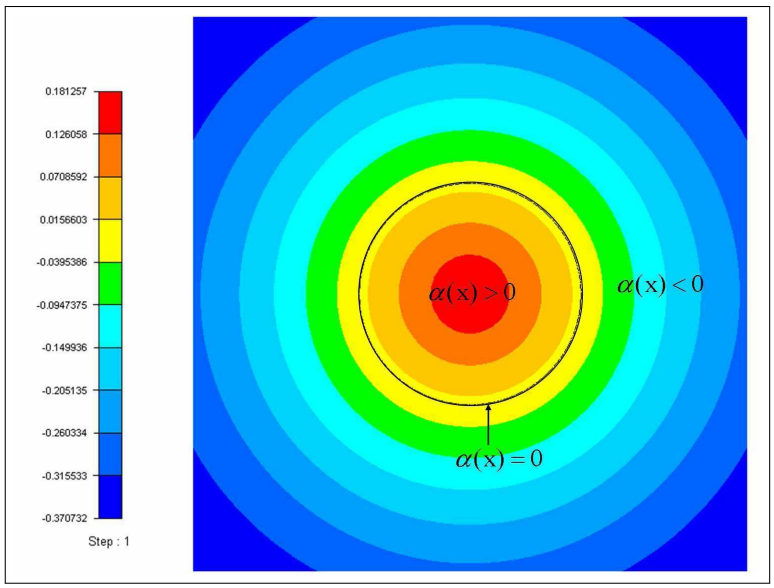


Figure 2.1: The level-set function of a circular domain. The interface of the circle is highlighted in black

The treated solids can have simple geometry, such as the presented circular domain, thus simple analytical level-set function is used. For complicated geometry, the solids are immersed using their discretized mesh. So the level-set function is the computed in CimLib with respect to the faces of the immersed mesh [50]. Figure 2.2illustrates the immersion of complex geometries: a helicopter and Ahmad body.

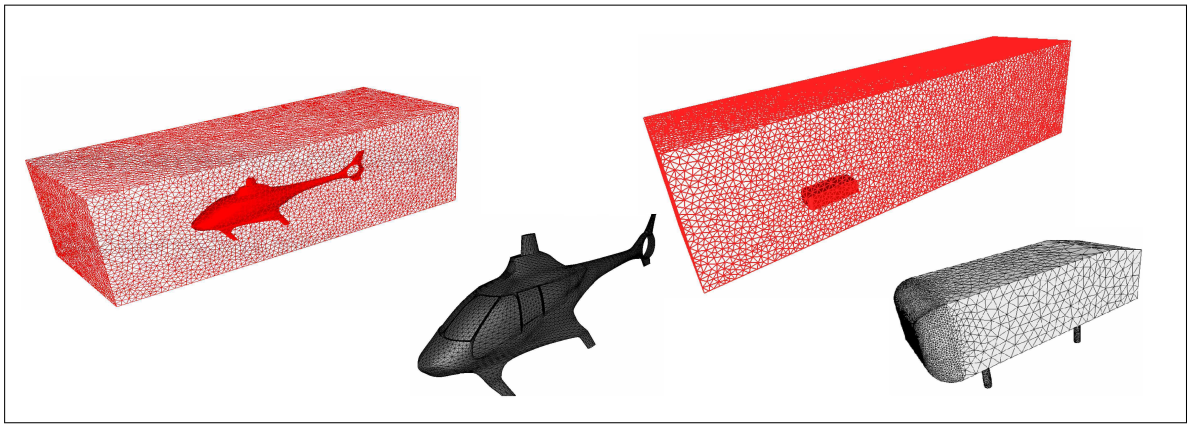


Figure 2.2: The immersion of complex geometries: a helicopter on the left, the Ahmad body on the right.

2.3 Mixing laws

The geometry and mechanical properties of each subdomain are characterized by one signed distance function. Once all the sub-domains are defined, the mechanical properties can then be determined on the whole domain in function of the level-set function. For the elements crossed by the level-set functions and their neighbours, fluid-solid mixtures are used to determine the element effective properties.

A heaviside function $H(\alpha)$ for each level-set function is defined by:

$$H(\alpha) = \begin{cases} 1 & \text{if } \alpha(\mathbf{x}) > 0 \\ 0 & \text{if } \alpha(\mathbf{x}) < 0 \end{cases} \tag{2.2}$$

In order to achieve a better continuity at the interface [73], the heaviside function can be smoothed using:

$$H(\alpha) = \begin{cases} 1 & \text{if } \alpha(\mathbf{x}) > \varepsilon, \\ \frac{1}{2}\left(1 + \frac{\alpha}{\varepsilon} + \frac{1}{\pi}\sin\left(\frac{\pi\alpha}{\varepsilon}\right)\right) & \text{if } |\alpha(\mathbf{x})| \leq \varepsilon, \\ 0 & \text{if } \alpha(\mathbf{x}) < -\varepsilon, \end{cases} \tag{2.3}$$

where ε is a small parameter such that $\varepsilon = O(h_i)$, known as the interface thickness, and h_i is the mesh size in the normal direction to the interface. In the vicinity of the interface, it can be computed using the following expression:

$$h_i = \max_{j,l \in K} \nabla\alpha \cdot \mathbf{x}^{jl}, \tag{2.4}$$

where $\mathbf{x}^{jl} = \mathbf{x}^l - \mathbf{x}^j$ and K is the mesh element. Thus, the linear $P1$ interpolations of the heaviside function are easily obtained since they are computed by looking at the sign

of $\alpha(\mathbf{x})$ at each node $\mathbf{x}$ of the mesh. For a piecewise constant $P0$ interpolation, $H(\alpha)$ is computed from the distance function α as follows:

$$H(\alpha)_{|k} = \frac{\alpha_k^+}{\mid \alpha \mid_k}, \tag{2.5}$$

where α_k^+ is the sum of all positive α evaluated at nodes of element K and $\mid \alpha \mid_k$ is the sum of absolute values of α.

According to the chosen approximations, the physical properties in the domain are calculated as a function of $H(\alpha)$. For instance the density ρ can be calculated between its values in the fluid ρ_{fluid} and the solid ρ_{solid} :

$$\rho = \rho_{\text{solid}} H(\alpha) + \rho_{\text{fluid}}(1 - H(\alpha)). \tag{2.6}$$

The density evolution across the interface is presented in figure 2.3, it's calculated using a linear and piecewise interpolation. For a $P0$ approximation, the mixing zone is applied across an element on the fluid-structure interface. While for a $P1$ approximation, the mixing zone depend on the chosen thickness ε (eventually $1.5h$ where h is the mesh size).

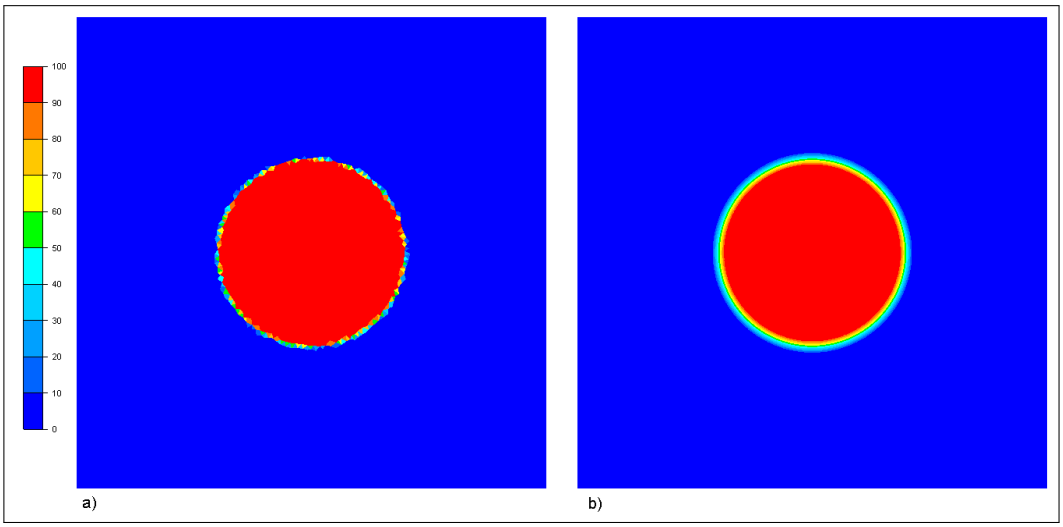


Figure 2.3: Density distribution across the interface using a $P0$ approximation a), a $P1$ approximation b)

2.4 Construction of an anisotropic mesh

An accurate calculation of the velocities, strains and stresses along the fluid-solid interface is critical for a correct modelling of different FSI applications. The difficulty arises due to the high discontinuity of the properties of the material across the interface from

one hand, and due to the interface transition controlled by the element size from another hand.

Isotropic refinement of the mesh can be used to reach a desired accuracy in the interface description. However, this strategy leads to a significant increase of computation resources. An adaptive anisotropic remeshing technique is therefore preferred. Different ways exist to generate adapted anisotropic meshes. In the following sections of this chapter we will present different mesh adaptation methods that are applied in this work.

2.4.1 Anisotropic local remeshing method

The main idea of this method is to couple the level-set process with anisotropic mesh adaptation, described in [52], in order to pre-adapt the mesh at the interface. The mesh becomes locally refined in a narrow zone surrounding the interface. The refinement operates on both directions, perpendicular and tangential to the interface, which leads to highly stretched element in one direction and very fine one in the other direction. This anisotropic meshing method enables to sharply define the interface and to save a great number of elements compared to classical isotropic refinement [52].

Let us briefly described the main principles of this technique. First of all, the generation of such meshes requires the definition of a metric field and the use of a topological mesher. Recall that a metric is a symmetric positive defined tensor representing a local base that modify the distance computation, such that:

$$||\mathbf{x}||_{\mathrm{M}} = \sqrt{{}^{T}\mathbf{x}\cdot\mathbb{M}\cdot\mathbf{x}}\ , \quad <\mathbf{x},\mathbf{y}>_{\mathrm{M}}={}^{T}\mathbf{x}\cdot\mathbb{M}\cdot\mathbf{y}\ . \tag{2.7}$$

If $\mathbb{M}$ is the identity tensor, one recovers the usual distances and directions of the Euclidean space. As $\mathbb{M}$ is a symmetric positive definite tensor, it is diagonalizable in an orthonormal basis of eigenvectors, and all the eigenvalues are strictly positive. The metric $\mathbb{M}$ can be regarded as a tensor whose eigenvalues are related to the mesh sizes, and whose eigenvectors define the directions for which these sizes are applied. In fact, when a metric is utilized in mesh construction, the size of the element in the direction of $\mathbf{v}_{\mathrm{i}}$ becomes $\frac{1}{\sqrt{\lambda_{\mathrm{i}}}}$, where λ_{i} is the i^{th} eigenvalue of $\mathbb{M}$ and $\mathbf{v}_{\mathrm{i}}$ is the associated eigenvector.

Let us consider the simple case of only one interface. The iso-zero of the level set function represents the boundary, Γ , and the gradient of the level set function:$\mathbf{x}' = \nabla\alpha/||\nabla\alpha||$ defines the normal to the boundary which corresponds to the direction of mesh refinement. To define the mesh size in that direction, and its distribution in space, a characteristic thickness e is introduced:

$$\begin{cases} |\alpha(\mathbf{x})| \leq \frac{e}{2} & \text{near the interface} \\ |\alpha(\mathbf{x})| > \frac{e}{2} & \text{far from the interface} \end{cases} \tag{2.8}$$

A default mesh size, or background mesh size is imposed far from the interface and it is reduced in the direction perpendicular to the interface as $|\alpha(\mathbf{x})|$ is reduced e.g. as the interface comes closer. Let us require an isotropic mesh size equal to h_d outside the anisotropic boundary layer. A likely choice for the mesh size evolution is the following:

$$h = \begin{cases} h_d & \text{if } |\alpha(\mathbf{x})| > e/2 \\ h_e = \dfrac{2h_d(m-1)}{m\ e}|\alpha(\mathbf{x})| + \dfrac{h_d}{m} & \text{if } |\alpha(\mathbf{x})| \leq e/2 \end{cases} \tag{2.9}$$

Eventually, at the interface, the mesh size is reduced by a factor m with respect to the default value h_d. Then this size increases until equalling h_d for a distance that corresponds to the half of a given thickness e. The unit normal to the interface $\mathbf{x}'$ and the mesh size h_e defined above, lead to the following metric:

$$\mathbb{M} = C\,(\mathbf{x}' \otimes \mathbf{x}') + \frac{1}{h_d}\,\mathbb{I} \quad \text{with} \quad C = \begin{cases} 0 & \text{if } |\alpha(\mathbf{x})| \geq e/2 \\ \dfrac{1}{h_e^2} - \dfrac{1}{h_d^2} & \text{if } |\alpha(\mathbf{x})| < e/2 \end{cases} \tag{2.10}$$

where $\mathbb{I}$ is the identity tensor. The mesh resolution is forced to concentrate in particular areas of interest. This metric returns to isotropic far from the interface (with a mesh size equal to h_d for all directions) and to anisotropic near the interface (with a mesh size equal to h_i in the direction $\mathbf{x}$ and equal to h_d in the others).

In practice, anisotropic meshes are generated in several steps using the MTC mesher and remesher developed by Coupez [51, 74]. It is based on local mesh topology optimizations and works for all meshing applications from adaptive remeshing to mesh generation by using a minimal volume principle. MTC improves the mesh topology by considering the quality of the elements. The quality of an element is defined through a shape factor which takes into account the considered metric [75].

Figure 2.4 illustrates a result obtained for an immersed disk in a 2D unit square. The anisotropic mesh adaptation was realized with $h_d = 0.02$, $m = 40$ and $e = 0.03$. The anisotropic mesh is made of 12502 elements. Figure 2.4b presents a close-up on the interface, the mesh has been refined when approaching the interface. Consequently, only additional nodes are locally added in this region, whereas the rest of domain keeps the same background size.

The proposed mesh generation algorithm works well for 2D or 3D complex shapes. It allows the creation of meshes with extremely anisotropic elements stretched along the interface. The mesh size is then only refined in the direction of the gradient of the level-set and as a consequence in the wake of the high physical and mechanical properties gradients. This allow conserving a high precision in the calculus and in the geometry description, in spite of an important decrease of the total number of degrees of freedom. The grid is furthermore only modified in the vicinity of the interface which keeps the computational work devoted to the grid generation low.

2.4.2 An *a posteriori* error estimate method

In this section, a different route to compute the metric and to account for the anisotropic mesh adaptation along the interfaces is presented. The proposed procedure is controlled by a directional error estimator based on local interpolation error and recovery of the second derivatives of the level-set function (the so-called Hessian strategy) [76].

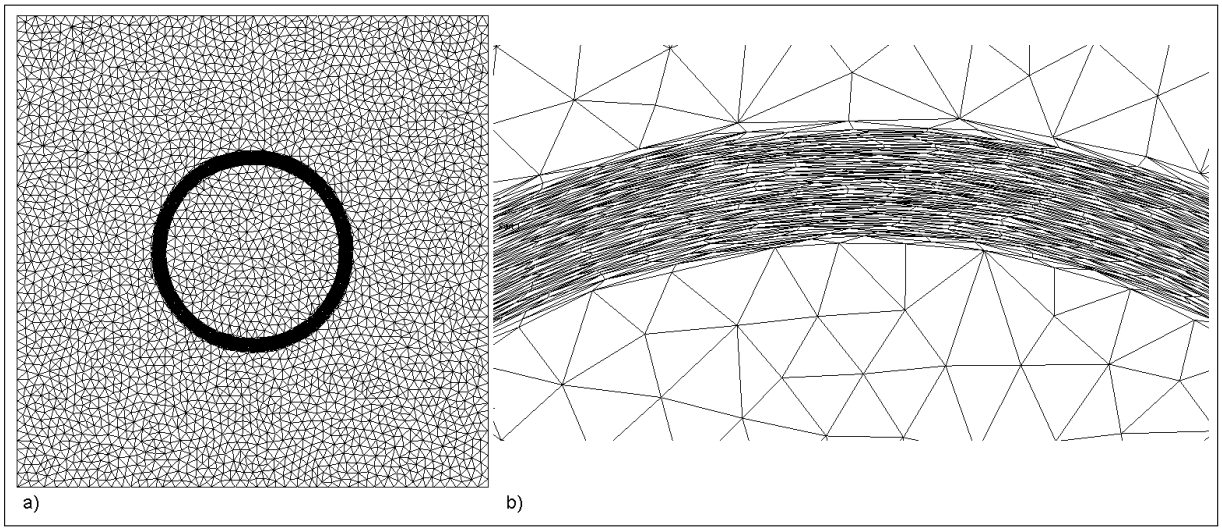


Figure 2.4: Anisotropic mesh adaptation, using the 1^{rst} method, for an immersed disk a), zoom on the fluid-solid interface b)

The goal of this approach is to achieve a mesh-adaptative strategy minimizing the directional error estimation in the mesh. Such approach allows us to refine the mesh close to the fluid-structure interface, stretch and orient the elements in such a way that, along the adaptation process, not only accurate representation of the level-set is obtained but also it tolerates keeping the number of unknowns affordably low and fixed by the user.

The Hessian strategy [77] is used to obtain better directional information of the error. The level-set scalar component is used to compute the Hessian. As shown in the previous section, this directional information can be converted into a mesh metric field $\mathbb{M}$ which prescribes the desired element size and orientation. However, it was applied without an error estimator or error control.

Figure 2.5 presents the mesh adaptation of an immersed disk as well as the zoom at the interface. As noticed, in this method, the background mesh size has nothing to do with the mesh size at the interface. While in the previous formulation, it was the same as the mesh size in the perpendicular direction to $\nabla\alpha$. The anisotropic mesh is made of 12593 elements.

The final mesh adaptation technique, used in this work, is an extension of the *a posteriori* estimation based on the length distribution tensor approach and the associated edge based error analysis. It combines the simultaneous adaptivity to the level-set scalar field and to the velocity field without increasing the complexity of the computation or intersecting different metrics [54]. Using this approach, the adaptivity will also focus on the change of direction rather than only the intensity of the velocity.

At the beginning, the unit mesh metric is defined and well justified on a node basis, by using the statistical concept of length distribution tensors. Then, the interpolation error

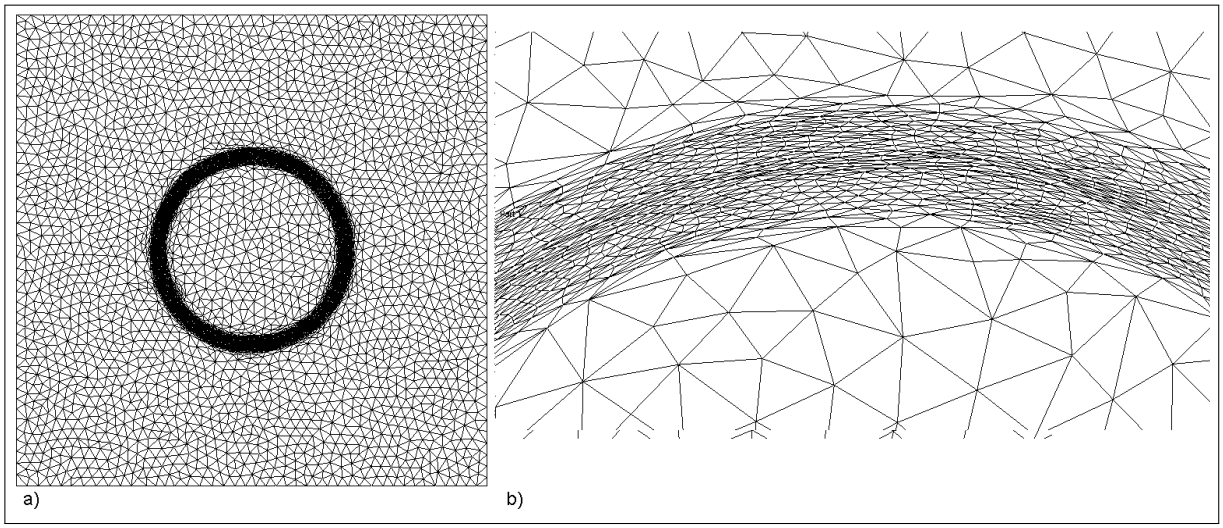


Figure 2.5: Anisotropic mesh adaptation, using the 2^{nd} method, for an immersed disk a), zoom on the fluid-solid interface b)

analysis is performed on the projected approximate scalar field along the edges. The error estimate is established on each edge whatever the dimension is. It enables to calculate a stretching factor providing a new edge length distribution, its associated tensor and the corresponding metric. The optimal stretching factor field is obtained by solving an optimization problem under the constraint of a fixed number of edges in the mesh. Details of the method can be found in [54]. and in chapter 3 section 4

As observed in figure 2.6, the adaptivity is applied to the level-set scalar field, as a result, the mesh is refined in the wake region of the interface, while far across the interface, the elements become extremely large. The anisotropic mesh is made of 12645 elements.

In order to compare the three proposed mesh adaptation methods, the minimal and maximal mesh sizes, denoted by $h_{\min}$ and $h_{\max}$ respectively, as well as the number on nodes are shown in table 2.1. The three methods present approximately same number

mesh adaptation method	$h_{\min}$	$h_{\max}$	number of nodes
First	0.0045	0.0331	6345
Second	0.0025	0.0298	6478
Third	0.0012	0.6981	6327

Table 2.1: Comparison of the three mesh adaptation methods

of nodes, the third one presents the smallest $h_{\min}$ as well as the largest $h_{\max}$. The fact that the third method applies the mesh refinement only on the scalar field allowing an important ratio between the minimal and maximal mesh size. Note that, the proposed

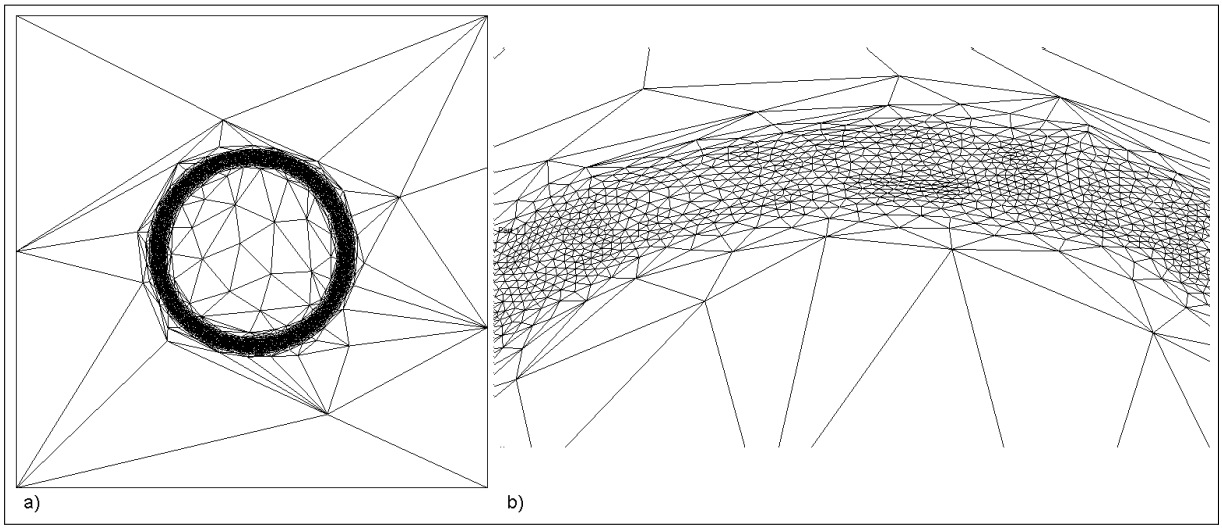


Figure 2.6: Anisotropic mesh adaptation, using the 3^{rd} method, for an immersed disk a), zoom on the fluid-solid interface b)

technique is able to construct a metric from a multi-component field, for instance the components of the velocity and/or different level-set functions.

Finally, it worth mentioning that all the proposed method can handle arbitrary complex geometries see figure 2.7 where the mesh adaptation technique for an immersed helicopter and Ahmad body is presented.

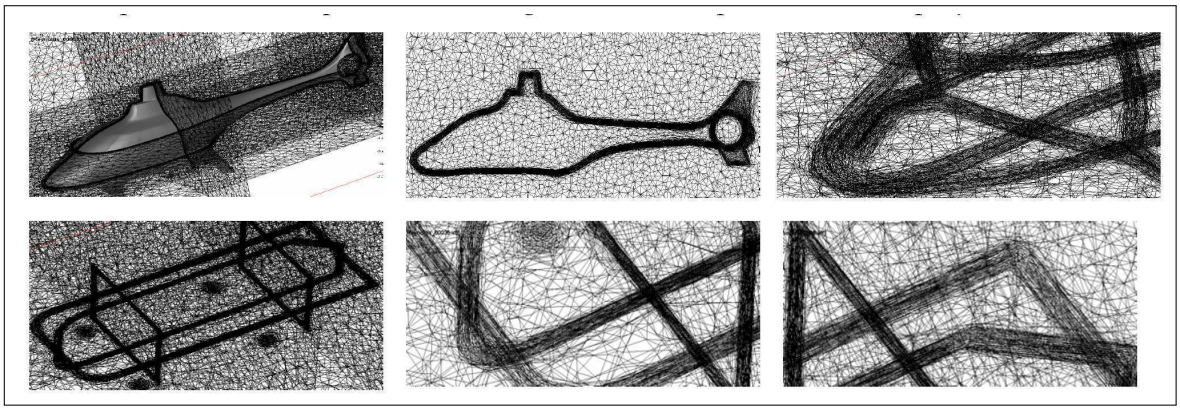


Figure 2.7: Anisotropic mesh adaptation for an immersed helicopter (upper part) and Ahmad body (lower part)

2.5 Interface tracking

The proposed approach works well with fixed immersed structures represented by fixed level-set functions. However, in most FSI applications, the fluid-structure interface evolves in time and thus, interface tracking is needed. Hence, the new structure position and form is presented by solving a convected Level-Set function as introduced in [78]. Results obtained show that mass conservation is ensured and computation is simpler, efficient and robust, even in three dimensions. The basic idea of this method is to use both the physical time and the convective time derivative in the classical Hamilton-Jacobi reinitialisation equation [79]. Consequently, a smoothed level-set function is given first as follows:

$$\alpha' = \begin{cases} \dfrac{2\epsilon}{\pi} & \text{if } \alpha > \epsilon \\ \dfrac{2\epsilon}{\pi}\sin\left(\dfrac{\pi}{2\epsilon}\alpha\right) & \text{if } |\alpha| < \epsilon \\ -\dfrac{2\epsilon}{\pi} & \text{if } \alpha < -\epsilon \end{cases} \tag{2.11}$$

where α stands for the standard distance function, and ϵ is the truncation thickness. The level-set evolution equation is then given by

$$\begin{cases} \partial_t \alpha' + \mathbf{v}\cdot\nabla\alpha' + \lambda s\left(|\nabla\alpha'| - \sqrt{1-\left(\dfrac{\pi}{2E}\alpha'\right)^2}\right) = 0 \\ \alpha'(t=0,\mathbf{x}) = \alpha'_0(\mathbf{x}) \end{cases} \tag{2.12}$$

where λ is a coupling constant depending on time discretisation and spatial discretisation, typically $\lambda \simeq h/\Delta t$. Finally, the authors in [80] show that by setting $\mathbf{w} = s\dfrac{\nabla\alpha'}{|\nabla\alpha'|}$ and $g(\alpha') = \sqrt{1-\left(\dfrac{\pi}{2E}\alpha'\right)^2}$, a rearranged form of (2.12) leads to the following simple convection equation:

$$\begin{cases} \partial_t \alpha' + (\mathbf{v}+\lambda\mathbf{w})\cdot\nabla\alpha' = \lambda\cdot\mathbf{s}\cdot\mathbf{g}(\alpha') \\ \alpha'(t=0,\mathbf{x}) = \alpha'_0(\mathbf{x}) \end{cases} \tag{2.13}$$

We use a stabilized finite element formulation, based on the classical SUPG method to discretize and solve this equation [81]. This choice of method controls the spurious oscillations in the advection dominated regime. More details are given in [80]. In brief, the FE formulation of equation (2.13) can be written as follows: find $\alpha'_h \in W_h$, such that, $\forall \mathbf{z_h} \in W_h^0$

$$\begin{cases} \int \left(\partial_t\alpha' + (\mathbf{v_h}+\lambda\mathbf{w}_h)\cdot\nabla\alpha'_h\right)\mathbf{z_h}\mathrm{d}\Omega \\ \quad + \displaystyle\sum_{e=1}^{n_{el}} \int_{\Omega^e} \tau_{SUPG}\left((\partial_t\alpha' + (\mathbf{v_h}+\lambda\mathbf{w}_h)\cdot\nabla\alpha'_h - \lambda s g(\alpha'))(\mathbf{v_h}+\lambda\mathbf{w}_h)\cdot\nabla\mathbf{z_h}\right)\mathrm{d}\Omega^e = 0 \end{cases} \tag{2.14}$$

where W_h and W_h^0 are standard test and weight finite element spaces:

$$W_h = \{w_h \in \mathcal{C}^0(\Omega),\ w_{h|K} \in \mathcal{P}^1(K),\ \forall K \in \mathcal{K}_h\}$$
$$W_h^0 = \{w_h \in W_h,\ w_{h|K} = 0\}$$

and the discretized domain is noted by $\Omega_h = \cup_{K \in \mathcal{K}_h} K$.
The classical Galerkin terms (equation 2.14) are represented by the first integral whereas the element-wise summation, tuned by the stabilization parameter τ_{SUPG}, represents the SUPG term needed to control the convection in the streamline direction. More details about the use of stabilized finite element method for the convection equation and the evaluation of this parameter can be found in [80, 82].

2.6 Conclusion

We presented in this chapter all the necessary numerical tools to immerse a structure in a domain. We began by detailing the level-set approach for defining the interface. Then, the mixing law was explained in order to treat the fluid-solid as a single fluid with different physical properties. Concerning mesh adaptation, a general overview of the existing methods in CimLib, used in this work, was presented and applied for 2D and 3D illustrative cases. These methods enable a better capture of the fluid-solid interface and allow handling the discontinuities of the material properties. The advantage of the *a posteriori* error estimate technique is that it allows generating a metric as a minimum of an error indicator function(s) for a given number of elements. Furthermore, when dealing with a deformable and or moving structure, interface tracking was exposed, which is solving the convection level-set equation and maintaining its definition as a signed distance function.

2.7 Résumé français

Tous les problèmes IFS présentés dans ce travail ont été simulés à l'aide de la méthode d'immersion de volume. Ce chapitre est consacré à la présentation de cette technique. Dans la première partie, nous détaillons le calcul des fonctions level-set qui définissent la structure. La loi de mélange est ensuite introduite, afin de définir les propriétés du fluide et du solide sur tout le domaine. Les différentes méthodes de remaillage existantes dans CimLib et employées dans ce travail sont exposés. Toutes ces méthodes sont basées sur la construction dŠune métrique qui permet de modifier la manière de calculer les longueurs dans l'espace. Les métriques obtenues sont transmises à MTC, le mailleur topologique utilisé dans CimLib. Enfin, Pour déterminer le/la déplacement/déformation du solide, nous présentons la méthode de transport de la fonction level-set qui sŠappuie sur une réinitialisation nécessaires pour redonner à la level-set une forme de type distance.

Chapter 3

FSI with Rigid Body structure

Contents

3.1 Introduction 29

3.2 Rigid body motion 30

3.3 Monolithic SFEM for rigid body motions in the incompressible navier-stokes flow 32

3.3.1 Introduction 32

3.3.2 Immersed volume method 34

3.3.2.1 Level-set approach 34

3.3.2.2 Mixing laws 34

3.3.2.3 Anisotropic mesh adaptation 35

3.3.3 Governing equations 36

3.3.4 Stabilized finite-element method (SFEM) 38

3.3.5 Numerical scheme 41

3.3.6 Validation for 2D cases 43

3.3.6.1 Immersion of solid bodies in fluid 43

3.3.6.2 Several disks in an imposed flow 45

3.3.6.3 Falling disk in a channel 47

3.3.6.4 Tetris benchmark 50

3.3.7 Conclusion 51

3.4 Immersed Stress Method for FSI at high Reynolds number . 53

3.4.1 Introduction 54

3.4.2 Immersed Volume Method 56

3.4.2.1 Level-set approach 56

3.4.2.2 Mixing laws 56

3.4.2.3 Anisotropic mesh adaptivity 57
3.4.3 Governing equations 58
3.4.3.1 Rigid body restriction in a stationary Stokes flow . . . 59
3.4.3.2 The Navier-Stokes equations with a rigid body 61
3.4.4 Stabilized Finite-Element Method (SFEM) 64
3.4.5 Numerical experiments 68
3.4.5.1 2D immersion of solid bodies in an incompressible fluid 68
3.4.5.2 Immersion of solid bodies in fluid 3D 70
3.4.5.3 Flow around a fixed circular cylinder (2-D) 71
3.4.5.4 Oscillating circular cylinder in a channel 74
3.4.5.5 Unsteady flow past an immersed helicopter in forward flight 75
3.4.6 Conclusion 77
3.5 Monolithic VMS method for FSI with anisotropic adaptive meshing 78
3.5.1 Introduction 78
3.5.2 Construction of an anisotropic mesh 80
3.5.2.1 Level-set function 80
3.5.2.2 Edge based error estimation 80
3.5.2.3 Gradient Recovery 82
3.5.2.4 Metric construction from the edge distribution tensor 82
3.5.2.5 Error behaviour due to varying the edge length 83
3.5.2.6 Extension to multi-component field 84
3.5.2.7 Mixing laws 85
3.5.3 Governing equations 86
3.5.3.1 The Navier-Stokes equations with a rigid body 86
3.5.3.2 Full Euleurian formulation 87
3.5.3.3 Rigid body kinetics 89
3.5.4 Stabilized Finite-Element Method (SFEM) 89
3.5.5 Numerical experiments 92
3.5.5.1 Falling disk in a channel 92
3.5.5.2 Falling cylinder in an incompressible fluid 94
3.5.5.3 Tetris benchmark 95
3.5.5.4 2D immersion of a NACA0012 airfoil in an incompressible fluid at Reynolds 5000 98

3.5.5.5 Unsteady flow past a 3D immersed simplified vehicle model 100
3.5.6 Conclusion 101
3.6 Conclusion 102
3.7 Résumé 102

3.1 Introduction

This chapter is dedicated to the fluid-rigid body interaction. The used formulation and the FE discretization for fixed or moving bodies are presented. Recall that, for moving solids different techniques can be found. Johnson and co-workers [83] simulate up to 100 rigid particles in $3D$ using an unstructured moving mesh. An ALE moving finite element mesh can also be used to simulate rigid particles [84]. In [19, 85], the motion of the fluid domain is accounted for by an ALE strategy and the motion of the rigid body is described by ridid body dynamics. The strong fluid-structure coupling is solved by the Newton-Raphson methodology. The motion of the fluid-structure interface, in [19], is modelled with the combination of an ALE strategy and an adaptive remeshing procedure.

As noticed, when working with moving grids, the fluid domain must be remeshed and adapted frequently to avoid element distortion. Fixed methods reduce these difficulties as the fictitious domain, the immersed boundary method and the immersed interface method. The fictitious domain method proposes an Eulerian approach where the computations are made on a domain which contains the fluid and structure phases [86, 87]. Along with the fictitious domain, the rigid body constraint can be satisfied using the XFEM as in [88]. The rigidity constraint can also be applied using a Lagrange multiplier [89, 90, 91]. In this case, the Navier-Stokes is extended to the whole domain and the solid domain is treated as a fluid subjected to an additional rigidity constraint. Another method capable of handling rigid body in an incompressible Navier-Stokes flow is the immersed interface method [92, 93]. Singular forces are applied on the fluid to ensure the no-slip boundary condition on the rigid boundary. The immersed boundary method has also been used for FSI with rigid body [94, 95], which is similar to the immersed interface method. The imposition of a no-slip boundary condition over the body-fluid interface is achieved by adding a force source term to the Navier-Stokes equations. The immersed boundaries are represented by a finite number of Lagrangian points along the solid-fluid interface.

Recall that the objective of this work is to reach a similar monolithic Eulerian approach for FSI problems treating rigid or elastic structures. Moreover, in order to simulate a rigid body in a monolithic approach, the focus is to be able to prescribe the equation of the rigid body motion together with the fluid momentum and continuity equation in the same system of equations. For this reason, the work developed by Pantakar and co-workers [89, 90, 91] have retained our attention. We start by writing the equations for each domain, the fluid and structure, and then we impose the rigidity constraint by an appropriate Lagrange multiplier stress tensor. Then by using the specific mixture laws, the final FSI system is obtained. This system is governed by the Navier-Stokes equation with an extra-stress tensor coming from the presence of the structure in the fluid. Thus a system with three fields: velocity, pressure and stress is formulated.

From another hand, any FE approximation for the fluid flow alone must verify the compatibility condition known by the inf-sup or "Brezzi-Babuska" condition which requires an appropriate pair of function spaces for velocity and pressure [64, 65, 66] and the stablility in the convection dominated flows [67, 68].For this purpose, we propose a stabi-

lized finite element formulation based on the multiscale approach. The velocity, pressure, and stress tensor are decomposed into two scales, the large and small one.

After this introduction, this chapter contains four main sections. Section 3.2 describes the rigid body motion. Section 3.3 presents the first developed FE formulation with equal order interpolation for the velocity and pressure and a lower order interpolation for the stress. Section 3.4 presents a more accurate formulation with equal order interpolation for the three fields. Furthermore, the capability of the method to simulate FSI problems at high Reynolds number is highlighted. And finally, section 3.5 represents FSI simulations with the latest anisotropic mesh adaptation technique. Each section is presented as a submitted paper in international Journals.

3.2 Rigid body motion

A description of the rigid body motion is presented in this section.
Let Ω be the spatial domain, Ω_{s}^t the solid domain at time t and let Ω_{s}^0 represent the initial domain of the structure. And let $\mathbf{v}(\mathbf{x}, t)$ be the velocity distribution on the entire domain and
$\mathbf{x}(\mathbf{X}, t) : \Omega_{\mathrm{s}}^0 :\longmapsto \Omega_{\mathrm{s}}^t$ at time t be the trajectories of solid points from Ω_{s}^0 to Ω_{s}. Then:

$$\frac{\partial \mathbf{x}(\mathbf{X}, t)}{\partial t} = \mathbf{v}(\mathbf{x}(\mathbf{X}, t), t), \ X \in \Omega_{\mathrm{s}}^0. \tag{3.1}$$

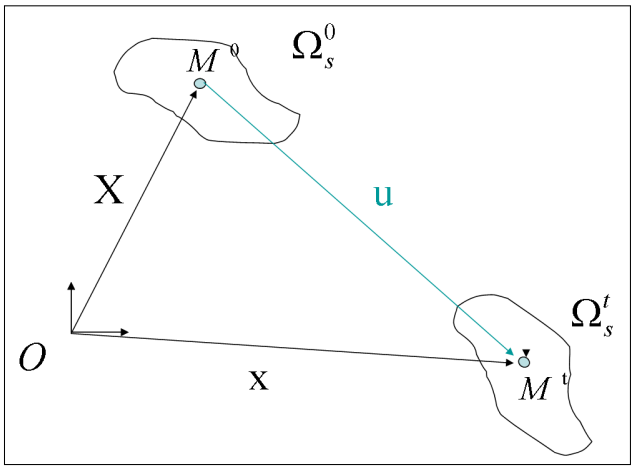


Figure 3.1: Motion of a rigid body

The rigid body motion is presented by :

$$\mathbf{v}(\mathbf{x}, t) = \mathbf{V} + \mathbf{x} \wedge \omega, \tag{3.2}$$

where $\mathbf{x}$ is any point subjected to the rigid movement, $\mathbf{V}$ and ω are repectively the velocity and angular velocity of the rigid body. Figure 3.1 illustrates the process of the rigid body motion.

The optimal $\mathbf{V}$ and ω would be calculated from the velocity field $\mathbf{v}$ computed from the Navier-Stokes equations, at each point $\mathbf{x}$, by minimizing:

$$\begin{aligned}\varphi(\mathbf{V},\omega) &= \int_{\Omega_s} \mid \mathbf{V} + \omega \wedge \boldsymbol{x} - \mathbf{v} \mid^2 \ \mathrm{dx} \\ &= \int_{\Omega_s} \mid \mathbf{V} + \omega \mathbf{x}^{\perp} - \mathbf{v} \mid^2 \ \mathrm{dx \ in} \ 2D \ \mathrm{cases.}\end{aligned} \tag{3.3}$$

where $\mathbf{x}^{\perp} = (-y, x)$. The minimum is achieved when:

$$\begin{aligned}\frac{\partial \varphi(\mathbf{V},\omega)}{\partial \mathbf{V}} &= 0 \\ \frac{\partial \varphi(\mathbf{V},\omega)}{\partial \omega} &= 0\end{aligned} \tag{3.4}$$

And the matrix formulation of the system to be solved reaches:

$$\begin{pmatrix} \sum_i \alpha_i & 0 & \sum_i -\alpha_i y_i \\ 0 & \sum_i \alpha_i & \sum_i \alpha_i x_i \\ \sum_i -\alpha_i y_i & \sum_i \alpha_i x_i & \sum_i \alpha_i (x_i^2 + y_i^2) \end{pmatrix} \begin{pmatrix} \mathbf{V}_x \\ \mathbf{V}_y \\ \omega \end{pmatrix} = \begin{pmatrix} \sum_i \alpha_i \mathbf{v}_{xi} \\ \sum_i \alpha_i \mathbf{v}_{yi} \\ \sum_i \alpha_i (\mathbf{v}_{yi} x_i - \mathbf{v}_x i y_i) \end{pmatrix}$$

where $\mathbf{x}_i = (x_i, y_i)$, $\mathbf{v}_i = (\mathbf{v}_{xi}, \mathbf{v}_{yi})$ and α_i are the coordinates, velocities, and the weight of the Gauss points respectively.

Once $\mathbf{V}$ and ω are determined, the coordinates of the origine $\mathbf{O}^t$ and the axes of the structure $\mathbf{A}_i^t (i = 1, 2)$ can be calculated from their initial positions, $\mathbf{O}^0$ and $\mathbf{A}_i^0$ respectively, as following:

$$\begin{cases} \mathbf{O}^t = \mathbf{O}^0 + \Delta t \left(\mathbf{V} + \omega \mathbf{O}^{0\perp} \right) \\ \mathbf{A}_i^t = \dfrac{\mathbf{A}_i^0 + \Delta t \omega \mathbf{A}_i^{0\perp}}{\parallel \mathbf{A}_i^0 + \Delta t \omega \mathbf{A}_i^0 \parallel} \end{cases} \tag{3.5}$$

And thus, the new position of the structure is calculated and obtained.

3.3 Monolithic SFEM for rigid body motions in the incompressible navier-stokes flow

In the following, the formulation of FSI problems with rigid body is detailed. We start by presenting the fluid-solid domain. Then, the stabilized finite element method (SFEM), along with the validation of the present formulation using $2D$ and $3D$ test cases are demonstrated. The same method as in chapter 2 is used to define the fluid-structure interface. The only difference is in the way the interface is tracked. Since the structure is a rigid one, there is no need to solve the convected level set equation; instead, the rigid body motion, detailed earlier, is used to define the new position of the structure in the domain.

3.3.1 Introduction

Numerical simulations of fluid-structure interaction (FSI) are of first interest in numerous industrial problems (aeronautics, heat treatments, aerodynamic, bioengineering...). Because of the high complexity of such problems, analytical studies are in general not sufficient to understand and solve them. Additionally, in spite of the available computers performance and the actual maturity of computational fluid dynamics, several key issues in the domain of computational FSI still prevent simulations from really helping in solving academic and industrial problems. FSI simulations are then nowadays the focus of numerous investigations, and various approaches are proposed to treat them.

Most of the commercial software packages solve FSI problems using an Arbitrary Lagrangian Eulerian (ALE) formulation [11, 12, 13]. The solid domain is treated with a Lagrangian formulation. The nodes belonging to the interface between the solid and the fluid are moved with the solid. The displacement of the nodes in the fluid domain do not depend on the fluid motion, but only ensures the continuity between the fluid and the solid domain, and a good mesh quality. ALE methods are robust and accurate, and do not need any extra degrees of freedom. However, important problems arise if the deformations, displacements and rotations of the solid becomes very important [15, 16, 17].

A higher popularity has been gained recently by partitioned approaches which allow the use specific solver for each domain. The difficulty remains in transfering the information between the codes. The coupling between the two phases can be enforced using different schemes: weakly or strongly coupled version. The former approach manages with just one solution of either field per time step but consequently lack accurate fulfilment of the coupling conditions. The latter requires sub-iterations. The predominant approach consists in solving the problem iteratively, using fixed-point schemes [96] or Newton Krylov methods [38, 36, 97, 98]. Actually, the fixed-point methods with dynamic relaxation seem to be the most interesting variant [99]. This approach allows the use of fluid and solid solvers for each of the two phases. It is accurate and quite efficient but present an inherent instability depending on the ratio of the densities and the geometry of the domain [40]. As a result, the numerical cost increases drastically and coupling

algorithms may not converge. For 3D problems, such difficulties become even more severe.

Monolithic approaches have been proposed to overcome these drawbacks. The whole domain (composed by fluid and solid phases) is considered as a single one, meshed by a single grid, and solved with an Eulerian framework. The continuity at the interface is then obtained naturally and there is no need to enforce it, as it was the case in partitioned methods. If the multi-mesh approaches permit the use of classical fluid and solid solvers, monolithic approaches impose the use of an appropriated unique constitutive equation describing both the fluid and the solid domain. Interface tracking, between the two different domains, can be completed by Immersed Boundary (IB) methods [27] where the interface is convected on a Lagrangian way. Other methods such as the fictitious domain [27, 28] treat the coupling between the domains by applying a constraints across the rigid body using a Lagrange multiplier.

Here in this work, we use the immersed volume method based on the level-set approach [61]. Mesh adaptation, and particularly anisotropic mesh adaptation is used to track the fluid-solid interface with a good precision and reasonable computational time [100, 61].

The rigid solid is treated using the Navier-Stokes solver under constrains to impose the nullity of the deformations. It can be done by simply penalizing the strain rate using a very important viscosity in the solid, which can sometimes be sufficient [59, 60, 61]. It is also possible to enforce directly the nullity of the strain by using an Augmented Lagrange Mulptipliers method [29, 62, 63], solved by an iterative Uzawa algorithm. The problem is solved by adding an extra-stress tensor comming from the presence of the structure in the fluid. Linear or harmonic mixture laws of the mechanical properties characterizing each domain are then applied at the interface.

However, in the presence of high discontinuity materials properties at the interface between the fluid and solid, numerical oscillations appear at the interface and pollute the global solutions. Therefore, we propose an extension of the multiscale-stabilized Navier-Stokes solver [61, 67] taking into account the solid constraint as an extra tensor. Recall that the classical finite element approximation for the flow problem must verifies two criterias: the compatibility condition known by the inf-sup or 'Brezzi-Babuska' condition which requires an appropriate pair of the function spaces for the velocity and the pressure [64, 65, 66] and the stability in the convection dominated flows [67, 68]. For these reasons, a robust monolithic Navier-Stokes solver is extended with a stabilization procedure for rigid body motion. It uses a multiscale stabilized finite element method based on the enrichment of the functional spaces for the velocity, the pressure and the stress.

The Immersed Volume Method is revisited next. Then, the strong and weak form of the equations of motion is presented. Afterwards, the stabilizing schemes from a Variational MultiScale point of view are described followed by the numerical scheme. Finally, some benchmark problems to validate the method and the numerical simulation of a falling disk in a channel are examined.

3.3.2 Immersed volume method

The immersed volume method is based on solving the single set of equations by differentiating the subdomains and refining the mesh at this interface using the level-set method. This section presents the complete description of the method, which is structured into three subsections: immerse the solid using level-set function, mix the physical properties and finally apply the anisotropic mesh adaptation at the vicinity of the interface [61].

3.3.2.1 Level-set approach

A signed distance function of an interface Γ_i is used to localize the interface of the immersed body Ω_i and initialize the desirable properties on both sides of this latter. At any point $\mathbf{x}$ of the computational domain Ω, the level-set function α_i corresponds to the distance from Γ_i. In turn, the interface Γ_i is then given by the iso-zero of the function α_i :

$$\begin{cases} \alpha_i(\mathbf{x}) = \pm d(\mathbf{x}, \Gamma_i), \mathbf{x} \in \Omega, \\ \Gamma_i = \{\mathbf{x}, \alpha_i(\mathbf{x}) = 0\} \end{cases} \tag{3.6}$$

In this paper, a sign convention is used: $\alpha_i \geq 0$ inside the solid domain defined by the interface Γ_i and $\alpha_i \leq 0$ outside this domain. Further details about the algorithm used to compute the distance are available in [72].

3.3.2.2 Mixing laws

The geometry and mechanical properties of each subdomain are characterized by one signed distance function. Once all the sub-domains are defined, the mechanical properties can then be determined on the whole domain in function of the level-set function. For the elements crossed by the level-set functions and the their neighbours, fluid-solid mixtures are used to determine the element effective properties.

A heaviside function $H(\alpha)$ for each level-set function is defined by:

$$H(\alpha) = \begin{cases} 1 & \text{if } \alpha > 0 \\ 0 & \text{if } \alpha < 0 \end{cases} \tag{3.7}$$

In order to achieve a better continuity at the interface [73], the heaviside function can be smoothed using:

$$H_\varepsilon(\alpha) = \begin{cases} 1 & \text{if } \alpha > \varepsilon \\ \frac{1}{2}\left(1 + \frac{\alpha}{\varepsilon} + \frac{1}{\pi}\sin\left(\frac{\pi\alpha}{\varepsilon}\right)\right) & \text{if } |\alpha| \leq \varepsilon \\ 0 & \text{if } \alpha < -\varepsilon \end{cases} \tag{3.8}$$

where ε is a small parameter such that $\varepsilon = O(h_i)$, known as the interface thickness, and h_i is the mesh size in the normal direction to the interface. In the vicinity of the interface,

it can be computed using the following expression:

$$h_i = \max_{j,l \in K} \boldsymbol{\nabla}\alpha \cdot \mathbf{x}^{jl} \tag{3.9}$$

where $\mathbf{x}^{jl} = \mathbf{x}^l - \mathbf{x}^j$ and K is the mesh element.

According to the chosen approximations, the heaviside function is then approximated using linear interpolations $P1$ between fluid and solid properties or a piecewise constant interpolation $P0$.

3.3.2.3 Anisotropic mesh adaptation

Accurate calculation of the velocities, strains and stresses along the fluid-solid interface is critical for a correct modelling of industrial applications. The difficulty arises due to the discontinuity of the properties of the material across the interface. If this latter is not aligned with the element edges, it may intersect the element arbitrarily such that the accuracy of the finite element approach can be compromised. In order to circumvent this issue, the level-set process is thus coupled to an anisotropic mesh adaptation as described in [52]. The idea of this method is to pre-adapt the mesh at the interface. The mesh becomes locally refined, elements are stretched, which enables to sharply define the interface and to save a great number of elements compared to classical isotropic refinement. This anisotropic adaptation is performed by constructing a metric map that allows the mesh size to be imposed in the direction of the distance function gradient. Let us briefly describe the main principles of this technique. First of all, one has to resort to a so-called metric which is a symmetric positive defined tensor representing a local base that modifies the distance computation, such that:

$$||\mathbf{x}||_{\mathrm{M}} = \sqrt{{}^T\mathbf{x} \cdot \mathbb{M} \cdot \mathbf{x}}\ , \quad < \mathbf{x}, \mathbf{y} >_{\mathrm{M}} = {}^T\mathbf{x} \cdot \mathbb{M} \cdot \mathbf{y}\ . \tag{3.10}$$

The metric $\mathbb{M}$ can be regarded as a tensor whose eigenvalues are related to the mesh sizes, and whose eigenvectors define the directions for which these sizes are applied. For instance, using the identity tensor, one recovers the usual distances and directions of the Euclidean space. In our case the direction of mesh refinement is given by the unit normal to the interface which corresponds to the gradient of the level-set function: $\mathbf{x} = \boldsymbol{\nabla}\alpha / ||\boldsymbol{\nabla}\alpha||$. A default mesh size, or background mesh size, h_d is imposed far from the interface and it is reduced as the interface comes closer. A likely choice for the mesh size evolution is the following:

$$h = \begin{cases} h_d & \text{if } |\alpha(\mathbf{x})| > e/2 \\ \dfrac{2h_d(m-1)}{m\ e}|\alpha(\mathbf{x})| + \dfrac{h_d}{m} & \text{if } |\alpha(\mathbf{x})| \leq e/2 \end{cases} \tag{3.11}$$

Eventually, at the interface, the mesh size is reduced by a factor m with respect to the default value h_d. Then this size increases until equalling h_d for a distance that corresponds to the half of a given thickness e. The unit normal to the interface $\mathbf{x}$ and the mesh size

h defined above, lead to the following metric:

$$\mathbb{M} = C\,(\mathbf{x} \otimes \mathbf{x}) + \frac{1}{h_d}\,\mathbb{I} \quad \text{with} \quad C = \begin{cases} 0 & \text{if } |\alpha(\mathbf{x})| \geq e/2 \\ \dfrac{1}{h^2} - \dfrac{1}{h_d^2} & \text{if } |\alpha(\mathbf{x})| < e/2 \end{cases} \tag{3.12}$$

where $\mathbb{I}$ is the identity tensor. This metric returns to isotropic far from the interface (with a mesh size equal to h_d for all directions) and to anisotropic near the interface (with a mesh size equal to h_i in the direction $\mathbf{x}$ and equal to h_d in the others). This method can be assisted by a posteriori anisotropic error estimator, the search of the optimal mesh (metric) that minimizes the error estimator. As a result, an optimal metric as a minimum of an error indicator function and for a given number of elements is obtained.

In practice, the mesh is generated in several steps using the MTC mesher and remesher developed by [51]. Further details on the anisotropic mesh generation can be found in [52]. The proposed mesh generation algorithm works well for 2D or 3D complex shapes. It allows the creation of meshes with extremely anisotropic elements stretched along the interface. The mesh size is then only refined in the direction of the high physical and mechanical properties gradients. This allow both conserving a high precision in the calculus and in the geometry description, in spite of an important decrease of the total number of degrees of freedom. The grid is furthermore only modified in the vicinity of the interface which keeps the computational work devoted to the grid generation low. Note also that the proposed method can easily handle arbitrary complex geometries. As shown in Figure 3.2 which presents a close-up on the interface zone at the end of the anisotropic adaptation process, the mesh has been gradually refined when approaching the interface. Consequently, only additional nodes are locally added in this region, whereas the rest of domain keeps the same background size.

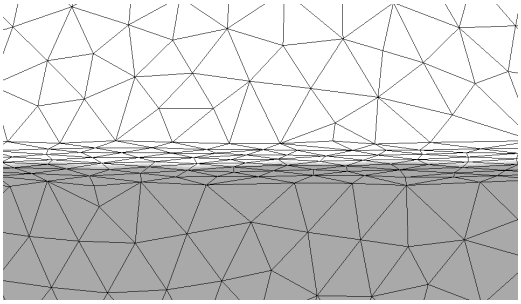


Figure 3.2: Zoom on the fluid-solid interface after anisotropic adaptation

3.3.3 Governing equations

This section is devoted to the mathematical formulation for rigid body immersed in an incompressible fluid. The governing equations are considered to be three-dimensional, unsteady. As the proposed approach is monolithic, a unique constitutive equation will be

solved on the whole domain, with a variation of the parameters depending on the phase that should be modelled.

First, each system of equation is presented separately. Let $\Omega \subset \mathbb{R}^n$ be the spatial domain at time $t \in [0, T]$, where n is the space dimension. Let $\partial\Omega$ denote the boundary of Ω. Ω_f, Ω_s and Ω_{fsi} be respectively the fluid domain, the solid domain and the interface. They verify:

$$\Omega_f \cup \Omega_s = \Omega \quad \text{and} \quad \Omega_f \cap \Omega_s = \Omega_{fsi} \tag{3.13}$$

The dynamic of the flow is given by the classical incompressible Navier-Stokes equations:

$$\rho_f \ (\partial_t \mathbf{v} + \mathbf{v} \cdot \boldsymbol{\nabla}\mathbf{v}) - \boldsymbol{\nabla} \cdot \boldsymbol{\sigma} = \mathbf{f} \quad \text{in } \Omega_f \tag{3.14}$$

$$\boldsymbol{\nabla} \cdot \mathbf{v} = 0 \quad \text{in } \Omega_f \tag{3.15}$$

$$\mathbf{v} = \mathbf{v}_\Gamma \quad \text{on } \Gamma \tag{3.16}$$

$$\mathbf{v} = \mathbf{v_i} \quad \text{on } \Omega_{fsi} \tag{3.17}$$

$$\boldsymbol{\sigma} \cdot \mathbf{n} = \mathbf{d} \quad \text{on } \Omega_{fsi} \tag{3.18}$$

$$\mathbf{v}(\mathbf{x}, \mathbf{0}) = \mathbf{v_0}(\mathbf{x}) \quad \text{in } \Omega_f \tag{3.19}$$

where $\mathbf{v}$ is the velocity vector, ρ_f is the fluid density, , $\mathbf{n}$ is the outward normal on the solid surface, $\mathbf{v_i}$ is the velocity at fluid-solid interface Ω_{fsi} and $\mathbf{f}$ the applied force vector. For an incompressible fluid the divergence-free constraint (3.15) gives rise to the pressure in the fluid. The stress tensor for a Newtonian fluid is then given by:

$$\boldsymbol{\sigma} = 2\eta_f \ \boldsymbol{\varepsilon}(\mathbf{v}) - p \ \mathbf{I_d} \tag{3.20}$$

where p is the pressure, $\mathbf{I_d}$ is the identity tensor, $\boldsymbol{\varepsilon}(\mathbf{v}) = (\boldsymbol{\nabla}\mathbf{v} + ^T \boldsymbol{\nabla}\mathbf{v})/2$ the deformation-rate tensor and η_f is the dynamic viscosity.

In the present formulation we treat the rigid body as a continuous domain subjected to an additional rigidity constraint. The governing equations for particle motion are then given by:

$$\rho_s \ (\partial_t \mathbf{v} + \mathbf{v} \cdot \boldsymbol{\nabla}\mathbf{v}) - \boldsymbol{\nabla} \cdot \sigma = \mathbf{f} \quad \text{in } \Omega_s \tag{3.21}$$

$$\boldsymbol{\nabla} \cdot \mathbf{v} = 0 \quad \text{in } \Omega_s \tag{3.22}$$

$$\boldsymbol{\varepsilon}(\mathbf{v}) = 0 \quad \text{in } \Omega_s \tag{3.23}$$

$$\mathbf{v} = \mathbf{v_i} \quad \text{on } \Omega_{fsi} \tag{3.24}$$

$$\boldsymbol{\sigma} \cdot \mathbf{n} = -\mathbf{d} \quad \text{on } \Omega_{fsi} \tag{3.25}$$

$$\mathbf{v}(\mathbf{x}, \mathbf{0}) = \mathbf{v_0}(\mathbf{x}) \quad \text{in } \Omega_s \tag{3.26}$$

where ρ_s the solid density. In a rigid body there is no deformation $\boldsymbol{\varepsilon}(\mathbf{u}) = 0$ ($\mathbf{u}$ is the displacement field) and $\partial_t \mathbf{u} = \mathbf{v}$. These two equations implies a null value of the deformation-rate tensor (3.23). From another part the rigidity constraint (3.23) ensures that the velocity field is a divergence-free. Hence Equation (3.22) is a redundant equation. Nevertheless we choose to keep this constraint to account the pressure term. As noted

earlier Equation (3.22) gives rise to the fluid pressure. Similarly, Equation (3.23) gives rise to a stress field $\boldsymbol{\tau}$. The stress tensor is then given by:

$$\boldsymbol{\sigma} = -p\ \mathbf{I_d} + \boldsymbol{\tau}_s \tag{3.27}$$

Adding both systems, the strong form for the whole domain reads:

$$\begin{cases} \rho\ (\partial_t \mathbf{v} + \mathbf{v} \cdot \boldsymbol{\nabla}\mathbf{v}) - \boldsymbol{\nabla} \cdot (2\eta\ \boldsymbol{\varepsilon}(\mathbf{v}) + \boldsymbol{\tau} - p\ \mathbf{I_d}) = \mathbf{f} \\ \boldsymbol{\nabla} \cdot \mathbf{v} = 0 \\ \boldsymbol{\varepsilon}_s(\mathbf{v}) = 0 \\ \mathbf{v} = \mathbf{v_b} \qquad\qquad \text{on } \partial\Omega \\ \mathbf{v}(\mathbf{x}, \mathbf{0}) = \mathbf{v_0}(\mathbf{x}) \end{cases} \tag{3.28}$$

where $\boldsymbol{\varepsilon}_s(\mathbf{v}) = H(\alpha)\boldsymbol{\varepsilon}(\mathbf{v})$, $\eta = (1-H(\alpha))\eta_f$, $\rho = \rho_s H(\alpha) + \rho_f(1-H(\alpha))$ and $\boldsymbol{\tau} = H(\alpha)\boldsymbol{\tau}_s$. Once the object is immersed inside the computational domain using the proposed technique, the equations at the fluid-solid interface are naturally satisfied. As a consequence, the boundary conditions (3.17)-(3.18)-(3.24)-(3.25) are no longer needed. The boundary velocity $\mathbf{v_b}$ results from Equation '3.16). If the solid boundary intersects with the domain boundary, $\mathbf{v_b}$ can be easily adapted.

Weak form01

Multiplying by the test functions and integrating by parts, the associated standard weak form of the system (3.28), can be stated as: Find $\mathbf{v} \in V = \left(H_0^1(\Omega)\right)^n$, $p \in Q = L^2(\Omega)$ and $\tau \in \mathcal{T} = L^2(\Omega)^{n\times n}$ such that:

$$\begin{cases} \rho\ (\partial_t \mathbf{v}, \mathbf{w}) + \rho(\mathbf{v} \cdot \boldsymbol{\nabla}\mathbf{v}, \mathbf{w}) - (p\, \boldsymbol{\nabla} \cdot \mathbf{w}) + (2\eta\boldsymbol{\varepsilon}(\mathbf{v}) : \boldsymbol{\varepsilon}(\mathbf{w})) + (\boldsymbol{\tau} : \boldsymbol{\varepsilon}(\mathbf{w})) \\ \qquad\qquad = (\mathbf{f}, \mathbf{w}) \\ (\boldsymbol{\nabla}\mathbf{v}, q) = 0 \\ (\varepsilon_s(\mathbf{v}) : \boldsymbol{\tau}^*) = 0 \end{cases} \tag{3.29}$$

A penalization factor η_s will be added to this formulation, so that $\eta = H(\alpha)\eta_s + (1 - H(\alpha))\eta_f$. As a consequence an extra term is added $(2\eta_s\boldsymbol{\varepsilon}(\mathbf{v}) : \boldsymbol{\varepsilon}(\mathbf{w}))$. This can be done as long as $\boldsymbol{\varepsilon}(\mathbf{w})$ belongs to the functional space of $\boldsymbol{\tau}$.

3.3.4 Stabilized finite-element method (SFEM)

In this section, we describe briefly the Galerkin finite-element approximation and the corresponding stabilization method for the resulting discrete system of Equations (3.29). Based on a mesh $\mathcal{K}_h$ of Ω into set of N_{el} elements K, the functional spaces for the velocity, the pressure and the stress are approached by the finite dimensional spaces spanned by

V_h, P_h and $\mathcal{T}_h$. As it is well known, the stability of the discrete formulation depends on appropriate compatibility restrictions on the choice of the finite element spaces, as stated by the inf-sup condition. According to this, standard Galerkin mixed elements with continuous equal order linear/linear interpolation for the three fields are not stable. Lack of stability shows as uncontrollable oscillations that pollute the solution. Fortunately, the strictness of the inf-sup condition can be avoided by modifying the discrete variational form, for instance, by means of introducing appropriate numerical techniques that can provide the necessary stability to the desired choice of interpolation spaces. The objective of this work is precisely to present stabilization methods which allow the use of equal order continuous interpolations for velocities and pressures and piecewise constant interpolation for stresses. The basic idea of the sub-grid scale approach is to consider that the unknowns can be split in two components, *e.g.* coarse and fine, corresponding to different scales or levels of resolution [67]. First, we solve the fine scale and then we replace their effect into the large scale. This means approximating the velocity, pressure, stress solution space as $V_h \oplus V'$, $P_h \oplus P'$ and $\mathcal{T}_h \oplus \mathcal{T}'$. To this end, $\mathbf{v}, p, \boldsymbol{\tau}$ will be approximated as:

$$\left\{\begin{array}{rcll} \mathbf{v} & = & \mathbf{v}_h + \mathbf{v}' & \in\ V_h \oplus V' \\ p & = & p_h + p' & \in\ Q_h \oplus Q' \\ \boldsymbol{\tau} & = & \boldsymbol{\tau_h} + \boldsymbol{\tau'} & \in\ \mathcal{T}_h \oplus \mathcal{T}' \end{array}\right. \tag{3.30}$$

Introducing the splitting, the system of equations (3.29) is: Find $(\mathbf{v}, p, \boldsymbol{\tau})$ such that $\forall\ \mathbf{w}\ \in V_h^0 \oplus V'$, $q\ \in Q_h \oplus Q'$ et $\boldsymbol{\tau^*}\ \in \mathcal{T}_h \oplus \mathcal{T}'$

$$\left\{\begin{array}{l} \rho\left(\partial_t(\mathbf{v}_h + \mathbf{v}'), \mathbf{w}_h + \mathbf{w}'\right) + \rho((\mathbf{v}_h + \mathbf{v}') \cdot \nabla(\mathbf{v}_h + \mathbf{v}'), \mathbf{w}_h + \mathbf{w}') \\ \quad -(p_h + p', \nabla \cdot (\mathbf{w}_h + \mathbf{w}')) + (2\eta\boldsymbol{\varepsilon}(\mathbf{v}_h + \mathbf{v}') : \boldsymbol{\varepsilon}(\mathbf{w}_h + \mathbf{w}')) \\ \quad +((\boldsymbol{\tau_h} + \boldsymbol{\tau'}) : \varepsilon(\mathbf{w}_h + \mathbf{w}')) = (\mathbf{f}, \mathbf{w}_h + \mathbf{w}') \\ (\nabla \cdot (\mathbf{v}_h + \mathbf{v}'), q_h + q') = 0 \\ (\boldsymbol{\varepsilon}_s(\mathbf{v}_h + \mathbf{v}') : (\boldsymbol{\tau_h}^* + \boldsymbol{\tau_h}^{*'}))_{\Omega_s} = 0 \end{array}\right. \tag{3.31}$$

At this stage, three important remarks have to be made:

i) when using linear interpolation functions, the second derivatives vanish.

ii) the subscales are not tracked in time, therefore, quasi-static subscales are considered here; however, the subscale equations remain quasi time-dependent.

iii) the convective velocity of the non-linear term may be approximated using only large-scale part so that $(\mathbf{v_h} + \mathbf{v}')\nabla \cdot (\mathbf{v_h} + \mathbf{v}') \simeq \mathbf{v_h} \cdot \nabla(\mathbf{v_h} + \mathbf{v}')$.

Consequently, the coarse scale problem reduces to the following:

$$\begin{cases} \rho(\partial_t \mathbf{v}_h, \mathbf{w}_h) + \rho(\mathbf{v}_h \cdot \nabla(\mathbf{v}_h + \mathbf{v}'), \mathbf{w}_h) - (p_h + p', \nabla \cdot \mathbf{w}_h) \\ \quad +(2\eta\boldsymbol{\varepsilon}(\mathbf{v}_h) : \boldsymbol{\varepsilon}(\mathbf{w}_h)) + ((\boldsymbol{\tau_h} + \boldsymbol{\tau'}) : \boldsymbol{\varepsilon}(\mathbf{w}_h)) = (\mathbf{f}, \mathbf{w}_h) \\ (\nabla \cdot (\mathbf{v}_h + \mathbf{v}'), q_h) = 0 \\ (\boldsymbol{\varepsilon}_s(\mathbf{v}_h + \mathbf{v}') : \boldsymbol{\tau}_{\boldsymbol{h}}^*)_{\Omega_s} = 0 \end{cases} \tag{3.32}$$

and the fine scale problem:

$$\begin{cases} \rho(\mathbf{v}_h \cdot \nabla(\mathbf{v}_h + \mathbf{v}'), \mathbf{w}') - (p_h + p', \nabla \cdot \mathbf{w}') + (2\eta\boldsymbol{\varepsilon}(\mathbf{v}') : \varepsilon(\mathbf{w}')) \\ \quad +((\boldsymbol{\tau_h} + \boldsymbol{\tau'}) : \boldsymbol{\varepsilon}(\mathbf{w}')) = (\mathbf{f}, \mathbf{w}') \\ (\nabla \cdot (\mathbf{v}_h + \mathbf{v}'), q') = 0 \\ (\boldsymbol{\varepsilon}_s(\mathbf{v}_h + \mathbf{v}') : \boldsymbol{\tau}^{*'}) = 0 \end{cases} \tag{3.33}$$

Rearranging the terms of System (3.33) the fine scale problem reads to:

$$\begin{cases} \rho(\mathbf{v}_h \cdot \nabla \mathbf{v}', \mathbf{w}') + ((2\eta\boldsymbol{\varepsilon}(\mathbf{v}') : \boldsymbol{\varepsilon}(\mathbf{w}')) + (\boldsymbol{\tau'} : \boldsymbol{\varepsilon}(\mathbf{w}')) + (\nabla p', \mathbf{w}') = (\mathcal{R}, \mathbf{w}') \\ (\nabla \cdot \mathbf{v}', q') = -(\nabla \cdot \mathbf{v}_h, q') \\ (\boldsymbol{\varepsilon}_s(\mathbf{v}') : \boldsymbol{\tau}^{*'}) = -(\boldsymbol{\varepsilon}_s(\mathbf{v}_h) : \boldsymbol{\tau}^{*'}) \end{cases} \tag{3.34}$$

with $\mathcal{R}$ the momentum residuals:

$$\mathcal{R} = \mathbf{f} - \rho\partial_t \mathbf{v}_h - \rho\mathbf{v}_h \cdot \nabla \mathbf{v}_h - \nabla p_h + \nabla \cdot \boldsymbol{\tau_h} \tag{3.35}$$

Following the lines in [101] and using exactly the same procedure, it can be shown that $\mathbf{v}'$, p' and $\boldsymbol{\tau'}$ may be approximated within each element by :

$$\begin{cases} \mathbf{v}' = \sum_{K \in \mathcal{K}_h} \tau_k \tilde{P}_{\mathbf{v}}(\mathcal{R}) \\ p' = -\sum_{K \in \mathcal{K}_h} \tau_c \tilde{P}_p(\nabla \cdot \mathbf{v}) \\ \boldsymbol{\tau'} = -\sum_{K \in \mathcal{K}_h} \tau_t \tilde{P}_{\boldsymbol{\tau}}(\boldsymbol{\varepsilon}(\mathbf{v}_h)) \end{cases} \tag{3.36}$$

where the so called stabilization parameters τ_k, τ_c and τ_t can be computed as [102]:

$$\begin{aligned} \tau_k &= \left((\frac{2}{\Delta t})^2 + (\frac{4\eta}{\rho h^2})^2 + (\frac{2 \parallel v \parallel_k}{h})^2 \right)^{-1/2}, \\ \tau_c &= \left((\frac{\eta}{\rho})^2 + (\frac{c_2 \parallel \mathbf{v_k} \parallel_{\mathbf{k}}}{c_1 h})^2 \right)^{1/2}, \\ \tau_t &= c_3 \frac{h}{L}. \end{aligned} \tag{3.37}$$

The constants c_1, c_2 and c_3 are independent from h, h being the characteristic length of the element, L the characteristic length of the domain and $\| \mathbf{v} \|_{\mathbf{k}}$ the norm of the velocity in the centre of the element. The simplest choice is to take $\tilde{P}_{\mathbf{v}}$, $\tilde{P}_p$ and $\tilde{P}_{\boldsymbol{\tau}}$ as the identity when applied to the residuals. As a hindrance of choosing a piecewise constant interpolation for $\boldsymbol{\tau_h}$, the last term in the momentum residuals $\mathcal{R}$ is not adequately represented. To this end, one can employ either of the two strategies: a simplified recovery using the least squares approach or the DEVSS approach. A reconstruction of $\boldsymbol{\tau_h}$ in the stabilization term would be made as the difference of the projected value on the continuous piecewise space $\tilde{\boldsymbol{\tau}}_{\boldsymbol{h}}$ and $\boldsymbol{\tau_h}$. Considering the coarse-scale sub problem (3.32) and substituting $\mathbf{v}'$, p' and $\boldsymbol{\tau}'$ in terms that contain the fine scale velocity we get:

$$
\begin{cases}
\rho(\partial_t \mathbf{v}_h, \mathbf{w}_h) + \rho(\mathbf{v}_h \cdot \nabla(\mathbf{v}_h), \mathbf{w}_h) - (p_h, \nabla \cdot \mathbf{w}_h) + (2\eta\boldsymbol{\varepsilon}(\mathbf{v}_h) : \boldsymbol{\varepsilon}(\mathbf{w}_h)) \\
\quad +(\boldsymbol{\tau_h} : \boldsymbol{\varepsilon}(\mathbf{w}_h)) - (\mathbf{f}, \mathbf{w}_h) \\
\quad +\sum_{K\in\mathcal{K}_h} \tau_k \left(\rho(\partial_t \mathbf{v}_h + \mathbf{v}_h \cdot \nabla \mathbf{v}_h)_k + \nabla p_h - \nabla \cdot \tilde{\boldsymbol{\tau}}_{\boldsymbol{h}} - \mathbf{f}, \rho \mathbf{v}_h \nabla \mathbf{w}_h\right)_k \\
\quad +\sum_{K\in\mathcal{K}_h} \tau_c (\nabla \cdot \mathbf{v}_h, \nabla \cdot \mathbf{w}_h)_k \\
\quad -\sum_{K\in\mathcal{K}_h} \tau_t (\boldsymbol{\varepsilon}(\mathbf{v}_h), \boldsymbol{\varepsilon}(\mathbf{w}_h))_k = 0 \\
(\nabla \mathbf{v}_h, q_h) \\
\quad +\sum_{K\in\mathcal{K}_h} \tau_k \left(\rho(\partial_t \mathbf{v}_h + \mathbf{v}_h \cdot \nabla \mathbf{v}_h) + \nabla p_h - \nabla \cdot \tilde{\boldsymbol{\tau}}_{\boldsymbol{h}} - \mathbf{f}, \nabla q_h\right)_k = 0 \\
(\boldsymbol{\varepsilon_s}(\mathbf{v}_h) : \boldsymbol{\tau}^*_{\boldsymbol{h}}) \\
\quad +\sum_{K\in\mathcal{K}_h} \tau_k \left(\rho(\partial_t \mathbf{v}_h + \mathbf{v}_h \cdot \nabla \mathbf{v}_h) + \nabla p_h - \nabla \cdot \tilde{\boldsymbol{\tau}}_{\boldsymbol{h}} - \mathbf{f}, \nabla \cdot \boldsymbol{\tau}^*_{\boldsymbol{h}}\right)_k = 0
\end{cases}
\tag{3.38}
$$

3.3.5 Numerical scheme

Three equations with three primary variables require larger computational coast. To circumvent this issue an augmented Lagragian method and Uzawa's algorithm would be used to solve the system without increasing the size of linear system. In the same iteration, the problem of non-linearity, time integration and computation of the Lagrange multiplier would be solved. An implicit time scheme with a Newton method for the non linear term is used. At each time step t_n the procedure is the following:

1. Initialization with values obtained at the previous time step:

$$
\mathbf{v}_h = \mathbf{v}_h(t_{n-1}),\ p_h = p_h(t_{n-1}),\ \boldsymbol{\tau}^{\mathbf{0}}_{\boldsymbol{h}} = 0, \tilde{\boldsymbol{\tau}}_{\boldsymbol{h}} = 0 \tag{3.39}
$$

2. At step k find $\mathbf{v_h^k}$ and p_h^k with system:

$$\left\{\begin{array}{l} \rho\left(\dfrac{\mathbf{v}_h^k}{\Delta t}+\mathbf{v}_h\cdot\nabla\mathbf{v}_h^k,\mathbf{w}_h\right)-(p_h^k,\nabla\cdot\mathbf{w}_h)+(2\eta\boldsymbol{\varepsilon}(\mathbf{v}_h^k),\boldsymbol{\varepsilon}(\mathbf{w}_h)) \\ \quad+\sum_{K\in\mathcal{K}_h}\tau_k\left(\rho\left(\dfrac{\mathbf{v}_h^k}{\Delta t}+\mathbf{v}_h\cdot\nabla\mathbf{v}_h^k\right)+\nabla p_h^k,\rho\mathbf{v}_h\nabla\mathbf{w}_h\right)_k \\ \quad+\sum_{K\in\mathcal{K}_h}\tau_c(\nabla\cdot\mathbf{v}_h^k,\nabla\cdot\mathbf{w}_h)_k \\ \quad-\sum_{K\in\mathcal{K}_h}\tau_t(\boldsymbol{\varepsilon}(\mathbf{v}_h),\boldsymbol{\varepsilon}(\mathbf{w}_h))_k \\ \qquad\qquad=-(\boldsymbol{\tau_h^k}:\boldsymbol{\varepsilon}(\mathbf{w}_h))+\left(\mathbf{f}+\dfrac{\mathbf{v}_h}{\Delta t},\mathbf{w}_h\right) \\ \qquad\qquad\quad+\sum_{K\in\mathcal{K}_h}\tau_k\left(\rho\tfrac{\mathbf{v}_h}{\Delta t}+\nabla\cdot\tilde{\boldsymbol{\tau}}_{\boldsymbol{h}}^{\boldsymbol{k}}+\mathbf{f},\rho\mathbf{v}_h\nabla\mathbf{w}_h\right)_k \\ (\nabla\cdot\mathbf{v}_h^k,q_h)+\sum_{K\in\mathcal{K}_h}\tau_k\left(\rho\left(\dfrac{\mathbf{v}_h^k}{\Delta t}+\mathbf{v}_h\cdot\nabla\mathbf{v}_h^k\right)+\nabla p_h^k,\nabla q_h\right)_k \\ \qquad\qquad=\sum_{K\in\mathcal{K}_h}\tau_k\left(\rho\tfrac{\mathbf{v}_h}{\Delta t}+\nabla\cdot\tilde{\boldsymbol{\tau}}_{\boldsymbol{h}}^{\boldsymbol{k}}+\mathbf{f},\nabla q_h\right)_k \end{array}\right. \tag{3.40}$$

3. update $\tilde{\boldsymbol{\tau}}_{\boldsymbol{h}}$ and $\boldsymbol{\tau_h}$:

$$\left\{\begin{array}{ll} \boldsymbol{\tau}_{\boldsymbol{h}}^{\boldsymbol{k+1}} & =\boldsymbol{\tau}_{\boldsymbol{h}}^{\boldsymbol{k}}+\eta_u\boldsymbol{\varepsilon}(\mathbf{v}_h^k) \qquad \text{where} \qquad \eta_u=H(\alpha)\eta_s. \\ \tilde{\boldsymbol{\tau}}_{h|_i}^{k+1} & =\dfrac{1}{\sum_{k\in\mathcal{K}(i)}\mid K\mid}\sum_{\sum_{k\in\mathcal{K}(i)}\mid K\mid}\boldsymbol{\tau}_{h|_i}^{k+1}\mid K\mid \end{array}\right. \tag{3.41}$$

where $\mathcal{K}(i)$ set of nodes connected to node i.

4. Check $\parallel\mathcal{R}e(\mathbf{v}_h^k)\parallel<e_1$ to stop the loop on k, where $\mathcal{R}e(\mathbf{v}_h^k)$ is the residual of the inner uzawa's iterrations compared to the initial residual of the global iterations.

5. Calculate the rigid body motion : Once $\mathbf{v}_h(t_n)$ is computed for a point with $\boldsymbol{x}$ as coordinates, the optimal angular velocity $\boldsymbol{\omega}^n$ and translational velocity $\mathbf{V}^n$ are calculated by minimizing $\varphi(\mathbf{V}^n,\boldsymbol{\omega}^n)$ defined by:

$$\varphi(\mathbf{V}^n,\boldsymbol{\omega}^n)=\int_{\Omega_s}\mid\mathbf{V}^n+\boldsymbol{\omega}^n\wedge\boldsymbol{x}-\mathbf{v}_h(t_n)\mid^2dx \tag{3.42}$$

the minimum is atteint once

$$\left\{\begin{array}{l}\dfrac{\partial\varphi(\mathbf{V}^n,\boldsymbol{\omega}^n)}{\partial\mathbf{V}^n}=0 \\ \dfrac{\partial\varphi(\mathbf{V}^n,\boldsymbol{\omega}^n)}{\partial\boldsymbol{\omega}^n}=0\end{array}\right. \tag{3.43}$$

6. Update the rigid body position, compute $\mathbf{X}(t^{n+1})$:

$$\mathbf{X}(t^{n+1})=\mathbf{X}(t^n)+\Delta t\,(\mathbf{V}^n+\boldsymbol{\omega}^n\wedge\mathbf{X}(t^n)) \tag{3.44}$$

A more accurate scheme for updating the rigid body position would be the Adams-Bashfort scheme [103]. This scheme will be investigated in a future work.

3.3.6 Validation for 2D cases

In this section, we present relatively simple 2D and 3D test cases in order to validate the proposed formulation and to check the accuracy and the efficiency of the immersed volume method. All the numerical simulations were carried out by using the C++ CimLib finite element library (see [46, 69]). The results obtained with the implemented code, referred as IVM, are then compared with those obtained either by standard solution or by other approaches.

3.3.6.1 Immersion of solid bodies in fluid

In the first model problem, we consider a square fluid domain with two immersed rigid bodies, as shown in Figure 3.3, induced by an imposed gradient pressure at the intlet and outlet of the fluid domain, with the following boundary conditions:

$$\begin{aligned} \mathbf{v} &= 0 \quad \text{at} \quad \partial\Omega_2 \cap \Omega_4 \\ p &= 100 \quad \text{at} \quad \partial\Omega_1 \\ p &= 0 \quad \text{at} \quad \partial\Omega_3 \end{aligned} \tag{3.45}$$

The objective of this test is to illustrate the formulation and to check the implementation

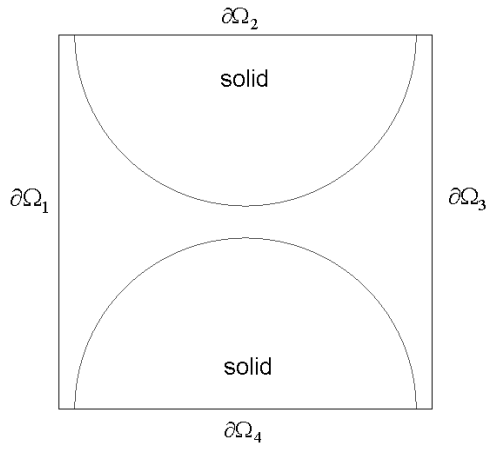


Figure 3.3: Schematic representation of two rigid bodies in an incompressible flow

of the proposed method by comparing results to the solution representing only the fluid domain. The used parameters are tabulated in Table 3.1. The velocity and pressure fields computed with the proposed method are shown in Figures 3.4 and 3.5 and compared to

Table 3.1: Parameter of two rigid bodies in a viscous fluid

Parameter	ρ_f	ρ_s	η_f
Unit	kg/m^3	kg/m^3	$Pa.s$
Value	1000	1000	1000

results calculated only on the fluid domain. The agreement between the two calculations shows that the present solver is able to predict accurately the behaviour of the fluid and the presence of the solid. The pressure distribution caused by the interaction is more interesting, which is depicted in Figure 3.5 on both domains. The effect of the stabilization is depicted in the zoomed-in view of the pressure near the interface as shown in Figure 3.6. The variational multiscale method eliminates the pollution in the solution especially on the interface.

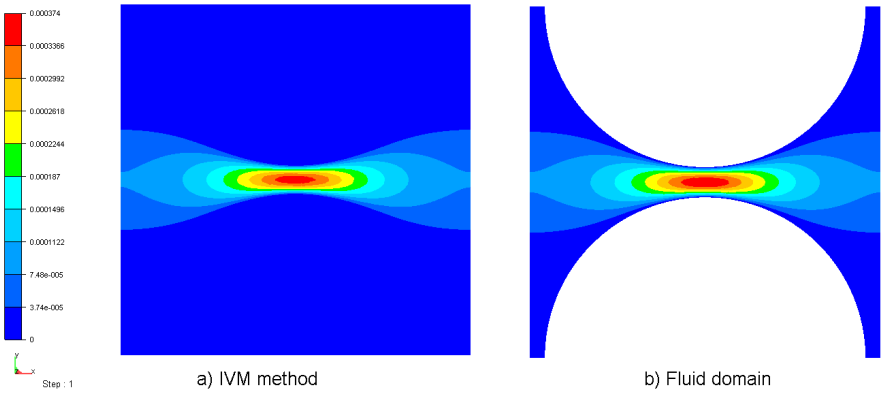


Figure 3.4: Norme of the velocity with and without IVM

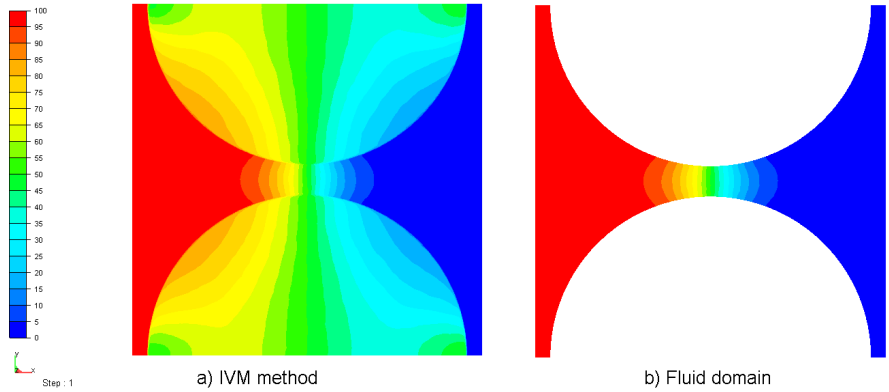


Figure 3.5: Pressure distribution with and without IVM

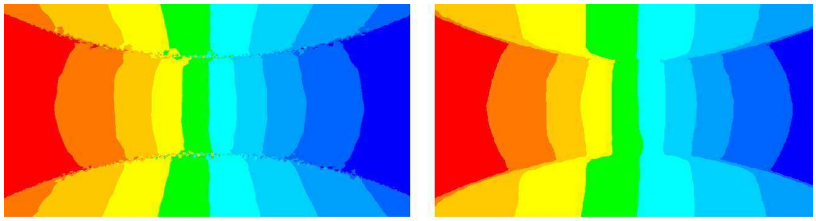


Figure 3.6: Close up view for the pressure at the interface with and without stabilization

3.3.6.2 Several disks in an imposed flow

For further validation with several small particles immersed in a fluid, fifteen rigid circular disks and ten rigid semi-circular disks with radius $R = 5mm$ are immersed in an imposed fluid flow, with a velocity at the inlet $u = 0.015m.s^{-1}$ (see Figure 3.7). The no-slip boundary conditions are imposed on the tube wall and bottom of the domain. The length of the tube is $L = 19R$ and its width is $D = 12R$. The density and viscosity of the fluid used in this example are $\rho_f = 1370kg/m^3$ and $\eta_f = 0.001Pa.s$, and the density of the particle is $\rho_s = 2000kg/m^3$. The mesh size is $h = 0.0005m$.

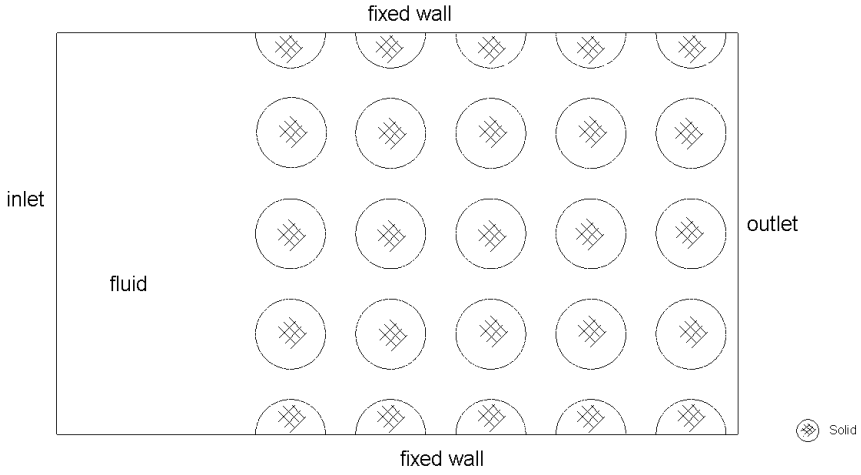


Figure 3.7: Modelling several rigid disks in an imposed flow

Figure 3.8 shows the velocity vectors of the flow. The restriction of the velocity profile is well highlighted in the wake region of the disks. Figures 3.9 and 3.10 illustrate the contour plots for u and v velocity respectively. These figures also show the behaviour of the fluid flow commonly observed in several obstacles. It can be noticed, the maximum velocity is attained in the region where the separation distance between the two disks is minimum. The pressure is presented in Figure 3.11. As mentioned earlier, only the real pressure of fluid is highlighted. The same example is repeated in $3D$. As shown in Figure

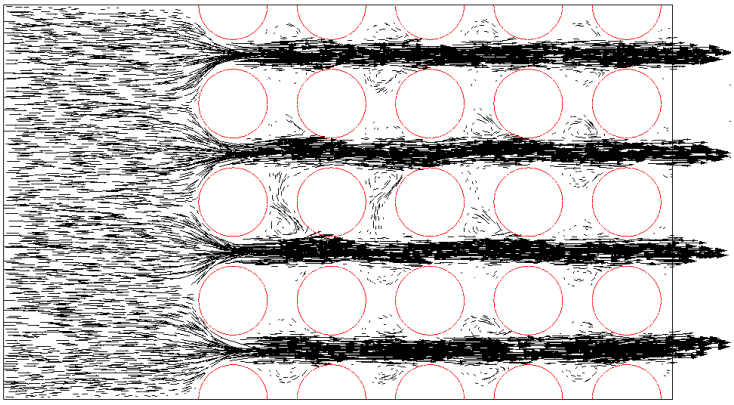


Figure 3.8: Velocity distribution between the rigid disks (the circles present the zero isovalue of the level-set)

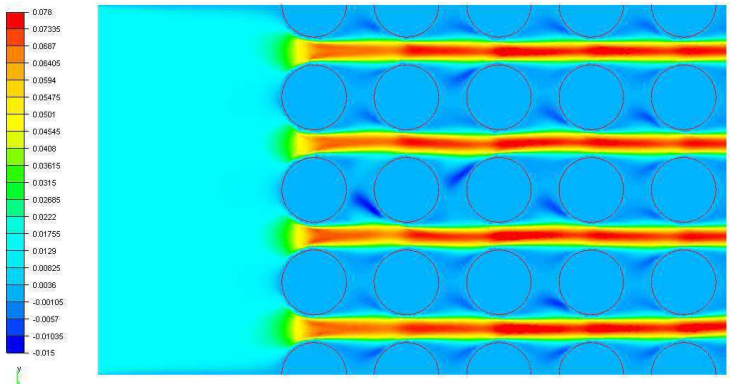


Figure 3.9: u-velocity in an imposed fluid flow (the circles present the zero isovalue of the level-set)

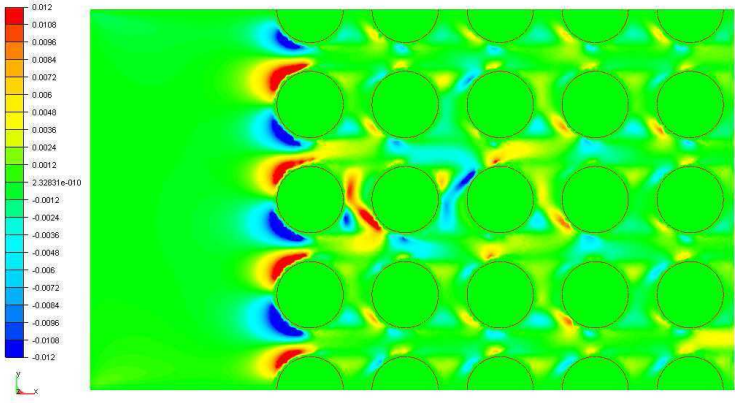


Figure 3.10: v-velocity in an imposed fluid flow (the circles present the zero isovalue of the level-set)

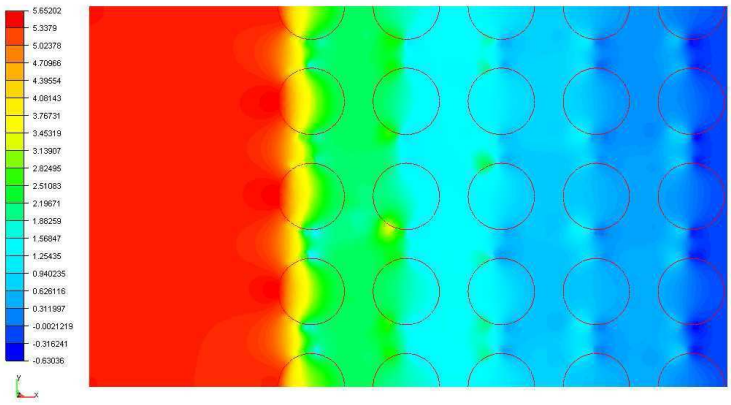


Figure 3.11: Pressure distribution in an imposed fluid flow (the circles present the zero isovalue of the level-set)

3.12, the fluid-solid interface is well captured. The behaviour of the fluid flow is similar to the $2D$ case. Once again, the proposed $3D$ FSI solver exhibits good stability properties on anisotropic unstructured meshes. The extension of this problem is to take one of the disks as an elastic body.

3.3.6.3 Falling disk in a channel

We consider a disk with radius $R = 0.125cm$ falling under the action of gravitational force inside a channel of dimension $[0, 2] \times [0, 6]$. Parameters used in this example are tabulated in Table 3.2. Among these parameters, h denotes the mesh size. In [29]

Table 3.2: Parameter used in the computation of a falling disk in a channel

Parameter	ρ_f	ρ_s	η_f	$\triangle t$	g	h
Unit	g/cm^3	g/cm^3	g/cms	s	cm/s^2	cm
Value	1	1.25	0.1	0.005	980	0.04

the velocity of particulate flow with rigid circular disks using fictitious domain method is calculated. We compare our computational results to this reference. This test case is well documented in the literature and considered as a challenging benchmark. Close agreements in Figure 3.13 are found for the velocity and position of the center of the disk as t goes on. The slight differences noticed in here are mostly related to the use of a first order time interpolation scheme for the solid motion. This matter can be adjusted using the Adams-Bashfort scheme. Figures 3.14 and 3.15 illustrate, respectively, the velocity contour plot for u and v at selected instances. It can be observed from Figure 3.16 that the pressure computed at different time is not affected by the presence of the solid and free of any spurious oscillations. This result endorses the computation of the fluid pressure only.

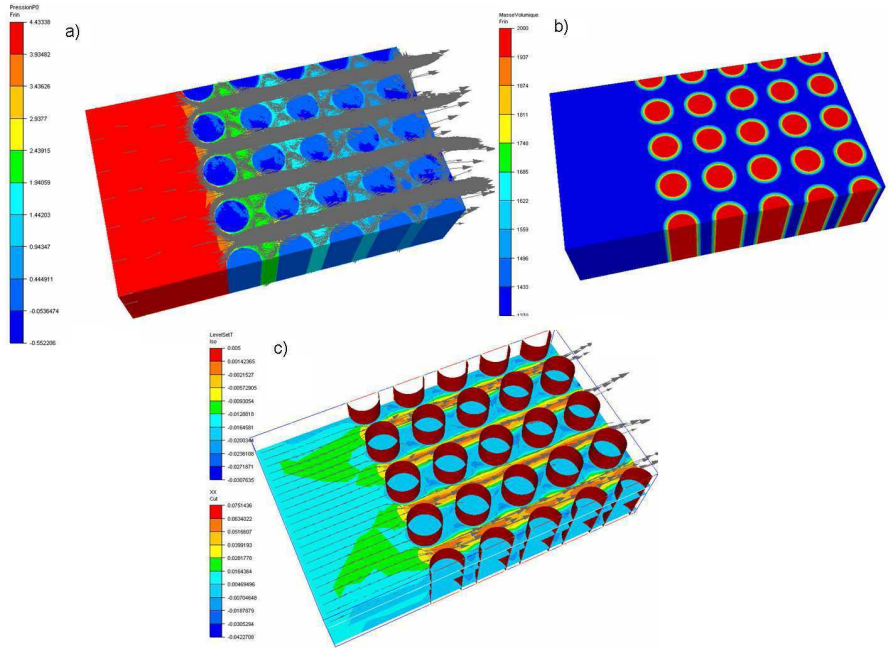


Figure 3.12: 3D modelling of several rigid disks in an imposed flow a) velocity b) density c) Level-set

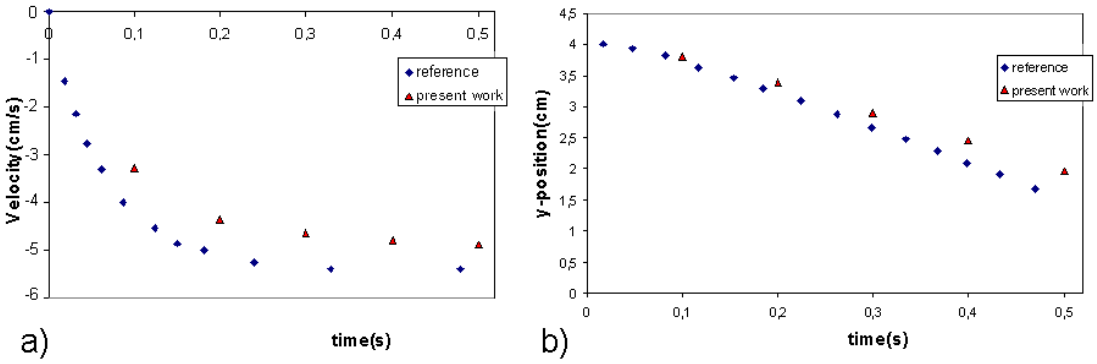


Figure 3.13: The vertical velocity a) and the vertical postition b) of the center of a disk in a channel

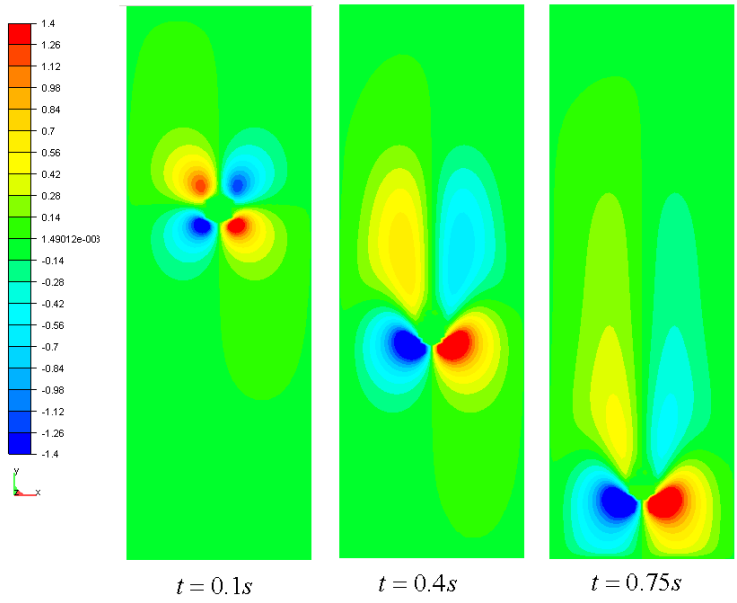


Figure 3.14: u-velocity on the entire domain due to the falling disk in a channel

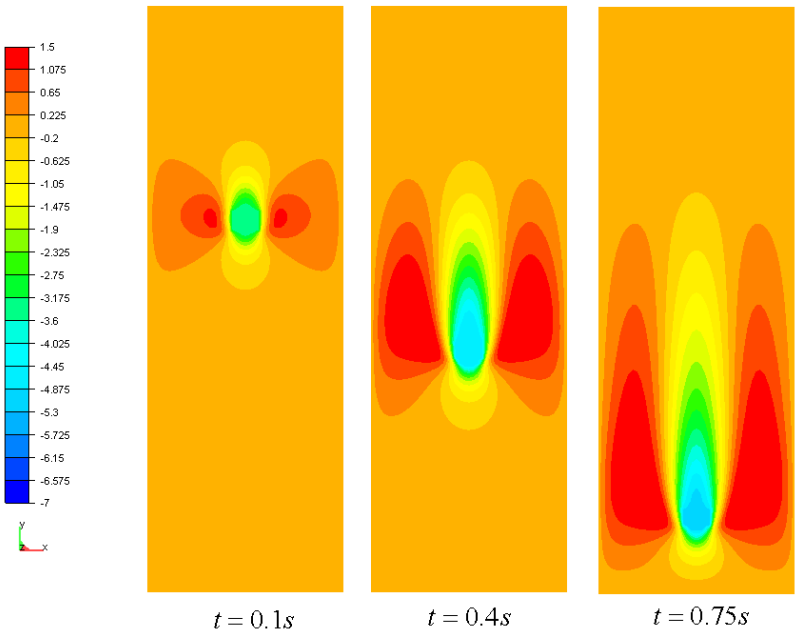


Figure 3.15: v-velocity on the entire domain due to the falling disk in a channel

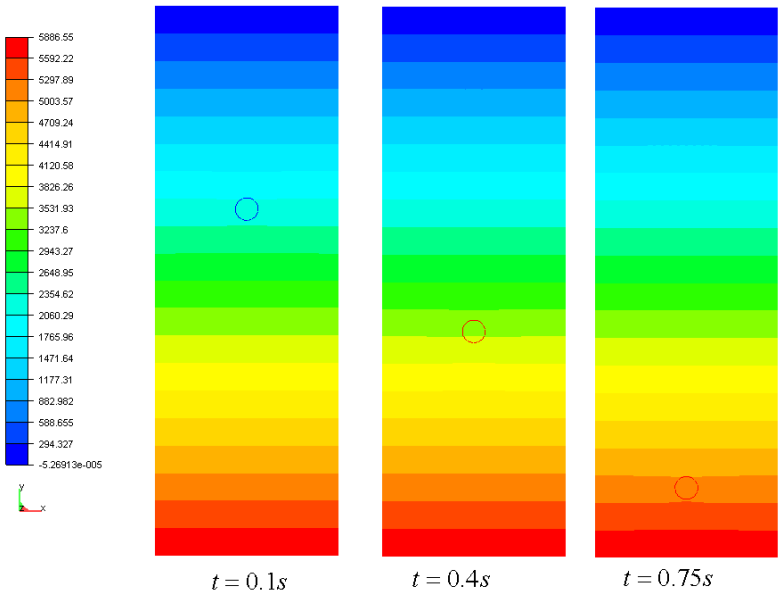


Figure 3.16: Excess pressure on the entire domain due to the falling disk in a channel

3.3.6.4 Tetris benchmark

Four rigid bodies with different density $\rho_{s_1} = 3000kg/m^3$, $\rho_{s_2} = \rho_{s_3} = 8000kg/m^3$, $\rho_{s_4} = 8000kg/m^3$ are falling under the gravitationnal force. When several rigid bodies in the incompressible fluid channel at the initial time are falling, the interactive motions of these bodies inside the fluid have an interesting phenomenon. At the beginning, each body has the same acceleration by gravitational force. As time passes more, the velocity of the upper bodies becomes faster than that of the lower ones since the lower bodies undergo more resistance against the fluid comparing to the upper ones. The rigid bodies are arranged, initially, as shown in Figure 3.17, together with the finite element mesh at $t = 0$. Mesh adaptation is needed to better capture all the interfaces. The error estimator method is used in this example, with a fixed number of 26423 elements. The density and viscosity of the fluid used in this example are $\rho_f = 1kg/m^3$ and $\eta_f = 0.0005Pa.s$. The objective of this test is to show the capability of the method to handle high discontinuities of the solids and fluid physical properties. The Figures 3.18 and 3.19 show, respectively, the finite element mesh and the effect of the anisotropic mesh adaptation on respecting the geometry of the rigid bodies at different time instants. While the velocity vectors at different time instants is depicted in Figure 3.20. All the vortices behind the solid objects are well computed. The developed solver is able, at the same time, to take into account different solid bodies in an incompressible fluid flow with very low viscosity. Interaction between the solids is highlighted.

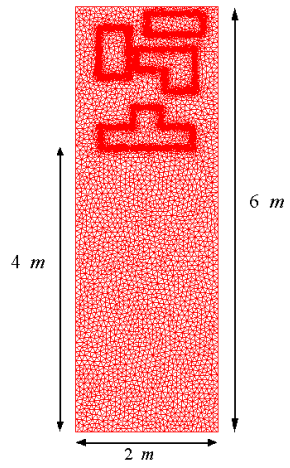


Figure 3.17: Immersion of four rigid bodies: geometry and finite element mesh at $t = 0$

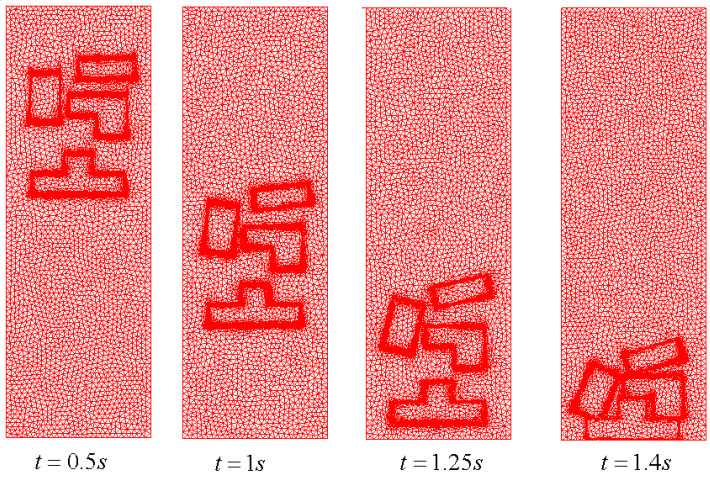


Figure 3.18: Immersion of four rigid bodies: finite element mesh of four rigid bodies at different time instants

3.3.7 Conclusion

In this part we have described an evaluation of the stabilized three-field velocity-pressure-stress, designed for the computation of rigid bodies in an incompressible Navier-Stokes flow. The proposed approach solves one set of equation in both domains with different materials properties. The presence of the solid is taken into account as an extra stress in the Navier-Stokes equation. The formulation considered allows equal-order interpolation for the velocity and pressure. The use of Uzawa's algorithm to solve the system requires a lower-order interpolation for the stress field, since if not, the left side of the system will totally changed and another system would be reached. A new developed monolithic multiscale-stabilized finite element method is presented. The approach is applied to

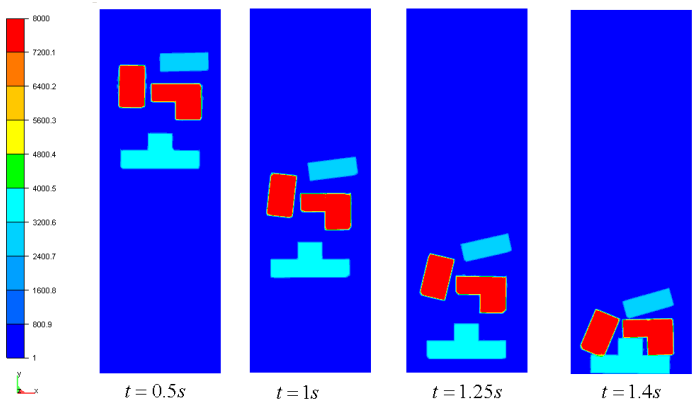


Figure 3.19: Density distribution for different time step with anisotropic adapted interfaces

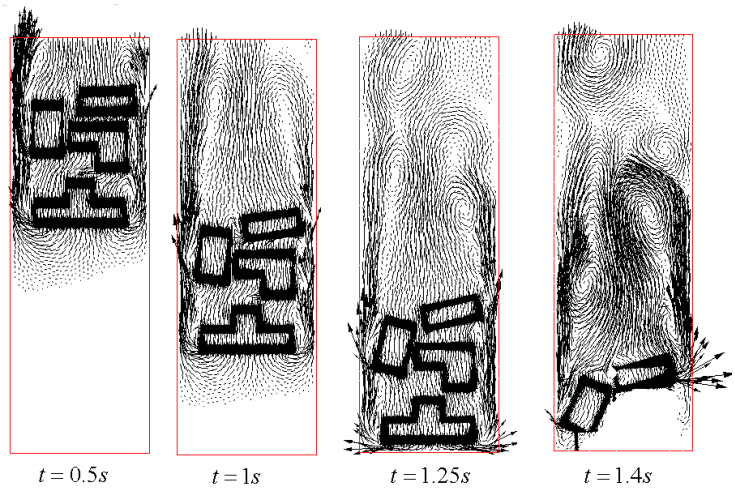


Figure 3.20: Immersion of four rigid bodies: velocity vectors at different time instants

the numerical simulation of 2D and 3D test cases. The capability of the model to simulate the fluid-rigid body interaction was demonstrated. Results are assessed by comparing the predictions with reference results or other approaches. Further research will focus on the use of a continuous piecewise interpolation for the stress field. The improvement of this methodology could be also taking a better scheme for particle displacement with a higher order time integration schemes. Enlarge the field of application and tackling deformable solid interaction and more 3D numerical simulation are considered as perspective work.

3.4 Immersed Stress Method for FSI at high Reynolds number

In this section, we highlight several remarks about the initial formulation and we present a novel extension to obtain a stable formulation.

As stated, several remarks on the previous paper are the following:

- The order of interpolation of the velocity, pressure and stress tensor fields is not the same. A continuous approximation was used for the velocity and pressure and a discontinuous approximation was applied for the stress tensor.
- Some stabilized terms were neglected for simplicity when reducing the system and applying an augmented Lagrangian scheme together with an Uzawa's algorithm.
- The term $\nabla \cdot \boldsymbol{\tau}_h$ needs to be reconstructed, otherwise, additional terms would also be neglected and there would be only one stabilized term coming from the presence of the stress tensor.
- Some clarifications were missed in order to prove the well-posedness of the problem.

Based on these remarks, we conducted a new study to complete the formulation. A novel way to compute all the missing terms was analyzed and presented in this section. Inspired from the work of Codina and co-workes [104, 101, 55], we revisited the rigid body restriction in the Stokes problem for a better understanding of the extension to Navier-Stokes equations and the way the Lagrange multiplier is chosen.

Furthermore, to analyse and check the new implemented method, we compute the drag and lift coefficients which are two important parameters enabling to verify the rigid body behaviour. Recall the drag, c_d, and lift, c_l, expressions are:

$$c_d = \frac{F_x}{\frac{1}{2}\rho {u_\infty}^2 D} \text{ and } c_l = \frac{F_y}{\frac{1}{2}\rho {u_\infty}^2 D}, \tag{3.46}$$

where u_∞ is the maximum inflow velocity, F_x and F_y is the x and y-component respectively of $\mathbf{F}$, the total force on the structural surface S:

$$\mathbf{F} = \int_S (-p\mathbf{I} + \mathbf{S}) \cdot \mathbf{n}\, dS, \tag{3.47}$$

$\mathbf{S}$ being the deviatoric stress tensor.

Since the interface is not prescribed explicitly, it's the iso-zero of the level-set function, a reformulation of c_d and c_l is made to be able to calculate these parameters. We used

the definition of c_d and c_l given in [105] leading to the following calculations:

$$\begin{aligned} c_d &= -\frac{2}{\rho {u_\infty}^2 D} \int_\Omega \left[\eta \nabla \mathbf{v} : \mathbf{v}_d + (\mathbf{v} \cdot \nabla)\mathbf{v} \cdot \mathbf{v}_d - p(\nabla \cdot \mathbf{v}_d)\right] d\Omega, \\ c_l &= -\frac{2}{\rho {u_\infty}^2 D} \int_\Omega \left[\eta \nabla \mathbf{v} : \mathbf{v}_l + (\mathbf{v} \cdot \nabla)\mathbf{v} \cdot \mathbf{v}_l - p(\nabla \cdot \mathbf{v}_l)\right] d\Omega, \end{aligned} \tag{3.48}$$

for all test functions $\mathbf{v}_d$ and $\mathbf{v}_l \in (H^1(\Omega))^2$, with $\mathbf{v}_d = (0, 1)$, $\mathbf{v}_l = (1, 0)$ on Ω_s and vanish otherwise and η is the fluid viscosity.

3.4.1 Introduction

Numerical simulations of Fluid-Structure Interaction (FSI) with complex geometries pose many challenges for computational simulations. In spite of the available computer performance and the actual maturity of computational fluid dynamics and computational structural dynamics, several key issues in the domain of computational FSI still prevent simulations from really helping in solving some academic and industrial problems. FSI simulations are then nowadays the focus of numerous investigations and various approaches are proposed to treat them.

Most of the commercial software packages solve FSI problems using an Arbitrary Lagrangian Eulerian (ALE) formulation [11, 12, 13]. The solid domain is treated with a Lagrangian formulation. The nodes belonging to the interface between the solid and the fluid are moved with the solid. The displacement of the nodes in the fluid domain does not depend on the fluid motion, but only ensures the continuity between the fluid and the solid domains and a good mesh quality (see [15, 16, 17]). A higher popularity has been gained lately by partitioned approaches that allow the use of specific solver for each domain. The difficulty remains in transferring the information between the codes. The coupling between the two phases can be enforced usually using two schemes: weakly or strongly coupled version. The former approach manages with just one solution of either field per time step but consequently lack accurate fulfilment of the coupling conditions. The latter requires sub-iterations. The predominant approach consists in solving the problem iteratively, using fixed-point schemes [106, 96, 107] or Newton Krylov methods [38, 36, 98]. Actually, the fixed-point methods with dynamic relaxation seem to be the most interesting variant [99]. This approach allows the use of fluid and solid solvers for each of the two phases. Although this has proven to be an accurate and efficient approach, it presents an inherent instability depending on the ratio of the densities and the complex geometry of the domain [40].

Alternatively, monolithic approach consists of considering the whole domain as a single one, meshed by a single grid, and solved with an Eulerian framework. Continuity at the interface is then obtained naturally and there is no need to enforce it. The monolithic approaches impose the use of an appropriate constitutive equation describing both the fluid and the solid domain. Interface tracking between the two different domains, can be completed by the level-set method. Other fixed mesh methods such as the Immersed Boundary (IB) methods [27] or the fictitious domain method [27, 28] treat the coupling

between the domains by applying constraints across the rigid body using an Augmented Lagrange multiplier, possibly solved by an iterative Uzawa algorithm. These constraints may lead to uncoupled physics in the different subdomains of the problem (in the fluid and the solid, for example), yielding inconsistencies when the subdomains evolve in time. This problem may be solved using the so called Fixed-mesh ALE formulation introduced in [108] (see also [109, 110] for applications to fluid-structure interaction problems and rigid bodies floating in fluids).

In this work, we retain the advantages of the monolithic approaches and we propose a new stabilized finite element method combined with a fast anisotropic mesh adaptation algorithm. It can be seen as an extension of the Immersed Volume Method (IVM) developed in [111, 59, 67, 47]. The motivation behind pursuing such general approach comes from the desire to easily deal with a large diversity of shapes, dimensions and physical properties of structures. By computing the signed distance function (level-set) of a given geometry to each node of the mesh we can easily identify the solid part from the surrounding fluid as the zero level of this function. Consequently, different parts (i.e. helicopter) are immersed in a larger domain (i.e. wind channel) of different material properties.

In general, the latter intersects the element arbitrarily and consequently the accuracy of the finite element approach can be compromised. In order to circumvent this issue, the level-set solution is coupled to advanced methods in anisotropic mesh adaptation at the interface. The algorithm allows the creation of extremely stretched elements along the interface, which is an important requirement for FSI problems and turbulence modelling having internal/boundary layers.

The last ingredient focuses more on the finite element solver: on modelling the interaction between the fluid (laminar or turbulent) and the structure in question. The presence of the structure will be taken into account by means of an extra stress in the Navier-Stokes equations [111]. For illustration, the rigid immersed body is treated using the Navier-Stokes solver under constraints of imposing the nullity of the deformation rate tensor by means of a Lagrange multiplier. This will require the extension of the Variational Multiscale finite element method to deal with both fluid and solid using the appropriate constitutive model. Thus the decomposition for both the velocity and the pressure fields into coarse/resolved scales and fine/unresolved scales needed to deal with convection dominated problems and pressure instabilities will be extended with an efficient enrichment of the extra constraint. This choice of decomposition is shown to be favourable a variational multiscale for simulating flows at high Reynolds number and to remove spurious oscillations at the interface due to the high discontinuity in the material properties.

In the following, the Immersed Volume Method is introduced. Section 3.5.3 is dedicated to present the governing equations. The stabilizing schemes from a Variational MultiScale point of view are described in section 3.4.4. Section 3.4.5 presents some benchmark problems and comparisons with the literature and the numerical simulation of unsteady flow past an immersed helicopter in forward flight. Finally, section 3.4.6 is dedicated to conclusions and future work.

3.4.2 Immersed Volume Method

The immersed volume method has shown to be an effective geometric representation tool [47]. It is used to immerse and to represent different complex geometries inside a unique mesh. First we compute the signed distance function (level-set) of a given geometry to each node of the mesh, then we refine anisotropically the mesh at the interface using the gradient of the distance function and finally we mix and attribute the physical properties of each domain using appropriate laws. In this section, we revisit briefly these steps.

3.4.2.1 Level-set approach

A signed distance function of an interface Γ_{im} is used to localize the interface of the immersed body Ω_{im} and initialize the desirable properties on both sides of the latter. At any point $\mathbf{x}$ of the computational domain Ω, the level-set function α_{im} corresponds to the distance from Γ_{im}. In turn, the interface Γ_{im} is then given by the iso-zero of the function α_{im}:

$$\begin{cases} \alpha_{\text{im}}(\mathbf{x}) = \pm d(\mathbf{x}, \Gamma_{\text{im}}), \mathbf{x} \in \Omega, \\ \Gamma_{\text{im}} = \{\mathbf{x}, \alpha_{\text{im}}(\mathbf{x}) = 0\} \end{cases} \tag{3.49}$$

In this paper, a sign convention is used: $\alpha_{\text{im}} \geq 0$ inside the solid domain defined by the interface Γ_{im} and $\alpha_{\text{im}} \leq 0$ outside this domain. Further details about the algorithm used to compute the distance are available in [72]. It is also possible to use functions smoother than $d(\mathbf{x}, \Gamma_{\text{im}})$ away from Γ_{im} (see for example [112]).

3.4.2.2 Mixing laws

The geometry and mechanical properties of each subdomain are characterized by one signed distance function. Once all the sub-domains are defined, the mechanical properties can then be determined on the whole domain in terms of the level-set function. For the elements crossed by the level-set functions and the their neighbours, fluid-solid mixtures are used to determine the element effective properties. A Heaviside function $H(\alpha)$ for each level-set function is defined by:

$$H(\alpha) = \begin{cases} 1 & \text{if } \alpha > 0 \\ 0 & \text{if } \alpha < 0 \end{cases} \tag{3.50}$$

In order to achieve a better continuity at the interface [73], the Heaviside function can be smoothed using:

$$H_\varepsilon(\alpha) = \begin{cases} 1 & \text{if } \alpha > \varepsilon \\ \frac{1}{2}\left(1 + \frac{\alpha}{\varepsilon} + \frac{1}{\pi}\sin\left(\frac{\pi\alpha}{\varepsilon}\right)\right) & \text{if } |\alpha| \leq \varepsilon \\ 0 & \text{if } \alpha < -\varepsilon \end{cases} \tag{3.51}$$

where ε is a small parameter such that $\varepsilon = O(h_{\text{im}})$, known as the interface thickness, and h_{im} is the mesh size in the normal direction to the interface. In the vicinity of the interface, it can be computed using the following expression:

$$h_{\text{im}} = \max_{j,l \in K} \boldsymbol{\nabla}\alpha \cdot \mathbf{x}^{jl} \tag{3.52}$$

where $\mathbf{x}^{jl} = \mathbf{x}^l - \mathbf{x}^j$ and K is the mesh element under consideration.

According to the chosen approximations, the Heaviside function is then approximated using linear interpolations $P1$ between fluid and solid properties or a piecewise constant interpolation $P0$.

3.4.2.3 Anisotropic mesh adaptivity

The anisotropic mesh adaptation is aimed at improving the quality of the mesh. This algorithm relies on an appropriate metric map construction that allows the mesh size to be imposed in the direction of the distance function gradient. The mesh is refined locally; elements are stretched, which enables to sharply define the interface and to save a great number of elements compared to classical isotropic refinement. The details of this technique can be found in [52, 51], hence a brief description is presented here. First, a modified distance computation is achieved via a symmetric positive defined tensor $\mathbb{M}$ which acts as a metric with the inner product and associated norm

$$\langle \mathbf{x}, \mathbf{y} \rangle_{\text{M}} = {}^T\mathbf{x} \cdot \mathbb{M} \cdot \mathbf{y} \ , \quad ||\mathbf{x}||_{\text{M}} = \sqrt{{}^T\mathbf{x} \cdot \mathbb{M} \cdot \mathbf{x}}, \tag{3.53}$$

which can be defined at each point of the computational domain. The metric $\mathbb{M}$ can be regarded as a tensor whose eigenvalues are related to the mesh sizes, and whose eigenvectors define the directions for which these sizes are applied. For instance, using the identity tensor, one recovers the usual distances and directions of the Euclidean space. In our case the direction of mesh refinement is given by the unit normal to the interface which corresponds to the gradient of the level-set function: $\mathbf{x} = \boldsymbol{\nabla}\alpha / ||\boldsymbol{\nabla}\alpha||$. A default mesh size, or background mesh size, h_d is imposed far from the interface and it is reduced as the interface comes closer. A likely choice for the mesh size evolution is the following:

$$h = \begin{cases} h_d & \text{if } |\alpha(\mathbf{x})| > e/2 \\ \dfrac{2h_d(m-1)}{m\ e}|\alpha(\mathbf{x})| + \dfrac{h_d}{m} & \text{if } |\alpha(\mathbf{x})| \leq e/2 \end{cases} \tag{3.54}$$

Eventually, at the interface, the mesh size is reduced by a factor m with respect to the default value h_d. Then this size increases until equalling h_d for a distance that corresponds to the half of a given thickness e. The unit normal to the interface $\mathbf{x}$ and the mesh size h defined above, lead to the following metric:

$$\mathbb{M} = C\,(\mathbf{x} \otimes \mathbf{x}) + \frac{1}{h_d^2}\,\mathbb{I} \quad \text{with} \quad C = \begin{cases} 0 & \text{if } |\alpha(\mathbf{x})| \geq e/2 \\ \dfrac{1}{h^2} - \dfrac{1}{h_d^2} & \text{if } |\alpha(\mathbf{x})| < e/2 \end{cases} \tag{3.55}$$

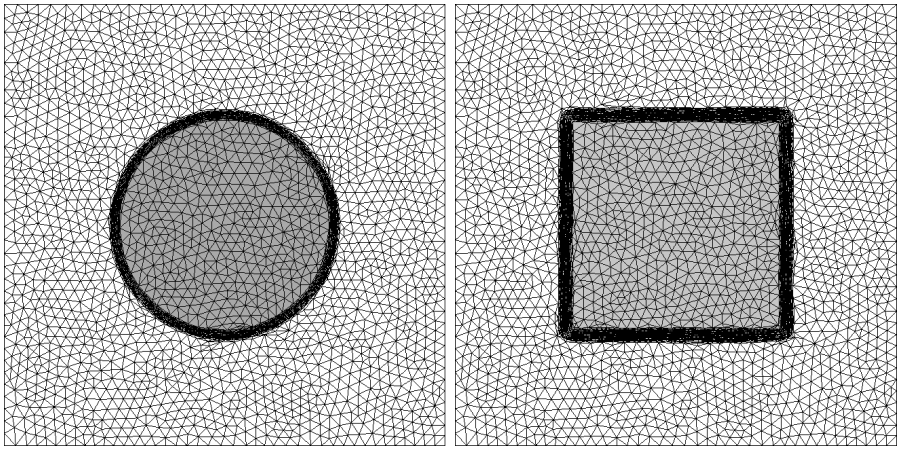


Figure 3.21: Anisotropic refined fluid-solid interface of an immersed disk (left) and square (right).

where $\mathbb{I}$ is the identity tensor. The mesh resolution can be forced to concentrate in particular areas of interest. The metric returns to isotropic far from the interface (with a mesh size equal to h_d for all directions) and to anisotropic near the interface (with a mesh size equal to h_{im} in the direction $\mathbf{x}$ and equal to h_d in the others). This method can be assisted by a posteriori anisotropic error estimator, the search of the optimal mesh (metric) that minimizes the error estimator. As a result, an optimal metric as a minimum of an error indicator function and for a given number of elements may be obtained.

The proposed mesh generation algorithm provides a high precision in the calculus and in the geometry description, in spite of an important decrease of the total number of degrees of freedom. Note also that the proposed method can easily handle arbitrary complex geometries. As shown in figure 3.21 which presents a close-up on the interface zone at the end of the anisotropic adaptation process, the mesh has been gradually refined when approaching the interface. Consequently, only additional nodes are locally added in this region, whereas the rest of domain keeps the same background size.

3.4.3 Governing equations

This section is devoted to the mathematical formulation for a rigid body immersed in an incompressible fluid. The governing equations are considered to be three-dimensional and time-dependent. As the proposed approach is monolithic, a unique constitutive equation will be solved on the whole domain with variable physical properties separated by a prescribed levelset function. We shall start presenting the formulation in the case of the stationary Stokes problem, and then we shall move to the general transient and nonlinear problem.

3.4.3.1 Rigid body restriction in a stationary Stokes flow

Let $\Omega \subset \mathbb{R}^n$ be the spatial domain at time $t \in [0, T]$, where n is the space dimension. Let $\partial\Omega$ denote the boundary of Ω. The fluid domain, the solid domain and the interface will be Ω_f, Ω_s and Γ_im, respectively. They verify:

$$\overline{\Omega}_\mathrm{f} \cup \overline{\Omega}_\mathrm{s} = \overline{\Omega} \quad \text{and} \quad \overline{\Omega}_\mathrm{f} \cap \overline{\Omega}_\mathrm{s} = \Gamma_\mathrm{im}.$$

Consider the Stokes problem, first posed on the whole domain Ω: find a velocity $\mathbf{v} : \Omega \longrightarrow \mathbb{R}^n$ and a pressure $p : \Omega \longrightarrow \mathbb{R}$ such that

$$\begin{aligned} -2\eta_\mathrm{f} \nabla \cdot \boldsymbol{\varepsilon}(\mathbf{v}) + \nabla p &= \mathbf{f} \\ \nabla \cdot \mathbf{v} &= 0 \end{aligned}$$

where η_f is the fluid viscosity, $\boldsymbol{\varepsilon}(\mathbf{v})$ the strain rate tensor and $\mathbf{f}$ the vector of body forces. We may assume for simplicity homogeneous Dirichlet boundary conditions.

The solution is the optimal point of the functional

$$L_1(\mathbf{v}, p) = \eta_\mathrm{f}(\boldsymbol{\varepsilon}(\mathbf{v}), \boldsymbol{\varepsilon}(\mathbf{v})) - (p, \nabla \cdot \mathbf{v}) - \langle \mathbf{f}, \mathbf{v} \rangle$$

Here and below, $(\cdot, \cdot)$ stands for the standard L^2 product of two functions and $\langle \cdot, \cdot \rangle$ for the integral of the product of two functions in the general case, including appropriate duality pairings if necessary.

Consider now the presence of the rigid body Ω_s in Ω. *It may be characterized by the fact that* $\boldsymbol{\varepsilon}(\mathbf{v}) = \mathbf{0}$ *in* Ω_s. Imposing this restriction through an appropriate Lagrange multiplier $\boldsymbol{\tau}$, the problem to be solved consists of finding the optimal point of the functional

$$L_2(\mathbf{v}, p, \boldsymbol{\tau}) = \eta_\mathrm{f}(\boldsymbol{\varepsilon}(\mathbf{v}), \boldsymbol{\varepsilon}(\mathbf{v})) - (p, \nabla \cdot \mathbf{v}) + (\boldsymbol{\tau}, \boldsymbol{\varepsilon}(\mathbf{v}))_\mathrm{s} - \langle \mathbf{f}, \mathbf{v} \rangle$$

where $(\cdot, \cdot)_\mathrm{s}$ denotes the inner product in Ω_s. If $(\mathbf{w}, q, \boldsymbol{\xi})$ are the test functions for $(\mathbf{v}, p, \boldsymbol{\tau})$, the weak form of the problem consists of finding $(\mathbf{v}, p, \boldsymbol{\tau})$ in the adequate functional spaces such that

$$2\eta_\mathrm{f}(\boldsymbol{\varepsilon}(\mathbf{v}), \boldsymbol{\varepsilon}(\mathbf{w})) + (\boldsymbol{\tau}, \boldsymbol{\varepsilon}(\mathbf{w}))_\mathrm{s} - (p, \nabla \cdot \mathbf{w}) = \langle \mathbf{f}, \mathbf{w} \rangle \tag{3.56}$$

$$(q, \nabla \cdot \mathbf{v}) = 0 \tag{3.57}$$

$$(\boldsymbol{\xi}, \boldsymbol{\varepsilon}(\mathbf{v}))_\mathrm{s} = 0 \tag{3.58}$$

which must hold for all appropriate $(\mathbf{w}, q, \boldsymbol{\xi})$. The strong form of the problem reads

$$-2\eta_\mathrm{f} \nabla \cdot \boldsymbol{\varepsilon}(\mathbf{v}) - \nabla \cdot \chi_\mathrm{s} \boldsymbol{\tau} + \nabla p = \mathbf{f} \tag{3.59}$$

$$\nabla \cdot \mathbf{v} = 0 \tag{3.60}$$

$$\chi_\mathrm{s} \boldsymbol{\varepsilon}(\mathbf{v}) = \mathbf{0} \tag{3.61}$$

where χ_s is the characteristic function of Ω_s.

The critical point is the setting of the Lagrange multiplier $\boldsymbol{\tau}$. The equation $(\boldsymbol{\xi}, \boldsymbol{\varepsilon}(\mathbf{v}))_\mathrm{s} = 0$ for all $\boldsymbol{\xi}$ has to have enough "restrictions" to yield $\boldsymbol{\varepsilon}(\mathbf{v}) = 0$ on Ω_s, but not too many.

Loosely speaking, there are only three functions to be set (the components of $\mathbf{v}$), and therefore there cannot be more than three scalar multipliers to be determined, whereas $\boldsymbol{\tau}$ has, in principle, six components (assuming it is symmetric).

A possible way to choose $\boldsymbol{\tau}$ that leads to a stable scheme is to take it as $\boldsymbol{\tau} = 2\eta_{\rm s}\boldsymbol{\varepsilon}(\mathbf{g})$, where $\mathbf{g}$ is *a vector field to be determined* and $\eta_{\rm s}$ is a viscosity acting as scaling coefficient. If $\mathbf{h}$ is the test function for $\mathbf{g}$, the final weak form of the problem would be

$$2\eta_{\rm f}(\boldsymbol{\varepsilon}(\mathbf{v}),\boldsymbol{\varepsilon}(\mathbf{w})) + 2\eta_{\rm s}(\boldsymbol{\varepsilon}(\mathbf{g}),\boldsymbol{\varepsilon}(\mathbf{w}))_{\rm s} - (p,\nabla\cdot\mathbf{w}) = \langle\mathbf{f},\mathbf{w}\rangle \tag{3.62}$$

$$(q,\nabla\cdot\mathbf{v}) = 0 \tag{3.63}$$

$$-2\eta_{\rm s}(\boldsymbol{\varepsilon}(\mathbf{h}),\boldsymbol{\varepsilon}(\mathbf{v}))_{\rm s} = 0 \tag{3.64}$$

which must hold for all appropriate $(\mathbf{w}, q, \mathbf{h})$. It is not our intention to pursue here the analysis of the well posedness of (3.62)-(3.64), which will be presented elsewhere.

Remarks:

- Note that the resulting problem is completely different to what would be obtained using a penalty method, in which $\boldsymbol{\tau} = 2\eta_{\rm s}\chi_{\rm s}\boldsymbol{\varepsilon}(\mathbf{v})$ with $\eta_{\rm s}\to\infty$.
- Equation (3.63) has to be imposed only in the fluid, since in the solid it is implied by (3.64). At the discrete level, this is not necessary if one can guarantee that (3.63) is compatible with (3.64).
- The vector field $\mathbf{g}$ is undetermined by infinitessimal rigid body motions.

Equation (3.64) can be relaxed iteratively using an augmented Lagrangian formulation coupled with a Uzawa scheme (iterative penalization). Let $r > 1$ be a given penalty parameter. A possible iterative scheme to solve (3.62)-(3.64) would be

$$2\frac{\eta_{\rm s}}{r}(\boldsymbol{\varepsilon}(\mathbf{h}),\boldsymbol{\varepsilon}(\mathbf{g}^k) - \boldsymbol{\varepsilon}(\mathbf{g}^{k-1}))_{\rm s} - 2\eta_{\rm s}(\boldsymbol{\varepsilon}(\mathbf{h}),\boldsymbol{\varepsilon}(\mathbf{v}^{k-1}))_{\rm s} = 0 \tag{3.65}$$

$$2\eta_{\rm f}(\boldsymbol{\varepsilon}(\mathbf{v}^k),\boldsymbol{\varepsilon}(\mathbf{w})) + 2\eta_{\rm s}(\boldsymbol{\varepsilon}(\mathbf{g}^k),\boldsymbol{\varepsilon}(\mathbf{w}))_{\rm s} - (p^k,\nabla\cdot\mathbf{w}) = \langle\mathbf{f},\mathbf{w}\rangle \tag{3.66}$$

$$(q,\nabla\cdot\mathbf{v}^k) = 0 \tag{3.67}$$

where the superscript denotes the iteration counter.

Let us *call* $\boldsymbol{\tau} = 2\eta_{\rm s}\boldsymbol{\varepsilon}(\mathbf{g})$, $\boldsymbol{\xi} = 2\eta_{\rm s}\boldsymbol{\varepsilon}(\mathbf{h})$. This definition allows us to write (3.65)-(3.67) as

$$\frac{1}{2\eta_{\rm s}\,r}(\boldsymbol{\xi},\boldsymbol{\tau}^k - \boldsymbol{\tau}^{k-1})_{\rm s} - (\boldsymbol{\xi},\boldsymbol{\varepsilon}(\mathbf{v}^{k-1}))_{\rm s} = 0 \tag{3.68}$$

$$2\eta_{\rm f}(\boldsymbol{\varepsilon}(\mathbf{v}^k),\boldsymbol{\varepsilon}(\mathbf{w})) + (\boldsymbol{\tau}^k,\boldsymbol{\varepsilon}(\mathbf{w}))_{\rm s} - (p^k,\nabla\cdot\mathbf{w}) = \langle\mathbf{f},\mathbf{w}\rangle \tag{3.69}$$

$$(q,\nabla\cdot\mathbf{v}^k) = 0 \tag{3.70}$$

If P_τ is the projection onto the space of $\boldsymbol{\tau}$'s, (3.68) can be written as

$$\boldsymbol{\tau}^k = \boldsymbol{\tau}^{k-1} + 2\eta_{\rm s}\,r\,P_\tau(\boldsymbol{\varepsilon}(\mathbf{v}^{k-1})) \tag{3.71}$$

In the iterative procedure described, the velocity could be treated implicitly in the evaluation of $\boldsymbol{\tau}$, that is to say, $\mathbf{v}^{k-1}$ in (3.65), (3.68) and (3.71) could be replaced by $\mathbf{v}^k$. In this case, there would be an additional contribution to $\boldsymbol{\varepsilon}(\mathbf{v}^k)$ in (3.66) and (3.69).

For numerical purposes, it could be interesting *to interpolate $\boldsymbol{\tau}$ as an independent variable*. The problem to be solved would be exactly the same as the previous one, which converges to the original problem (3.56)-(3.58). However, it is expected that, *because of the iterative way to compute $\boldsymbol{\tau}$*, its space will automatically have the appropriate dimension. Note also that infinitessimal rigid body motions will be filtered because $\mathbf{v}$ is uniquely determined by the boundary conditions.

3.4.3.2 The Navier-Stokes equations with a rigid body

The dynamics of the flow is given by the classical incompressible Navier-Stokes equations, which may be written as

$$\rho_{\mathrm{f}}\ (\partial_t \mathbf{v} + \mathbf{v}\cdot\nabla\mathbf{v}) - \nabla\cdot\boldsymbol{\sigma} = \mathbf{f} \quad \text{in } \Omega_{\mathrm{f}},\ t>0 \tag{3.72}$$

$$\nabla\cdot\mathbf{v} = 0 \quad \text{in } \Omega_{\mathrm{f}},\ t>0 \tag{3.73}$$

where now the velocity $\mathbf{v}(\mathbf{x},t)$ is time dependent, ρ_{f} is the fluid density and the Cauchy stress tensor for a Newtonian fluid is given by:

$$\boldsymbol{\sigma} = 2\eta_{\mathrm{f}}\ \boldsymbol{\varepsilon}(\mathbf{v}) - p\ \mathbf{I}_d \tag{3.74}$$

where $\mathbf{I}_d$ is the d-dimensional identity tensor. Equations (A.10)-(A.11) are subject to the boundary and initial conditions

$$\mathbf{v} = \mathbf{v}_{\Gamma,\mathrm{f}} \quad \text{on } \partial\Omega_{\mathrm{f}} \setminus \Gamma_{\mathrm{im}},\ t>0 \tag{3.75}$$

$$\mathbf{v} = \mathbf{v}_{\mathrm{im}} \quad \text{on } \Gamma_{\mathrm{im}},\ t>0 \tag{3.76}$$

$$\boldsymbol{\sigma}\cdot\mathbf{n} = \mathbf{t}_{\mathrm{im}} \quad \text{on } \Gamma_{\mathrm{im}},\ t>0 \tag{3.77}$$

$$\mathbf{v}(\mathbf{x},0) = \mathbf{v}_0(\mathbf{x}) \quad \text{in } \Omega_{\mathrm{f}} \tag{3.78}$$

where $\mathbf{v}_{\Gamma,\mathrm{f}}$ is a given velocity boundary condition, $\mathbf{v}_{\mathrm{im}}$ is the velocity at the fluid-solid interface Γ_{im} (the boundary of the immersed body), $\mathbf{n}$ is the outward normal on the solid surface, $\mathbf{t}_{\mathrm{im}}$ the normal stress on this boundary and $\mathbf{v}_0(\mathbf{x})$ is a given initial condition. For simplicity, only Dirichlet-type boundary conditions will be considered on the exterior boundary. For incompressible flows the divergence-free constraint (A.11) gives rise to the pressure in the fluid.

In the present formulation we treat the rigid body as a continuous domain subjected to an additional rigidity constraint. We may write the equations of motion as the Navier-Stokes equations with this constraint as:

$$\rho_{\mathrm{s}}\ (\partial_t \mathbf{v} + \mathbf{v}\cdot\nabla\mathbf{v}) - \nabla\cdot\boldsymbol{\sigma} = \mathbf{f} \quad \text{in } \Omega_{\mathrm{s}},\ t>0 \tag{3.79}$$

$$\nabla\cdot\mathbf{v} = 0 \quad \text{in } \Omega_{\mathrm{s}},\ t>0 \tag{3.80}$$

$$\boldsymbol{\varepsilon}(\mathbf{v}) = \mathbf{0} \quad \text{in } \Omega_{\mathrm{s}},\ t>0 \tag{3.81}$$

where $\rho_{\rm s}$ the solid density. In a rigid body there is no deformation, that is to say, $\boldsymbol{\varepsilon}(\mathbf{u}) = \mathbf{0}$ ($\mathbf{u}$ is the displacement field) and $\partial_t \mathbf{u} = \mathbf{v}$. These two equations imply a null value of the deformation-rate tensor (A.19). Note also that the rigidity constraint (A.19) ensures that the velocity field is divergence-free. Hence (A.18) is a redundant equation. Nevertheless we choose to keep it to account for the pressure term. As noted earlier, (A.18) gives rise to a pressure fluid. Similarly, as explained in the previous subsection for the Stokes problem, (A.19) gives rise to a stress field $\boldsymbol{\tau}$. The stress tensor is then given by:

$$\boldsymbol{\sigma} = \boldsymbol{\tau}_{\rm s} - p\, \mathbf{I}_d \tag{3.82}$$

Equations (A.17)-(A.19) need to be supplied with the boundary and initial conditions

$$\mathbf{v} = \mathbf{v}_{\Gamma,{\rm s}} \quad \text{on } \partial\Omega_{\rm s} \setminus \Gamma_{\rm im},\ t > 0 \tag{3.83}$$

$$\mathbf{v} = \mathbf{v}_{\rm im} \quad \text{on } \Gamma_{\rm im},\ t > 0 \tag{3.84}$$

$$\boldsymbol{\sigma} \cdot \mathbf{n} = -\mathbf{t}_{\rm im} \quad \text{on } \Gamma_{\rm im},\ t > 0 \tag{3.85}$$

$$\mathbf{v}(\mathbf{x}, 0) = \mathbf{v}_0(\mathbf{x}) \quad \text{in } \Omega_{\rm s} \tag{3.86}$$

where $\mathbf{v}_{\Gamma,{\rm f}}$ is a given velocity boundary condition that needs to be compatible with a rigid body motion if $\partial\Omega_{\rm s} \setminus \Gamma_{\rm im} \neq \emptyset$, and the initial condition $\mathbf{v}_0(\mathbf{x})$ must be also compatible with a rigid body motion.

Making use of the notation introduced in section 2, we may write problem (A.10)-(A.15) and problem (A.17)-(A.22) in a unified way in the whole computational domain Ω as

$$\begin{aligned} \rho\,(\partial_t \mathbf{v} + \mathbf{v}\cdot\nabla\mathbf{v}) - \nabla\cdot(2\eta\,\boldsymbol{\varepsilon}(\mathbf{v}) + \boldsymbol{\tau} - p\,\mathbf{I}_d) &= \mathbf{f} \quad && \text{in } \Omega,\ t>0 \\ \nabla\cdot\mathbf{v} &= 0 \quad && \text{in } \Omega,\ t>0 \\ \boldsymbol{\varepsilon}_{\rm s}(\mathbf{v}) &= \mathbf{0} \quad && \text{in } \Omega,\ t>0 \\ \mathbf{v} &= \mathbf{v}_\Gamma \quad && \text{on } \partial\Omega,\ t>0 \\ \mathbf{v}(\mathbf{x},0) &= \mathbf{v}_0(\mathbf{x}) \quad && \text{in } \Omega \end{aligned} \tag{3.87}$$

where $\mathbf{v}_\Gamma = \mathbf{v}_{\Gamma,{\rm s}}$ on $\partial\Omega_{\rm s} \cap \partial\Omega$ and $\mathbf{v}_\Gamma = \mathbf{v}_{\Gamma,{\rm f}}$ on $\partial\Omega_{\rm f} \cap \partial\Omega$, $\boldsymbol{\varepsilon}_{\rm s}(\mathbf{v}) = H(\alpha)\boldsymbol{\varepsilon}(\mathbf{v})$, $\eta = (1 - H(\alpha))\eta_{\rm f}$, $\rho = \rho_{\rm s}H(\alpha) + \rho_{\rm f}(1 - H(\alpha))$ and $\boldsymbol{\tau} = H(\alpha)\boldsymbol{\tau}_{\rm s}$. The boundary conditions (A.13)-(A.14) and (A.20)-(A.21) are no longer needed.

Let $V \times P \times \mathcal{T}$ the space where the unknown $(\mathbf{v}, p, \boldsymbol{\tau})$ is sought. The first space, V, is made of vector fields which are square integrable in time with values in $H^1(\Omega)^n$ and satisfying the Dirichlet conditions, where the last two, P and $\mathcal{T}$, are made of distributions in time with values in $P_0 = L^2(\Omega)/\mathbb{R}$ and $\mathcal{T}_0 = L^2(\Omega)^{n\times n}$, respectively (in fact, a subspace of $L^2(\Omega)^{n\times n}$ would be enough, see below). The corresponding test functions will be denoted $\mathbf{w} \in V_0 = H_0^1(\Omega)^n$, $q \in P_0$ and $\boldsymbol{\xi} \in \mathcal{T}_0$. Multiplying by the test functions and integrating by parts, the associated standard weak form of the system (3.87), can be stated as: Find $\mathbf{v} \in V$, $p \in P$ and $\boldsymbol{\tau} \in \mathcal{T}$ such that

$$\begin{aligned} \rho(\partial_t \mathbf{v}, \mathbf{w}) + \rho(\mathbf{v}\cdot\nabla\mathbf{v}, \mathbf{w}) - (p, \nabla\cdot\mathbf{w}) + (2\eta\boldsymbol{\varepsilon}(\mathbf{v}), \boldsymbol{\varepsilon}(\mathbf{w})) + (\boldsymbol{\tau}, \boldsymbol{\varepsilon}_{\rm s}(\mathbf{w})) &= \langle \mathbf{f}, \mathbf{w}\rangle \\ (q, \nabla\cdot\mathbf{v}) &= 0 \\ -(\boldsymbol{\xi}, \boldsymbol{\varepsilon}_{\rm s}(\mathbf{v})) &= 0 \end{aligned} \tag{3.88}$$

for all $(\mathbf{w}, q, \boldsymbol{\xi}) \in V_0 \times P_0 \times \mathcal{T}_0$.

As explained in the previous subsection for the Stokes case, the problem is not well posed without additional conditions on $\boldsymbol{\tau}$. A possible way to choose it is to take it as a symmetric gradient of a vector field. Moreover, this field needs not to be computed if an augmented Lagrangian scheme together with an Uzawa iterative scheme are employed. This is what we describe next.

Suppose that we discretize in time problem (3.88) using a finite difference scheme, and still denote by $\mathbf{v}$, p and $\boldsymbol{\tau}$ the fields to be computed at a given time step. Let $\delta_t \mathbf{v}$ the discrete time derivative and r the penalty parameter in the Uzawa scheme. Treating implicitly the velocity in the calculation of the stress in the solid (i.e., using $\mathbf{v}^k$ in (3.65), (3.68) and (3.71) instead of $\mathbf{v}^{k-1}$), the iterative scheme to be performed *within each time step* reads:

1. Set $k = 0$
2. Initalize $\mathbf{v}^0$, p^0 and $\boldsymbol{\tau}^0$ (for example to values in the last time step)
3. $k \leftarrow k + 1$
4. Solve for $\mathbf{v}^k$ and p^k:

$$\begin{aligned} &\rho(\delta_t \mathbf{v}^k, \mathbf{w}) + \rho(\mathbf{v}^k \cdot \nabla \mathbf{v}^k, \mathbf{w}) - (p^k, \nabla \cdot \mathbf{w}) \\ &\qquad + 2(\eta \boldsymbol{\varepsilon}(\mathbf{v}^k) + H(\alpha)\eta_{\mathrm{s}}\, r\, P_\tau(\boldsymbol{\varepsilon}(\mathbf{v}^k)), \boldsymbol{\varepsilon}(\mathbf{w})) + (\boldsymbol{\tau}^{k-1}, \boldsymbol{\varepsilon}_{\mathrm{s}}(\mathbf{w})) = \langle \mathbf{f}, \mathbf{w} \rangle \\ &(q, \nabla \cdot \mathbf{v}^k) = 0 \end{aligned}$$

5. Update $\boldsymbol{\tau}^k = \boldsymbol{\tau}^{k-1} + 2\eta_{\mathrm{s}}\, r\, P_\tau(\boldsymbol{\varepsilon}(\mathbf{v}^k))$ in Ω_{s}.
6. Check convergence: if $\|\mathbf{v}^k - \mathbf{v}^{k-1}\| > \texttt{tol}$ (given tolerance in a given norm), go to 3. Otherwise, proceed to the next time step.

Remarks:

- If the space for $\boldsymbol{\tau}$ contains all symmetric gradients of vector fields, $P_\tau = I$ (identity) and we could solve the momentum equation in step 4 with the viscosity $\eta + H(\alpha)\eta_{\mathrm{s}}\, r$. However, at the discrete level it can be of interest to take the space for the approximation to $\boldsymbol{\tau}$ different from symmetric gradients.

- In the previous scheme we have considered Uzawa's iterations uncoupled from the iterations required to linearize the convective term and the time stepping itself. Obviously, it could also be possible to deal with these in a coupled way.

3.4.4 Stabilized Finite-Element Method (SFEM)

In this section, we describe briefly the Galerkin finite element approximation and the corresponding stabilization method for the resulting discrete system of equations (3.88). Based on a mesh $\mathcal{K}_h$ of Ω made of N_{el} elements K, the functional spaces for the velocity, the pressure and the stress are approximated by the finite dimensional spaces V_h, P_h and $\mathcal{T}_h$, respectively.

As it is well known, the stability of the discrete formulation depends on appropriate compatibility restrictions on the choice of the finite element spaces. According to this, standard Galerkin mixed elements with, for example, continuous equal order linear/linear interpolation for the three fields are not stable. Lack of stability shows as uncontrollable oscillations that pollute the solution. We propose in here a Variational MultiScale method (see [113]), which allows one the use of equal order continuous interpolations for the three fields, apart from preventing from oscillations due to convection dominated flows. The basic idea is to consider that the unknowns can be split in two components, coarse and fine, corresponding to different scales or levels of resolution [67]. First, we solve the fine scales in an approximate manner and then we replace their effect into the large scales.

Let us split the velocity, pressure and stress solution spaces as $V_h \oplus V'$, $P_h \oplus P'$ and $\mathcal{T}_h \oplus \mathcal{T}'$, respectively. Subscript h is used here and in the following to denote the finite element (coarse) component, whereas the prime is used for the so called subgrid scale (fine) component of the unknowns. According to this, we have

$$\begin{aligned}\mathbf{v} &= \mathbf{v}_h + \mathbf{v}' \ \in \ V_h \oplus V' \\ p &= p_h + p' \ \in \ P_h \oplus P' \\ \boldsymbol{\tau} &= \boldsymbol{\tau}_h + \boldsymbol{\tau}' \ \in \ \mathcal{T}_h \oplus \mathcal{T}'\end{aligned}$$

If the spaces for the test functions are split likewise, with a subscript 0 to identify them, problem (3.88) becomes: find $(\mathbf{v}_h + \mathbf{v}', p_h + p', \boldsymbol{\tau}_h + \boldsymbol{\tau}') \in V_h \oplus V' \times P_h \oplus P' \times \mathcal{T}_h \oplus \mathcal{T}'$ such that

$$\begin{aligned}\rho(\delta_t(\mathbf{v}_h + \mathbf{v}'), \mathbf{w}_h + \mathbf{w}') + \rho((\mathbf{v}_h + \mathbf{v}') \cdot \nabla(\mathbf{v}_h + \mathbf{v}'), \mathbf{w}_h + \mathbf{w}') - (p_h + p', \nabla\cdot(\mathbf{w}_h + \mathbf{w}')) \\ +2(\eta\boldsymbol{\varepsilon}(\mathbf{v}_h + \mathbf{v}'), \boldsymbol{\varepsilon}(\mathbf{w}_h + \mathbf{w}')) + (\boldsymbol{\tau}_h + \boldsymbol{\tau}', \boldsymbol{\varepsilon}_{\mathrm{s}}(\mathbf{w}_h + \mathbf{w}')) = \langle \mathbf{f}, \mathbf{w}_h + \mathbf{w}' \rangle \qquad (3.89)\end{aligned}$$

$$(q_h + q', \nabla \cdot (\mathbf{v}_h + \mathbf{v}')) = 0 \qquad (3.90)$$

$$-(\boldsymbol{\xi}_h + \boldsymbol{\xi}', \boldsymbol{\varepsilon}_{\mathrm{s}}(\mathbf{v}_h + \mathbf{v}')) = 0 \qquad (3.91)$$

for all $(\mathbf{w}_h + \mathbf{w}', q_h + q', \boldsymbol{\xi}_h + \boldsymbol{\xi}') \in V_{h,0} \oplus V_0' \times P_{h,0} \oplus P_0' \times \mathcal{T}_{h,0} \oplus \mathcal{T}_0'$. Recall that δ_t stands for an approximation to the time derivative ∂_t. Even if time has been discretized, we have kept the notation for the functional spaces for simplicity.

Even though the subgrid scales (or subscales) could be approximated without further assumptions and inserted into the previous equations (see [104]), we will make use of some common approximations:

i) The subscales are not tracked in time, therefore, quasi-static subscales are considered here. However, the subscale equation remains quasi time-dependent.

ii) The convective velocity of the non-linear term may be approximated using only the large-scale component, so that $(\mathbf{v}_h + \mathbf{v}') \cdot \nabla(\mathbf{v}_h + \mathbf{v}') \approx \mathbf{v}_h \cdot \nabla(\mathbf{v}_h + \mathbf{v}')$. Moreover, this approximation can be done also if the convective term is written as $\nabla \cdot (\mathbf{v}_h + \mathbf{v}') \otimes (\mathbf{v}_h + \mathbf{v}')$, which is relevant when integrating by parts the convective term.

iii) Terms involving subscales can be integrated by parts and the subscales on the element boundaries neglected.

The equations for the coarse scales are obtained taking the subscale test functions equal to zero. Doing this and using the previous assumptions, we get

$$\rho(\delta_t \mathbf{v}_h, \mathbf{w}_h) + \rho(\mathbf{v}_h \cdot \nabla \mathbf{v}_h, \mathbf{w}_h) - (p_h + p', \nabla \cdot \mathbf{w}_h) + 2(\eta \boldsymbol{\varepsilon}(\mathbf{v}_h), \boldsymbol{\varepsilon}(\mathbf{w}_h)) + (\boldsymbol{\tau}_h + \boldsymbol{\tau}', \boldsymbol{\varepsilon}_{\mathrm{s}}(\mathbf{w}_h)) + \sum_K (\mathbf{v}', -\rho \mathbf{v}_h \cdot \nabla \mathbf{w}_h - \nabla \cdot (2\eta \boldsymbol{\varepsilon}(\mathbf{w}_h)))_K = \langle \mathbf{f}, \mathbf{w}_h \rangle \tag{3.92}$$

$$(q_h, \nabla \cdot \mathbf{v}_h) - \sum_K (\mathbf{v}', \nabla q_h)_K = 0 \tag{3.93}$$

$$-(\boldsymbol{\varepsilon}_{\mathrm{s}}(\mathbf{v}_h), \boldsymbol{\xi}_h) + \sum_K (\mathbf{v}', \chi_{\mathrm{s}} \nabla \cdot \boldsymbol{\xi}_h)_K = 0 \tag{3.94}$$

for all $(\mathbf{w}_h, q_h, \boldsymbol{\xi}_h) \in V_{h,0} \times P_{h,0} \times \mathcal{T}_{h,0}$, where $\sum_K$ stands for the summation over all the elements of the finite element partition $\mathcal{K}_h$ and $(\cdot, \cdot)_K$ denotes the L^2 product in each K.

The problem for the fine scales is obtained taking $(\mathbf{w}_h, q_h, \boldsymbol{\xi}_h) = (\mathbf{0}, 0, \mathbf{0})$ in (3.89)-(3.91) and using approximations i)-iii) described above. Introducing the finite element residuals

$$\begin{aligned}
\mathcal{R}_v &= \mathbf{f} - \rho \delta_t \mathbf{v}_h - \rho \mathbf{v}_h \cdot \nabla \mathbf{v}_h - \nabla p_h + \chi_{\mathrm{s}} \nabla \cdot \boldsymbol{\tau}_h + \nabla \cdot (2\eta \boldsymbol{\varepsilon}(\mathbf{v}_h)) \\
\mathcal{R}_p &= -\nabla \cdot \mathbf{v}_h \\
\mathcal{R}_\tau &= \boldsymbol{\varepsilon}_{\mathrm{s}}(\mathbf{v}_h)
\end{aligned}$$

and using the same ideas as in [101, 114], it turns out that the subscales may be approximated within each element $K \in \mathcal{K}_h$ by

$$\mathbf{v}' = \alpha_v \Pi_v'(\mathcal{R}_v), \quad p' = \alpha_p \Pi_p'(\mathcal{R}_p), \quad \boldsymbol{\tau}' = \alpha_\tau \Pi_\tau'(\mathcal{R}_\tau)$$

where Π_v', Π_p' and Π_τ' are the projections onto V', P' and $\mathcal{T}'$, respectively, and α_v, α_p and α_τ are the so called stabilization parameters. The most common choice is to take the former as the identity when applied to finite element residuals (see [113, 101]), and this is what we will do here, although it is also possible to take them as the projection orthogonal to the finite element space (see [114] and references therein). Referring to the

stabilization parameters, we compute them within each element as

$$\alpha_v = \left[\left(\frac{c_1 \eta}{\rho h^2} \right)^2 + \left(\frac{c_2 \|\mathbf{v}_h\|_K}{h} \right)^2 \right]^{-1/2} \tag{3.95}$$

$$\alpha_p = \left[\left(\frac{\eta}{\rho} \right)^2 + \left(\frac{c_2 \|\mathbf{v}_h\|_K h}{c_1} \right)^2 \right]^{1/2} \tag{3.96}$$

$$\alpha_\tau = c_3 \frac{h}{L} 2\eta_{\mathrm{s}} \tag{3.97}$$

where h is the element size, L a characteristic length of the computational domain, $\|\mathbf{v}\|_K$ a characteristic norm of $\mathbf{v}_h$ (with the same units as $\mathbf{v}_h$) in element K and c_1, c_2 and c_3 are algorithmic constants. We take them as $c_1 = 4$, $c_2 = 2$ and $c_3 = 1$ for linear elements.

Remarks:

- Very often, the time step size of the temporal discretization is included in the expression of α_v. This improves the convergence behaviour of the algorithm to deal with the nonlinearity of the problem, but has several conceptual drawbacks, as explained in [115, 116]. In order to make α_v more uniform over the computational domain and, as a consequence, improve the behaviour of the scheme, one may take

$$\alpha_v = \left[\frac{1}{\alpha_0^2} + \left(\frac{c_1 \eta}{\rho h^2} \right)^2 + \left(\frac{c_2 \|\mathbf{v}_h\|_K}{h} \right)^2 \right]^{-1/2}$$

  where α_0 is a reference value of α_v given by (3.95) computed over the whole mesh (for example the minimum over all the elements). This value in fact should be related to the time step size of the time discretization, Δt.

- The factor h/L in (3.97) improves convergence of stresses when equal interpolation is used for all variables [101, 102]. However, it is possible to take it out (that is to say, to take $L = h$) and get optimal convergence for velocity and pressure [114].

- For the linear elements used in the numerical examples, terms of the form $\nabla \cdot (2\eta \boldsymbol{\varepsilon}(\mathbf{w}_h))$ involving second derivatives within each element can be neglected.

Inserting the expression for the subscales obtained in (3.92)-(3.94) we finally obtain the stabilized finite element problem we were seeking. It consists of finding $(\mathbf{v}_h, p_h, \boldsymbol{\tau}_h) \in$

$V_h \times P_h \times \mathcal{T}_h$ such that

$$\begin{aligned}
&\rho(\delta_t \mathbf{v}_h, \mathbf{w}_h) + \rho(\mathbf{v}_h \cdot \nabla \mathbf{v}_h, \mathbf{w}_h) - (p_h, \nabla \cdot \mathbf{w}_h) + 2(\eta \boldsymbol{\varepsilon}(\mathbf{v}_h), \boldsymbol{\varepsilon}(\mathbf{w}_h)) + (\boldsymbol{\tau}_h, \boldsymbol{\varepsilon}_{\mathrm{s}}(\mathbf{w}_h)) \\
&\quad + \sum_K \alpha_v (\rho \delta_t \mathbf{v}_h + \rho \mathbf{v}_h \cdot \nabla \mathbf{v}_h + \nabla p_h - \chi_{\mathrm{s}} \nabla \cdot \boldsymbol{\tau}_h - \nabla \cdot (2\eta \boldsymbol{\varepsilon}(\mathbf{v}_h)), \rho \mathbf{v}_h \cdot \nabla \mathbf{w}_h + \nabla \cdot (2\eta \boldsymbol{\varepsilon}(\mathbf{w}_h)))_K \\
&\quad + \sum_K \alpha_p (\nabla \cdot \mathbf{v}_h, \nabla \cdot \mathbf{w}_h) + \sum_K \alpha_\tau (\boldsymbol{\varepsilon}_{\mathrm{s}}(\mathbf{v}_h), \boldsymbol{\varepsilon}_{\mathrm{s}}(\mathbf{w}_h)) \\
&\quad = \langle \mathbf{f}, \mathbf{w}_h \rangle + \sum_K \alpha_v (\mathbf{f}, \rho \mathbf{v}_h \cdot \nabla \mathbf{w}_h + 2\eta \nabla \cdot \boldsymbol{\varepsilon}(\mathbf{w}_h))_K \qquad (3.98)
\end{aligned}$$

$$\begin{aligned}
&(q_h, \nabla \cdot \mathbf{v}_h) + \sum_K \alpha_v (\rho \delta_t \mathbf{v}_h + \rho \mathbf{v}_h \cdot \nabla \mathbf{v}_h + \nabla p_h - \chi_{\mathrm{s}} \nabla \cdot \boldsymbol{\tau}_h - \nabla \cdot (2\eta \boldsymbol{\varepsilon}(\mathbf{v}_h)), \nabla q_h)_K \\
&\quad = \sum_K \alpha_v (\mathbf{f}, \nabla q_h)_K \qquad (3.99)
\end{aligned}$$

$$\begin{aligned}
&-(\boldsymbol{\varepsilon}_{\mathrm{s}}(\mathbf{v}_h), \boldsymbol{\xi}_h) + \sum_K \alpha_v (\rho \delta_t \mathbf{v}_h + \rho \mathbf{v}_h \cdot \nabla \mathbf{v}_h + \nabla p_h - \chi_{\mathrm{s}} \nabla \cdot \boldsymbol{\tau}_h - \nabla \cdot (2\eta \boldsymbol{\varepsilon}(\mathbf{v}_h)), -\chi_{\mathrm{s}} \nabla \cdot \boldsymbol{\xi}_h)_K \\
&\quad = \sum_K \alpha_v (\mathbf{f}, -\chi_{\mathrm{s}} \nabla \cdot \boldsymbol{\xi}_h)_K \qquad (3.100)
\end{aligned}$$

for all $(\mathbf{w}_h, q_h, \boldsymbol{\xi}_h) \in V_{h,0} \times P_{h,0} \times \mathcal{T}_{h,0}$. We have assumed $\mathbf{f} \in L^2(K)^n$ for simplicity.

At this point the problem suffers from the lack of an appropriate choice for $\mathcal{T}_h$ to make system (3.98)-(3.100) uniquely solvable. This can be circumvented by using a sort of augmented Lagrangian scheme coupled with an Uzawa iterative scheme, as explained at the continuous level. In order to explain how to introduce this, let us write first the matrix form of problem (3.98)-(3.100). If X_v, X_p and X_τ are the nodal values of $\mathbf{v}_h$, p_h and $\boldsymbol{\tau}_h$, respectively, this matrix form reads:

$$\begin{pmatrix} A_{vv} & A_{vp} & A_{v\tau} \\ A_{pv} & A_{pp} & A_{p\tau} \\ A_{\tau v}^{(1)} + A_{\tau v}^{(2)} & A_{\tau p} & A_{\tau\tau} \end{pmatrix} \begin{pmatrix} X_v \\ X_p \\ X_\tau \end{pmatrix} = \begin{pmatrix} F_v \\ F_p \\ F_\tau \end{pmatrix} \qquad (3.101)$$

where the matrix components and the forcing terms are identified in Table 1. There, we have considered the approximation to the temporal derivative written as $\delta_t \mathbf{v}_h = \gamma \mathbf{v}_h - \mathbf{f}_t$, where γ is the coefficient that multiplies the unknown velocity and $\mathbf{f}_t$ is a combination of previous velocity values. For example, for the backward Euler scheme, $\gamma = \Delta t^{-1}$ and $\mathbf{f}_t = \Delta t^{-1} \mathbf{v}_h^{n-1}$, $\mathbf{v}_h^{n-1}$ being the velocity of the previous time step.

The iterative scheme we propose to solve (3.101) at each time step is

$$\begin{pmatrix} A_{vv} & A_{vp} & 0 \\ A_{pv} & A_{pp} & 0 \\ A_{\tau v}^{(1)} + A_{\tau v}^{(2)} & A_{\tau p} & \frac{1}{2\eta_{\mathrm{s}} r} M \end{pmatrix} \begin{pmatrix} X_v^k \\ X_p^k \\ X_\tau^k \end{pmatrix} = \begin{pmatrix} F_v - A_{v\tau} X_\tau^{k-1} \\ F_p - A_{p\tau} X_\tau^{k-1} \\ F_\tau + \frac{1}{2\eta_{\mathrm{s}} r} M X_\tau^{k-1} - A_{\tau\tau} X_\tau^{k-1} \end{pmatrix} \qquad (3.102)$$

where M is the mass matrix corresponding to the interpolation of $\boldsymbol{\tau}_h$ (the integral of the product of shape functions) and, as before, r is the penalty parameter. Obviously, the

first two equations in (3.102) can be solved in a coupled way and then the values of X_v^k and X_p^k can be used in the third equation.

Scheme (3.102) can be slightly modified in order to treat part of X_τ implicitly in the first equation, in the spirit of the remark after (3.71). From the third equation in (3.102) we have

$$\begin{aligned} X_\tau^k &= X_\tau^{k-1} + 2\eta_s r M^{-1}\left[F_\tau - A_{\tau v}^{(2)} X_v^k - A_{\tau p} X_p^k - A_{\tau\tau} X_\tau^{k-1}\right] + 2\eta_s r M^{-1}\left[-A_{\tau v}^{(1)} X_v^k\right] \\ &:= X_\tau^{k-1} + \delta X_\tau^{k,1} + \delta X_\tau^{k,2} \end{aligned}$$

with the obvious definition of arrays $\delta X_\tau^{k,1}$ and $\delta X_\tau^{k,2}$. A possible modification of the first equation in (3.102) is to replace X_τ^{k-1} by $X_\tau^{k-1} + \delta X_\tau^{k,2}$. From the expression of $A_{\tau v}^{(1)}$ in Table 1 it follows that the nodal values $\delta X_\tau^{k,2} = -2\eta_s r M^{-1} A_{\tau v}^{(1)} X_v^k$ are nothing but those of $-2\eta_s r P_\tau(\boldsymbol{\varepsilon}(\mathbf{v}_h))$. This term can therefore be moved to the left-hand-side of the first equation in (3.102). This in fact is achieved by simply replacing $2(\eta\boldsymbol{\varepsilon}(\mathbf{v}_h), \boldsymbol{\varepsilon}(\mathbf{w}_h))$ by $2(\eta\boldsymbol{\varepsilon}(\mathbf{v}_h) + H(\alpha)\eta_s\, r\, P_\tau(\boldsymbol{\varepsilon}(\mathbf{v}_h)), \boldsymbol{\varepsilon}(\mathbf{w}_h))$, as explained for the continuous problem.

3.4.5 Numerical experiments

In this section, we present several numerical examples to illustrate the flexibility of the approach dealing with complex geometry and to asses its accuracy. The numerical simulations were carried out using the C++ CimLib finite element library (see [46, 69]). The results obtained with the proposed approach, referred as ISM, are compared to solutions obtained either by standard solution (classical boundary conditions) or by other approaches.

3.4.5.1 2D immersion of solid bodies in an incompressible fluid

We first consider a numerical test of flow around four fixed cylinders in a square channel. This study is considered as a first step to investigate the feasibility of fluid-structure computations and could be used later on a tube bundle configuration, like those existing in nuclear steam generators.

We consider two cases. In the first case we apply the Immersed Stress Method: (i) we consider a very simple square domain $[0,1]\times[0,1]$, (ii) we compute analytically the signed distance function of four circles located on each corner of the domain, (iii) we apply the anisotropic mesh adaptation using the variation of the gradients of the level-set function, and finally, (iv) we mix and assign the physical properties. In the second case, the effort will be concentrated on the geometry and on building the fluid mesh while well respecting the curvatures. The obtained finite element meshes that will be used in the two cases are depicted in Figure 3.22.

We apply the same conditions on both test cases and we compare the solutions. We impose a pressure gradient at the inlet and outlet equal to $\Delta p = 100$. For simplicity, we set the density of the fluid $\rho_\mathrm{f} = 1$, the density of the solid $\rho_\mathrm{s} = 1$, and the viscosity of the fluid $\eta_\mathrm{f} = 1$.

Table 3.3: Contributions to the matrix form of the problem

Matrix/vector in (3.101)	Term (3.98)-(3.100)
A_{vv}	$\rho(\gamma\mathbf{v}_h, \mathbf{w}_h) + \rho(\mathbf{v}_h \cdot \nabla\mathbf{v}_h, \mathbf{w}_h) + 2(\eta\boldsymbol{\varepsilon}(\mathbf{v}_h), \boldsymbol{\varepsilon}(\mathbf{w}_h))$ $+ \sum_K \alpha_v(\rho\gamma\mathbf{v}_h + \rho\mathbf{v}_h \cdot \nabla\mathbf{v}_h - \nabla \cdot (2\eta\boldsymbol{\varepsilon}(\mathbf{v}_h)), \rho\mathbf{v}_h \cdot \nabla\mathbf{w}_h + \nabla \cdot (2\eta\boldsymbol{\varepsilon}(\mathbf{w}_h)))_K$ $+ \sum_K \alpha_p(\nabla \cdot \mathbf{v}_h, \nabla \cdot \mathbf{w}_h) + \sum_K \alpha_\tau(\boldsymbol{\varepsilon}_{\mathrm{s}}(\mathbf{v}_h), \boldsymbol{\varepsilon}_{\mathrm{s}}(\mathbf{w}_h))$
A_{vp}	$-(p_h, \nabla \cdot \mathbf{w}_h) + \sum_K \alpha_v(\nabla p_h, \rho\mathbf{v}_h \cdot \nabla\mathbf{w}_h + \nabla \cdot (2\eta\boldsymbol{\varepsilon}(\mathbf{w}_h)))_K$
$A_{v\tau}$	$(\boldsymbol{\tau}_h, \boldsymbol{\varepsilon}_{\mathrm{s}}(\mathbf{w}_h)) + \sum_K \alpha_v(-\chi_{\mathrm{s}}\nabla \cdot \boldsymbol{\tau}_h, \rho\mathbf{v}_h \cdot \nabla\mathbf{w}_h + \nabla \cdot (2\eta\boldsymbol{\varepsilon}(\mathbf{w}_h)))_K$
A_{pv}	$(q_h, \nabla \cdot \mathbf{v}_h) + \sum_K \alpha_v(\rho\gamma\mathbf{v}_h + \rho\mathbf{v}_h \cdot \nabla\mathbf{v}_h - \nabla \cdot (2\eta\boldsymbol{\varepsilon}(\mathbf{v}_h)), \nabla q_h)_K$
A_{pp}	$\sum_K \alpha_v(\nabla p_h, \nabla q_h)_K$
$A_{p\tau}$	$\sum_K \alpha_v(-\chi_{\mathrm{s}}\nabla \cdot \boldsymbol{\tau}_h, \nabla q_h)_K$
$A_{\tau v}^{(1)}$	$-(\boldsymbol{\varepsilon}_{\mathrm{s}}(\mathbf{v}_h), \boldsymbol{\xi}_h)$
$A_{\tau v}^{(2)}$	$\sum_K \alpha_v(\rho\gamma\mathbf{v}_h + \rho\mathbf{v}_h \cdot \nabla\mathbf{v}_h - \nabla \cdot (2\eta\boldsymbol{\varepsilon}(\mathbf{v}_h)), -\chi_{\mathrm{s}}\nabla \cdot \boldsymbol{\xi}_h)_K$
$A_{\tau p}$	$\sum_K \alpha_v(\nabla p_h, -\chi_{\mathrm{s}}\nabla \cdot \boldsymbol{\xi}_h)_K$
$A_{\tau\tau}$	$\sum_K \alpha_v(\chi_{\mathrm{s}}\nabla \cdot \boldsymbol{\tau}_h, \chi_{\mathrm{s}}\nabla \cdot \boldsymbol{\xi}_h)_K$
F_v	$\langle \mathbf{f} + \rho\mathbf{f}_t, \mathbf{w}_h \rangle + \sum_K \alpha_v(\mathbf{f} + \rho\mathbf{f}_t, \rho\mathbf{v}_h \cdot \nabla\mathbf{w}_h + 2\eta\nabla \cdot \boldsymbol{\varepsilon}(\mathbf{w}_h))_K$
F_p	$\sum_K \alpha_v(\mathbf{f} + \rho\mathbf{f}_t, \nabla q_h)_K$
F_τ	$\sum_K \alpha_v(\mathbf{f} + \rho\mathbf{f}_t, -\chi_{\mathrm{s}}\nabla \cdot \boldsymbol{\xi}_h)_K$

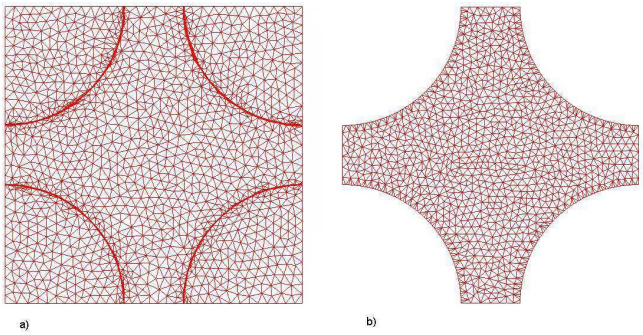


Figure 3.22: Finite element mesh and geometry of a) the immersed obstacles, b) the fluid domain.

A comparison of the velocity and the pressure fields computed on the entire square domain (fluid and solid) and on only the fluid domain are shown in Figures 3.23 and 3.24. The agreement between the two numerical solutions shows that the present solver is able to predict accurately the behaviour of the fluid and the presence of the solid. The pressure distribution caused by the interaction is more interesting, which is depicted in Figure 3.24.

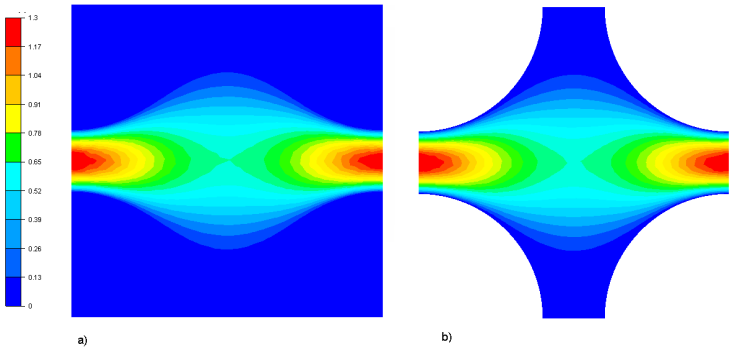


Figure 3.23: Norme of the velocity calculated over a) the entire domain b) the fluid domain

3.4.5.2 Immersion of solid bodies in fluid 3D

A similar test case is aimed at exploring the capabilities of the model when used in a situation involving more complex geometries in 3D. Here, we simulate the flow through two half spheres. As before, we choose to compare the results to those calculated only on the fluid domain. The mesh representation of the fluid domain case is shown in Figure 3.25. As sketched in Figure 3.26 mesh adaptation is required for a good capturing of the solid-fluid interface, a zoom of the adapted mesh is also depicted. The velocity and pressure fields computed with the proposed method are shown in Figure 3.27 and 3.28, respectively, and compared to results calculated only on the fluid domain. Again the

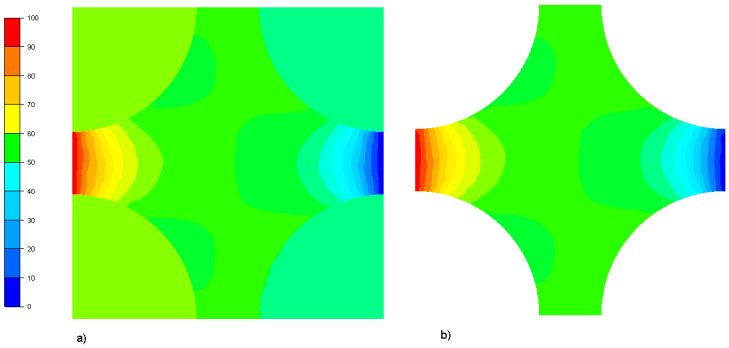


Figure 3.24: Pressure distribution of a) the entire domain b) the fluid domain

agreement between the two numerical simulations shows that the present solver is able to predict accurately the behaviour of the fluid and the presence of the solid.

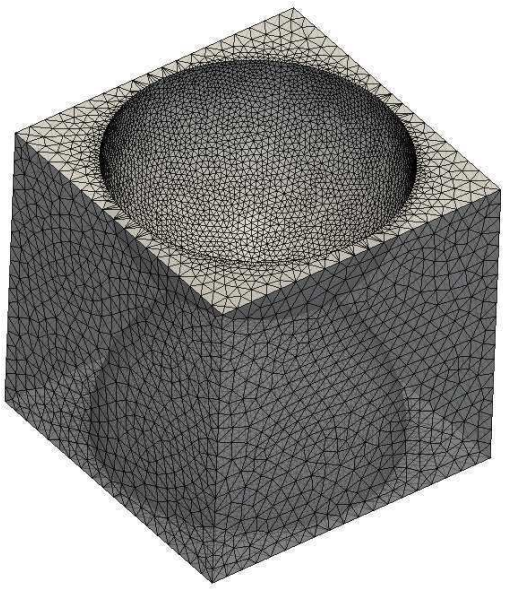


Figure 3.25: Finite element mesh of the fluid domain

3.4.5.3 Flow around a fixed circular cylinder (2-D)

We consider in this section another well-studied problem, namely the one of a channel flow with a cylindrical obstruction [117, 118, 119, 105].

The setting of the problem is shown in figure 3.29. It consists of a rectangular channel with a circular obstruction of diameter 0.1. Zero initial condition is considered all over the domain. On the inflow and outflow boundaries the velocity is defined by:

$$u(t;0,y) = u(t;2.2,y) = 0.41^{-2}\sin\left(\frac{\pi t}{8}\right)(6y(0.41-y),0)$$

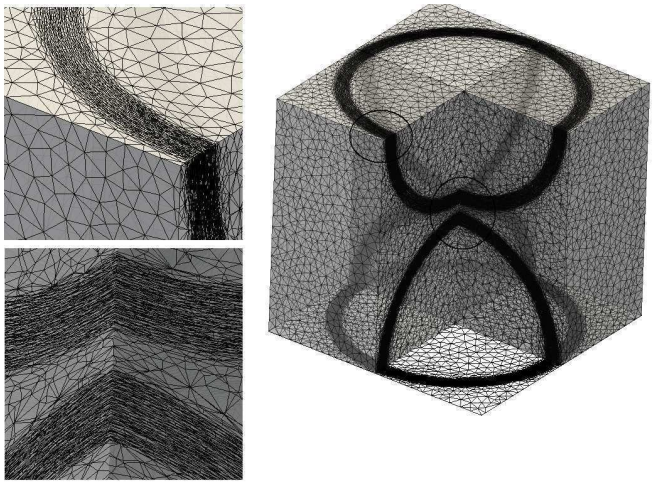


Figure 3.26: Finite element mesh of two half spheres in a fluid domain

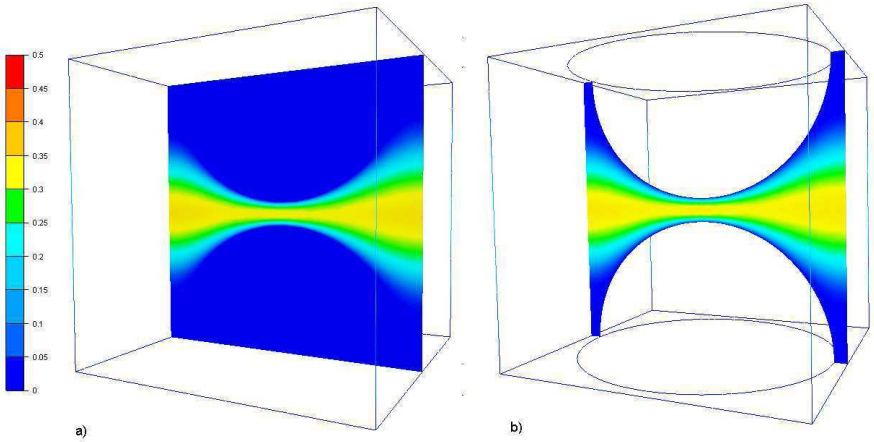


Figure 3.27: Velocity distribution of a) the entire domain b) the fluid domain

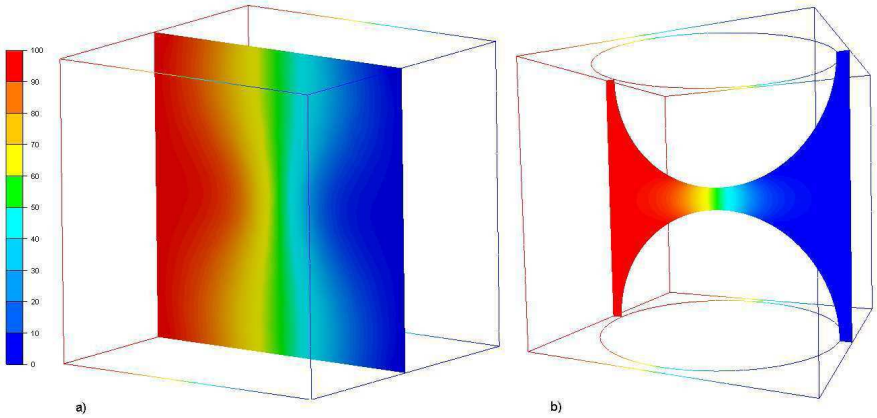


Figure 3.28: Pressure distribution of a) the entire domain b) the fluid domain

No-slip conditions are prescribed at the other boundaries.

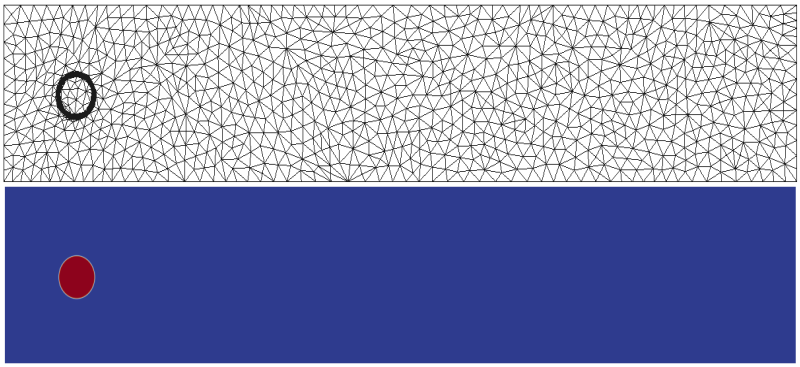


Figure 3.29: Finite element mesh around the circular cylinder.

The circular cylinder is represented by means of a signed distance function (the levelset function), and an anisotropic mesh adaptation is applied to capture well the interface. Figure 3.29 shows the extremly refined solid fluid interface. The Reynolds number is defined by $\mathrm{Re} = \frac{UD}{\mu}$, where D is the diameter of the cylinder, U is the free-stream mean inflow velocity and μ is the kinematic viscosity set to 10^{-3} in order to obtain Reynolds numbers $0 \leq \mathrm{Re} \leq 100$.

After a while from the beginning of the simulation, the inflow increases and two vortices start to develop behind the cylinder. These vortices are first attached behind the cylinder at a moderate Reynolds number and by increasing the Reynolds number, they become stretched and the flow will be distorted and broken apart. At a time of around $(4 \sim 5)$ the separation of the vortices from the cylinder occurs and an alternative vortex shedding known as Karmen vortex street develops. Important benchmark parameters of the flows around bodies are the drag and the difference in the pressure between two points at the edge of the obstacle. To get proper values for these parameters one needs to have a high accuracy.

Figure 3.30 shows the profiles of the benchmark parameters obtained on a $40,000$ elements mesh with a constant time-step $\Delta t = 0.0025$. The plots show the good tendency of the approximated solution obtained with the numerical scheme to reproduce the profile of the coefficients.

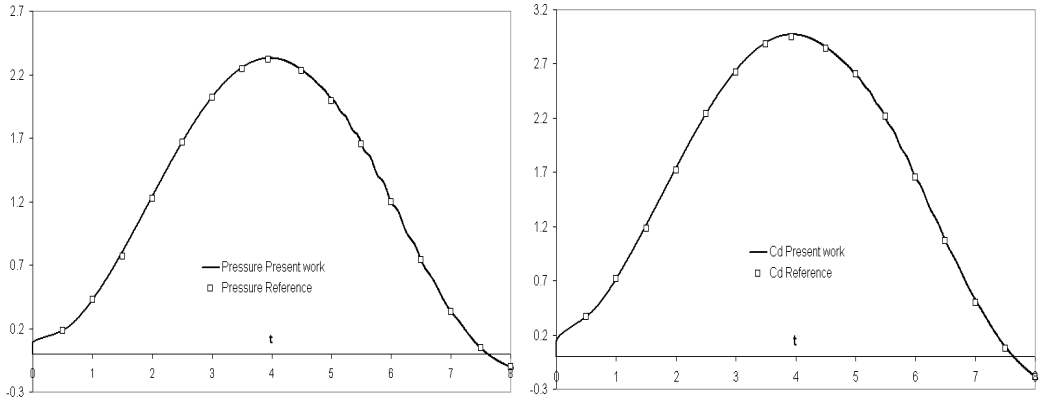
Recall that the drag coefficient can be computed using:

$$c_d = \frac{F_x}{\frac{1}{2}\rho {u_\infty}^2 D}, \tag{3.103}$$

where u_∞ is the maximum inflow velocity and F_x is the x-component of $\mathbf{F}$, the total force on the cylinder surface S:

$$\mathbf{F} = \int_S (-p\mathbf{I} + \mathbf{S}) \cdot \mathbf{n}\, dS. \tag{3.104}$$

$\mathbf{S}$ being the deviatoric stresses.



(a) $P_{diff} = P(0.15, 0.2) - P(0.25, 0.2)$ (b) Drag coefficient

Figure 3.30: Comparisons of the pressure difference and the drag coefficients

3.4.5.4 Oscillating circular cylinder in a channel

This test has been widely used as a benchmark for rigid particulate flows and has been analyzed by a number of authors [120]. We consider an oscillating circular cylinder of diameter 0.1 inside a channel (height $H = 0.41$, length $L = 2.2$). The cylinder moves from his initial position $(1.1, 0.2)$ and starts oscillating along with a prescribed velocity $u = 2\pi f A \cos(2\pi f t)$, with $A = 0.25$, $f = 0.25$, and $v = 0$. No-slip velocity conditions are imposed at the two walls, inlet and outlet of the channel. The dynamic viscosity of the fluid is $\eta = 10^{-3}$ and the density is equal to $\rho = 1$. The fluid in the channel is initially at rest. A time step equal to 0.005 is used.

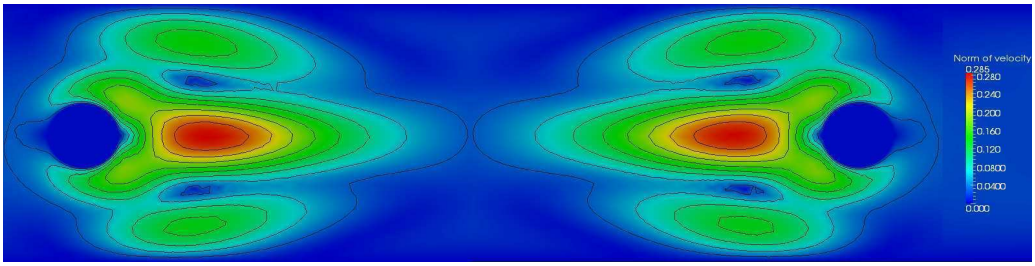


Figure 3.31: Norm of velocity at t = 18.9s (left) and t = 21s (right)

We compute first the level set function that identifies the solid part from the fluid region and then apply the anisotropic mesh adaptation at the interface. Thus, a single set of equations is solved for the whole computational domain by treating the different subdomains as a single fluid with variable material properties. As the cylinder starts oscillating, we repeat the adaptivity steps to ensure accurate interface representation. Figure 3.31 and 3.32 show two snapshots results at two different times ($t = 18.9$ and $t = 21$) which reflect the oscillating behaviour of the cylinder. For comparisons, we

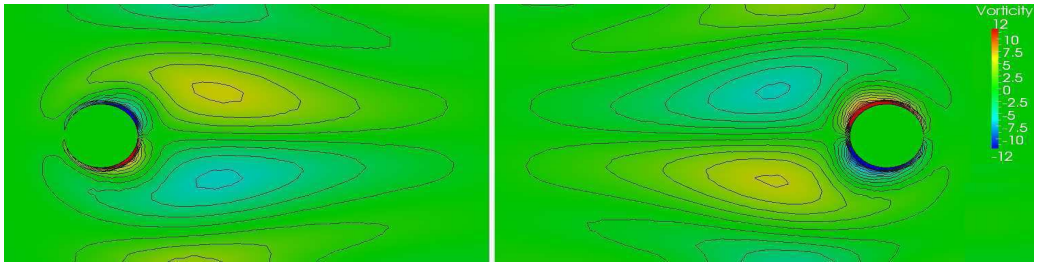


Figure 3.32: Local vorticity value at t = 18.9s (left) and t = 21s (right)

present in figure 3.33 the computed drag coefficient c_d. As expected, the presented results using the immersed stress method agree very well with the reference results.

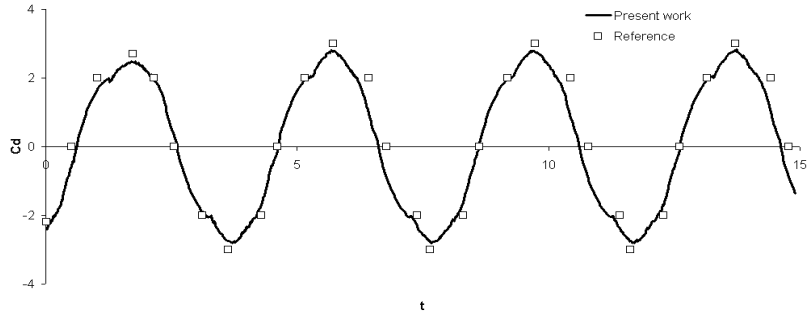


Figure 3.33: Drag coefficients for one oscillating circular cylinder in a channel.

3.4.5.5 Unsteady flow past an immersed helicopter in forward flight

Figure 3.34 and 3.35 present the parallel numerical simulation of unsteady flow around a 3D helicopter in forward flight using the proposed monolithic fluid-structure approach with anisotropic mesh adaptation. The mesh generation algorithm allows the creation of extremely anisotropic elements stretched along the interface, which is an important requirement for FSI problems having internal/boundary layers. The final obtained mesh reflects the capability of the method to render a well respected geometry in terms of curvature, angles and complexity. Contrary to others techniques, this promising method can provide an alternative to body-fitted mesh for very complex geometry.

This simulation is obtained using 96 2.4 Ghz Opteron cores in parallel (linked by an Infiniband network). The mesh consists of $1.6M$ tetrahedral elements and $300,000$ nodes. The reasonable nature of the results shows a good potential for the developed formulations. The purpose of this example is to confirm the motivation behind pursuing such general approach. Indeed, it allows to easily: (i) deal with a large diversity of complex shapes and dimensions without mesh reconstructions, (ii) use and affect different physical properties for the surrounding fluid (air, water...) and for the immersed structures and (iii) handle the interfaces through anisotropic mesh adaptation.

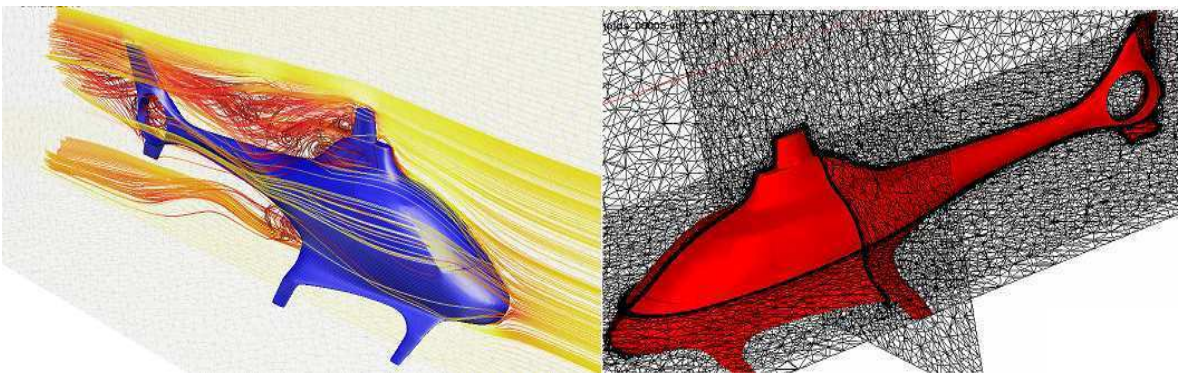


Figure 3.34: Numerical simulation of unsteady flow around a helicopter in forward flight

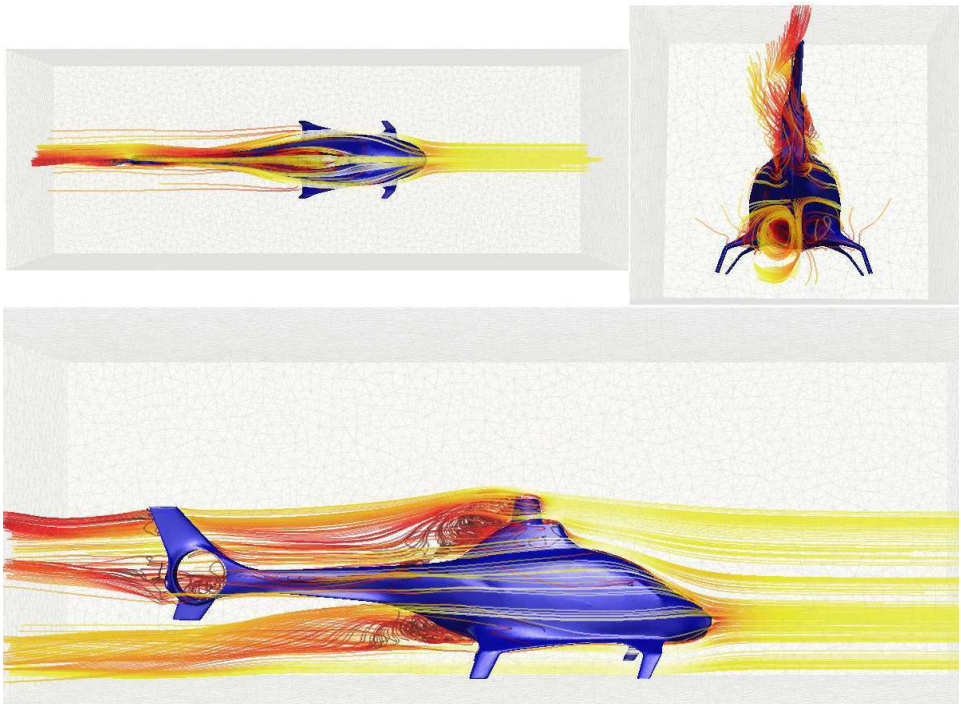


Figure 3.35: Different snapshots of the flow around a helicopter in forward flight

3.4.6 Conclusion

In this part we have described a stabilized three-fields velocity-pressure-stress, designed for the computation of rigid bodies in an incompressible Navier-Stokes flow at high Reynolds number. The method is based on treating a single set of equations for the whole domain. The presence of the solid is taken into account as an extra stress in the Navier-Stokes equation. The formulation considered allows equal-order interpolation for the three-fields. We combine this approach with the mesh adaptivity to resolve complex structure geometries. 2D and 3D numerical experiments were presented and results were compared against reference or other approaches. The capability of the method to simulate the fluid-rigid body interaction at high Reynolds number was demonstrated. The results presented here show that this method can be used in a wide range of applications for multi body fluid-solid problems. Further research will focus on tackling deformable solid interaction.

3.5 Monolithic VMS method for FSI with anisotropic adaptive meshing

In this section, emphasis on the use of a new anisotropic mesh adaptation technique is presented. A new *a posteriori* error estimate, based on the length distribution tensor approach and the associated edge based error analysis, is used to ensure an accurate capturing of the discontinuities at the fluid-solid interface. When such adaptive technique is coupled to the previous formulation, it engenders a very useful and powerful numerical tool for a wide range of FSI applications. Same numerical tests are revised enabling us to prove the benefits of this new adaptive technique. New 2D and 3D tests are also conducted such as: flow past a NACA profile and flow past a simplified vehicle model.

3.5.1 Introduction

Fluid-Structure Interaction (FSI) describes a wide variety of industrial problems arising in engineering, technology and biomechanics. Due to the high complexity of these problems, FSI simulations are nowadays the focus of numerous investigations and various approaches are proposed to treat them.

Two main approaches for the simulation of FSI problems are still gaining attention lately: partitioned and monolithic approaches. The partitioned approaches allow the use of a specific solver for each domain. The fluid and the structure equations are alternatively integrated in time and the interface conditions are enforced asynchronously. The difficulty remains in transferring the information between the codes. The coupling between the two phases can be enforced using different schemes: weakly or strongly coupled versions. The former approach manages with just one solution of either field per time step but consequently lack accurate fulfilment of the coupling conditions. The latter requires sub-iterations [106, 96, 107, 38, 36, 98]. It is accurate and quite efficient but presents an inherent instability depending on the ratio of the densities and the geometry of the domain [40]. For 3D problems, the numerical cost can increase drastically. Alternatively, authors in [121] propose an immersed particle method able to handle complicated FSI problems including cracking and perforation with ease.

An increased interest in monolithic methods, which treat the interaction of the fluid and the structure at the interface synchronously, has been noticed lately. The continuity at the interface is obtained naturally and there is no need to enforce it. It imposes the use of an appropriate unique constitutive equation describing both the fluid and the solid domains. Interface tracking between the two different domains can be completed by Immersed Boundary (IB) methods [27] where the interface is convected in a Lagrangian way. Other methods such as the fictitious domain method [27, 28] treat the coupling between the domains by applying a constraint across the body using a Lagrange multiplier. These constraints may lead to uncoupled physics in the different subdomains of the problem (in the fluid and the solid, for example), yielding inconsistencies when the subdomains evolve in time. This problem may be solved using the so called Fixed-mesh ALE formula-

tion introduced in [108] (see also [109, 110] for applications to fluid-structure interaction problems and rigid bodies floating in fluids).

In this paper, we focus on a monolithic formulation where the complete problem is written in a fully Eulerian framework. A convected level-set function, commonly employed in the simulation of multiphase flows [80], is used to distinguish between phases. Such approach allows easily dealing with very complex geometries, large structural deformations and free movements of the structure within a flow domain.

However, the level-set intersects the elements arbitrarily and lacks the ability to reproduce the interfaces of complex geometries (i.e. sharp corners). Therefore, we combine it with anisotropic mesh adaptation. An *a posteriori* edge based spatial error indicator relying on the length distribution tensor approach is presented. The anisotropic adaptation involves building a mesh based on a metric map. It provides both the size and the stretching of elements in a very condensed information data. Working on a nodal based metric, an anisotropic mesh adaptation procedure is obtained under the constraint of a fixed number of nodes. With such an advantage, it becomes a very useful and practical numerical tool. A such algorithm allows the creation of extremely stretched elements along the interface, which is an important requirement for FSI problems with high density ratios [47]. The details of this technique can be found in [54].

The last ingredient of this paper resides in the development of a new FE solver: on modelling easily the interaction between the fluid (laminar or turbulent) and the structure in question. Consequently, the presence of the structure will be taken into account by means of an extra stress tensor in the Navier-Stokes equations. For illustration, the rigid immersed body is treated using the Navier-Stokes solver under constraints of imposing the nullity of the deformations by means of a Lagrange multiplier [111]. The system is solved using a new Variational MultiScale FE method. Thus we propose to extend the decomposition for both the velocity and the pressure fields into coarse/resolved scales and fine/unresolved scales, needed to deal with convection dominated problems and pressure instabilities, with an efficient enrichment of the extra constraint. This choice of decomposition is shown to be favourable for simulating flows at high Reynolds number and to remove spurious oscillations at the interface due to the high discontinuity in the material properties. We retain in this work the advantages of using linear approximations (P1 finite elements) regarding the accuracy and the computational cost, especially for 3D real applications.

The present work is inspired notably from [122] where the stabilized three field FE formulation is described in details notably for fluid-fixed rigid bodies. In this sense, the main contributions of this work, considered as a continuation of this reference, are a systematic use of this FE formulation for rigid body motion and thus an implementation of an *a posteriori* error estimator to control anisotropic mesh adaptation suitable for complex FSI problems. Consequently, a particular emphasis is placed on the performance of the implemented method for two-dimensional and three-dimensional problems with high Reynolds number and high density ratios.

An outline of this part is as follow. In the next section, the adaptive level-set method is presented. Section 3.5.3 is dedicated to present the governing equations and the general

monolithic formulation. Section 3.5.4 describes the stabilizing schemes from a Variational MultiScale point of view. Section 3.5.5 presents some benchmark problems and results for fluid-rigid interactions. Section 6 contains concluding remarks. Note that some section are repeated from [122] for completeness.

3.5.2 Construction of an anisotropic mesh

In this section, we retrace the main steps of the adaptive procedure used to immerse and to represent different complex geometries inside a unique mesh. First we compute the signed distance function (level-set) of a given geometry to each node of the mesh, then we refine anisotropically the mesh at the interface and finally we mix and attribute the physical properties of each domain using appropriate laws. This procedure is repeated iteratively for moving solids.

3.5.2.1 Level-set function

A signed distance function of an interface Γ_{im} is used to localize the interface of the immersed body and initialize the desirable properties on both sides of the latter. At any point $\mathbf{x}$ of the computational domain Ω, the level-set function α_{im} corresponds to the signed distance from Γ_{im}. In turn, the interface Γ_{im} is given by the iso-zero of the function α_{im}:

$$\begin{cases} \alpha_{\text{im}}(\mathbf{x}) = \pm d(\mathbf{x}, \Gamma_{\text{im}}), \mathbf{x} \in \Omega, \\ \Gamma_{\text{im}} = \{\mathbf{x}, \alpha_{\text{im}}(\mathbf{x}) = 0\} \end{cases} \tag{3.105}$$

In this paper, a sign convention is used: $\alpha_{\text{im}} \geq 0$ inside the solid domain defined by the interface Γ_{im} and $\alpha_{\text{im}} \leq 0$ outside this domain. Further details about the algorithm used to compute the distance are available in [72]. It is also possible to use functions smoother than $d(\mathbf{x}, \Gamma_{\text{im}})$ away from Γ_{im} (see for example [112]).

3.5.2.2 Edge based error estimation

An *a posteriori* error estimate based on the length distribution tensor approach and the associated edge based error analysis [54] is presented. It enables to calculate a stretching factor providing a new edge length distribution, its associated tensor and the corresponding metric. The optimal stretching factor field is obtained by solving an optimization problem under the constraint of a fixed number of edges in the mesh. In this work, we emphasise the application of this new technique to multi-domain problems. Therefore, for addressing a high contrast in the physical parameters, we propose an extension of the *a posteriori* estimation. It combines the simultaneous adaptivity to the level-set scalar field and to the velocity field without increasing the complexity of the computation or intersecting different metrics. Using this approach, the adaptivity will also focus on the change of direction rather than the intensity of the velocity. This is clearly shown behind the obstacle in figure 3.36, whereas the adaptation on the level-set function renders extremely stretched elements along the fluid-solid interface. With such a method, we can

provide a very useful and practical tool for the simulation of complex FSI problems. In the following subsections, details of the adaptivity approach will be discussed.

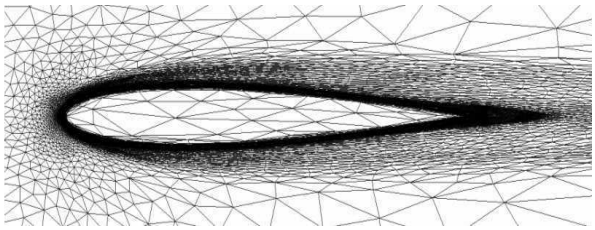


Figure 3.36: Anisotropic refined fluid-solid interface of an immersed NACA0012.

We consider a variable $u \in \mathcal{C}^2(\Omega) = \mathcal{V}$ and $\mathcal{V}_h$ a simple P^1 finite element approximation space:
$\mathcal{V}_h = \{w_h \in \mathcal{C}^0(\Omega), w_h|_K \in P^1(K), K \in \mathcal{K}\}$ where $\Omega = \bigcup_{K\in\mathcal{K}} K$ and K is a simplex (segment, triangle, tetrahedron, ...).

We define $\mathbf{X} = \left\{\mathbf{X}^i \in \mathbb{R}^d,\, i = 1, \cdots, N\right\}$ as the set of nodes of the mesh and we denote by U^i the nodal value of u at $\mathbf{X}^i$ and we let Π_h be the Lagrange interpolation operator from $\mathcal{V}$ to $\mathcal{V}_h$ such that: $\Pi_h u(\mathbf{X}^i) = u(\mathbf{X}^i) = U^i\,,\ \forall i = 1, \cdots, N$. As shown in figure 3.37, we denote the set of nodes connected to node i by $\Gamma(i) = \{j\,,\ \exists K \in \mathcal{K}\,,\ \mathbf{X}^i, \mathbf{X}^j \text{ are nodes of } K\}$.

By introducing the notation: $\mathbf{X}^{ij} = \mathbf{X}^j - \mathbf{X}^i$ and using the analysis carried in [54], we can set:

$$\nabla u_h \cdot \mathbf{X}^{ij} = U^{ij}\,, \tag{3.106}$$

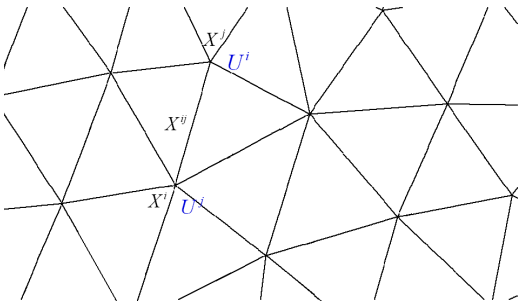


Figure 3.37: Length $\boldsymbol{X}^{ij}$ of the edge joining nodes i and j.

$$||\underbrace{\nabla u_h \cdot \mathbf{X}^{ij}}_{U^{ij}} - \nabla u(\mathbf{X}^i) \cdot \mathbf{X}^{ij}|| \leq \max_{\mathbf{Y}\in[\mathbf{X}^i,\mathbf{X}^j]} |\mathbb{H}(u)(Y)\mathbf{X}^{ij} \cdot \mathbf{X}^{ij}|\,, \tag{3.107}$$

where $\mathbb{H}(u) = \nabla^{(2)}u$ is the associated Hessian of u. Recall that taking $u \in \mathcal{C}^2(\Omega)$ we obtain $\nabla u \in \mathcal{C}^1(\Omega)$.

Applying the interpolation operator on ∇u together with (3.106) we obtain a definition of the projected second derivative of u in terms of only the values of the gradient at the extremities of the edge:

$$\nabla \mathbf{g}_h \mathbf{X}^{ij} \cdot \mathbf{X}^{ij} = \mathbf{g}^{ij} \cdot \mathbf{X}^{ij}, \tag{3.108}$$

where $\mathbf{g}_h = \Pi_h \nabla u$, $\mathbf{g}^i = \nabla u(\mathbf{X}^i)$ and $\mathbf{g}^{ij} = \mathbf{g}^j - \mathbf{g}^i$.
Using a mean value argument, we set that: $\exists \mathbf{Y} \in [\mathbf{X}^i, \mathbf{X}^j] | \mathbf{g}^{ij} \cdot \mathbf{X}^{ij} = \mathbb{H}(u)(Y)\mathbf{X}^{ij} \cdot \mathbf{X}^{ij}$.
We use this projection as an approximation of the error along the edge:

$$e_{ij} = \mathbf{g}^{ij} \cdot \mathbf{X}^{ij}. \tag{3.109}$$

However this equation cannot be evaluated exactly as it requires knowing the gradient of u and also its continuity at the nodes of the mesh. For that reason, we resort to a gradient recovery procedure.

3.5.2.3 Gradient Recovery

Based on an optimization analysis, the author in [54] proposes a recovery gradient operator defined by:

$$\mathbf{G}^i = (\mathbb{X}^i)^{-1} \sum_{j \in \Gamma(i)} U^{ij} \mathbf{X}^{ij}, \tag{3.110}$$

where $\mathbb{X}^i = \frac{d}{|\Gamma(i)|} \sum_{j \in \Gamma(i)} \mathbf{X}^{ij} \otimes \mathbf{X}^{ij}$ is what we call the length distribution tensor at node $\mathbf{X}^i$.
Note that this construction preserves the second order: $\left|\left(\mathbf{G}^i - \mathbf{g}^i\right) \cdot \mathbf{X}^{ij}\right| \sim \left(\mathbb{H}(u)\mathbf{X}^{ij} \cdot \mathbf{X}^{ij}\right)$ where $\mathbf{G}^i$ is the recovery gradient at node i (given by (3.110)) and $\mathbf{g}^i$ being the exact value of the gradient at node i.
The approximated error is evaluated by substituting $\mathbf{G}$ by $\mathbf{g}$ in (3.109):

$$e_{ij} = \mathbf{G}^{ij} \cdot \mathbf{X}^{ij}.$$

3.5.2.4 Metric construction from the edge distribution tensor

Taking into account this error analysis, we construct the metric for the unit mesh as follows:

$$\mathbb{M}^i = \left(\frac{d}{|\Gamma(i)|} \sum_{j \in \Gamma(i)} \mathbf{X}^{ij} \otimes \mathbf{X}^{ij} \right)^{-1}.$$

For a complete justification of this result, the reader is referred to [54].

3.5.2.5 Error behaviour due to varying the edge length

We examine now how the error behaves when the length of the edges changes by stretching coefficients $s_{ij} \in \mathcal{S}$ defined by :

$$\mathcal{S} = \left\{ s_{ij} \in \mathbb{R}^+ \, , \, i = 1, \cdots, N \, , \, j = 1, \cdots, N \, , \, \Gamma(i) \cap \Gamma(j) \neq \emptyset \right\}.$$

To obtain a new metric depending on the error analysis, a new length for each edge has to be calculated and then used for rebuilding the length distribution tensor. An interesting way of linking the error variations to the changes in edge lengths is by introducing a stretching factor $s \in \mathbb{R}^+$ such that

$$\begin{cases} \widetilde{\mathbf{X}^{ij}} = s\mathbf{X}^{ij} \\ ||\widetilde{e_{ij}}|| = s^2||e_{ij}|| = s^2||\mathbf{G}^{ij} \cdot \mathbf{X}^{ij}|| \end{cases} \tag{3.111}$$

where $\widetilde{e_{ij}}$ and $\widetilde{\mathbf{X}^{ij}}$ are the target error at edge ij and its associated edge length repectively. Following the lines of [54] we can simply define the metric associated with $\mathcal{S}$ by:

$$\widetilde{\mathbb{M}^i} = \frac{|\Gamma(i)|}{d} \left(\widetilde{\mathbb{X}^i} \right)^{-1}, \tag{3.112}$$

where $\widetilde{\mathbb{X}^i} = \frac{d}{|\Gamma(i)|} \sum_{j \in \Gamma(i)} s_{ij}^2 \mathbf{X}^{ij} \otimes \mathbf{X}^{ij}$ is the length distribution tensor and $|\Gamma(i)|$ is the cardinal of $\Gamma(i)$. Let n_{ij} be the number of created nodes in relation with the stretching factor s_{ij} and along the edge ij. When scaling the edges by a factor s_{ij}, the error changes quadratically so that the number of created nodes along the edge ij is given by:

$$n_{ij} = \left(\frac{\widetilde{e_{ij}}}{e_{ij}} \right)^{-\frac{1}{2}} = s_{ij}^{-1}.$$

As per node i, the created nodes along the different edge directions is given by the following tensor:

$$N^i = \left(\frac{d}{|\Gamma(i)|} \sum_{j \in \Gamma(i)} n_{ij} \frac{\mathbf{X}^{ij}}{\left|\mathbf{X}^{ij}\right|} \otimes \frac{\mathbf{X}^{ij}}{\left|\mathbf{X}^{ij}\right|} \right).$$

So that the total number of created nodes per node i is:

$$n^i = \det \left(\frac{d}{|\Gamma(i)|} \sum_{j \in \Gamma(i)} n_{ij} \frac{\mathbf{X}^{ij}}{\left|\mathbf{X}^{ij}\right|} \otimes \frac{\mathbf{X}^{ij}}{\left|\mathbf{X}^{ij}\right|} \right).$$

By considering the averaging process of the number of nodes distribution function, the total number of nodes in the adapted mesh is given by

$$N = \sum_i n^i.$$

A direct relation between N and e, assuming a uniform totally balanced error along the edge $\widetilde{e_{ij}} = e = \text{constant}$, is given by:

$$n^{ij}(e) = s_{ij}^{-1}(e) = \left(\frac{e}{e_{ij}}\right)^{-\frac{1}{2}}.$$

Hence, for a node i we have

$$n^i(e) = e^{-\frac{d}{2}} \det\left(\frac{d}{|\Gamma(i)|}\sum_{j\in\Gamma(i)}\left(\frac{1}{e_{ij}}\right)^{-\frac{1}{2}}\frac{\mathbf{X}^{ij}}{|\mathbf{X}^{ij}|}\otimes\frac{\mathbf{X}^{ij}}{|\mathbf{X}^{ij}|}\right) \Leftrightarrow n^i(e) = e^{-\frac{d}{2}}n^i(1),$$

so that

$$N = e^{-\frac{d}{2}}\sum_i n^i(1).$$

Therefore, the global induced error for a given total number of nodes N can be determined by:

$$e(N) = \left(\frac{N}{\sum_i n^i(1)}\right)^{-\frac{2}{d}}.$$

Thus, the corresponding stretching factors under the constraint of a fixed number of nodes N are given by:

$$s_{ij} = \left(\frac{e}{e(N)}\right)^{-\frac{1}{2}} = \left(\frac{\sum_i n^i(1)}{N}\right)^{\frac{2}{d}} e_{ij}^{-1/2}.$$

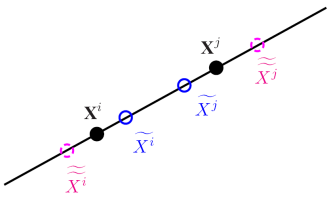


Figure 3.38: Varying the edge in its own direction.

3.5.2.6 Extension to multi-component field

Here, we propose to construct a unique metric directly from a multi-component vectors field containing, for instance, all the components of the velocity field and/or different level-set functions. Consequently, we do not need to intersect several metrics as in [123] but construct it using the following error vector $\vec{e_{ij}} = \left\{e_{ij}^1, e_{ij}^2, \cdots, e_{ij}^n\right\}$ where n is the number of components . Let $u = \{u_1, u_2, \cdots, u_n\}$, $\mathcal{Z} = \mathcal{V}^n$ and $\mathcal{Z}_h = \mathcal{V}_h^n$. In the view

of constructing a unique metric, the above theory is applied for each component of u. It comes out immediately that the error is now a vector given by: $\overrightarrow{e_{ij}} = \left\{e_{ij}^1, e_{ij}^2, \cdots, e_{ij}^n\right\}$ and then

$$s_{ij} = \left(\frac{||e(N)||}{||\overrightarrow{e_{ij}}||}\right)^{\frac{1}{2}}.$$

Here, the norm can be the discrete L_2, L_1 or L_∞ norms.

Rather than considering several metric intersections and thus having much computations to perform, we propose herein an easy way to account for different fields in an *a posteriori* analysis while producing a single metric field. We propose then to combine, into one global vector field, both the level-set function and all components of the velocity field in only one metric tensor.

Denote by v_h the finite element solution of the Navier Stokes equations and $\Pi_h v$ its interpolant. In general, we have that

$$\exists c > 0, \;\; ||v_h - v|| \leq c||\Pi_h v - v||\,.$$

Let $v_h(X^i) = V^i \in \mathbb{R}^d, d = 2, 3$ and $\mathcal{Y} = \left(\frac{v}{|v|}, |v|, \alpha\right)$ be the vector field made of $d+1$ components vector fields, with α the level-set function used to localize an immersed body. We obtain for every node i,

$$\Pi_h \mathcal{Y}(\mathbf{X}^i) = \left(\frac{V^i}{|V^i|}, |V^i|, \alpha\right) = \mathcal{Y}^i.$$

3.5.2.7 Mixing laws

The geometry and mechanical properties of each subdomain are characterized by one signed distance function. Once all the sub-domains are defined, the mechanical properties can be determined on the whole domain in terms of the level-set function. For the elements crossed by the level-set functions and the their neighbours, fluid-solid mixtures are used to determine the element effective properties. A Heaviside function $H(\alpha)$ for each level-set function is defined by:

$$H(\alpha) = \begin{cases} 1 & \text{if } \alpha > 0 \\ 0 & \text{if } \alpha < 0 \end{cases} \tag{3.113}$$

In order to achieve a better continuity at the interface [73], the Heaviside function can be smoothed using:

$$H_\varepsilon(\alpha) = \begin{cases} 1 & \text{if } \alpha > \varepsilon \\ \dfrac{1}{2}\left(1 + \dfrac{\alpha}{\varepsilon} + \dfrac{1}{\pi}\sin\left(\dfrac{\pi\alpha}{\varepsilon}\right)\right) & \text{if } |\alpha| \leq \varepsilon \\ 0 & \text{if } \alpha < -\varepsilon \end{cases} \tag{3.114}$$

where ε is a small parameter such that $\varepsilon = O(h_{\text{im}})$, known as the interface thickness, and h_{im} is the mesh size in the normal direction to the interface. In the vicinity of the

interface, it can be computed using the following expression:

$$h_{\text{im}} = \max_{j,l \in K} \boldsymbol{\nabla}\alpha \cdot \mathbf{x}^{jl}, \tag{3.115}$$

where $\mathbf{x}^{jl} = \mathbf{x}^l - \mathbf{x}^j$ and K is the mesh element under consideration.

According to the chosen approximations, the Heaviside function is then approximated using linear interpolations $P1$ between fluid and solid properties or a piecewise constant interpolation $P0$.

3.5.3 Governing equations

This section is devoted to the mathematical formulation for a rigid body immersed in an incompressible fluid. The governing equations are considered to be three-dimensional and time-dependent. As the proposed approach is monolithic, a unique constitutive equation will be solved on the whole domain with variable physical properties separated by a prescribed level-set function. Details are prescribed in [122].

3.5.3.1 The Navier-Stokes equations with a rigid body

Let $\Omega \subset \mathbb{R}^d$ be the spatial domain at time $t \in [0, T]$, where d is the space dimension. Let $\partial\Omega$ denote the boundary of Ω. The fluid domain, the solid domain and the interface will be Ω_{f}, Ω_{s} and Γ_{im}, respectively. They verify:

$$\overline{\Omega}_{\text{f}} \cup \overline{\Omega}_{\text{s}} = \overline{\Omega} \quad \text{and} \quad \overline{\Omega}_{\text{f}} \cap \overline{\Omega}_{\text{s}} = \Gamma_{\text{im}}.$$

The dynamics of the flow is given by the classical incompressible Navier-Stokes equations, which may be written as

$$\rho_{\text{f}} \left(\partial_t \mathbf{v} + \mathbf{v} \cdot \nabla \mathbf{v}\right) - \nabla \cdot \boldsymbol{\sigma} = \mathbf{f} \quad \text{in } \Omega_{\text{f}},\ t > 0 \tag{3.116}$$

$$\nabla \cdot \mathbf{v} = 0 \quad \text{in } \Omega_{\text{f}},\ t > 0 \tag{3.117}$$

where $\mathbf{v}(\mathbf{x}, t)$ is the velocity, $p(\mathbf{x}, t)$ is the pressure, ρ_{f} is the fluid density and the Cauchy stress tensor for a Newtonian fluid is given by:

$$\boldsymbol{\sigma} = 2\eta_{\text{f}}\ \boldsymbol{\varepsilon}(\mathbf{v}) - p\ \mathbf{I}_d, \tag{3.118}$$

where $\mathbf{I}_d$ is the d-dimensional identity tensor and η_{f} is the fluid viscosity. Equations (3.116)-(3.117) are subject to the boundary and initial conditions

$$\mathbf{v} = \mathbf{v}_{\Gamma,\text{f}} \quad \text{on } \partial\Omega_{\text{f}} \setminus \Gamma_{\text{im}},\ t > 0 \tag{3.119}$$

$$\mathbf{v} = \mathbf{v}_{\text{im}} \quad \text{on } \Gamma_{\text{im}},\ t > 0 \tag{3.120}$$

$$\boldsymbol{\sigma} \cdot \mathbf{n} = \mathbf{t}_{\text{im}} \quad \text{on } \Gamma_{\text{im}},\ t > 0 \tag{3.121}$$

$$\mathbf{v}(\mathbf{x}, 0) = \mathbf{v}_0(\mathbf{x}) \quad \text{in } \Omega_{\text{f}}, \tag{3.122}$$

where $\mathbf{v}_{\Gamma,\mathrm{f}}$ is a given velocity boundary condition, $\mathbf{v}_{\mathrm{im}}$ is the velocity at the fluid-solid interface Γ_{im} (the boundary of the immersed body), $\mathbf{n}$ is the outward normal on the solid surface, $\mathbf{t}_{\mathrm{im}}$ the normal stress on this boundary and $\mathbf{v}_0(\mathbf{x})$ is a given initial condition. For simplicity, only Dirichlet-type boundary conditions will be considered on the exterior boundary.

In the present formulation we treat the rigid body as a continuous domain subjected to an additional rigidity constraint. As shown in [122], we may write the equations of motion as the Navier-Stokes equations with this constraint as:

$$\rho_{\mathrm{s}} \left(\partial_t \mathbf{v} + \mathbf{v} \cdot \nabla \mathbf{v}\right) - \nabla \cdot \boldsymbol{\sigma} = \mathbf{f} \quad \text{in } \Omega_{\mathrm{s}},\ t > 0 \tag{3.123}$$

$$\nabla \cdot \mathbf{v} = 0 \quad \text{in } \Omega_{\mathrm{s}},\ t > 0 \tag{3.124}$$

$$\boldsymbol{\varepsilon}(\mathbf{v}) = \mathbf{0} \quad \text{in } \Omega_{\mathrm{s}},\ t > 0 \tag{3.125}$$

where ρ_{s} the solid density. In a rigid body there is no deformation, that is to say, $\boldsymbol{\varepsilon}(\mathbf{u}) = \mathbf{0}$ ($\mathbf{u}$ is the displacement field) and $\partial_t \mathbf{u} = \mathbf{v}$. These two equations imply a null value of the deformation-rate tensor (3.125). The stress tensor is then given by:

$$\boldsymbol{\sigma} = \boldsymbol{\tau}_{\mathrm{s}} - p\, \mathbf{I}_d. \tag{3.126}$$

Equations (3.123)-(3.125) need to be supplied with the boundary and initial conditions

$$\mathbf{v} = \mathbf{v}_{\Gamma,\mathrm{s}} \quad \text{on } \partial\Omega_{\mathrm{s}} \setminus \Gamma_{\mathrm{im}},\ t > 0 \tag{3.127}$$

$$\mathbf{v} = \mathbf{v}_{\mathrm{im}} \quad \text{on } \Gamma_{\mathrm{im}},\ t > 0 \tag{3.128}$$

$$\boldsymbol{\sigma} \cdot \mathbf{n} = -\mathbf{t}_{\mathrm{im}} \quad \text{on } \Gamma_{\mathrm{im}},\ t > 0 \tag{3.129}$$

$$\mathbf{v}(\mathbf{x}, 0) = \mathbf{v}_0(\mathbf{x}) \quad \text{in } \Omega_{\mathrm{s}}, \tag{3.130}$$

where $\mathbf{v}_{\Gamma,\mathrm{f}}$ is a given velocity boundary condition that needs to be compatible with a rigid body motion if $\partial\Omega_{\mathrm{s}} \setminus \Gamma_{\mathrm{im}} \neq \emptyset$, and the initial condition $\mathbf{v}_0(\mathbf{x})$ must be also compatible with a rigid body motion.

3.5.3.2 Full Euleurian formulation

Making use of the notation introduced in section 1, we may write problem (3.116)-(3.122) and problem (3.123)-(3.130) in a unified way in the whole computational domain Ω as

$$\begin{aligned} \rho \left(\partial_t \mathbf{v} + \mathbf{v} \cdot \nabla \mathbf{v}\right) - \nabla \cdot \left(2\eta\, \boldsymbol{\varepsilon}(\mathbf{v}) + \boldsymbol{\tau} - p\, \mathbf{I}_d\right) &= \mathbf{f} && \text{in } \Omega,\ t > 0 \\ \nabla \cdot \mathbf{v} &= 0 && \text{in } \Omega,\ t > 0 \\ \boldsymbol{\varepsilon}_{\mathrm{s}}(\mathbf{v}) &= \mathbf{0} && \text{in } \Omega,\ t > 0 \\ \mathbf{v} &= \mathbf{v}_\Gamma && \text{on } \partial\Omega,\ t > 0 \\ \mathbf{v}(\mathbf{x}, 0) &= \mathbf{v}_0(\mathbf{x}) && \text{in } \Omega, \end{aligned} \tag{3.131}$$

where $\mathbf{v}_\Gamma = \mathbf{v}_{\Gamma,\mathrm{s}}$ on $\partial\Omega_{\mathrm{s}} \cap \partial\Omega$ and $\mathbf{v}_\Gamma = \mathbf{v}_{\Gamma,\mathrm{f}}$ on $\partial\Omega_{\mathrm{f}} \cap \partial\Omega$, $\boldsymbol{\varepsilon}_{\mathrm{s}}(\mathbf{v}) = H(\alpha)\boldsymbol{\varepsilon}(\mathbf{v})$, $\eta = (1 - H(\alpha))\eta_{\mathrm{f}}$, $\rho = \rho_{\mathrm{s}} H(\alpha) + \rho_{\mathrm{f}}(1 - H(\alpha))$ and $\boldsymbol{\tau} = H(\alpha)\boldsymbol{\tau}_{\mathrm{s}}$. The boundary conditions (3.120)-(3.121) and (3.128)-(3.129) are no longer needed.

Let $V \times P \times \mathcal{T}$ be the space where the unknown $(\mathbf{v}, p, \boldsymbol{\tau})$ is sought. The first space, V, is made of vector fields which are square integrable in time with values in $H^1(\Omega)^d$ and satisfying the Dirichlet conditions, where the last two, P and $\mathcal{T}$, are made of distributions in time with values in $P_0 = L^2(\Omega)/\mathbb{R}$ and $\mathcal{T}_0 = L^2(\Omega)^{d\times d}$, respectively (in fact, a subspace of $L^2(\Omega)^{d\times d}$ would be enough, see below). The corresponding test functions will be denoted $\mathbf{w} \in V_0 = H_0^1(\Omega)^d$, $q \in P_0$ and $\boldsymbol{\xi} \in \mathcal{T}_0$. Multiplying by the test functions and integrating by parts, the associated standard weak form of the system (3.131), can be stated as: Find $\mathbf{v} \in V$, $p \in P$ and $\boldsymbol{\tau} \in \mathcal{T}$ such that

$$\begin{aligned} \rho(\partial_t \mathbf{v}, \mathbf{w}) + \rho(\mathbf{v}\cdot\nabla\mathbf{v}, \mathbf{w}) - (p, \nabla\cdot\mathbf{w}) + (2\eta\boldsymbol{\varepsilon}(\mathbf{v}), \boldsymbol{\varepsilon}(\mathbf{w})) + (\boldsymbol{\tau}, \boldsymbol{\varepsilon}_{\mathrm{s}}(\mathbf{w},))) &= \langle \mathbf{f}, \mathbf{w}\rangle, \\ (q, \nabla\cdot\mathbf{v}) &= 0, \\ -(\boldsymbol{\xi}, \boldsymbol{\varepsilon}_{\mathrm{s}}(\mathbf{v})) &= 0, \end{aligned} \tag{3.132}$$

for all $(\mathbf{w}, q, \boldsymbol{\xi}) \in V_0 \times P_0 \times \mathcal{T}_0$.

As explained in [122], a possible way to choose $\boldsymbol{\tau}$ is to take it as a symmetric gradient of a vector field. Moreover, this field needs not to be computed if an augmented Lagrangian scheme together with an Uzawa iterative scheme are employed to relax iteratively $(\boldsymbol{\xi}, \boldsymbol{\varepsilon}_{\mathrm{s}}(\mathbf{v})) = 0$. This is what we describe next.

Suppose that we discretize in time problem (3.132) using a finite difference scheme, and still denote by $\mathbf{v}$, p and $\boldsymbol{\tau}$ the fields to be computed at a given time step. Let $\delta_t\mathbf{v}$ the discrete time derivative and r the penalty parameter in the Uzawa scheme. Treating implicitly the velocity in the calculation of the stress in the solid, the iterative scheme to be performed *within each time step* reads:

1. Set $k = 0$

2. Initalize $\mathbf{v}^0$, p^0 and $\boldsymbol{\tau}^0$ (for example to values in the last time step)

3. $k \leftarrow k + 1$

4. Solve for $\mathbf{v}^k$ and p^k:

$$\begin{aligned} &\rho(\delta_t\mathbf{v}^k, \mathbf{w}) + \rho(\mathbf{v}^k\cdot\nabla\mathbf{v}^k, \mathbf{w}) - (p^k, \nabla\cdot\mathbf{w}) \\ &\qquad + 2(\eta\boldsymbol{\varepsilon}(\mathbf{v}^k) + H(\alpha)\eta_{\mathrm{s}}\, r\, P_\tau(\boldsymbol{\varepsilon}(\mathbf{v}^k)), \boldsymbol{\varepsilon}(\mathbf{w})) + (\boldsymbol{\tau}^{k-1}, \boldsymbol{\varepsilon}_{\mathrm{s}}(\mathbf{w})) = \langle \mathbf{f}, \mathbf{w}\rangle, \\ &(q, \nabla\cdot\mathbf{v}^k) = 0. \end{aligned}$$

5. Update $\boldsymbol{\tau}^k = \boldsymbol{\tau}^{k-1} + 2\eta_{\mathrm{s}}\, r\, P_\tau(\boldsymbol{\varepsilon}(\mathbf{v}^k))$ in Ω_{s}.

6. Check convergence: if $\|\mathbf{v}^k - \mathbf{v}^{k-1}\| >$ `tol` (given tolerance in a given norm), go to 3. Otherwise, proceed to the next time step.

3.5.3.3 Rigid body kinetics

For the rigid body motion, when the geometry is simple and the distance function can be computed analytically, it can be sufficient to calculate the optimal angular velocity $\boldsymbol{\omega}$ and the translational velocity $\mathbf{V}$. In fact, once the Navier-Stokes is solved, the velocity $\mathbf{v}_h$ is computed at each a point $\mathbf{x}$ of the domain. $\boldsymbol{\omega}$ and $\mathbf{V}$ are computed by minimizing $\varphi(\mathbf{V}, \boldsymbol{\omega})$ defined by:

$$\varphi(\mathbf{V}, \boldsymbol{\omega}) = \int_{\Omega_s} \mid \mathbf{V} + \boldsymbol{\omega} \wedge \mathbf{x} - \mathbf{v}_h \mid^2 . \tag{3.133}$$

Note that if $\mathbf{v}_h$ were the true rigid body velocity (as the third equation in (3.132) imposes), the minimum of φ would be 0. The rigid body position will then be updated as follows:

$$\mathbf{X}^t = \mathbf{X}^0 + \Delta t \left(\mathbf{V} + \boldsymbol{\omega} \wedge \mathbf{X}^0 \right), \tag{3.134}$$

where $\mathbf{X}^t$ and $\mathbf{X}^0$ are the new and previous coordinates of any point belonging to the rigid body respectively.

3.5.4 Stabilized Finite-Element Method (SFEM)

In this section, we describe briefly the Galerkin finite element approximation and the corresponding stabilization method for the resulting discrete system of equations (3.132) explained in more details in [122]. Based on a mesh $\mathcal{K}_h$ of Ω made of N_{el} elements K, the functional spaces for the velocity, the pressure and the stress are approximated by the finite dimensional spaces V_h, P_h and $\mathcal{T}_h$, respectively.

The stability of the discrete formulation depends on appropriate compatibility restrictions on the choice of the FE spaces. We propose here a Variational MultiScale method (see [113]), which allows the use of equal order continuous interpolations for the three fields, apart from preventing oscillations due to convection dominated flows [67].

Let us split the velocity, pressure and stress solution spaces as $V_h \oplus V'$, $P_h \oplus P'$ and $\mathcal{T}_h \oplus \mathcal{T}'$, respectively. Subscript h is used here and in the following to denote the FE (coarse) component, whereas the prime is used for the so called subgrid scale (fine) component of the unknowns. According to this, we have

$$\begin{aligned} \mathbf{v} &= \mathbf{v}_h + \mathbf{v}' \ \in \ V_h \oplus V', \\ p &= p_h + p' \ \in \ P_h \oplus P', \\ \boldsymbol{\tau} &= \boldsymbol{\tau}_h + \boldsymbol{\tau}' \ \in \ \mathcal{T}_h \oplus \mathcal{T}'. \end{aligned}$$

If the spaces for the test functions are split likewise, with a subscript 0 to identify them, problem (3.132) becomes: find $(\mathbf{v}_h + \mathbf{v}', p_h + p', \boldsymbol{\tau}_h + \boldsymbol{\tau}') \in V_h \oplus V' \times P_h \oplus P' \times \mathcal{T}_h \oplus \mathcal{T}'$

such that

$$\rho(\delta_t(\mathbf{v}_h+\mathbf{v}'),\mathbf{w}_h+\mathbf{w}')+\rho((\mathbf{v}_h+\mathbf{v}')\cdot\nabla(\mathbf{v}_h+\mathbf{v}'),\mathbf{w}_h+\mathbf{w}')-(p_h+p',\nabla\cdot(\mathbf{w}_h+\mathbf{w}'))$$
$$+2(\eta\boldsymbol{\varepsilon}(\mathbf{v}_h+\mathbf{v}'),\boldsymbol{\varepsilon}(\mathbf{w}_h+\mathbf{w}'))+(\boldsymbol{\tau}_h+\boldsymbol{\tau}',\boldsymbol{\varepsilon}_{\mathrm{s}}(\mathbf{w}_h+\mathbf{w}'))=\langle\mathbf{f},\mathbf{w}_h+\mathbf{w}'\rangle, \tag{3.135}$$

$$(q_h+q',\nabla\cdot(\mathbf{v}_h+\mathbf{v}'))=0, \tag{3.136}$$

$$-(\boldsymbol{\xi}_h+\boldsymbol{\xi}',\boldsymbol{\varepsilon}_{\mathrm{s}}(\mathbf{v}_h+\mathbf{v}'))=0, \tag{3.137}$$

for all $(\mathbf{w}_h+\mathbf{w}',q_h+q',\boldsymbol{\xi}_h+\boldsymbol{\xi}')\in V_{h,0}\oplus V_0'\times P_{h,0}\oplus P_0'\times\mathcal{T}_{h,0}\oplus\mathcal{T}_0'$. Recall that δ_t stands for an approximation to the time derivative ∂_t. Even if time has been discretized, we have kept the notation for the functional spaces for simplicity. Even though the subgrid scales (or subscales) could be approximated without further assumptions and inserted into the previous equations (see [104]), we will make use of some common approximations that are explained in [122] and lead to the discrete variational problem:

$$\rho(\delta_t\mathbf{v}_h,\mathbf{w}_h)+\rho(\mathbf{v}_h\cdot\nabla\mathbf{v}_h,\mathbf{w}_h)-(p_h+p',\nabla\cdot\mathbf{w}_h)+2(\eta\boldsymbol{\varepsilon}(\mathbf{v}_h),\boldsymbol{\varepsilon}(\mathbf{w}_h))+(\boldsymbol{\tau}_h+\boldsymbol{\tau}',\boldsymbol{\varepsilon}_{\mathrm{s}}(\mathbf{w}_h))$$
$$+\sum_K(\mathbf{v}',-\rho\mathbf{v}_h\cdot\nabla\mathbf{w}_h-\nabla\cdot(2\eta\boldsymbol{\varepsilon}(\mathbf{w}_h)))_K=\langle\mathbf{f},\mathbf{w}_h\rangle, \tag{3.138}$$

$$(q_h,\nabla\cdot\mathbf{v}_h)-\sum_K(\mathbf{v}',\nabla q_h)_K=0, \tag{3.139}$$

$$-(\boldsymbol{\varepsilon}_{\mathrm{s}}(\mathbf{v}_h),\boldsymbol{\xi}_h)+\sum_K(\mathbf{v}',\chi_{\mathrm{s}}\nabla\cdot\boldsymbol{\xi}_h)_K=0, \tag{3.140}$$

for all $(\mathbf{w}_h,q_h,\boldsymbol{\xi}_h)\in V_{h,0}\times P_{h,0}\times\mathcal{T}_{h,0}$, where $\sum_K$ stands for the summation over all the elements of the finite element partition $\mathcal{K}_h$ and $(\cdot,\cdot)_K$ denotes the L^2 product in each K.

The problem for the fine scales is obtained taking $(\mathbf{w}_h,q_h,\boldsymbol{\xi}_h)=(\mathbf{0},0,\mathbf{0})$ in 3.135-3.137. Introducing the finite element residuals

$$\begin{aligned}\mathcal{R}_v&=\mathbf{f}-\rho\delta_t\mathbf{v}_h-\rho\mathbf{v}_h\cdot\nabla\mathbf{v}_h-\nabla p_h+\chi_{\mathrm{s}}\nabla\cdot\boldsymbol{\tau}_h+\nabla\cdot(2\eta\boldsymbol{\varepsilon}(\mathbf{v}_h)),\\ \mathcal{R}_p&=-\nabla\cdot\mathbf{v}_h,\\ \mathcal{R}_\tau&=\boldsymbol{\varepsilon}_{\mathrm{s}}(\mathbf{v}_h),\end{aligned}$$

and using the same ideas as in [101, 114], it turns out that the subscales may be approximated within each element $K\in\mathcal{K}_h$ by

$$\mathbf{v}'=\alpha_v(\mathcal{R}_v),\quad p'=\alpha_p(\mathcal{R}_p),\quad \boldsymbol{\tau}'=\alpha_\tau(\mathcal{R}_\tau),$$

where α_v, α_p and α_τ are the so called stabilization parameters that we compute within each element as

$$\alpha_v = \left[\left(\frac{c_1 \eta}{\rho h^2} \right)^2 + \left(\frac{c_2 \|\mathbf{v}_h\|_K}{h} \right)^2 \right]^{-1/2}, \tag{3.141}$$

$$\alpha_p = \left[\left(\frac{\eta}{\rho} \right)^2 + \left(\frac{c_2 \|\mathbf{v}_h\|_K h}{c_1} \right)^2 \right]^{1/2}, \tag{3.142}$$

$$\alpha_\tau = c_3 \frac{h}{L} 2\eta_{\mathrm{s}}, \tag{3.143}$$

where h is the element size, L a characteristic length of the computational domain, $\|\mathbf{v}\|_K$ a characteristic norm of $\mathbf{v}_h$ (with the same units as $\mathbf{v}_h$) in element K and c_1, c_2 and c_3 are algorithmic constants. We take them as $c_1 = 4$, $c_2 = 2$ and $c_3 = 1$ for linear elements. See [122] for additional remarks concerning the choice (3.141)-(3.143).

For the linear elements used in the numerical examples, terms of the form $\nabla \cdot (2\eta \boldsymbol{\varepsilon}(\mathbf{w}_h))$ involving second derivatives within each element can be neglected.

Inserting the expression for the subscales obtained in (3.138)-(3.140) we finally obtain the stabilized finite element problem seeked. It consists of finding $(\mathbf{v}_h, p_h, \boldsymbol{\tau}_h) \in V_h \times P_h \times \mathcal{T}_h$ such that

$$\begin{aligned}
&\rho(\delta_t \mathbf{v}_h, \mathbf{w}_h) + \rho(\mathbf{v}_h \cdot \nabla \mathbf{v}_h, \mathbf{w}_h) - (p_h, \nabla \cdot \mathbf{w}_h) + 2(\eta \boldsymbol{\varepsilon}(\mathbf{v}_h), \boldsymbol{\varepsilon}(\mathbf{w}_h)) + (\boldsymbol{\tau}_h, \boldsymbol{\varepsilon}_{\mathrm{s}}(\mathbf{w}_h)) \\
&\quad + \sum_K \alpha_v (\rho \delta_t \mathbf{v}_h + \rho \mathbf{v}_h \cdot \nabla \mathbf{v}_h + \nabla p_h - \chi_{\mathrm{s}} \nabla \cdot \boldsymbol{\tau}_h - \nabla \cdot (2\eta \boldsymbol{\varepsilon}(\mathbf{v}_h)), \rho \mathbf{v}_h \cdot \nabla \mathbf{w}_h + \nabla \cdot (2\eta \boldsymbol{\varepsilon}(\mathbf{w}_h)))_K \\
&\quad + \sum_K \alpha_p (\nabla \cdot \mathbf{v}_h, \nabla \cdot \mathbf{w}_h) + \sum_K \alpha_\tau (\boldsymbol{\varepsilon}_{\mathrm{s}}(\mathbf{v}_h), \boldsymbol{\varepsilon}_{\mathrm{s}}(\mathbf{w}_h)) \\
&\quad = \langle \mathbf{f}, \mathbf{w}_h \rangle + \sum_K \alpha_v (\mathbf{f}, \rho \mathbf{v}_h \cdot \nabla \mathbf{w}_h + 2\eta \nabla \cdot \boldsymbol{\varepsilon}(\mathbf{w}_h))_K,
\end{aligned} \tag{3.144}$$

$$\begin{aligned}
&(q_h, \nabla \cdot \mathbf{v}_h) + \sum_K \alpha_v (\rho \delta_t \mathbf{v}_h + \rho \mathbf{v}_h \cdot \nabla \mathbf{v}_h + \nabla p_h - \chi_{\mathrm{s}} \nabla \cdot \boldsymbol{\tau}_h - \nabla \cdot (2\eta \boldsymbol{\varepsilon}(\mathbf{v}_h)), \nabla q_h)_K \\
&\quad = \sum_K \alpha_v (\mathbf{f}, \nabla q_h)_K,
\end{aligned} \tag{3.145}$$

$$\begin{aligned}
&-(\boldsymbol{\varepsilon}_{\mathrm{s}}(\mathbf{v}_h), \boldsymbol{\xi}_h) + \sum_K \alpha_v (\rho \delta_t \mathbf{v}_h + \rho \mathbf{v}_h \cdot \nabla \mathbf{v}_h + \nabla p_h - \chi_{\mathrm{s}} \nabla \cdot \boldsymbol{\tau}_h - \nabla \cdot (2\eta \boldsymbol{\varepsilon}(\mathbf{v}_h)), -\chi_{\mathrm{s}} \nabla \cdot \boldsymbol{\xi}_h)_K \\
&\quad = \sum_K \alpha_v (\mathbf{f}, -\chi_{\mathrm{s}} \nabla \cdot \boldsymbol{\xi}_h)_K,
\end{aligned} \tag{3.146}$$

for all $(\mathbf{w}_h, q_h, \boldsymbol{\xi}_h) \in V_{h,0} \times P_{h,0} \times \mathcal{T}_{h,0}$. We have assumed $\mathbf{f} \in L^2(K)^n$ for simplicity.

At this point the problem suffers from the lack of an appropriate choice for $\mathcal{T}_h$ to make system 3.144-3.145 uniquely solvable. This can be circumvented by using a sort of augmented Lagrangian scheme coupled with an Uzawa iterative scheme, as explained in the algorithm of section 2. The final fully discrete iterative scheme is described in [122] and will be not repeated here.

3.5.5 Numerical experiments

In this section, we present five numerical examples to illustrate the flexibility of the approach dealing with complex geometry and to asses its accuracy. The numerical simulations were carried out using the C++ CimLib finite element library (see [46, 69]). The first obtained results with the proposed approach are compared to solutions obtained by standard solution (classical boundary conditions).

3.5.5.1 Falling disk in a channel

We consider first a classical benchmark: a rigid disk with radius $R = 0.125$ cm falling under the action of gravitational force inside a 2-D channel of dimension $[0, 2] \times [0, 6]$. Parameters used in this example are tabulated in Table 3.4.

Parameter	ρ_{f}	ρ_{s}	η_{f}	$\triangle t$	g
Unit	g/cm^3	g/cm^3	g/cms	s	cm/s^2
Value	1	1.25	0.1	0.005	980

Table 3.4: Parameter used in the computation of a falling disk in a channel

In [29] the velocity of particulate flow with rigid circular disks using fictitious domain method is calculated and reported. We compare our computational results to this reference. This test case is well documented in the literature and considered as a challenging benchmark.

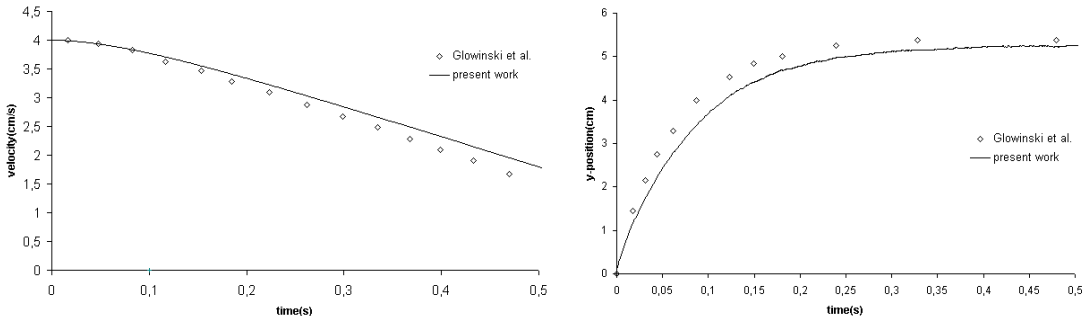


Figure 3.39: The evolution of the vertical velocity and position of the falling disk.

Close agreements in figure 3.39 are found for both the velocity and the position of the center of the disk in function of the time. Figures 3.40 and 3.41 illustrate respectively the velocity contour plot for v_x and v_y at selected instances surrounding the zero iso-zero of the disk level-set function. The agreement between the two numerical solutions shows that the present approach is able to predict well the behaviour of the fluid in the presence of rigid body.

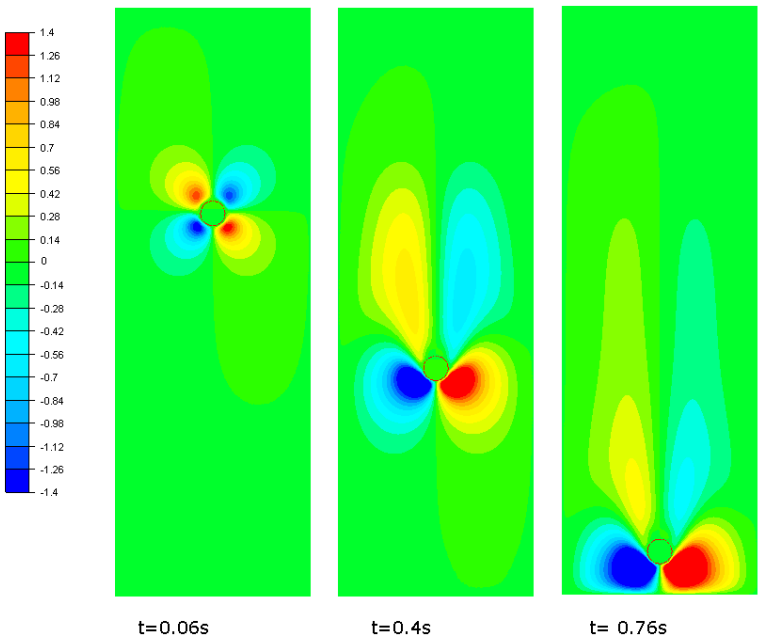


Figure 3.40: The profile of the velocity v_x surrounding the iso-zero of the disk level-set function.

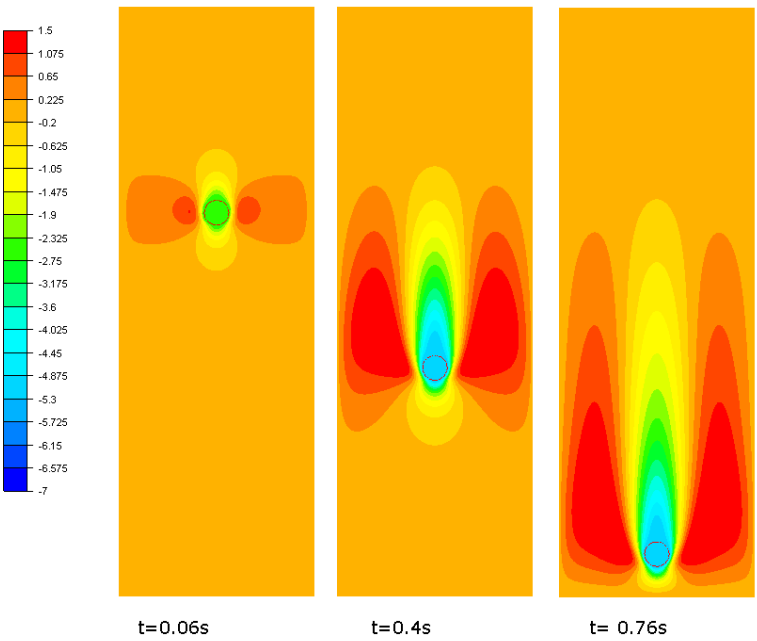


Figure 3.41: The profile of the velocity v_y surrounding the iso-zero of the disk level-set function.

3.5.5.2 Falling cylinder in an incompressible fluid

We follow the lines in [124] to analyze extensively the terminal velocity v_T of a falling cylinder in an incompressible fluid. The same parameters as [124] are used to assess the solution using for instance different viscosity values and different meshes. The rigid cylinder falls under the gravitational force. We prescribe then a zero pressure on the top of the fluid channel and no slip walls on the sides and bottom. The dimension of the fluid domain is $2L \times 8L$ with $L = 0.02m$ and the cylinder radius is $r = 5 \times 10^{-3}$. The fluid is considered incompressible with density 1000 kg/m^3 and the solid density is 2000 kg/m^3. The gravitational force is $9.8ms^{-1}$. Note that for comparisons, we choose from the reference the most precise results computed using a 160×640 grid. The values of the viscosity are: $\eta_f = 0.1kgs^{-1}$, $0.2kgs^{-1}$, $0.5kgs^{-1}$, $1kgs^{-1}$, $2kgs^{-1}$, $5kgs^{-1}$ and $10kgs^{-1}$.

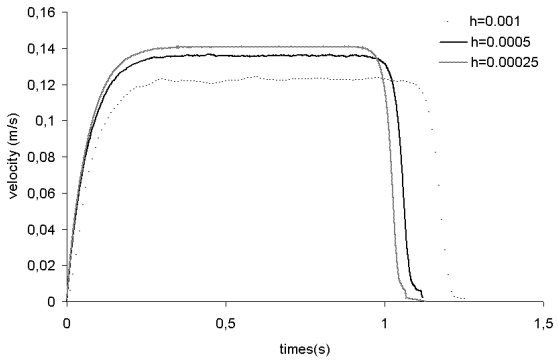


Figure 3.42: The evolution of the terminal velocity of the cylinder for $\eta_f = 0.2kg/s$ and $h = 0.001$, $h = 0.0005$ and $h = 0.00025$.

η_f	ref. [124] 160×640	$h = 0.001$	$h = 0.0005$	$h = 0.00025$
0.1	-0.1966	-0.167770	-0.19230704	-0.196834
0.2	-0.1417	-0.12367	-0.13596088	-0.14087306
0.5	-0.06721	-0.059924	-0.06253623	-0.066432
1	-0.03399	-0.030207	-0.03266043	-0.0335803
2	-0.01702	-0.01523	-0.0160292	-0.0165884
5	-0.006828	-0.00617	-0.0066192	-0.00674716
10	-0.003417	-0.003104	-0.0032519	-0.00338712

Table 3.5: Terminal velocity for the falling cylinder problem

The computed data and results are tabulated in table 3.5. Note that we are solving the Navier-Stokes equations while the terminal velocity is derived under a Stokes flow assumption. As a result, the terminal velocity calculated will be usually lower than the analytic solution. As observed in figure 3.42 and in table 3.5, we obtain a closer

agreement on the finer mesh. Robinson et al. [124] solve the FSI problem in a monolithic framework using a MAC grid dicretization of the fluid and a fully Lagrangian discretization of the structure. Comparing our computational results to those reported in [124], we can find good agreements for the terminal velocities and a good potential for the developed formulation.

3.5.5.3 Tetris benchmark

Four rigid bodies with different density are falling under the gravitational force in a $[0, 2] \times [0, 6]$ channel. When several rigid bodies fall in an incompressible fluid channel, the interactive motions of these bodies show an interesting phenomenon. At the beginning, each body has the same acceleration by the gravitational force. As time passes, the velocity of the upper bodies becomes faster than the lower ones since they undergo more resistance against the fluid comparing to the upper ones.

Solid	Initial position	$\rho_s(kg/m^3)$
a	$(0.35; 4)$	4000
b	$(0.32; 5)$	8000
c	$(1; 5.6)$	3000
d	$(1.25; 4.8)$	8000

Table 3.6: The properties of the four rigid bodies

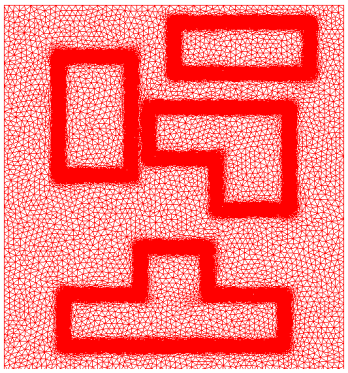


Figure 3.43: Zoom at the upper part of the domain showing the initial used finite element mesh

The coordinates of the lower left corner of each solid, the corresponding geometries as well as the densities are given in Table 3.6 and presented in figures 3.44 and 3.45. The arrangement of the four rigid bodies at $t = 0$ and the used refined FE mesh are shown in figure 3.43. Indeed, to track the bodies and to render a well respected geometry in terms of angles and accurate interfaces, the proposed mesh adaptation algorithm is applied iteratively. The number of elements is fixed to 35000. The density and viscosity

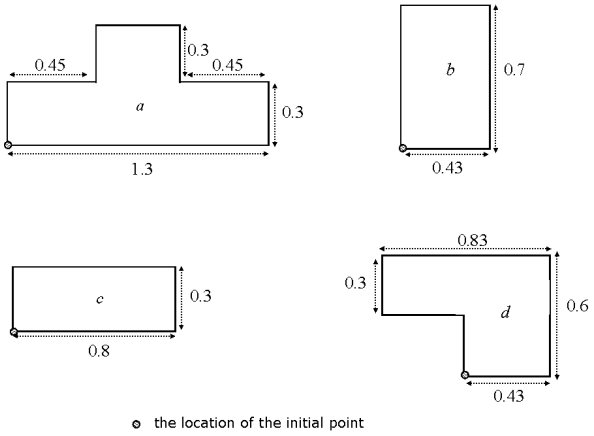


Figure 3.44: The proposed geometry for the four rigid bodies.

of the fluid used in this example are $\rho_{\mathrm{f}} = 1kg/m^3$ and $\eta_{\mathrm{f}} = 0.005Pa.s$. The objective of this test is to show the capability of the method to handle high density ratios. Figure 3.46 illustrates the respected geometry due to the use of the anisotropic mesh adaptation and the velocity vectors at different time instants. All the vortices behind the solid objects confirm the capability of the proposed stabilized monolithic formulation to solve at the same time a convection dominated flow in the fluid and a rigid body velocity in the solid. The evolution of the velocity and the corresponding position taken at the center of the body a are plotted in figure 3.47. We acknowledge that the solution of this test case is direct and similar to the previous numerical examples without assessing the interaction between the bodies. The purpose is merely to demonstrate the capability of the high density difference and the use of low fluid viscosity that the proposed monolithic formulation can handle.

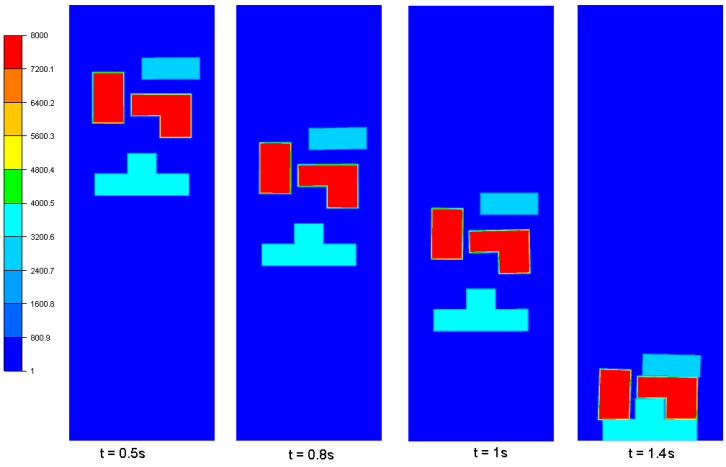


Figure 3.45: The density distribution at different time instants with anisotropic adapted interfaces.

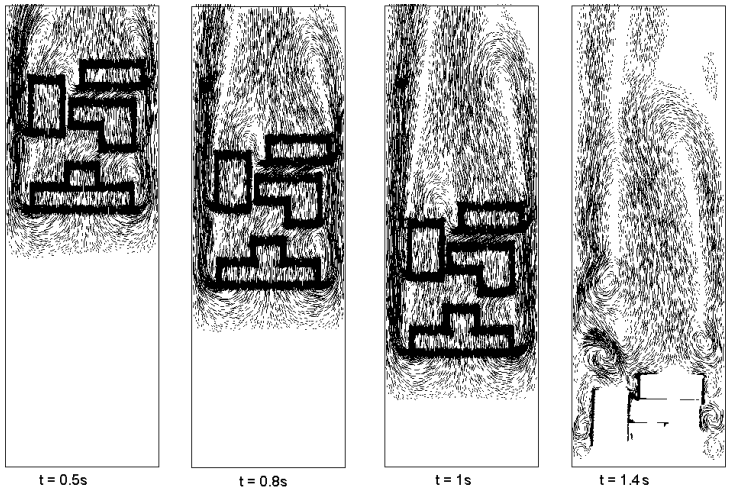


Figure 3.46: The velocity vectors at different time instants.

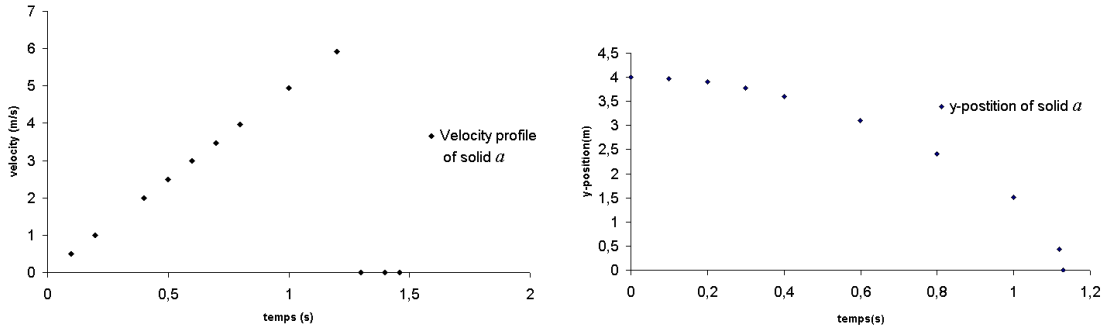


Figure 3.47: The evolution of the velocity and the position taken at the center of the body a.

3.5.5.4 2D immersion of a NACA0012 airfoil in an incompressible fluid at Reynolds 5000

We continue by investigating the flow around a NACA0012 airfoil in a channel [125]. This study is considered as an important step to investigate the feasibility of the proposed monolithic fluid-structure formulation. The purpose is to show the flexibility of the method to deal with a large variety of geometries. Rather than spending the effort on the mesh construction around the airfoil, we bypass this step and we consider the simplest rectangular domain. As mentioned before, the NACA profile will be represented then using a simple distance function.

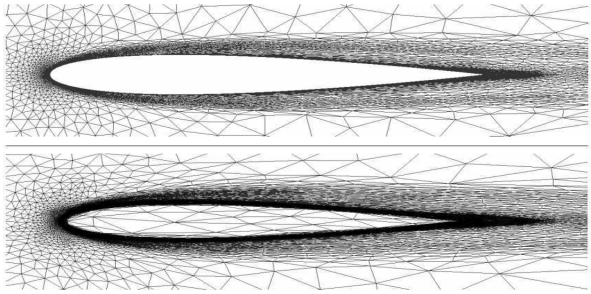


Figure 3.48: Finite element meshes: only the fluid domain (up) - the air-NACA domain (bottom).

Therefore, we consider two cases. In the first one, we use the classical approach and we impose zero boundary conditions on the profile. So the effort will be concentrated on the geometry and on building the fluid mesh while well respecting the curvatures of the airfoil profile. In the second case, (i) we consider a large simple channel domain, (ii) we compute analytically the distance function of the NACA profile located at the center, (iii) we apply the anisotropic mesh adptation using the variation of the gradients of the level-set function, and finally, (iv) we mix and assign the physical properties. The obtained finite element meshes that will be used in the two cases are depicted in figure 3.48.

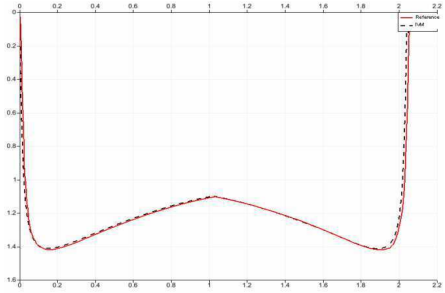


Figure 3.49: Comparisons of the pressure coefficients. (-) reference, (· · ·) present work

We apply the same conditions on both test cases and we compare the solutions. The Reynolds number Re_∞ based on the cord c is equal to 5000 and the angle of incidence to 0. The number of elements is fixed to 45000.

As the proposed *a posteriori* estimation combines the simultaneous adaptivity on the level-set scalar field and the velocity field, boundary layers and inner layers are automatically captured due to the anisotropically adapted mesh exhibiting highly stretched elements.

A comparison of the pressure coefficients using the classical and the new approach is presented in figure 3.49. Recall that the drag coefficient is computed using the following formula

$$C_p = \frac{p - p_\infty}{\frac{1}{2}\rho u_\infty} \tag{3.147}$$

Snapshots of the norm of the velocity, the pressure fields and the streamlines computed on the entire domain (fluid and structure) and on only the fluid domain are shown in figures 3.50, 3.51 and 3.52 respectively. The very good agreement between the two numerical solutions shows that the present solver is able to predict accurately the behaviour of the fluid and the presence of the solid.

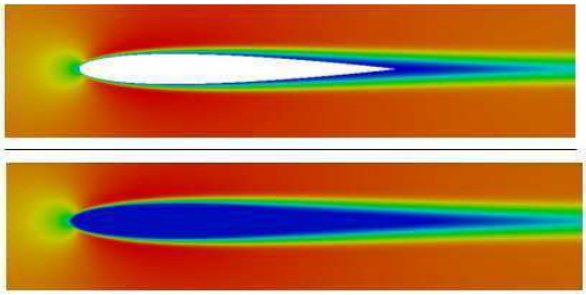


Figure 3.50: Norm of the velocity calculated over the fluid domain (up) and the entire domain (bottom).

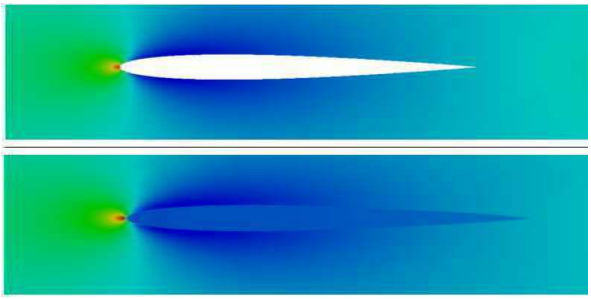


Figure 3.51: Pressure distribution calculated over the fluid domain (up) and the entire domain (bottom).

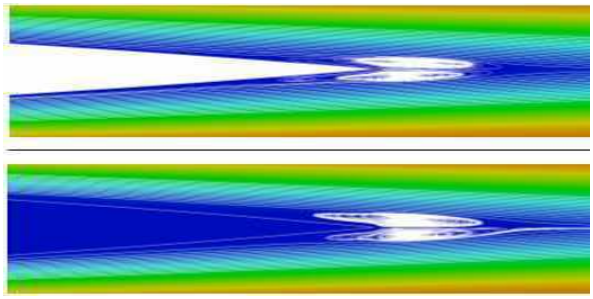


Figure 3.52: Streamlines distribution calculated over the fluid domain (up) and the entire domain (bottom).

3.5.5.5 Unsteady flow past a 3D immersed simplified vehicle model

A similar test case is aimed at exploring the capabilities of the model when used in a situation involving more complex geometries in 3D. Here, we simulate the flow past an immersed simplified vehicle model. The Ahmed body is one of the first benchmark proposed to investigate the stability and fuel consumption of an automobile at high cruising speeds. It represents a simplified car geometry that can be used to study the automotive aerodynamics and isolate relevant flow phenomena. A critical slant angle of 30° was found to lead to a dramatic change in the flow pattern.

The flexibility of the proposed monolithic approach resides in the possibility to vary easily the rear slant angle of the immersed vehicle from 25° to 35°. It also allows to add/remove small appendices to the geometry in order to study their effects and to reduce eventually the turbulent behaviour behind the immersed body. Figure 3.53 presents a plane cut of the adapted meshes showing different slant angles.

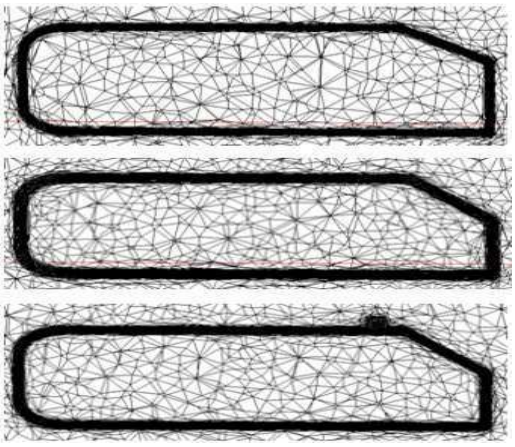


Figure 3.53: Remeshing the fluid-solid interfaces and modifying the rear angle from 25° (up) to 35° (center) and adding a small cylinder on the top (buttom)

The simulations for the two different slant angles are given in figure 3.54. The 35° angle case shows more complex flow behaviour. For this reason, we have added an appendix, a small cylinder on the top of the vehicle to study and reduce the turbulent behaviour behind the immersed body.

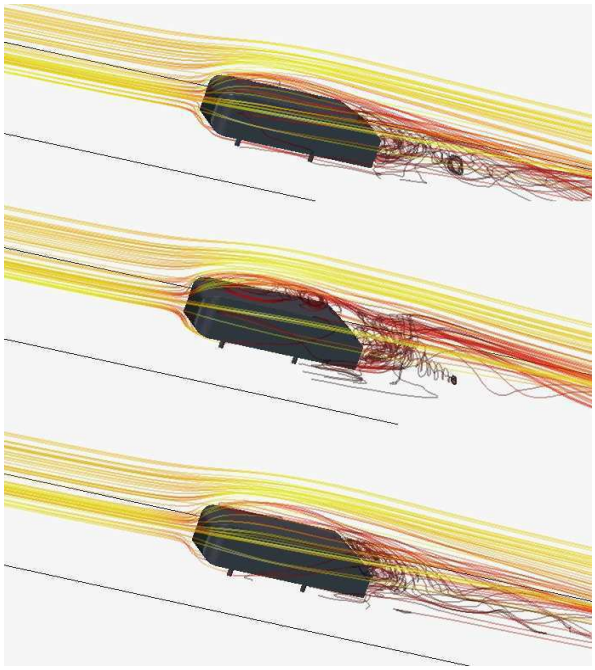


Figure 3.54: Streamlines behind the vehicle (rendered by the zero-isovalues of the distance function) at different slant angle a) 25° b) 35° and c) with the small cylinder.

3.5.6 Conclusion

In this part a stabilized three-field velocity-pressure-stress finite element model, designed for the computation of rigid bodies in an incompressible Navier-Stokes flow, has been described. The method is based on treating a single set of equations for the whole domain. The presence of the solid, rendered by a distance function, is taken into account as an extra stress tensor in the Navier-Stokes equations. The considered formulation allows equal-order interpolation for the three-fields. An *a posteriori* edge based spatial error estimator, relying on the length distribution tensor approach, is developed. It allows the creation of extremely stretched elements along the interface, which is an important requirement for problems with high density ratios, for large structural deformations and for free movements of the structure within a flow domain. 2D and 3D numerical experiments were presented and results were compared against reference or other approaches. The capability of the method to simulate the fluid-rigid body interaction with complex geometries was demonstrated. The results presented here show that this method can be

used in a wide range of application for multi body fluid-solid problems. Further research will focus on tackling deformable solid interaction.

3.6 Conclusion

In this chapter, a stabilized three-filed velocity-pressure-stress, based on the Variational multiscale method, has been presented to simulate rigid bodies in the incompressible Navier-Stokes flow. The simulations were solved by a monolithic formulation in an Eulerian framework with anisotropic mesh adaptation. The presence of the solid is taken into account as an extra-stress in the Navier-Stokes equations.

The first paper allows equal order of interpolation for the velocity and pressure field and a lower-order interpolation for the stress. Fixed and moving rigid bodies simulations were performed. The results yielded that the rigid body is well represented in the proposed formulation. The test case of the falling disk in a channel was compared with an existing one in the literature, results show close agreement. The possibility of taking several moving rigid bodies was also demonstrated.

Secondly, an amelioration of the method was proposed allowing equal order of interpolation for the three fields. The method was validated for a fixed rigid body, immersed in a fluid, in $2D$ and $3D$ domain. The test cases compared very well to simulations where only the fluid domain is presented. Moreover, simulations of a fixed and oscillating disk were compared with results present in literature showing good agreement. Finally, a simulation at high Reynolds number with complex geometry was performed. The results presented here show that this method can be used in a wide range of application for multi-body fluid-solid problems.

In the last part, an *a posteriori* edge based spatial error estimator, relying on the length distribution tensor approach, was added to the previous formulation. The falling disk in a channel and the Tetris test cases were revisited showing better and more accurate results. The influence of the mesh size was also presented for different fluid viscosities of a falling cylinder and compared with results present in the literature. Finally, the NACA problem and Ahmad body problem with different rear angles, were also carried out showing the capability and flexibility of the method to simulate fluid-rigid body interaction with complex geometries.

3.7 Résumé

La formulation stabilisée est présentée pour résoudre le problème IFS de corps rigides dans un écoulement fluide. Les simulations sont effectuées en utilisant une formulation monolithique eulérienne avec la possibilité d'adaptation de maillage anisotrope. La présence du solide est prise en compte comme une contrainte supplémentaire dans l'équation de Navier-Stokes. La stabilisation est basée sur la méthode variationnelle multi-échelle qui consiste à décomposer les champs de vitesse, pression et contrainte en une petite échelle et une grande échelles.

Le premier papier présenté utilise une approximation éléments finis avec un degré d'interpolation pour le champs de vitesse et pression plus élevé que celui associé au tenseur de contraintes. Des simulations avec des corps rigides fixes et mobiles sont réalisées. Les résultats obtenus permettent de conclure que le corps rigide est bien représenté avec la formulation proposée. Le cas test d'un disque qui tombe dans un canal sous l'action de la gravité est présenté et les résultats montrent un bon accord avec la littérature. La possibilité de prendre en compte plusieurs corps rigides en mouvement ou au repos a également été démontrée. Deuxièmement, une amélioration de la méthode est proposée pour résoudre le système avec le même ordre d'interpolation pour les trois champs. La méthode est validée pour un corps rigide fixe immergés dans un fluide en 2 et en 3 D. Ensuite, les simulations d'un disque fixe et oscillant ont montré un bon accord avec la littérature. Enfin, la simulation avec un nombre de Reynolds élevé et une géométrie complexe a été réalisée.

Dans le dernier papier, l'adaptation de maillage basée sur l'estimateur d'erreur a posteriori est ajoutée à la formulation précédente. Le cas d'un disque qui tombe dans un canal et le cas ŚTd'ŠAhmad etrisŠ sont repris et calculés avec la nouvelle méthode. Les résultats obtenus montrent que la nouvelle méthode est plus précise. L'influence de la taille de maille est également présentée avec des différentes viscosités du fluide pour le cas d'un cylindre qui tombe et comparé avec la littérature. Le problème de Naca est calculés et les résultats sont comparer entre la simulation sur le domaine fluide seul contre celle calculée sur l'ensemble du domaine: fluide et structure. En plus le problème d'ŠAhmad bodyŠ est réalisé, avec différents angles, ce qui montre la capacité de la méthode pour simuler l'interaction entre un fluide et une structure rigide avec des géométries complexes.

Chapter 4

Lagrangian and Eulerian description

Contents

4.1 Introduction 106
4.2 Lagrangian description 106
4.2.1 Elementary Deformation 107
4.2.2 Mass conservation 109
4.2.3 Conservation of momentum 109
4.2.3.1 St. Venant-Kirchhoff material 109
4.2.3.2 Neo-Hookean material 110
4.3 Eulerian description 110
4.3.1 Deformation 111
4.3.2 Mass conservation 112
4.3.3 Conservation of momentum 113
4.3.3.1 Fluid momentum equation 113
4.3.3.2 Structural momentum equation 114
4.4 Conclusion 114
4.5 Résumé français 115

4.1 Introduction

The purpose of this work is to be able to solve the FSI problem in a unified formulation for the fluid and the structure. This formulation was achieved for fluid-rigid body problems. In order to accomplish that for the fluid-elastic problems, we introduce in this chapter some notation, definition and transformation needed to develop a fluid-elastic interaction in an Eulerian framework.

In the literature, when modelling a problem with a single substance the solid or fluid, the Eulerian approach is naturally used to describe fluid dynamics flow problems and the Lagrangian approach is the most convenient framework to describe the structural deformation. When modelling fluid-structure problems in a monolithic framework, the ALE approach is widely used [126, 127, 128] as well as the Eulerian approach [129, 130, 131, 132, 126].

In this chapter, the Eulerian and Lagrangian descriptions are presented based on the detailed works in [133, 134]. For each framework, the governing equations, used to model fluid and solid problems, are detailed. For both systems, the mass conservation is a common equation. Another essential conservation equation introduced in this chapter, is the momentum equation. It varies along with the structure and the fluid, if a compressible or incompressible material is used, depending on the proper constitutive laws used.

In this work, the incompressible fluid will be considered. As a result, the mass and momentum conservations are sufficient to model the fluid problem. For the structural part, different behaviour laws are pointed out. The incompressible Neo-Hookean material will be used for simulation.

4.2 Lagrangian description

The Lagrangian approach follows the movement and deformation of a given particle. The Lagrangian view-point refers to the reference configuration. Consider the initial position of point M^0 as $\overrightarrow{OM^0} = \mathbf{X}$. The new position of M^0 at time t is then $\overrightarrow{OM} = \mathbf{x}$ as presented in figure 4.1.

Thus, we can define the displacement vector $\mathbf{u}$ such that:

$$\mathbf{x} = \mathbf{X} + \mathbf{u}(\mathbf{X}, \mathbf{t}). \tag{4.1}$$

And the velocity $\mathbf{v}$ as :

$$\mathbf{v} = \frac{\mathrm{d}\ \mathbf{x}}{\mathrm{d}\ t} = \frac{\partial \mathbf{u}}{\partial t}, \tag{4.2}$$

For any "Lagrangian" function $f(\mathbf{X}, t)$, the time derivative is :

$$\frac{\mathrm{d}\ f}{\mathrm{d}\ t} = \frac{\partial f}{\partial t}\ . \tag{4.3}$$

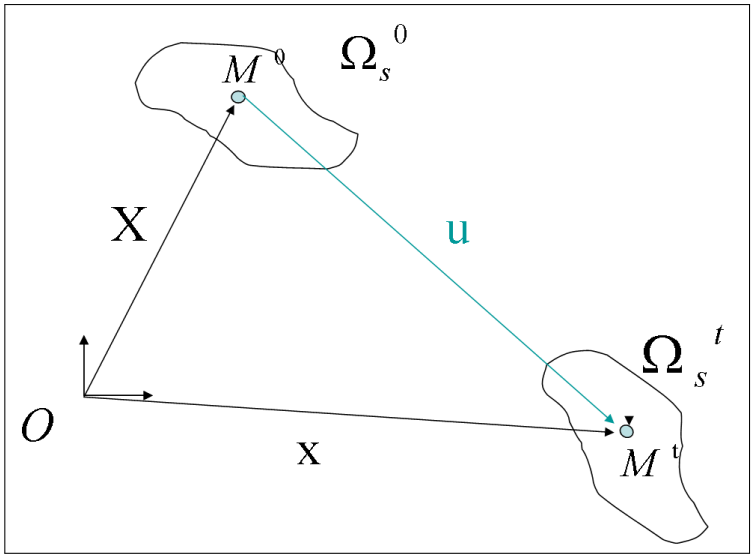


Figure 4.1: Initial and final configuration of a system

4.2.1 Elementary Deformation

If an initial domain is deforming to a new configuration at time t, denoted by Ω^0 and Ω^t respectively, then the deformation is studied at an elementary level **dx** (see figure 4.2).

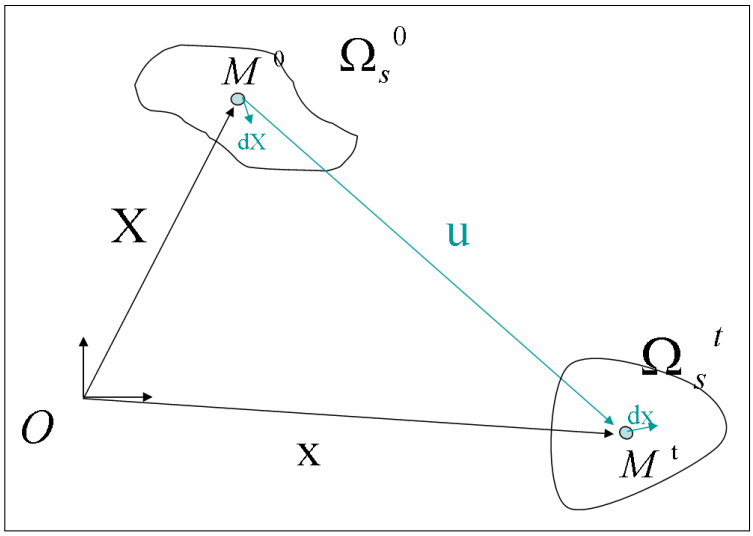


Figure 4.2: Elementary Transformation

Introducing the mapping $f : \Omega^0 \rightarrow \Omega$, the corresponding deformation gradient tensor

$\mathbf{F}$ for the transformation : $\mathbf{X} \rightarrow \mathbf{x}$ is defined by:

$$\begin{aligned} \mathbf{F} = \nabla_{\mathbf{X}} f = \frac{\partial \mathbf{x}}{\partial \mathbf{X}} &= \mathbf{I}_d + \frac{\partial \mathbf{u}}{\partial \mathbf{X}}, \\ &= \mathbf{I}_d + \nabla_{\mathbf{X}} \mathbf{u}. \end{aligned} \tag{4.4}$$

The deformation gradient tensor $\mathbf{F}$, as noticed, is a tensor connecting the material's initial and current configurations. For example, an elementary vector $\mathbf{dX}$ is transformed into $\mathbf{dx} = \mathbf{F}\mathbf{dX}$. Moreover, if the position of M is known, then the position M^0 can be calculated, thus $\mathbf{F}$ is invertible. As a result, the Jacobian of the transformation $J = \det \mathbf{F}$ is always greater than zero.

The local deformation denoted by $\mathbf{C}$, known as the Cauchy-Green tensor, is defined by :

$$\begin{aligned} \mathbf{C} &= \mathbf{F}^T \cdot \mathbf{F}, \\ &= \mathbf{I}_d + \nabla_{\mathbf{X}} \mathbf{u} + \nabla_{\mathbf{X}} \mathbf{u}^{\mathbf{T}} + (\nabla_{\mathbf{X}} \mathbf{u})^{\mathbf{T}} \cdot (\nabla_{\mathbf{X}} \mathbf{u}), \end{aligned} \tag{4.5}$$

where $\mathbf{C}$ is a symmetric tensor. The corresponding terms of this tensor are associated with the length variation of material vectors as well as the angular variation between them.

A more accurate strain measure is the Green-Lagrange tensor defined by:

$$\mathbf{L} = \frac{1}{2}(\mathbf{C} - \mathbf{I}_d). \tag{4.6}$$

$\mathbf{L}$ is also a symmetric tensor having the same principal directions as $\mathbf{C}$. Introducing the displacement field $\mathbf{u}$ in the defintion of $\mathbf{L}$, one gets:

$$\mathbf{L} = \frac{1}{2}\left(\nabla_{\mathbf{X}} \mathbf{u} + \nabla_{\mathbf{X}} \mathbf{u}^{\mathbf{T}} + (\nabla_{\mathbf{X}} \mathbf{u})^{\mathbf{T}} \cdot (\nabla_{\mathbf{X}} \mathbf{u})\right). \tag{4.7}$$

At this level, several remarks can be made:

- When dealing with a rigid body $\Rightarrow$ no deformation: no length and angular variation
  $\Rightarrow \mathbf{C} = \mathbf{I}_d \Rightarrow \mathbf{L} = 0$
- When dealing with infinitesimal small deformation $\Rightarrow (\nabla_{\mathbf{X}} \mathbf{u})^{\mathbf{T}} \cdot (\nabla_{\mathbf{X}} \mathbf{u})$ can be neglected
  $\Rightarrow \mathbf{L} \approx \boldsymbol{\varepsilon}(\mathbf{u})$
  where $\boldsymbol{\varepsilon}(\mathbf{u}) = \dfrac{\mathbf{1}}{\mathbf{2}}\left((\nabla_{\mathbf{X}} \mathbf{u}) + (\nabla_{\mathbf{X}} \mathbf{u})^{\mathbf{T}}\right)$ the linearized strain tensor.
- If an elementary volume vector $\mathrm{d}V^0$ is transformed to $\mathrm{d}V \Rightarrow \mathrm{d}V = J\ \mathrm{d}V^0$
  $= \sqrt{\det(\mathbf{C})}\ \mathrm{d}V^0$.
  The corresponding surface vector $\mathrm{d}S^0$ is transformed to $dS \Rightarrow \mathrm{d}S = J\mathbf{F}^{-T} \cdot \mathrm{d}S^0$.
- When dealing with an "isochoric" deformations $\Leftrightarrow$ the deformation conserves the volume
  $\Rightarrow J = 1$ (as for an incompressible material).

4.2.2 Mass conservation

If an elementary volume $\mathrm{d}V^0$ is transformed to $\mathrm{d}V$ at time t, the corresponding masses $\mathrm{d}M^0$ and $\mathrm{d}M$ respectively are equal. Then, using the third remark $\mathrm{d}V = J\ \mathrm{d}V^0$, and knowing that the mass is conserved, we get:

$$\begin{aligned} \rho^t \mathrm{d}V &= \rho^0 \mathrm{d}V^0, \\ \rho^t J \mathrm{d}V^0 &= \rho^0 \mathrm{d}V^0, \\ \rho^t J &= \rho^0, \end{aligned} \tag{4.8}$$

where ρ^0 is the density at time $t = 0$ and ρ^t is the density at time t. Thus the mass conservation in a Lagrangian description is nothing but $\rho J = \rho_0$.
As noted earlier, when dealing with an incompressible material $J = 1$. Hence, $\rho = \rho_0$, the density is constant once following the movement.

4.2.3 Conservation of momentum

Usually, the balance momentum is written with respect to the displacement since it is a primary variable for the structural system of equation. Additionally, the material derivative of the velocity is:

$$\frac{\mathrm{d}\mathbf{v}}{\mathrm{d}t} = \frac{\partial \mathbf{v}}{\partial t} = \frac{\partial^2 \mathbf{u}}{\partial t^2}. \tag{4.9}$$

Hence, the structural dynamic equilibrium with respect to the Lagrangian configuration in the reference domain Ω_{s}^0, using Newton's second law of motion, yields:

$$\rho^0 \frac{\partial^2 \mathbf{u}}{\partial t^2} - \nabla_{\mathbf{X}}(\mathbf{F} \cdot \mathbf{S}) = \rho^0 \mathbf{f}^0 \quad \text{in } \Omega_{\mathrm{s}}^0, \tag{4.10}$$

where $\mathbf{f}^0$ is the external volume forces and $\mathbf{S}$ is the second Piola-Kirchhoff stress tensor obtained from the Cauchy-Stress tensor $\boldsymbol{\sigma}_{\mathrm{s}}$:

$$\mathbf{S} = J\mathbf{F}^{-1} \cdot \boldsymbol{\sigma}_{\mathrm{s}} \cdot \mathbf{F}^{-T}. \tag{4.11}$$

4.2.3.1 St. Venant-Kirchhoff material

For a St. Venant-Kirchhoff material, which is a nonlinear model for compressible elastic materials, the specific strain energy is given by:

$$\mathbf{S} = 2\mu\mathbf{L} + \lambda tr(\mathbf{L})\mathbf{I}_d, \tag{4.12}$$

where μ and λ are the two Lamé constant coefficients. The Lamé coefficients are

related to the Young's modulus E and the Poisson ratio ν with the following expressions:

$$\begin{aligned} \lambda &= \frac{\nu E}{(1+\nu)(1-2\nu)}, \\ \mu &= \frac{E}{2(1+\nu)}. \end{aligned} \tag{4.13}$$

Note that these parameter are prescribed for different elastic structure, for example $\nu = \frac{1}{2}$ for incompressible materials and $\nu < \frac{1}{2}$ for compressible materials.

4.2.3.2 Neo-Hookean material

For a compressible Neo-Hookean material, which is a hyperelastic material model, the second Piola-Kirchhoff stress yields [135, 44]:

$$\mathbf{S} = \frac{\lambda}{2}(J^2 - 1)\mathbf{C}^{-1} + \mu(\mathbf{I}_d - \mathbf{C}^{-1}). \tag{4.14}$$

For incompressible material$J = 1$, therefore, the incompressibility constraint is $J - 1 = 0$. The hydrostatic pressure p is introduced as a Lagrangian multiplier to ensure the incompressibility constraint. $\mathbf{S}$ reaches:

$$\begin{aligned} \mathbf{S} &= -p\mathbf{C}^{-1} + \mu(\mathbf{I}_d - \mathbf{C}^{-1}), \\ &= -p\mathbf{F}^{-1}\mathbf{F}^{-T} + \mu(\mathbf{I}_d - \mathbf{F}^{-1}\mathbf{F}^{-T}), \\ \text{and } \mathbf{F}\cdot\mathbf{S} &= -p\mathbf{F}^{-T} + \mu(\mathbf{F} - \mathbf{F}^{-T}), \\ &= \left(-p\mathbf{I}_d + \mu(\mathbf{F}\mathbf{F}^T - \mathbf{I}_d)\right)\mathbf{F}^{-T}. \end{aligned} \tag{4.15}$$

4.3 Eulerian description

In an Eulerian framework, the evolution of the domain from a point M is observed. The velocity at point M at time t is the velocity of the material point with initial position M^0:

$$\mathbf{v} = \frac{\mathrm{d}\mathbf{x}}{\mathrm{d}t}. \tag{4.16}$$

In this case, as for the previous "Lagrangian" $f(\mathbf{X}, t)$ denoted as $F(\mathbf{x}, t)$ in the Eulerian framework, the material derivative would be:

$$\begin{aligned} \frac{\mathrm{d}F}{\mathrm{d}t} &= \frac{\partial F}{\partial t} + \frac{\partial F}{\partial \mathbf{x}}\frac{\partial \mathbf{x}}{\partial t} \\ &= \frac{\partial F}{\partial t} + (\mathbf{v}\cdot\nabla_{\mathbf{x}})F. \end{aligned} \tag{4.17}$$

The gradients $\nabla_{\mathbf{X}} f$ and $\nabla_{\mathbf{x}} F$ are related to each other, using the chain rule, by:

$$\nabla_{\mathbf{X}} f = \nabla_{\mathbf{x}} F \mathbf{F} \quad \text{since } \frac{\partial f}{\partial \mathbf{X}_i} = \sum_j \frac{\partial F}{\partial \mathbf{x}_j} \frac{\partial \mathbf{x}_i}{\partial \mathbf{X}_j}. \tag{4.18}$$

4.3.1 Deformation

In the Lagrangian description, the deformation gradient tensor was determined in equation (4.4). In an Eulerian framework, there is also the deformation, but $\nabla_{\mathbf{x}} \mathbf{u}$ is different than $\nabla_{\mathbf{X}} \mathbf{u}$.
Recall that:

$$\begin{aligned} f : \Omega^0 &\longrightarrow \Omega \\ \mathbf{X} &\longrightarrow \mathbf{x} = \mathbf{X} + \mathbf{u}(\mathbf{X}, t) \end{aligned}$$

The inverse mapping to the Eulerian framework can be easily introduced by:

$$\begin{aligned} f^{-1} : \Omega &\longrightarrow \Omega^0 \\ \mathbf{x} &\longrightarrow \mathbf{X} = \mathbf{x} - \mathbf{u}(\mathbf{x}, t) \end{aligned}$$

Differentiating spatially, we obtain:

$$\begin{aligned} \frac{\partial \mathbf{X}}{\partial \mathbf{x}} &= \mathbf{I}_d - \nabla_{\mathbf{x}} \mathbf{u} \\ \text{and} \qquad \frac{\partial \mathbf{u}}{\partial \mathbf{x}} &= \mathbf{I}_d - \frac{\partial \mathbf{X}}{\partial \mathbf{x}} \end{aligned} \tag{4.19}$$

Expressing $\nabla_{\mathbf{X}} \mathbf{u}$ in terms of $\nabla_{\mathbf{x}} \mathbf{u}$ will lead to:

$$\begin{aligned} \nabla_{\mathbf{X}} \mathbf{u} &= \frac{\partial \mathbf{u}}{\partial \mathbf{X}}, \\ &= \frac{\partial \mathbf{u}}{\partial \mathbf{x}} \left(\frac{\partial \mathbf{X}}{\partial \mathbf{x}} \right)^{-1}, \\ &= (\mathbf{I}_d - \frac{\partial \mathbf{X}}{\partial \mathbf{x}}) \left(\frac{\partial \mathbf{X}}{\partial \mathbf{x}} \right)^{-1}, \\ &= \left(\frac{\partial \mathbf{X}}{\partial \mathbf{x}} \right)^{-1} - \mathbf{I}_d, \\ &= (\mathbf{I}_d - \nabla_{\mathbf{x}} \mathbf{u})^{-1} - \mathbf{I}_d. \end{aligned} \tag{4.20}$$

Thus, the inverse of the gradient deformation tensor $\mathbf{F}^{-1}$, that is written in an Eulerian description $\mathbf{F}_{\mathbf{x}}$, and the gradient deformation tensor are finally given by:

$$\begin{aligned} \mathbf{F} &= \mathbf{I}_d + (\mathbf{I}_d - \nabla_{\mathrm{x}} \mathbf{u})^{-1} - \mathbf{I}_d, \\ &= (\mathbf{I}_d - \nabla_{\mathbf{x}} \mathbf{u})^{-1}, \\ \text{and } \mathbf{F}^{-1} &= \mathbf{I}_d - \nabla_{\mathbf{x}} \mathbf{u}. \end{aligned} \tag{4.21}$$

The inverse deformation and its corresponding Jacobian are related to each other in the following manner:

$$J^{-1} = \det \mathbf{F}^{-1}. \tag{4.22}$$

And finally, the Cauchy-Green tensor and Green-Lagrange tensor can be written in an Eulerian description as:

$$\begin{aligned} \mathbf{C} &= \mathbf{F}^T \cdot \mathbf{F}, \\ &= (\mathbf{I}_d - \nabla_{\mathrm{x}}\mathbf{u})^{-T} \cdot (\mathbf{I}_d - \nabla_{\mathrm{x}}\mathbf{u})^{-1}, \end{aligned} \tag{4.23}$$

$$\begin{aligned} \text{and } \mathbf{L} &= \frac{1}{2}(\mathbf{F}^T \cdot \mathbf{F} - \mathbf{I}_d), \\ &= \frac{1}{2}[(\mathbf{I}_d - \nabla_{\mathrm{x}}\mathbf{u})^{-T} \cdot (\mathbf{I}_d - \nabla_{\mathrm{x}}\mathbf{u})^{-1} - \mathbf{I}_d], \\ &= \frac{1}{2}[((\mathbf{I}_d - \nabla_{\mathbf{x}}\mathbf{u})^{-1} - \mathbf{I}_d) + ((\mathbf{I}_d - \nabla_{\mathbf{x}}\mathbf{u})^{-1} - \mathbf{I}_d)^T \\ &\quad + ((\mathbf{I}_d - \nabla_{\mathbf{x}}\mathbf{u})^{-1} - \mathbf{I}_d)^T \cdot ((\mathbf{I}_d - \nabla_{\mathbf{x}}\mathbf{u})^{-1} - \mathbf{I}_d)]. \end{aligned} \tag{4.24}$$

The last equality is reached by writing $\nabla_{\mathbf{x}}\mathbf{u}$ in its Eulerian form using equation (4.7)

From another part, the Eulerian framework allows prescribing other characteristic tensors, for fluid flows in particular. The symmetric gradient of $\mathbf{v}$ is called the strain rate tensor:

$$\dot{\boldsymbol{\varepsilon}} = \frac{1}{2}(\nabla_{\mathbf{x}}\mathbf{v} + \nabla_{\mathbf{x}}\mathbf{v}^{\mathbf{T}}). \tag{4.25}$$

Note that $tr(\dot{\boldsymbol{\varepsilon}}) = \nabla \cdot \mathbf{v}$ is invariant and valid for any reference framework.

4.3.2 Mass conservation

Deriving the relation in equation (4.8) in time, the mass conservation in an Eulerian formulation is:

$$\frac{\mathrm{d}\rho}{\mathrm{d}t}J + \rho\frac{\mathrm{d}J}{\mathrm{d}t} = \frac{\partial\rho}{\partial t} + \nabla_{\mathbf{x}}(\rho\mathbf{v}) = 0. \tag{4.26}$$

When dealing with an incompressible material the mass conservation is nothing but

$$\nabla_{\mathrm{x}}\mathbf{v} = 0.$$

This equation is also valid for flows with small MACH number since, in this case, the effect of the compressibility can be neglected.

In the following ∇_{x} will be denoted by ∇ for sake of clarity.

4.3.3 Conservation of momentum

The dynamic equilibrium at any structural or fluid point inside a domain Ω, using Newton's second law of motion reads:

$$\rho \frac{\mathrm{d}\mathbf{v}}{\mathrm{d}t} - \nabla \cdot \boldsymbol{\sigma} = \rho \mathbf{f} \quad \text{in } \Omega, \tag{4.27}$$

where $\mathbf{f}$ is the external volume forces, $\dfrac{\mathrm{d}\mathbf{v}}{\mathrm{d}t}$ is the inertial forces and $\boldsymbol{\sigma}$ is the stress. Note that in the Eulerian formulation, the velocity is given as a function of spatial coordinates. Hence, the material derivative of the velocity is given by:

$$\begin{aligned} \frac{\mathrm{d}\mathbf{v}}{\mathrm{d}t} &= \frac{\partial \mathbf{v}}{\partial t} + \frac{\partial \mathbf{v}}{\partial x}\frac{\partial x}{\partial t}, \\ &= \frac{\partial \mathbf{v}}{\partial t} + \mathbf{v} \cdot \nabla \mathbf{v}. \end{aligned} \tag{4.28}$$

In the following, the conservation of momentum equation (4.27) is presented for the fluid and structural domain, in the Eulerian framework.

4.3.3.1 Fluid momentum equation

The balance of linear momentum at a fluid particle inside the fluid domain Ω_f using the dynamic equilibrium equation (4.27) is given by:

$$\rho_\mathrm{f} \frac{\partial \mathbf{v}}{\partial t} + \rho_\mathrm{f} \mathbf{v} \cdot \nabla \mathbf{v} - \nabla \cdot \boldsymbol{\sigma} = \rho_\mathrm{f} \mathbf{f} \quad \text{in } \Omega_\mathrm{f}, \tag{4.29}$$

where ρ_f is the fluid density.

Moreover, the constitutive equation for a Newtonian flow is given by:

$$\boldsymbol{\sigma} = -p\mathbf{I}_d + \lambda tr(\dot{\boldsymbol{\varepsilon}})\mathbf{I}_d + 2\eta\dot{\boldsymbol{\varepsilon}}, \tag{4.30}$$

where p is the pressure, λ and η parameters determining the viscosity. If the flow is incompressible: $tr(\dot{\boldsymbol{\varepsilon}}) = 0$, the strain rate tensor contains shear strain only. In this case, the constitutive equation yields:

$$\boldsymbol{\sigma} = -p\mathbf{I}_d + 2\eta\dot{\boldsymbol{\varepsilon}}, \tag{4.31}$$

with η the dynamic viscosity. Using equation (4.31), the momentum conservation equation (4.32) for the incompressible Navier-Stokes flow in the convective form can be written as:

$$\rho_\mathrm{f} \frac{\partial \mathbf{v}}{\partial t} + \rho_\mathrm{f} \mathbf{v} \cdot \nabla \mathbf{v} - 2\eta \nabla \cdot \dot{\boldsymbol{\varepsilon}} + \nabla p = \rho_\mathrm{f} \mathbf{f} \quad \text{in } \Omega_\mathrm{f}. \tag{4.32}$$

4.3.3.2 Structural momentum equation

The structural momentum equation is given by:

$$\rho_{\mathrm{s}}\frac{\partial \mathbf{v}}{\partial t} + \rho_{\mathrm{s}}\mathbf{v}\cdot\nabla\mathbf{v} - \nabla\cdot\boldsymbol{\sigma}_{\mathrm{s}} = \rho_{\mathrm{s}}\mathbf{f} \quad \text{in } \Omega_{\mathrm{s}}, \tag{4.33}$$

with ρ_{s} is the structural density expressed in its Eulerian prescription.
For a St. Venant-Kirchhoff material and a compressible Neo-Hookean material, their corresponding stresses can be transformed to the Eulerian reference system using the so-called Piola Transformation [136, 126]. The balance equation yields:

$$\rho_{\mathrm{s}}\frac{\partial \mathbf{v}}{\partial t} + \rho_{\mathrm{s}}\mathbf{v}\cdot\nabla\mathbf{v} - \nabla\cdot(J^{-1}\mathbf{F}\cdot\mathbf{S}\cdot\mathbf{F}^{T}) = \rho_{\mathrm{s}}\mathbf{f} \quad \text{in } \Omega_{\mathrm{s}}, \tag{4.34}$$

with $\mathbf{S}$ written in the Eulerian form. Note that having the different tensors, $\mathbf{C}$ and $\mathbf{L}$, written in an Eulerian form, the new form of tensor $\mathbf{S}$ can be easily deduced.

Writing the constitutive equation (4.15) in the Eulerian form for the incompressible Neo-Hookean material and replacing it in equation (4.34), the the balance equation reaches:

$$\rho_{\mathrm{s}}\frac{\partial \mathbf{v}}{\partial t} + \rho_{\mathrm{s}}\mathbf{v}\cdot\nabla\mathbf{v} - \nabla\cdot\big(-p\mathbf{I}_d + \mu(\mathbf{F}\cdot\mathbf{F}^{T} - \mathbf{I}_d)\big) = \rho_{\mathrm{s}}\mathbf{f} \quad \text{in } \Omega_{\mathrm{s}}. \tag{4.35}$$

A more general general expression of $\boldsymbol{\sigma}_{\mathrm{s}}$ can be found in [137].

4.4 Conclusion

In this chapter, the Lagrangian and Eulerian descriptions are reviewed. In each formulation, the deformation, mass and momentum conservations are detailed. The material deformation is usually prescribed in a Lagrangian framework. We began by presenting the elementary deformation in its natural system of reference along with the tensors used to illustrate the deformation. In the third section, the reformulation of the deformation is developed in an Eulerian context.

The main equations to model fluid and structure problems are mass and momentum conservations. The mass conservation for the fluid or structure is the same, this equation is defined easily in both framework. We reformulate the momentum conservation of the structure in the Eulerian framework after presenting the commonly used one, written in a Lagrangian framework, for different structural materials: St. Venant-Kirchhoff material, incompressible and compressible Neo-Hookean materials. Concerning the fluid balance equation, we prescribed it in the Eulerian system of reference since it is usually used in an Eulerian context. We consider in this work the incompressible fluid flow problem, so the Navier-Stokes equations are reached at the end.

As a result, the fluid and structure systems, mass equilibrium and momentum conservation equations, are expressed in an Eulerian framework.

4.5 Résumé français

Ce chapitre est consacré à la présentation des descriptions lagrangienne et eulérienne. La déformation, les équations d'équilibre et de conservation de la masse sont détaillées pour chaque formulation. La déformation d'un milieu est normalement définie dans un cadre de travail Lagrangien. Pour cela, nous avons commencé par présenter la déformation élémentaire dans la configuration de référence (Lagrangien), avec les différents tenseurs utilisés pour illustrer la déformation. La déformation est ensuite reformulée dans un contexte eulérien. Les principales équations pour décrire le comportement d'un fluide ou d'une structure sont la conservation de la masse et l'équation d'équilibre. L'équation de conservation de la masse est la même pour le fluide et pour la structure, elle est facilement définie dans les deux configurations. L'équation d'équilibre associé à la structure est reformulée dans un cadre eulérien après l'avoir présenté dans un cadre Lagrangien normalement utilisé pour présenter les milieux déformable. Différentes lois de comportement sont décrits pour la structure: matériaux 'St-Venant Kirchhoff', matériaux incompressibles et compressibles 'Néo-Hookean'. En ce qui concerne l'équation d'équilibre du fluide, ces équations sont décrites dans un contexte eulérien et non lagrangien. Nous considérons dans ce travail, le problème des fluides incompressible ainsi l'équation de Navier-Stokes est atteinte à la fin. A l'issue de ce chapitre, On atteint une description Eulérienne pour les équations décrivant la structure et le fluide.

Chapter 5

FSI with Elastic structure

Contents

5.1 Introduction 118
5.2 Governing equations 118
5.2.1 Complete Eulerian formulation 120
5.2.1.1 Weak form 121
5.3 Stabilized Finite-Element Method (SFEM) 124
5.3.1 MultiScale approach 125
5.3.2 Coarse scale formulation 126
5.3.3 Stablized formulation 128
5.4 Numerical Results 128
5.4.1 Ealstic flow cavity 129
5.4.2 Oscillating disk 131
5.4.3 Elastic plate in an imposed flow 131
5.5 Conclusion 134
5.6 Resumé français 135

5.1 Introduction

In this chapter, we present all the details needed to obtain is to develop a general solver capable of dealing with an FSI problem having an elastic or rigid structure. Usually, the FSI system with the rigid body is treated in another aspect than the one used with an elastic body [138, 139].

Very few developed work prescribe, somehow, in the same manner FSI simulations with a rigid and elastic body. As example, Zhang and co-workers [140] solve the FSI problem using an immersed smoothed FEM. The fluid mesh is proposed to evaluate the FSI forces exerted on the solid. In this work, largely deformable solids are treated and the rigid bodies can be considered by simply having a relatively high Young's modulus. An adaptive, staggered-grid version of the IB method, is applied in [141] to simulate FSI model of the aortic heart valve. The thin leaflets are described as immersed elastic boundaries and the wall of the aortic root is described as a thick, semi-rigid elastic structure. A monolithic FSI framework is considered in [124] for incompressible flow. A traditional MAC grid discretization of the fluid and a fully Lagrangian discretization of the structures are used. The ability to treat rigid bodies using the same formulas as deformable bodies is achieved based on treating the rigid bodies as in [142], where the coupling of rigid and deformable bodies is proposed.

To reach our purpose, we propose a new method for solving FSI problems with an elastic or rigid body in a similar way. This new formulation is considered as an extension of the previous elaborated method presented in chapter 3 for fluid-rigid body system in a monolithic framework and an Eulerian context. The details of this method are presented in this chapter. We begin by writing the governing equations of the fluid and structure in an Eulerian framework using all the notation and definition from chapter 4. Then the full Eulerian fluid-elastic formulation is reached. The stabilization method is an essential key to reach a stable finite element approximation. For this reason, we formulate the corresponding SFEM. And finally, simulations to demonstrate the efficiency of the methodology are established on several test cases well documented in the literature.

5.2 Governing equations

As the proposed approach is monolithic, a unique constitutive equations will be solved on the whole domain, with a variation of the parameters depending on the phase that should be modelled. But first each system of equation is presented separately.

Let $\Omega \subset \mathbb{R}^n$ be the spatial domain at time $t \in [0, T]$, where n is the space dimension. Let $\partial\Omega$ denote the boundary of Ω. The fluid domain, the solid domain and the interface will be Ω_{f}, Ω_{s} and Γ_{im}, respectively. They verify:

$$\overline{\Omega}_{\mathrm{f}} \cup \overline{\Omega}_{\mathrm{s}} = \overline{\Omega} \quad \text{and} \quad \overline{\Omega}_{\mathrm{f}} \cap \overline{\Omega}_{\mathrm{s}} = \Gamma_{\mathrm{im}}.$$

The dynamic of the flow is given by the classical incompressible Navier-Stokes equa-

tions as presented previously in equation (4.32):

$$\rho_{\mathrm{f}}\frac{\partial \mathbf{v}}{\partial t} + \rho_{\mathrm{f}}\mathbf{v}\cdot\nabla\mathbf{v} - 2\eta_{\mathrm{f}}\nabla\cdot\boldsymbol{\varepsilon}(\mathbf{v}) + \nabla p = \rho_{\mathrm{f}}\mathbf{f} \quad \text{in } \Omega_{\mathrm{f}}, \tag{5.1}$$

$$\nabla\cdot\mathbf{v} = 0 \quad \text{in } \Omega_{\mathrm{f}}, \tag{5.2}$$

where $\mathbf{v}$ is the velocity vector, ρ_f is the fluid density, p is the pressure, $\mathbf{I_d}$ is the identity tensor, $\boldsymbol{\varepsilon}(\mathbf{v}) = (\boldsymbol{\nabla}\mathbf{v}+^{T}\boldsymbol{\nabla}\mathbf{v})/2$ the deformation-rate tensor and η_f is the dynamic viscosity.

Equations (5.1) and(5.2) are subject to the boundary and initial conditions:

$$\mathbf{v} = \mathbf{v}_{\Gamma,\mathrm{f}} \quad \text{on } \partial\Omega_{\mathrm{f}} \setminus \Gamma_{\mathrm{im}},\ t > 0, \tag{5.3}$$

$$\mathbf{v} = \mathbf{v}_{\mathrm{im}} \quad \text{on } \Gamma_{\mathrm{im}},\ t >, 0 \tag{5.4}$$

$$\boldsymbol{\sigma}\cdot\mathbf{n} = \mathbf{t}_{\mathrm{im}} \quad \text{on } \Gamma_{\mathrm{im}},\ t > 0, \tag{5.5}$$

$$\mathbf{v}(\mathbf{x}, 0) = \mathbf{v}_0(\mathbf{x}) \quad \text{in } \Omega_{\mathrm{f}}, \tag{5.6}$$

where $\mathbf{v}_{\Gamma,\mathrm{f}}$ is a given velocity boundary condition, $\mathbf{v}_{\mathrm{im}}$ is the velocity at the fluid-solid interface Γ_{im} (the boundary of the immersed body), $\mathbf{n}$ is the outward normal on the solid surface, $\mathbf{t}_{\mathrm{im}}$ the normal stress on this boundary and $\mathbf{v}_0(\mathbf{x})$ is a given initial condition. For simplicity, only Dirichlet-type boundary conditions will be considered on the exterior boundary. For incompressible flows, the divergence-free constraint (5.2) gives rise to the pressure in the fluid.

In what follows, the elastic structure governing equations of the incompressible structure are prescribed. In the present formulation we treat the elastic body as a continuous domain subjected to an additional stress tensor. We may write the equations of motion as the Navier-Stokes equations and add the corresponding stress tensor as follows:

$$\rho_{\mathrm{s}}\left(\partial_t\mathbf{v} + \mathbf{v}\cdot\nabla\mathbf{v}\right) - \nabla\cdot\boldsymbol{\tau}_{\mathrm{s}} + \nabla p = \mathbf{f} \quad \text{in } \Omega_{\mathrm{s}},\ t > 0, \tag{5.7}$$

$$\nabla\cdot\mathbf{v} = 0 \quad \text{in } \Omega_{\mathrm{s}},\ t > 0, \tag{5.8}$$

$$\mathbf{L}_{\mathrm{s}}(\mathbf{u}) - \frac{1}{\mu}\boldsymbol{\tau}_{\mathrm{s}} = \mathbf{0} \quad \text{in } \Omega_{\mathrm{s}},\ t > 0 \tag{5.9}$$

$$\partial_t\mathbf{u} + \mathbf{v}\cdot\nabla\mathbf{u} = \mathbf{v} \quad \text{in } \Omega_{\mathrm{s}},\ t > 0, \tag{5.10}$$

where ρ_{s} the solid density, μ is the elastic constant and $\mathbf{L}_{\mathrm{s}}(\mathbf{u})$ defined previously as $\mathbf{L}$ in equation (4.24). Replacing μ by its value for incompressible materials, $\frac{1}{2}$, in equation (4.13), the lamé and Young modulus are related to each other using the following:

$$\begin{aligned}\mu &= \frac{E}{2(1+0.5)} \\ &= \frac{E}{3}\end{aligned} \tag{5.11}$$

Equation (5.9) is chosen to be written in this form to take into account the rigid body case. More precisely, if μ tends to infinity $\Rightarrow \frac{1}{\mu}\boldsymbol{\tau}_{\mathrm{s}}$ tends to zero
$\Rightarrow \mathbf{L}_{\mathrm{s}}(\mathbf{u})$ tends to zero
$\Rightarrow$ back to the rigid body case.
Hence if μ has a large value, equation (5.9) can be solved using an augmented Lagrangian method coupled with an Uzawa scheme. Otherwise, τ_s can be computed directly using this equation. More details concerning on each case can be found afterwards. In an incompressible elastic solid, the displacement is divergence free ($\nabla\cdot\mathbf{v} = 0$) and the velocity is the material derivative of the displacement. Hence the velocity is also divergence free.

Again equations (5.7)-(5.10) need to be supplied with the boundary and initial conditions:

$$\mathbf{v} = \mathbf{v}_{\Gamma,\mathrm{s}} \quad \text{on } \partial\Omega_{\mathrm{s}} \setminus \Gamma_{\mathrm{im}},\ t > 0, \tag{5.12}$$
$$\mathbf{v} = \mathbf{v}_{\mathrm{im}} \quad \text{on } \Gamma_{\mathrm{im}},\ t > 0, \tag{5.13}$$
$$\boldsymbol{\sigma}\cdot\mathbf{n} = -\mathbf{t}_{\mathrm{im}} \quad \text{on } \Gamma_{\mathrm{im}},\ t > 0, \tag{5.14}$$
$$\mathbf{v}(\mathbf{x},0) = \mathbf{v}_0(\mathbf{x}) \quad \text{in } \Omega_{\mathrm{s}}. \tag{5.15}$$

5.2.1 Complete Eulerian formulation

We may write problem (5.1)-(5.6) and problem (5.7) - (5.15) in a unified way, in the whole computational domain Ω, as

$$\begin{aligned}
\rho\,(\partial_t\mathbf{v} + \mathbf{v}\cdot\nabla\mathbf{v}) - \nabla\cdot(2\eta\,\boldsymbol{\varepsilon}(\mathbf{v}) + \boldsymbol{\tau} - p\,\mathbf{I}_d) &= \mathbf{f} && \text{in } \Omega,\ t > 0,\\
\nabla\cdot\mathbf{v} &= 0 && \text{in } \Omega,\ t > 0,\\
\mathbf{L}(\mathbf{u}) - \frac{1}{\mu}\boldsymbol{\tau} &= \mathbf{0} && \text{in } \Omega,\ t > 0,\\
\partial_t\mathbf{u} + \mathbf{v}\cdot\nabla\mathbf{u} &= \mathbf{v} && \text{in } \Omega_{\mathrm{s}},\ t > 0,\\
\mathbf{v} &= \mathbf{v}_\Gamma && \text{on } \partial\Omega,\ t > 0,\\
\mathbf{v}(\mathbf{x},0) &= \mathbf{v}_0(\mathbf{x}) && \text{in } \Omega,
\end{aligned} \tag{5.16}$$

$$\begin{aligned}
\text{where } \mathbf{v}_\Gamma &= \mathbf{v}_{\Gamma,\mathrm{s}} \quad \text{on } \partial\Omega_{\mathrm{s}} \cap \partial\Omega,\\
\text{and } \mathbf{v}_\Gamma &= \mathbf{v}_{\Gamma,\mathrm{f}} \quad \text{on } \partial\Omega_{\mathrm{f}} \cap \partial\Omega,\\
\mathbf{L}(\mathbf{u}) &= H(\alpha)\mathbf{L}_{\mathrm{s}}(\mathbf{u}),\\
\boldsymbol{\tau} &= H(\alpha)\boldsymbol{\tau}_{\mathrm{s}},\\
\eta &= (1 - H(\alpha))\eta_{\mathrm{f}},\\
\rho &= \rho_{\mathrm{s}}H(\alpha) + \rho_{\mathrm{f}}(1 - H(\alpha)).
\end{aligned}$$

The boundary conditions (5.4)-(5.5) and (5.10)-(5.12) are no longer needed.

5.2.1.1 Weak form

Let $V \times P \times \mathcal{T} \times U$ be the space where the unknowns $(\mathbf{v}, p, \boldsymbol{\tau}, \mathbf{u})$ are sought. The first and last spaces, V and U, are made of vector fields which are square integrable in time with values in $H^1(\Omega)^d$ and satisfying the Dirichlet conditions. The second and third spaces, P and $\mathcal{T}$, are made of distributions in time with values in $P_0 = L^2(\Omega)/\mathbb{R}$ and $\mathcal{T}_0 = L^2(\Omega)^{d\times d}$, respectively (in fact, a subspace of $L^2(\Omega)^{d\times d}$ would be enough).

The corresponding test functions will be denoted $\mathbf{w} \in V_0 = H_0^1(\Omega)^d$, $q \in P_0$, and $\mathbf{z} \in U_0 = H_0^1(\Omega)^d$, $\boldsymbol{\xi} \in \mathcal{T}_0$.
Multiplying by the test functions and integrating by parts, the associated standard weak form of the system (5.16), can be stated as: Find $\mathbf{v} \in V$, $p \in P$, $\boldsymbol{\tau} \in \mathcal{T}$ and $\mathbf{u} \in U$, such that:

$$\begin{aligned}
\rho(\partial_t \mathbf{v}, \mathbf{w}) + \rho(\mathbf{v}\cdot\nabla\mathbf{v}, \mathbf{w}) - (p, \nabla\cdot\mathbf{w}) + (2\eta\boldsymbol{\varepsilon}(\mathbf{v}), \boldsymbol{\varepsilon}(\mathbf{w})) + (\boldsymbol{\tau}, \boldsymbol{\varepsilon}(\mathbf{w}))_{\mathrm{s}} &= \langle \mathbf{f}, \mathbf{w}\rangle, \\
(q, \nabla\cdot\mathbf{v}) &= 0, \qquad (5.17)\\
-(\boldsymbol{\xi}, \mathbf{L}(\mathbf{u})) - \frac{1}{\mu}\boldsymbol{\tau}) &= 0, \\
(\partial_t \mathbf{u}, \mathbf{z}) + (\mathbf{v}\cdot\nabla\mathbf{u}, \mathbf{z}) &= (\mathbf{v}, \mathbf{z}),
\end{aligned}$$

for all $(\mathbf{w}, q, \boldsymbol{\xi}, \mathbf{z}) \in V_0 \times P_0 \times \mathcal{T}_0 \times U_0$.
Here and below, $(\cdot,\cdot)$ stands for the standard L^2 product of two functions, $\langle\cdot,\cdot\rangle$ for the integral of the product of two functions in the general case and $(\cdot,\cdot)_{\mathrm{s}}$ the inner prodduct in Ω_{s}, including appropriate duality pairings if necessary.

Suppose that we discretize in time problem (5.17) using a finite difference scheme, and still denote by $\mathbf{v}$, p, $\boldsymbol{\tau}$ and $\mathbf{u}$ the fields to be computed at a given time step. Let $\delta_t\mathbf{v}$ and $\delta_t\mathbf{u}$ the discrete time derivatives. Two ways for proceeding will be prescribed next. Either the third equation of this system is treated explicitly or not. For both cases, the system is reduced and $\mathbf{L}(\mathbf{u})$ is expressed as a function of $\boldsymbol{\varepsilon}(\mathbf{v})$ and the displacement is solved separately using the last equation.
In the following, $\mathbf{L}(\mathbf{u}+\delta\mathbf{u})$ is decomposed, where $\delta\mathbf{u}$ is a small variation of the displacement.

Considering the following approximation:

$$(\mathbf{I_d} - \nabla\mathbf{u})^{-1} \simeq (\mathbf{I_d} + \nabla\mathbf{u}) \qquad (5.18)$$

Note that this approximation is just used to compute the new $\mathbf{L}(\mathbf{u}+\delta\mathbf{u})$.

The new $\nabla_{\mathrm{X}}(\mathbf{u}+\delta\mathbf{u})$ would be:

$$\begin{aligned}\nabla_{\mathrm{X}}(\mathbf{u}+\delta\mathbf{u}) &= (\mathbf{I_d}-\nabla(\mathbf{u}+\delta\mathbf{u}))^{-1}-\mathbf{I_d},\\ &\simeq (\mathbf{I_d}+\nabla(\mathbf{u}+\delta\mathbf{u}))-\mathbf{I_d},\\ &\simeq (\mathbf{I_d}+\nabla\mathbf{u}+\nabla\delta\mathbf{u})-\mathbf{I_d},\\ &\simeq (\mathbf{I_d}+\nabla\mathbf{u})-\mathbf{I_d}+\delta\mathbf{u}\\ &\simeq \nabla_{\mathrm{X}}\mathbf{u}+\nabla\delta\mathbf{u}.\end{aligned}$$

Thus $\mathbf{L}(\mathbf{u}+\delta\mathbf{u})$ reaches:

$$\begin{aligned}\mathbf{L}(\mathbf{u}+\delta\mathbf{u}) \simeq H(\alpha)\frac{1}{2}({}^t\nabla_{\mathrm{X}}\mathbf{u}+\nabla_{\mathrm{X}}\mathbf{u}+{}^t\nabla_{\mathrm{X}}\mathbf{u}\nabla_{\mathrm{X}}\mathbf{u}\\ +\nabla\delta\mathbf{u}+{}^t\nabla\delta\mathbf{u}+\underbrace{{}^t\nabla\delta\mathbf{u}\nabla\delta\mathbf{u}}_{\simeq 0})\\ +{}^t\nabla\mathbf{u}\nabla\delta\mathbf{u}+{}^t\nabla\delta\mathbf{u}\nabla\mathbf{u}),\end{aligned} \tag{5.19}$$

in the full Eulerian form and in the way the terms will be computed:

$$\begin{aligned}\mathbf{L}(\mathbf{u}+\delta\mathbf{u}) \simeq H(\alpha)\frac{1}{2}[(\mathbf{I_d}-\nabla\mathbf{u})^{-1}-\mathbf{I_d}+{}^t((\mathbf{I_d}-\nabla\mathbf{u})^{-1}-\mathbf{I_d})\\ +{}^t((\mathbf{I_d}-\nabla\mathbf{u})^{-1}-\mathbf{I_d})(\mathbf{I_d}-\nabla\mathbf{u})^{-1}-\mathbf{I_d})\\ +\nabla\delta\mathbf{u}+{}^t\nabla\delta\mathbf{u}+{}^t\nabla\mathbf{u}\nabla\delta\mathbf{u}+{}^t\nabla\delta\mathbf{u}\nabla\mathbf{u}].\end{aligned} \tag{5.20}$$

Finally, $\mathbf{L}(\mathbf{u}+\delta\mathbf{u})$ is nothing but:

$$\mathbf{L}(\mathbf{u}+\delta\mathbf{u}) \simeq \mathbf{L}(\mathbf{u})+\frac{1}{2}H(\alpha)[\nabla\delta\mathbf{u}+{}^t\nabla\delta\mathbf{u}+\left({}^t\nabla\mathbf{u}\nabla\delta\mathbf{u}+{}^t\nabla\delta\mathbf{u}\nabla\mathbf{u}\right)]. \tag{5.21}$$

A possible choice of $\delta\mathbf{u}$ can be $\mathbf{v}\Delta t$. Thus $\mathbf{L}(\mathbf{u}+\mathbf{v}\Delta t)$ is :

$$\mathbf{L}(\mathbf{u}+\mathbf{v}\Delta t)=\mathbf{L}(\mathbf{u})+H(\alpha)[\Delta t\boldsymbol{\varepsilon}(\mathbf{v})+\frac{1}{2}\left(\Delta t{}^t\nabla\mathbf{u}\nabla\mathbf{v}+\Delta t{}^t\nabla\mathbf{v}\nabla\mathbf{u}\right)]. \tag{5.22}$$

Remark:

In case the chosen material is the incompressible Neo-Hookean material (INHM), $\mathbf{L}(\mathbf{u})$ would be changed to the corresponding behaviour law in the Eulerian form. As presented in equation (4.35) and compared to the final form of $\mathbf{L}(\mathbf{u})$, the stress of the incompressible Neo-Hookean material and $\mathbf{L}(\mathbf{u})$ are the same, only the last two terms would be switched. Let $\mathbf{L}'(\mathbf{u})$ be $(\mathbf{F}\cdot\mathbf{F}^T-\mathbf{I}_d)$, $\mathbf{L}'(\mathbf{u}+\mathbf{v}\Delta t)$ would be:

$$\begin{aligned}\mathbf{L}'(\mathbf{u}+\mathbf{v}\Delta t) =&(\mathbf{I_d}-\nabla\mathbf{u})^{-1}-\mathbf{I_d}+{}^t((\mathbf{I_d}-\nabla\mathbf{u})^{-1}-\mathbf{I_d})\\ &+((\mathbf{I_d}-\nabla\mathbf{u})^{-1}-\mathbf{I_d})^t(\mathbf{I_d}-\nabla\mathbf{u})^{-1}-\mathbf{I_d})\\ &+2\Delta t\boldsymbol{\varepsilon}(\mathbf{v})+\nabla\mathbf{u}^t\nabla\mathbf{v}\Delta t+\nabla\mathbf{v}^t\Delta t\nabla\mathbf{u}],\\ =&\mathbf{L}'(\mathbf{u})+2\Delta t\boldsymbol{\varepsilon}(\mathbf{v})+\left(\Delta t\nabla\mathbf{u}^t\nabla\mathbf{v}+\Delta t\nabla\mathbf{v}^t\nabla\mathbf{u}\right),\end{aligned} \tag{5.23}$$

Solving explicitly $\boldsymbol{\tau}$

As previously stated, two possible way to solve the third equation of system(5.17). If $\boldsymbol{\tau}$ is computed directly as $\mu\mathbf{L}(\mathbf{u}+\mathbf{v}\Delta t)$, then the new FSI numerical scheme yields:

1. Solve $\mathbf{v}$ and p at time t:

$$\begin{aligned}\rho(\delta_t\mathbf{v},\mathbf{w})+\rho(\mathbf{v}\cdot\nabla\mathbf{v},\mathbf{w})-(p,\nabla\cdot\mathbf{w})+(\eta\boldsymbol{\varepsilon}(\mathbf{v}),\boldsymbol{\varepsilon}(\mathbf{w}))\\ +\frac{\mu}{2}\Delta tH(\alpha)\left({}^t\nabla\mathbf{u}\nabla\mathbf{v}+{}^t\nabla\mathbf{v}\nabla\mathbf{u},\boldsymbol{\varepsilon}(\mathbf{w}))\right)=\langle\mathbf{f},\mathbf{w}\rangle+\mu(\mathbf{L}(\mathbf{u}),\boldsymbol{\varepsilon}(\mathbf{w}))_{\mathrm{s}}\\ (q,\nabla\cdot\mathbf{v})=0,\end{aligned}\tag{5.24}$$

   where $\eta=H(\alpha)\mu\Delta t+(1-H(\alpha))\eta_{\mathrm{f}}$

   For INHM, $\boldsymbol{\tau}$ is computed directly as $\mu\mathbf{L}'(\mathbf{u}+\mathbf{v}\Delta t)$, the corresponding system would be:

$$\begin{aligned}\rho(\delta_t\mathbf{v},\mathbf{w})+\rho(\mathbf{v}\cdot\nabla\mathbf{v},\mathbf{w})-(p,\nabla\cdot\mathbf{w})+(\eta\boldsymbol{\varepsilon}(\mathbf{v}),\boldsymbol{\varepsilon}(\mathbf{w}))\\ +\mu\Delta tH(\alpha)\left(\nabla\mathbf{u}^t\nabla\mathbf{v}+\nabla\mathbf{v}^t\nabla\mathbf{u},\boldsymbol{\varepsilon}(\mathbf{w}))\right)=\langle\mathbf{f},\mathbf{w}\rangle+\mu(\mathbf{L}'(\mathbf{u}),\boldsymbol{\varepsilon}(\mathbf{w}))_{\mathrm{s}}\\ (q,\nabla\cdot\mathbf{v})=0,\end{aligned}\tag{5.25}$$

   where $\eta=H(\alpha)2\mu\Delta t+(1-H(\alpha))\eta_{\mathrm{f}}$

2. Solve $\mathbf{u}$:

$$(\delta_t\mathbf{u},\mathbf{w})+(\mathbf{v}\cdot\nabla\mathbf{u},\mathbf{w})=(\mathbf{v}.\mathbf{w})\tag{5.26}$$

3. Update $\mathbf{L}(\mathbf{u})$ or $\mathbf{L}'(\mathbf{u})$:

$$\begin{aligned}\mathbf{L}(\mathbf{u})=&\frac{1}{2}H(\alpha)[(\mathbf{I_d}-\nabla\mathbf{u})^{-1}-\mathbf{I_d}+{}^t\left((\mathbf{I_d}-\nabla\mathbf{u})^{-1}-\mathbf{I_d}\right)\\ &+{}^t\left((\mathbf{I_d}-\nabla\mathbf{u})^{-1}-\mathbf{I_d}\right)(\mathbf{I_d}-\nabla\mathbf{u})^{-1}-\mathbf{I_d})],\\ \mathbf{L}'(\mathbf{u})=&H(\alpha)[(\mathbf{I_d}-\nabla\mathbf{u})^{-1}-\mathbf{I_d}+{}^t\left((\mathbf{I_d}-\nabla\mathbf{u})^{-1}-\mathbf{I_d}\right)\\ &+\left((\mathbf{I_d}-\nabla\mathbf{u})^{-1}-\mathbf{I_d}\right)^t(\mathbf{I_d}-\nabla\mathbf{u})^{-1}-\mathbf{I_d})],\end{aligned}\tag{5.27}$$

and we proceed to the next time step.

Solving iteratively $\boldsymbol{\tau}$

In case μ tends to infinity, an augmented Lagrangian formulation together with an Uzawa iterative scheme are employed to solve system (5.17). The possible iterative scheme would be:

$$
\begin{aligned}
&(\rho(\delta_t \mathbf{v}^k + \mathbf{v}^k \cdot \nabla \mathbf{v}^k), \mathbf{w}) - (p^k, \nabla \cdot \mathbf{w}) + (2\eta\boldsymbol{\varepsilon}(\mathbf{v}^k), \boldsymbol{\varepsilon}(\mathbf{w})) \\
&\quad + r(\mathbf{L}(\mathbf{u}^k + \mathbf{v}^\mathbf{k}\boldsymbol{\Delta}\mathbf{t}) - \frac{\mathbf{1}}{\mu}\boldsymbol{\tau}^\mathbf{k}, \boldsymbol{\varepsilon}(\mathbf{w}) +^\mathbf{t} \nabla \mathbf{u}^\mathbf{k}\nabla\mathbf{w} +^\mathbf{t} \nabla\mathbf{w}\nabla\mathbf{u}^\mathbf{k}) + (\boldsymbol{\tau}^\mathbf{k}, \boldsymbol{\varepsilon}(\mathbf{w})) \\
&\quad = (\mathbf{f}, \mathbf{w}) - (\boldsymbol{\lambda}_\mathrm{s}^{k-1}, \boldsymbol{\varepsilon}(\mathbf{w}) +^t \nabla \mathbf{u}^k\nabla\mathbf{w} +^t \nabla\mathbf{w}\nabla\mathbf{u}^k), \\
&(\nabla \cdot \mathbf{v}^\mathbf{k}, q) = 0, \\
&(\delta_t \mathbf{u}^k, \mathbf{z}) + (\mathbf{v}^k \cdot \nabla \mathbf{u}^k, \mathbf{z}) = (\mathbf{v}^k, \mathbf{z}).
\end{aligned}
$$

where r is a penalty parameter. If P_τ is the projection onto the space of $\boldsymbol{\tau}$'s, the update $\boldsymbol{\lambda}$ of can be written as:

$$\boldsymbol{\lambda}^{k+1} = \boldsymbol{\lambda}^k + rP_\tau(\mathbf{L}(\mathbf{u}^k + \mathbf{v}^\mathbf{k}\boldsymbol{\Delta}\mathbf{t}) - \frac{\mathbf{1}}{\mu}\boldsymbol{\tau}^\mathbf{k}). \tag{5.28}$$

$\mathbf{L}(\mathbf{u} + \mathbf{v}\boldsymbol{\Delta}\mathbf{t})$ is expressed using the approximation in equation(5.21) as follows:

$$\mathbf{L}(\mathbf{u}^k + \mathbf{v}^\mathbf{k}\boldsymbol{\Delta}\mathbf{t}) = \mathbf{L}(\mathbf{u}^\mathbf{k}) + \mathbf{H}(\alpha)[\boldsymbol{\Delta}\mathbf{t}\boldsymbol{\varepsilon}(\mathbf{v}^\mathbf{k}) + \frac{\mathbf{1}}{\mathbf{2}}\left(\boldsymbol{\Delta}\mathbf{t}^\mathbf{t}\nabla\mathbf{u}^\mathbf{k}\nabla\mathbf{v}^\mathbf{k} + \boldsymbol{\Delta}\mathbf{t}^\mathbf{t}\nabla\mathbf{v}^\mathbf{k}\nabla\mathbf{u}^\mathbf{k}\right)]. \tag{5.29}$$

Remarks:

- Comparing to the previous system, (5.24), the proposed formulation would be more adequate when dealing with large values of μ, in particular the rigid body case.

- As noticed, the same system of the FSI problem with rigid bodies is reached, the only difference is the additional terms containing the displacement field. As a result, the stabilization technique is mostly the same as detailed in the next section.

5.3 Stabilized Finite-Element Method (SFEM)

In this section, we describe briefly the Galerkin FE approximation and the corresponding stabilization method for the resulting discrete system of equations (5.17).
The purpose is to reach a similar system as for the SFEM of rigid body problem. For this reason, the displacement equation $\partial\mathbf{u} + \mathbf{v} \cdot \nabla\mathbf{u} = \mathbf{v}$ is solved and stabilized separately of the global system. This equation is also a simple convection equation as the level-set convection equation. As a result, both equations are stabilized in the same manner using the SUPG method. In the following, the FE approximation and the corresponding stabilization method of system (5.17)without the displacement equation are presented.

5.3.1 MultiScale approach

As presented previously for the FSI with rigid body, a Variational MultiScale (VMS) method (see [113]) is presented. Recall that the VMS method allows the use of equal order continuous interpolations for the three fields, apart from preventing from oscillations due to convection dominated flows. The basic idea is to consider that the unknowns can be split in two components, coarse and fine, corresponding to different scales or levels of resolution [67, 111, 47]. First, we solve the fine scales in an approximate manner and then we replace their effect into the large scales.

Based on a mesh $\mathcal{K}_h$ of Ω made of N_{el} elements K, the functional spaces for the velocity, the pressure and the stress are approximated by the finite dimensional spaces V_h, P_h and $\mathcal{T}_h$, respectively. Let us split the velocity, pressure and stress solution spaces as
$V_h \oplus V'$, $P_h \oplus P'$ and $\mathcal{T}_h \oplus \mathcal{T}'$, respectively. Subscript h is used here, and in the following, to denote the finite element (coarse) component, whereas the prime is used for the so called subgrid scale (fine) component of the unknowns. According to this, we have

$$\begin{aligned}\mathbf{v} &= \mathbf{v}_h + \mathbf{v}' \ \in \ V_h \oplus V',\\ p &= p_h + p' \ \in \ P_h \oplus P',\\ \boldsymbol{\tau} &= \boldsymbol{\tau}_h + \boldsymbol{\tau}' \ \in \ \mathcal{T}_h, \oplus \mathcal{T}'\end{aligned}$$

If the spaces for the test functions are split likewise, with a subscript 0 to identify them, problem (5.17) becomes:
Find $(\mathbf{v}_h + \mathbf{v}', p_h + p', \boldsymbol{\tau}_h + \boldsymbol{\tau}') \in V_h \oplus V' \times P_h \oplus P' \times \mathcal{T}_h \oplus \mathcal{T}'$ such that

$$\begin{aligned}\rho(\delta_t(\mathbf{v}_h + \mathbf{v}'), \mathbf{w}_h + \mathbf{w}') + \rho((\mathbf{v}_h + \mathbf{v}') \cdot \nabla(\mathbf{v}_h + \mathbf{v}'), \mathbf{w}_h + \mathbf{w}') - (p_h + p', \nabla\cdot(\mathbf{w}_h + \mathbf{w}'))\\ +2(\eta\boldsymbol{\varepsilon}(\mathbf{v}_h + \mathbf{v}'), \boldsymbol{\varepsilon}(\mathbf{w}_h + \mathbf{w}')) + (\boldsymbol{\tau}_h + \boldsymbol{\tau}', \boldsymbol{\varepsilon}_{\mathrm{s}}(\mathbf{w}_h + \mathbf{w}')) = \langle \mathbf{f}, \mathbf{w}_h + \mathbf{w}' \rangle, \qquad (5.30)\end{aligned}$$

$$(q_h + q', \nabla \cdot (\mathbf{v}_h + \mathbf{v}')) = 0, \qquad (5.31)$$

$$\begin{aligned}(\mathbf{L}(\mathbf{u}) - \chi_{\mathrm{s}}\Delta t[\boldsymbol{\varepsilon}(\mathbf{v}_h + \mathbf{v}') + \frac{1}{2}\left({}^t\nabla\mathbf{u}_h\nabla(\mathbf{v}_h + \mathbf{v}') + {}^t\nabla(\mathbf{v}_h + \mathbf{v}')\nabla\mathbf{u}_h\right)], \boldsymbol{\xi}_h + \boldsymbol{\xi}')\\ -(\frac{1}{2\mu}(\boldsymbol{\tau}_h + \boldsymbol{\tau})', \boldsymbol{\xi}_h + \boldsymbol{\xi}') = 0, \qquad (5.32)\end{aligned}$$

for all $(\mathbf{w}_h + \mathbf{w}', q_h + q', \boldsymbol{\xi}_h + \boldsymbol{\xi}') \in V_{h,0} \oplus V_0' \times P_{h,0} \oplus P_0' \times \mathcal{T}_{h,0} \oplus \mathcal{T}_0'$.
$\chi_{\mathrm{s}}$is the characteristic function of Ω_{s}. Even if time has been discretized, we have kept the notation for the functional spaces for simplicity.

Even though the subgrid scales (or subscales) could be approximated without further assumptions and inserted into the previous equations (see [104]), we will make use of some common approximations:

i) The subscales are not tracked in time, therefore, quasi-static subscales are considered here. However, the subscale equations remain quasi time-dependent.

ii) The convective velocity of the non-linear term may be approximated using only the large-scale component, so that $(\mathbf{v}_h + \mathbf{v}') \cdot \nabla(\mathbf{v}_h + \mathbf{v}') \approx \mathbf{v}_h \cdot \nabla(\mathbf{v}_h + \mathbf{v}')$. Moreover, this approximation can be done also if the convective term is written as $\nabla \cdot (\mathbf{v}_h + \mathbf{v}') \otimes (\mathbf{v}_h + \mathbf{v}')$, which is relevant when integrating by parts the convective term.

iii) Terms involving subscales can be integrated by parts and the subscales on the element boundaries neglected.

5.3.2 Coarse scale formulation

The equations for the coarse scales are obtained taking the subscale test functions equal to zero. Doing this and using the previous assumptions, we get

$$\rho(\delta_t \mathbf{v}\mathbf{v}_h, \mathbf{w}_h) + \rho(\mathbf{v}_h \cdot \nabla \mathbf{v}_h, \mathbf{w}_h) - (p_h + p', \nabla \cdot \mathbf{w}_h) + 2(\eta \boldsymbol{\varepsilon}(\mathbf{v}_h), \boldsymbol{\varepsilon}(\mathbf{w}_h) + (\boldsymbol{\tau}_h + \boldsymbol{\tau}', \boldsymbol{\varepsilon}_{\mathrm{s}}(\mathbf{w}_h)) + \sum_K (\mathbf{v}', -\rho \mathbf{v}_h \cdot \nabla \mathbf{w}_h - \nabla \cdot (2\eta \boldsymbol{\varepsilon}(\mathbf{w}_h)))_K = \langle \mathbf{f}, \mathbf{w}_h \rangle \tag{5.33}$$

$$(q_h, \nabla \cdot \mathbf{v}_h) - \sum_K (\mathbf{v}', \nabla q_h)_K = 0 \tag{5.34}$$

$$-(\mathbf{L}(\mathbf{u}) + \chi_{\mathrm{s}} \Delta t[\boldsymbol{\varepsilon}(\mathbf{v}_h) + \frac{1}{2}\left({}^t\nabla \mathbf{u}_h \nabla \mathbf{v}_h + {}^t\nabla \mathbf{v}_h \nabla \mathbf{u}_h\right)] + \frac{1}{\mu}\boldsymbol{\tau}_h, \boldsymbol{\xi}_h) + \sum_K (\mathbf{v}', \chi_{\mathrm{s}} \nabla \cdot \boldsymbol{\xi}_h + \Delta t \frac{1}{2}(\nabla \mathbf{u}_h \nabla \cdot \boldsymbol{\xi}_h + \nabla \cdot \boldsymbol{\xi}_h \nabla \mathbf{u}_h))_K = 0 \tag{5.35}$$

for all $(\mathbf{w}_h, q_h, \boldsymbol{\xi}_h) \in V_{h,0} \times P_{h,0} \times \mathcal{T}_{h,0}$, where $\sum_K$ stands for the summation over all the elements of the finite element partition $\mathcal{K}_h$ and $(\cdot, \cdot)_K$ denotes the L^2 product in each K. The problem for the fine scales is obtained taking $(\mathbf{w}_h, q_h, \boldsymbol{\xi}_h) = (\mathbf{0}, 0, \mathbf{0})$ in (5.30)-(5.32) and using approximations i)-iii) described above.
Introducing the FE residuals as:

$$\begin{aligned}
\mathcal{R}_v &= \mathbf{f} - \rho \delta_t \mathbf{v}_h - \rho \mathbf{v}_h \cdot \nabla \mathbf{v}_h - \nabla p_h + \chi_{\mathrm{s}} \nabla \cdot \boldsymbol{\tau}_h + \nabla \cdot (2\eta \boldsymbol{\varepsilon}(\mathbf{v}_h)), \\
\mathcal{R}_p &= -\nabla \cdot \mathbf{v}_h \\
\mathcal{R}_\tau &= (\mathbf{L}(\mathbf{u}) + \boldsymbol{\varepsilon}_{\mathrm{s}}(\mathbf{v}_h)\Delta t + \frac{1}{2}\Delta t({}^t\nabla \mathbf{u}_h \nabla \mathbf{v}_h + {}^t\nabla \mathbf{v}_h \nabla \mathbf{u}_h) - \frac{1}{\mu}\boldsymbol{\tau}_h,
\end{aligned}$$

and using the same ideas as in [101, 114], it turns out that the subscales may be approximated within each element $K \in \mathcal{K}_h$ by

$$\mathbf{v}' = \alpha_v \Pi_v'(\mathcal{R}_v), \quad p' = \alpha_p \Pi_p'(\mathcal{R}_p) \text{ and } \quad \boldsymbol{\tau}' = \alpha_\tau \Pi_\tau'(\mathcal{R}_\tau),$$

where Π_v', Π_p' and Π_τ' are the projections onto V', P' and $\mathcal{T}'$, respectively, and α_v, α_p and α_τ are the so called stabilization parameters. The most common choice is to take the former as the identity when applied to finite element residuals (see [113, 101]), and this is what we will do here, although it is also possible to take them as the orthogonal

projection to the FE space (see [114] and references there in). Referring to the stabilization parameters, we compute them within each element as

$$\alpha_v = \left[\left(\frac{c_1 \eta}{\rho h^2} \right)^2 + \left(\frac{c_2 \|\mathbf{v}_h\|_K}{h} \right)^2 \right]^{-1/2}, \tag{5.36}$$

$$\alpha_p = \left[\left(\frac{\eta}{\rho} \right)^2 + \left(\frac{c_2 \|\mathbf{v}_h\|_K h}{c_1} \right)^2 \right]^{1/2}, \tag{5.37}$$

$$\alpha_\tau = c_3 \frac{h}{L} 2\eta_s \Delta t, \tag{5.38}$$

where h is the element size, L a characteristic length of the computational domain, $\|\mathbf{v}\|_K$ a characteristic norm of $\mathbf{v}_h$ (with the same units as $\mathbf{v}_h$) in element K and c_1, c_2 and c_3 are algorithmic constants. We take them as $c_1 = 4$, $c_2 = 2$ and $c_3 = 1$ for linear elements.

Remarks:

- Very often, the time step size of the temporal discretization is included in the expression of α_v. This improves the convergence behavior of the algorithm to deal with the nonlinearity of the problem, but has several conceptual drawbacks, as explained in [115, 116]. In order to make α_v more uniform over the computational domain and, as a consequence, improve the behavior of the scheme, we may take:

  $$\alpha_v = \left[\frac{1}{\alpha_0^2} + \left(\frac{c_1 \eta}{\rho h^2} \right)^2 + \left(\frac{c_2 \|\mathbf{v}_h\|_K}{h} \right)^2 \right]^{-1/2}$$

  where α_0 is a reference value of α_v given by (5.36) computed over the whole mesh (for example the minimum over all the elements). This value in fact should be related to the time step size of the time discretization, Δt.

- The factor h/L in (5.38) improves convergence of stresses when equal interpolation is used for all variables [101, 102]. However, it is possible to take it out (that is to say, to take $L = h$) and get optimal convergence for velocity and pressure [114].

- For the linear elements used in the numerical examples, terms of the form $\nabla \cdot (2\eta \boldsymbol{\varepsilon}(\mathbf{w}_h))$ involving second derivatives within each element can be neglected.

- Rotational terms and terms containing the displacement field that are multiplied by a stabilization parameters are neglected.

- For the time being, the small scale of the stress is neglected in the third equation.

5.3.3 Stablized formulation

Inserting the expression for the subscales obtained in (5.33)-(5.35), we finally obtain the stabilized finite element problem we were seeking. It consists on:
Finding $(\mathbf{v}_h, p_h, \boldsymbol{\tau}_h) \in V_h \times P_h \times \mathcal{T}_h$ such that:

$$\begin{aligned}
&\rho(\delta_t \mathbf{v}_h, \mathbf{w}_h) + \rho(\mathbf{v}_h \cdot \nabla \mathbf{v}_h, \mathbf{w}_h) - (p_h, \nabla \cdot \mathbf{w}_h) + 2(\eta \boldsymbol{\varepsilon}(\mathbf{v}_h), \boldsymbol{\varepsilon}(\mathbf{w}_h)) + (\boldsymbol{\tau}_h, \boldsymbol{\varepsilon}_{\mathrm{s}}(\mathbf{w}_h)) \\
&\quad + \sum_K \alpha_v(\rho \delta_t \mathbf{v}_h + \rho \mathbf{v}_h \cdot \nabla \mathbf{v}_h + \nabla p_h - \chi_{\mathrm{s}} \nabla \cdot \boldsymbol{\tau}_h - \nabla \cdot (2\eta \boldsymbol{\varepsilon}(\mathbf{v}_h)), \rho \mathbf{v}_h \cdot \nabla \mathbf{w}_h + \nabla \cdot (2\eta \boldsymbol{\varepsilon}(\mathbf{w}_h)))_K \\
&\quad + \sum_K \alpha_p(\nabla \cdot \mathbf{v}_h, \nabla \cdot \mathbf{w}_h) + \sum_K \alpha_\tau(\boldsymbol{\varepsilon}_{\mathrm{s}}(\mathbf{v}_h), \boldsymbol{\varepsilon}_{\mathrm{s}}(\mathbf{w}_h)) \\
&\quad = \langle \mathbf{f}, \mathbf{w}_h \rangle + \sum_K \alpha_v(\mathbf{f}, \rho \mathbf{v}_h \cdot \nabla \mathbf{w}_h + 2\eta \nabla \cdot \boldsymbol{\varepsilon}(\mathbf{w}_h))_K \qquad (5.39) \\
&(q_h, \nabla \cdot \mathbf{v}_h) + \sum_K \alpha_v(\rho \delta_t \mathbf{v}_h + \rho \mathbf{v}_h \cdot \nabla \mathbf{v}_h + \nabla p_h - \chi_{\mathrm{s}} \nabla \cdot \boldsymbol{\tau}_h - \nabla \cdot (2\eta \boldsymbol{\varepsilon}(\mathbf{v}_h)), \nabla q_h)_K \\
&\quad = \sum_K \alpha_v(\mathbf{f}, \nabla q_h)_K \qquad (5.40) \\
&- (\mathbf{L}(\mathbf{u}) + \chi_{\mathrm{s}} \Delta t[\boldsymbol{\varepsilon}(\mathbf{v}_h) + \frac{1}{2}({}^t\nabla \mathbf{u}_h \nabla \mathbf{v}_h + {}^t \nabla \mathbf{v}_h \nabla \mathbf{u}_h)] - \frac{1}{\mu} \boldsymbol{\tau}_h, \boldsymbol{\xi}_h) \\
&\quad + \sum_K \alpha_v(\rho \delta_t \mathbf{v}_h + \rho \mathbf{v}_h \cdot \nabla \mathbf{v}_h + \nabla p_h - \chi_{\mathrm{s}} \nabla \cdot \boldsymbol{\tau}_h - \nabla \cdot (2\eta \boldsymbol{\varepsilon}(\mathbf{v}_h)), -\chi_{\mathrm{s}} \nabla \cdot \boldsymbol{\xi}_h)_K \\
&\quad = \sum_K \alpha_v(\mathbf{f}, -\chi_{\mathrm{s}} \nabla \cdot \boldsymbol{\xi}_h)_K \qquad (5.41)
\end{aligned}$$

for all $(\mathbf{w}_h, q_h, \boldsymbol{\xi}_h) \in V_{h,0} \times P_{h,0} \times \mathcal{T}_{h,0}$.
We have assumed $\mathbf{f} \in L^2(K)^n$ for simplicity. By comparing this final system to the one obtained for FSI simulation with a rigid body, it is very obvious that only few terms vary but the main idea and development remain the same. As our intention, the general solver using a "similar" monolithic formulation for solving FSI with a rigid or elastic body is obtained.

5.4 Numerical Results

In order to validate the proposed approach, several problems are presented in this section. Recall that interface tracking and the solid deformation are achieved by the level-set convection equation as detailed in Section 2.5. As mentioned previously, all the formulations were implemented in CimLib. The numerical performance of the method involving incompressible elastic bodies in a fluid flow is tested. The results obtained with the implemented code are compared with those obtained either by standard solution or by other approaches.

5.4.1 Ealstic flow cavity

We consider first a stationary example, the lid-driven cavity with an elastic bottom wall. The cavity domain is $[0, 2] \times [0, 2]$ square, occupied with a height of 0.5 by a Neo-Hookean wall whereas the upper part is filled with a fluid. The schematic representation of the problem is depicted in figure 5.1. The fluid viscosity is $\eta_{\mathrm{f}} = 0.2$, and the solid constant is $\mu = 2$, the density of both fluid and solid is $\rho_{\mathrm{f}} = \rho_{\mathrm{s}} = 1$. We prescribed a non-slip boundary conditions on all the walls except on the top lid where we impose $\mathbf{v_x}$ using the following expression:

$$\mathbf{v_x} = 0.5 \begin{cases} 4\mathbf{x} & \mathbf{x} \in [0; 0.25] \\ 1 & \mathbf{x} \in [0.25; 1.25] \\ 4(2 - \mathbf{x}) & \mathbf{x} \in [1.75; 2] \end{cases} \tag{5.42}$$

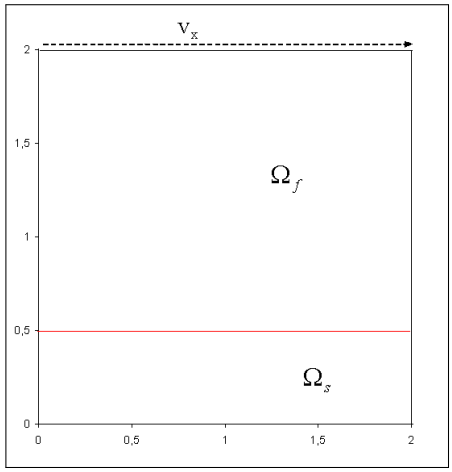


Figure 5.1: Schematic representation of the elastic flow cavity

The system reaches a steady state when the kinetic energy of the structure is below 10^{-8}. The velocity profile and the comparison of the final and initial position of the interface are shown in figure 5.2. The obtained result is well compared to the solution reported in [131, 132].

Another similar test case is compared with Zhao et al. [143] result. The domain is a square, the lower half is solid and the upper half is a fluid. A periodic velocity, $\mathbf{v}_{\mathrm{y}}$, is imposed at the top of the domain:

$$\mathbf{v}_{\mathrm{y}} = -(\mathbf{1cos(2\pi t)sin(2\pi x)}) \text{ and } \mathbf{v}_{\mathrm{x}} = \mathbf{0}$$

Figure 5.3(a) shows the schematic configuration of the test case as presented in reference

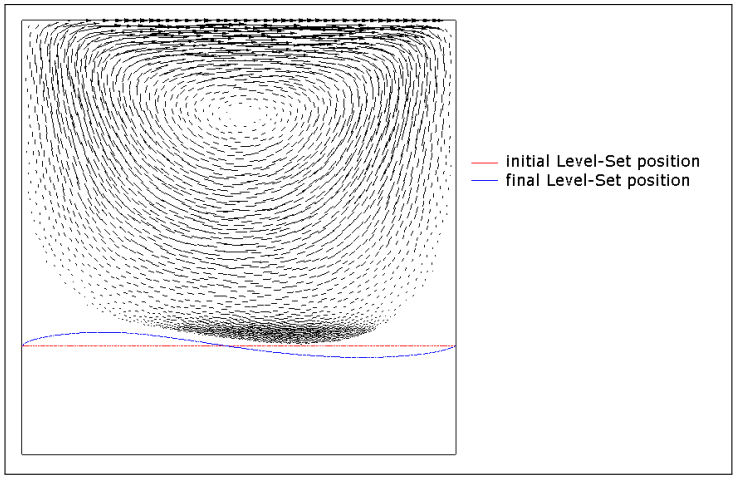


Figure 5.2: Velocity profile and the initial and final position of the interface

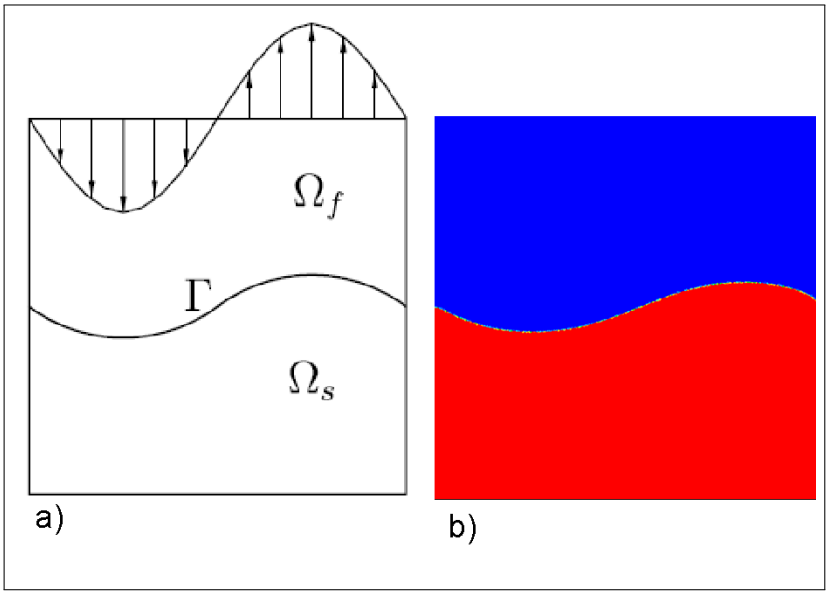


Figure 5.3: Comparaion of the deformation of an elastic wall driven by flow at time $t = 1s$ with [143]. a) schematic configuration. b) η distribution in the whole domain.

[143]. The fluid viscosity is $\eta_f = 0.2$, and the solid has $\mu = 2$. Close agreements are found for the deformed elastic wall at time t=1s, as depicted in Figure 5.3. The solid deforms due to the imposed fluid flow and the position of the FSI interface corresponds well with the one expected.

5.4.2 Oscillating disk

In this example, we study a $2D$ oscillating disk inside a cavity. The disk is placed at the center of a $1m^2$ square cavity. A periodic boundary condition and an initial velocity are applied for both the fluid and the structure using the stream function:

$$\phi = \sin(k_x x)\sin(k_y y),$$

where $\phi_0 = 0.05m^2s^{-1}$ and $k_x = k_y = 2\pi m^{-1}$.
A neo-Hookean constitutive model is considered for the structure with an elastic constant equal to 1. The structure and the fluid densities are set to $\rho = 1kgm^{-2}$ and the dynamic viscosity of the fluid is set to $\eta_{\text{f}} = 0.001kgs{-}1$. We performed the simulation for a period of $1s$. Figures 5.4 and 5.5 present snapshots of the simulation using the proposed approach, taken at various time instances.

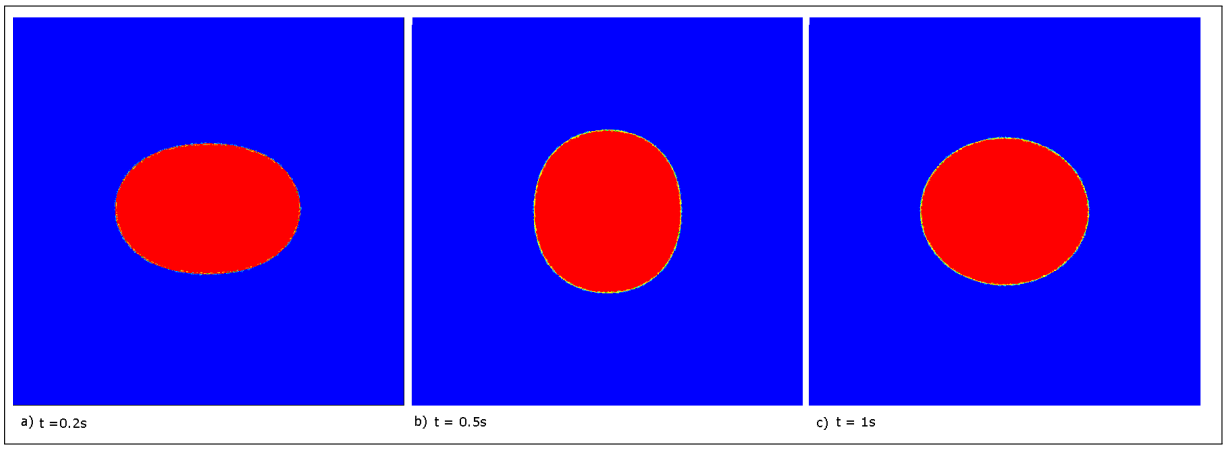


Figure 5.4: The evolution of the oscillating disk in time

Solutions of this test case obtained in [124] showing the velocity profile and the structure deformation agree very well to the results in figure 5.5. Moreover, the kinetic energy of the whole system is computed as:

$$E_k = \frac{1}{2}\int_{\Omega} |\mathbf{u}(\mathbf{x})|^2 d\mathbf{x}$$

The kinetic energy over time is plotted in figure 5.6, showing a good agreement with the results reported in [143, 124].

5.4.3 Elastic plate in an imposed flow

In this example, the grid convergence study and error analysis are performed to assess the accuracy of the proposed formulation for a flexible plate in a $2D$ channel, as reported in [144]. The channel has length $L = 0.2m$ and a height $H = 0.02m$. The flexible plate

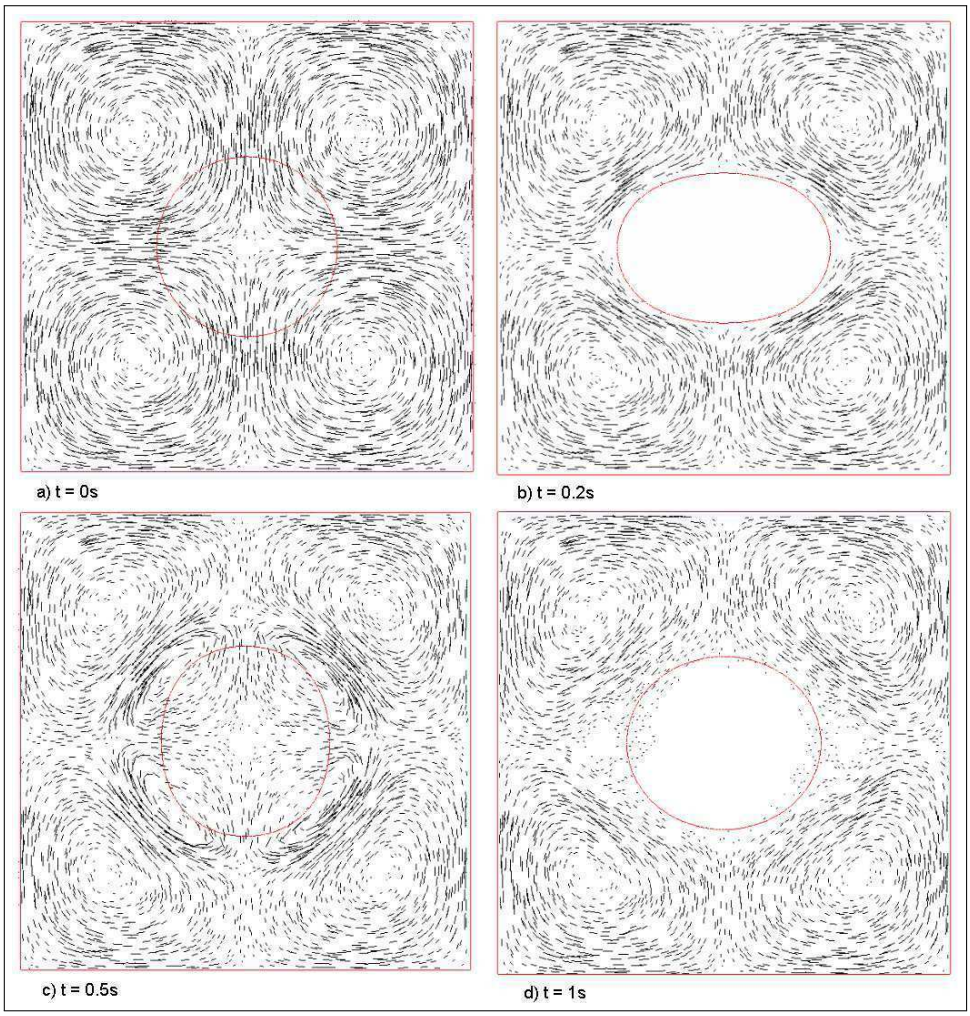


Figure 5.5: Velocities in the oscillating disk at different time instant

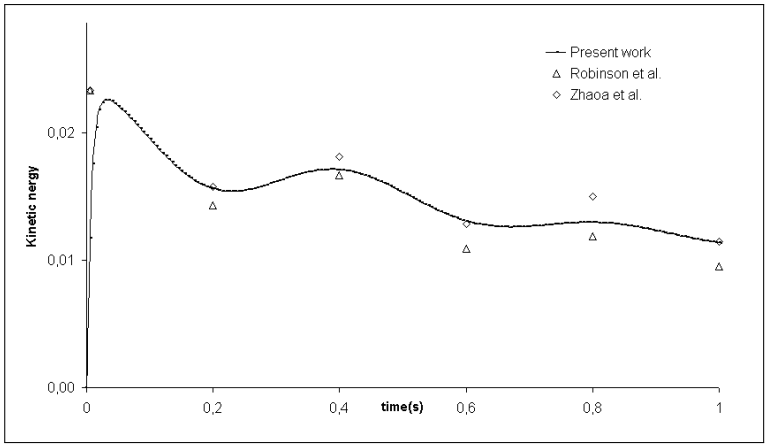


Figure 5.6: Comparisons of the kinetic energy evolution

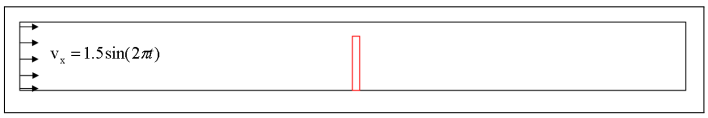


Figure 5.7: Schematic represetation of a flexible plate in an imposed flow

is situated at the center of the channel, the length and height of the plate are $0.002m$ and $0.016m$ respectively. The model is depicted in figure 5.7. A sinusoidal velocity $\mathbf{v_x} = 0.015sin(2\pi t)$ is imposed at the inlet with a period of $1s$. The fluid's density and viscosity are $1000kg./m^3$ and $10^{-3}Pa.s$ respectively. The structure is considered as an incompressible Neo-Hookean elastic material, it's density and the Young's modulus are $1000kg./m^3$ and $E = 5000Pa$ respectively. As in [144] and since there is no analytical solution to this problem, four unstructured meshes, with different mesh sizes, are used. The solution obtained using the finest mesh is considered as the reference solution. The four unstructured meshes used are named Mesh1, Mesh2, Mesh3 and Mesh4 with mesh sizes 0.002, 0.001, 0.0005 and 0.00025 respectively (see figure A.17). Figure A.17 shows that the geometric representation of the elastic plate in Mesh1 it's a very coarse mesh, revealing the importance of the mesh adaptation. Moreover, even if the elastic plate is well represented at the beginning due to mesh refinement, this representation may be lost during simulation, as the case of Mesh2. This is clearly shown in figure 5.9, where the iso-zero of the different level-set functions, obtained from the corresponding meshes, are represented at $t = 0.25s$. As expected, when the mesh is refined, the geometric representation becomes more precise and the position of the structural interface tends to the one computed on the reference mesh. The errors are calculated for the displacement $d\mathbf{x}$ of the whole domain. The L_2 error for the three meshes with respect to the finest one are depicted in figure 5.10. The convergence rate of the L_2 errors are compared to the slope 2, showing a potential in the proposed approach.

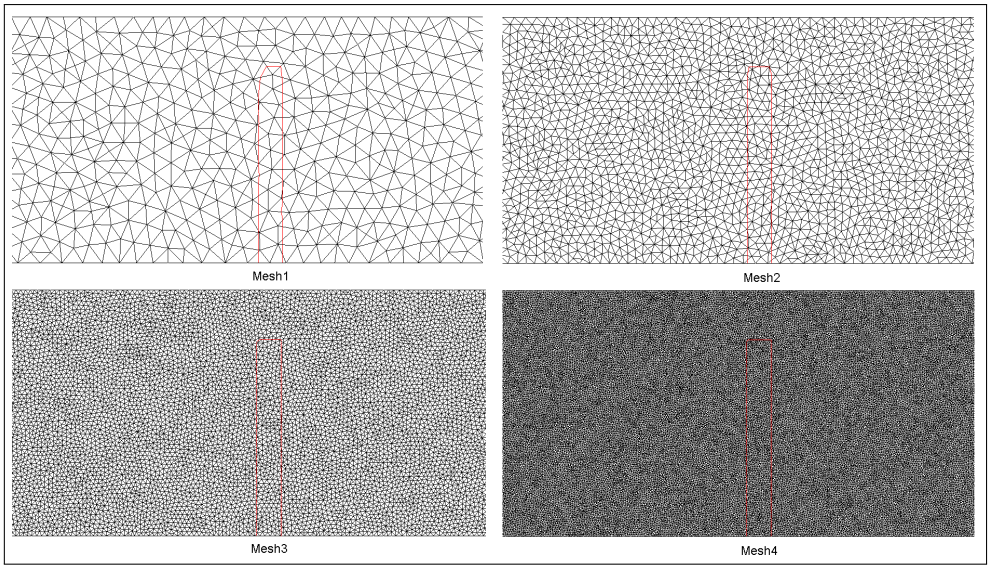


Figure 5.8: Four finer meshes used for grid convergence study and error analysis

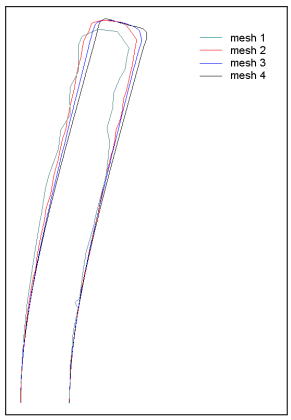


Figure 5.9: The iso-zero of the level-set function at $t = 0.25s$ obtained from the different meshes

5.5 Conclusion

The chapter presented the second mechanical application which is FSI with an elastic body. The governing equations and the corresponding FE approximation along with the stabilization technique have been detailed to simulate FSI problem with an incompressible elastic body. A similar system of the one obtained for FSI problem with a rigid body is reached showing the capability of the method to deal with a rigid or elastic body. Analogously, the system was solved by a monolithic formulation in an Eulerian framework.

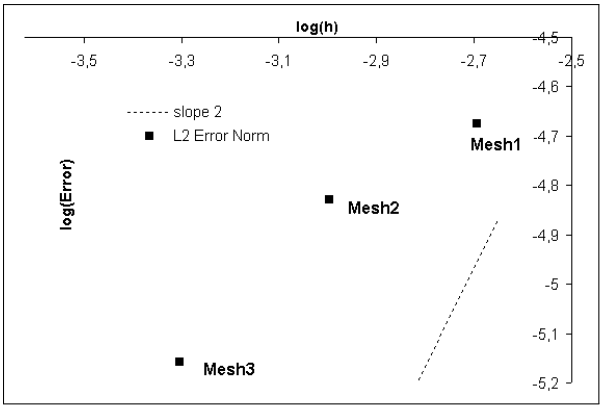


Figure 5.10: The L_2 errors for the three meshes with respect to the finest mesh

Again, the elastic body was examined as an extra-stress tensor in the Navier-Stokes equations. The stabilized three-field velocity-pressure-stress system was described reaching a resembling one. The results yielded the validation and accuracy of the methodology. Results were compared with references results in literature and other approaches.

5.6 Resumé français

Nous présentons la deuxième application mécanique de cette thèse. L'équation qui régit le problème IFS avec un corps élastique incompressible ainsi que l'approximation par éléments finis et la technique de stabilisation sont détaillés. Le système final correspond bien a celui obtenu lors de la simulation d'un problème IFS avec un corps rigide. Encore une fois, le système a été résolu par une formulation monolithique dans un cadre eulérien, le corps rigide étant pris en compte par lŠajout dŠun tenseur de contrainte dans les équations de Navier-Stokes. La formulation stabilisée à trois champs vitesse-pression-contrainte est décrite et il est bien semblable à celle obtenue pour le problème de FSI avec un corps rigide. En revanche, la capacité de la méthode pour faire face à un corps rigide ou élastique est atteinte. La validation et la précision de la méthode sont réalisées à partir des différents cas simulés. Résultats sont comparés avec la référence et dŠautres approches.

Chapter 6

General conclusion and perspectives

Fluid Structure Interaction (FSI) is nowadays a great interest in biomechanics, engineering, aeronautics and aerodynamic. The simulation of these problems are still of main importance. These two phrases express well the motivations of this thesis which is concentrated on two main objectives:
1- The development of a general solver for FSI problems in a monolithic context and an Eulerian framework.
2- The possibility to deal with rigid and elastic structure simultaneously.

The components of the developed FSI solver, which is the consideration of a single grid for both the solid and fluid where only one set of equations is solved, is achieved using the multidisciplinary expertise of CIMLib. All the numerical tools of the CIMlib library, used in this work, are detailed in chapter 2. Notably the Immersed Volume Method (IVM) which is the combination of the level-set method, mixing laws and mesh adaptation. The level-set approach is used to describe the position and the geometry of a given structure. The mixing laws enable the mixture of different physical properties of the fluid and the structure to reach a single domain with variable material properties. Moreover, the anisotropic mesh adaptation gives a better description of the fluid-solid interface and allows taking into account the possible discontinuities of the material properties. We present several mesh adaptation techniques: an anisotropic local remeshing method and an *a posteriori* error estimation method. The former refines the mesh at the interface by generating a metric field using the gradient of the level set function; the latter has an additional advantage of generating the metric filed as a minimum of an error indicator function for a given number of elements. The last method presented, is a new approach of the *a posteriori* error estimation. It is based on the length distribution tensor approach and the associated edge based error analysis. It combines the simultaneous adaptivity to the level-set scalar field and to any physical field. The last tool used is the interface tracking. When dealing with deformable and/or moving elastic structure, the new position of the fluid-structure interface is computed by solving the level-set convection equation.

The formulation of a single set of equation for FSI simulation with a rigid body is detailed in chapter 3. The basic idea is to extend the Navier-Stokes equations, used for describing a Newtonian flow, by an extra-stress tensor to take into account the presence of the solid in the fluid domain. In fact, the solid is treated under the constraints of imposing the nullity of the deformations. This restriction is prescribed through an appropriate Lagrange multiplier. Once the global system of equation for the FSI problem is set, using the developed technique along with the IVM, the next step is to develop the corresponding finite element approximation and the stabilized formulation. The stabilization technique is based on the variational multiscale method, where the velocity-pressure-stress fields are decomposed into a coarse and fine scales. The extension of the stabilizing technique is a necessity in order to reach a stable formulation free from oscillation. The last step of the method is to present the numerical scheme that reduces the system in a interesting way to facilitate the resolution of the system. This can be accomplished by using an augmented Lagrangian formulation coupled with an Uzawa scheme. When dealing with a rigid body,

the new position of the fluid-structure interface can be simply calculated using the rigid body motion. As a result, the resolution of the level-set convection equation is not needed.

The first development presented, used an equal order interpolation of the velocity and pressure fields, and a lower one for the extra-stress tensor. This method is applied at the beginning for simple $2D$ examples to prove the capability of the method to handle the presence of the structure. Then, it is tested for several spherical particles in an imposed flow in a $2D$ and $3D$ case. Furthermore, the falling disk benchmark is well stated in literature. Simulating this problem is essential to prove the reliability of our method. Comparison with the existing results in literature shows close agreement. At the same time, these results have provoked the detailed development of this method in order to achieve a better accuracy. This was the objective of the next part of this chapter. The last example presented is the Tetris benchmark where several rigid bodies with different densities are falling in a channel. In this example, the importance of the mesh adaptation technique is well shown, otherwise respecting the geometries cannot be achieved. This benchmark shows as well that the problem of overlapping solid domains is overcome naturally and there is no need to enforce it.

The amelioration of the method is presented in the next section. The FSI full Eulerian system is explained in a more detailed manner. The rigid body restriction in a stationary Stokes flow is interpreted, the chosen form of the Lagrangian multiplier and the iterative scheme is clarified. Afterwards, the Navier-Stokes equations with a rigid body are treated along with the corresponding iterative scheme and the stabilized finite element approximation. In this form, an equal order interpolation of the three fields can be performed. Then, the matching matrix formulation is detailed. We start by examining the new method for a simple $2D$ and $3D$ case where rigid bodies are immersed in an imposed flow to check the robustness of the method. $2D$ cases are compared with existing ones in the literature: the flow around a fixed disk and the oscillating disk in a channel and square domain respectively. The Drag coefficient is examined for the 2 cases displaying good agreement with the literature. The computational way of the drag and lift coefficients in an Eulerian context is presented at the beginning of this section. And the final simulation is the unsteady flow past an immersed helicopter in $3D$. This simulation illustrates the capability of the method to handle complex geometries at a high Reynolds's number. The formulation considered, in all these simulations, is combined with anisotropic mesh adaptation to respect the geometry of the structure while maintaining a reasonable and small number of elements.

The final part of this chapter highlights the combination of the formulation along with a new mesh adaptation technique based on an *a posteriori* edge based and spatial error estimator. The falling disk and the Tetris benchmarks are revisited revealing more accurate results. We observe a closer agreement with existing results in the literature for the former benchmark, and a better geometric representation for the latter. The mesh sensitivity and the convergence test are performed in this section for a falling cylinder for different fluid viscosities. Two well cited examples in literature are also carried out: the Naca ($2D$) and the Ahmad body ($3D$) simulations in an incompressible flow. The results presented show that this method can be used in a wide range of application for FSI with

multi-rigid bodies problems.

The second mechanical application performed is the FSI simulation with incompressible elastic bodies. Solid deformation is usually prescribed in a Lagrangian context. For this cause, the Lagrangian and Eulerian description are reviewed in chapter 4. In the first part of this chapter, the elementary deformation is presented in the usual reference, the Lagrangian one. Furthermore, the different deformation tensors are defined. Afterwards the two main equations used for modelling the structure are presented: mass conservation and conservation of momentum. Then, in the second part, the Eulerian description is observed. The deformation is presented, then the description of the different deformation tensors are transformed in the Eulerian framework. Finally, the mass conservation and the conservation of momentum are written in the Eulerian framework. The momentum equations of the fluid and structure are developed separately. For the fluid part, we consider an incompressible Newtonian flow, hence the Navier-Stokes equations are reached at the end. While for the structure, the corresponding momentum equation, written previously in a Lagrangian context, is formulated. And the relation of these two descriptions is well highlighted using the deformation gradient tensor.

Once the relation between Lagrangian and Eulerian descriptions is clarified, FSI simulation with an elastic structure can be treated (chapter 5). The governing equations of the fluid and structure are written at the beginning separately, then some small modification to the structural system should be made in order to reach a single set for both domains. A similar system than the one describing the fluid/rigid body is reached. The differences are in the addition the displacement fields and the modification of the rigidity constraint. The equation that modelled the rigidity constraint is changed in order to prescribe the behaviour law of the elastic body. In this work, two behaviour laws are treated and the elastic body is assumed to be incompressible. After establishing the single set of equation, some developments are applied for reducing the system. Two different iterative schemes are introduced. The common in both schemes is that the velocity and pressure fields are solved simultaneously then, the displacement and the stress tensor are treated. At the end, a stabilized finite element formulation is developed reaching also a similar system as in the rigid body case. After the full explanation of the method, we start by applying it to several $2D$ cases. At the beginning, a simple test case is presented to show the capability of the method to model the elastic behaviour along with the fluid flow: the elastic flow cavity. A comparison with the existing literature results shows good agreement. A more interesting example is the oscillating disk, the evolution of kinetic energy shows the reliability of the method in comparison with existing works. And the final example presented is the grid convergence study and error analysis for an elastic plate in an imposed flow. Results show a good order of accuracy of the proposed FSI formulation.

This work focuses on a new concept for computational methods to solve the FSI problem. When solving FSI with a rigid body, the proposed approach was applied and validated for several $2D$ and $3D$ cases, arranging from simple to complex geometry and low to high Reynolds number. In this sense, the extension to FSI with elastic body was consid-

ered. As exposed, it tends to be a difficult task. Additionally, not all the aspects are in the scope of this work. Hence, a number of other considerations have to be taken into account to cover other FSI problems. The first perspective of this work is a deeper investigation of the unified elastic formulation. Moreover, given the fact that the presented FSI solver can only model the interaction between an incompressible fluid and structure, the second perspective will be naturally the extension towards a compressible solver which can be interesting to model various types of structures and compressible fluid flows. Furthermore the formulation in this work deals only with rigid or elastic structures. Its extension for modelling viscoelastic, viscoplastic and elasto-viscoplastic materials is of main importance. Hence, FSI simulations can cover a wider range of application. These developments will also extend the stabilization technique. Additionally, developments should be made on the resolution method, iterative scheme and algebraic system. Different possibilities to improve the Uzawa iteration or to combine the three fields, velocity-pressure-stress tensor, in one system should be analyzed. Finally, the last perspective is related to applications, in particular to aerodynamic applications. In this domain, the computation of the drag and lift forces is of high importance to validate the model. Different routes should be examined to compute precisely these coefficients. We propose in this work a simple one, however, it can be improved by modifying the Navier-Stokes equations in means of introducing a reaction term [145], the so-called penalization method. In fact, the latter will quantify the needed forces to obtain the rigid body behaviour [146].

Appendices

Appendix A

Simulation of FSI in Nuclear Reactor

A.1 Introduction

In Power Water Reactors plants, the seismic design of a reactor cores requires the structural analysis of fuel rod assemblies undergoing transient excitations. The fuel assemblies are classically described by vibrating cylinder beams subject to a given flow. They are used to exchange heat between the primary circuit of the water which is from the heart of reactor and that of the secondary circuit intended to be made into steam to power the turbine.

The problem of flow around fixed and oscillating cylinders has received much attention in the past few decades: nuclear engineering, ocean engineering and wind engineering. Indeed, the interaction of the cylinder motion and the incident flow, gives rise to a number of interesting phenomena, such as vortex shedding patterns and bifurcations. Consequently, the periodic flow force, generated by the periodic vortex shedding, affects enormously the cylinder vibration, at the same time, the oscillating cylinder will also affect (i) the fluid flow around the cylinder, (ii) the fluid force and (iii) the vortex pattern, thus, a complex fluid-structure interaction forms. This kind of vibration may cause damages and even failures in the event of resonance, when the vortex shedding frequency of the fluid flow and the natural frequency of the structure coincide. Summing up, both the flow and the vortex-induced vibration form nowadays a very important research topic for CEA and EDF, partners of this project, needed for the safety and the design of a variety of reactors structures.

In the literature, numerous studies and computational methods used to simulate the problems of fluid flow past bluff bodies can be found. We can mention the "boundary element method" (BEM), the "finite difference method" (FDM), the "finite volume method" (FVM), the "spectral method" and the "finite element method" (FEM) are all employed to study the flow field depending upon the computational resources available. Chan et al. [147] have developed a numerical model based on the surface vortices method, which makes use of discrete vortex blobs to simulate the flow and to examine the flow-induced vibration problem arising from an infinitely long elastic circular cylinder in a uniform

cross flow. Mittal and Kumar [148] have used the stabilized finite element formulation to study the flow-induced oscillations of a pair of equal sized cylinders in tandem and staggered arrangement placed in a uniform incompressible flow. Huerta and Liu [149] have used the Arbitrary Lagrangian Eulerian (ALE) finite element formulation to include the flow separation and non-linear phenomena of steady streaming for arbitrarily shaped bodies undergoing large periodic motion in a viscous fluid. Anagnostopoulos and Bearman [150] conducted a vortex-induced vibration experiment with one degree of freedom over a $[90; 150]$ range of Reynolds number. Khalak [151] conducted a similar experiment. The results show that for large mass ratios, the actual cylinder oscillation frequency at resonance will be close to the vortex shedding frequency for the fixed cylinder, and also close to the vortex shedding frequency. But, that is not suitable for small mass ratios. Khalak and Williamson [151] examined a hydroelastic cylinder with a very low mass damping in the lateral-flow. It showed that the response of the cylinder has two resonance branches, a lower branch and an upper branch. Brika and Laneville [152] were the first to examine the 2P vortex pattern using a vibrating cable in a wind tunnel. They found a clear correspondence of the 2S pattern with the initial branch of response, and the 2P pattern with the lower branch.

As shown in this previous literature survey, this complicated Fluid-Structure Interaction (FSI) phenomenon has become the typical test case for numerical techniques. In particular, different methods were used to solve the Navier-Stokes equations, involving Reynolds Averaged Navier-Stokes method [153], Direct Numerical Simulations [154], Large Eddy Simulations [155], Finite Volume Method [156], Discrete Vortex Method [157], etc. Indeed, the solution of the time dependent Navier-Stokes equations is crucial to determine the unsteady fluid forces that simulates all the mechanisms that may be present based on the form of equations and method of solution selected.

On the other hand, the coupling between the fluid flow and the structure is still another matter. Most of the commercial software packages solve such interactions using an Arbitrary Lagrangian Eulerian (ALE) formulation [11, 12, 13]. A higher popularity has been gained lately by partitioned approaches. These approaches allow the use of fluid and solid solvers for each of the two phases. Although this has proven to be an accurate and efficient approach, it presents an inherent instability depending on the ratio of the densities and the complex geometry of the domain [40]. Alternatively, monolithic approaches consists of considering the whole domain as a single one, meshed by a single grid, and solved with an Eulerian framework. Continuity at the interface is then obtained naturally and there is no need to enforce it. The monolithic approaches impose the use of an appropriate constitutive equation describing both the fluid and the solid domain. The interface representation between the two different domains can be completed by the level-set method. Other methods such as the Immersed Boundary (IB) methods [27] or the fictitious domain [27, 28] treat the coupling between the domains by applying constraints across the rigid body using an Augmented Lagrange multiplier solved by an iterative Uzawa algorithm.

A.2 Context

In this work, we retain the advantages of the monolithic approach implemented in CimLib to study numerically the flow past fixed and oscillating cylinders. The motivation behind pursuing such general approach comes from the desire to:
(i) easily deal with a large diversity of shapes and dimensions without mesh reconstructions: the diameter, the number and the positions of the cylinders, the pitch ratio and the distance between the cylinders
(ii) easily use and affect different physical properties for the surrounding fluid (air, water...) and for the immersed structures: flexible or rigid
(iii) easily handle the vertical cylinder motion using dynamic mesh adaptation.

By computing the signed distance function (level-set) of a given geometry to each node of the mesh we can easily identify the cylinder part from the surrounding fluid as the zero level of this function. Consequently, different cylinders (i.e. rigid, flexible) are immersed in a larger domain of different material properties (i.e. water channel). In general, the latter intersects the element arbitrarily and consequently the accuracy of the finite element approach can be compromised. In order to circumvent this issue, the level-set solution is coupled with advanced methods in anisotropic mesh adaptation. The algorithm allows the creation of extremely stretched elements along the interface, which is an important requirement for FSI problems having internal/boundary layers [111, 67, 47]. Details on the used algorithm are given in the following sections.

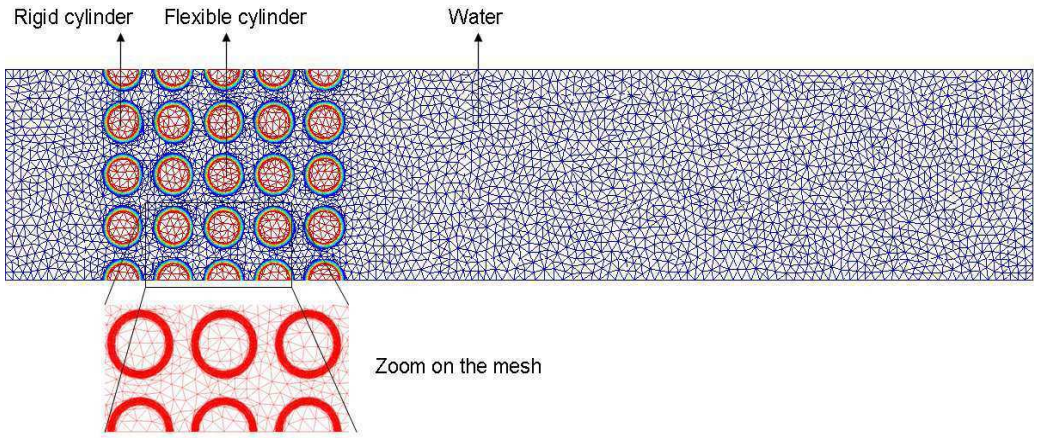


Figure A.1: The water channel and the immersed cylinders.

To illustrate the proposed approach, we show in Figure A.1 a simple rectangular mesh were:
(i) we have computed analytically the distance function for 25 cylinders located and arranged using a given pitch ratio (separating distance/diameter),
(ii) we have applied the anisotropic mesh adaptation using the variation of the gradients of the distance function,
(iii) we have assigned the physical properties (water, rigid, flexible).

Summing up, if we need for instance to add more cylinders, or to change the locations of the cylinders, or to adjust the pitch ratio, it can be easily handled using the proposed approach rather than concentrating the efforts on the mesh reconstructions (see example in figure A.2).



Figure A.2: Comparison of a constructed mesh around the cylinder and the monolithic approach

The last ingredient focuses more on the use of a finite element solver: on modelling the interaction between the fluid (laminar or turbulent) and the structure in question. The presence of the structure will be taken into account by means of an extra-stress tensor in the Navier-Stokes equations [111]. In particular, the rigid immersed body is treated using the Navier-Stokes solver under constraints of imposing its nullity of the deformations by means of a Lagrange multiplier. The flexible cylinder will also be considered as a rigid body but having a vertical cylinder motion model by an additional mass-spring system [156]. To do that, we will refer to the use of the extended solver based on the Variational MultiScale finite element method developed in CimLib [111, 122] that deals with both fluid and solid using the appropriate constitutive model.

A.3 Objectives

The objective of this paper is then to show the potential of the monolithic approach in CimLib for the numerical simulation of both fixed and oscillating cylinder in a cross-flow water channel. This initial part of the paper requires first the comprehension of the physics of the problem, secondly a deep survey in the literature about this subject, then, the understanding of the monolithic approach from both theoretical and numerical level and finally apply all the acquired information to simulate several test cases. Consequently, the potential of the proposed approach can be demonstrated through the validations and comparisons with the solution issued out of the literature (actual report), and with the EDF code (Code Saturn) having also some experimental results made on a small prototype and provided by the partners of the project (see figure A.3). As shown in this figure, it consists of a flexible tube surrounded by 14 rigid tubes, which represent a arrangement of three columns and five rows, with half-tubes on the sides. The test section is rectangular and measures 70 mm wide and 100 mm deep, which corresponds to the length of the tube

under flow. The pitch ratio is $P/D = 1.44$ with a tube diameter of $D = 12.15\ mm$. The flexible tube frequency without fluid is: $fs = 14.39$ and the damping ratio: $\xi_s = 0.25\%$



Figure A.3: Representation of the maquette Amvoi

To do so, three cases needed to achieve this goal are identified: fixed cylinder, forced oscillations cylinder, and free oscillations cylinder referred as Vortex-Induced Vibrations (VIV). Therefore, we propose to study in this paper all three cases using a one cylinder approach. For the validation, we compute and analyse different aerodynamic coefficients. Comparisons with the literature [156, 158, 159, 160, 161] are presented and discussed.

This paper is organized as follow. The Immersed Volume Method is introduced in section 4. Section 5 is dedicated to present the governing equations. Then, in section 6, all the numerical simulations are presented. Finally, Section 7 is dedicated to conclusions and future work.

A.4 Immersed Volume Method

The immersed volume method has shown to be an effective geometric representation tool [47]. It is used to immerse and to represent different complex geometries using a unique mesh. First we compute the level-set function of a given geometry to each node of the mesh, then we refine anisotropically the mesh at the interface using the gradient of the distance function and finally we mix and attribute the physical properties of each domain using appropriate laws. In this section, we revisit briefly these steps.

A.4.1 Level-set approach

A signed distance function of an interface Γ_i is used to localize the interface of the immersed cylinder Ω_i and initialize the desirable properties on both sides of this latter. At any point $\mathbf{x}$ of the computational domain Ω, the level-set function α_i corresponds to

the signed distance from Γ_i. In turn, the interface Γ_i is then given by the iso-zero of the function α_i :

$$\begin{cases} \alpha_i(\mathbf{x}) = \pm d(\mathbf{x}, \Gamma_i), \mathbf{x} \in \Omega, \\ \Gamma_i = \{\mathbf{x}, \alpha_i(\mathbf{x}) = 0\} \end{cases} \tag{A.1}$$

In this paper, a sign convention is used: $\alpha_i \geq 0$ inside the solid domain defined by the interface Γ_i and $\alpha_i \leq 0$ outside this domain. Further details about the algorithm used to compute the distance are available in [72].

A.4.2 Mixing laws

Once all the sub-domains are defined, the mechanical properties can then be determined on the whole domain in function of the level-set function. For the elements crossed by the level-set functions and the their neighbours, fluid-solid mixtures are used to determine the element effective properties. A heaviside function $H(\alpha)$ for each level-set function is defined by:

$$H(\alpha) = \begin{cases} 1 & \text{if } \alpha > 0 \\ 0 & \text{if } \alpha < 0 \end{cases} \tag{A.2}$$

In order to achieve a better continuity at the interface [73], the Heaviside function can be smoothed using:

$$H_\varepsilon(\alpha) = \begin{cases} 1 & \text{if } \alpha > \varepsilon \\ \frac{1}{2}\left(1 + \frac{\alpha}{\varepsilon} + \frac{1}{\pi}\sin\left(\frac{\pi\alpha}{\varepsilon}\right)\right) & \text{if } |\alpha| \leq \varepsilon \\ 0 & \text{if } \alpha < -\varepsilon \end{cases} \tag{A.3}$$

where ε is a small parameter such that $\varepsilon = O(h_i)$, known as the interface thickness, and h_i is the mesh size in the normal direction to the interface. In the vicinity of the interface, it can be computed using the following expression:

$$h_i = \max_{j,l \in K} \boldsymbol{\nabla}\alpha \cdot \mathbf{x}^{jl}, \tag{A.4}$$

where $\mathbf{x}^{jl} = \mathbf{x}^l - \mathbf{x}^j$ and K is the mesh element.

A.4.3 Anisotropic mesh adaptivity

The anisotropic mesh adaptation aims at improving the quality of the mesh and the interface representation. This algorithm relies on an appropriate metric map construction that allows the mesh size to be imposed in the direction of the distance function gradient. The mesh is refined locally and the elements are stretched which enables to sharply define the interface and to save a great number of elements compared to classical isotropic refinement. The details of this technique can be found in [52, 51], hence a brief description

is presented here. First, a modified distance computation is achieved via a symmetric positive defined tensor "the metric":

$$||\mathbf{x}||_{\mathrm{M}} = \sqrt{{}^{T}\mathbf{x}\cdot\mathbb{M}\cdot\mathbf{x}}\ , \quad <\mathbf{x},\mathbf{y}>_{\mathrm{M}}={}^{T}\mathbf{x}\cdot\mathbb{M}\cdot\mathbf{y}\ . \tag{A.5}$$

The metric $\mathbb{M}$ can be regarded as a tensor whose eigenvalues are related to the mesh sizes, and whose eigenvectors define the directions for which these sizes are applied. For instance, using the identity tensor, one recovers the usual distances and directions of the Euclidean space. In our case the direction of mesh refinement is given by the unit normal to the interface which corresponds to the gradient of the level-set function: $\boldsymbol{\nabla}\alpha/||\boldsymbol{\nabla}\alpha||$. A default mesh size, or background mesh size, h_d is imposed far from the interface and it is reduced as we come closer to the interface. A likely choice for the mesh size evolution is the following:

$$h = \begin{cases} h_d & \text{if } |\alpha(\mathbf{x})| > e/2 \\ \dfrac{2h_d(m-1)}{m\ e}|\alpha(\mathbf{x})| + \dfrac{h_d}{m} & \text{if } |\alpha(\mathbf{x})| \leq e/2 \end{cases} \tag{A.6}$$

Eventually, at the interface, the mesh size is reduced by a factor m with respect to the default value h_d. Then this size increases until equalling h_d for a distance that corresponds to the half of a given thickness e. The unit normal to the interface $\mathbf{x}$ and the mesh size h defined above, lead to the following metric:

$$\mathbb{M} = C\,(\boldsymbol{\nabla}\alpha/||\boldsymbol{\nabla}\alpha|| \otimes \boldsymbol{\nabla}\alpha/||\boldsymbol{\nabla}\alpha||) + \frac{1}{h_d}\,\mathbb{I} \tag{A.7}$$

where $\mathbb{I}$ is the identity tensor, and

$$C = \begin{cases} 0 & \text{if } |\alpha(\mathbf{x})| \geq e/2 \\ \dfrac{1}{h^2} - \dfrac{1}{h_d^2} & \text{if } |\alpha(\mathbf{x})| < e/2 \end{cases} \tag{A.8}$$

The mesh resolution can be forced to concentrate in particular areas of interest. The metric returns to isotropic far from the interface, with a mesh size equal to h_d for all directions, and to anisotropic near the interface.

A.5 Governing equations

This section is devoted to the mathematical formulation for rigid body immersed in an incompressible fluid. The governing equations are considered to be three-dimensional and time-dependant. As the proposed approach is monolithic, a unique constitutive equation will be solved on the whole domain with variable physical properties separated by a prescribed level-set function.

First, each system of equation is presented separately. Let $\Omega \subset \mathbb{R}^n$ be the spatial domain at time $t \in [0, T]$, where n is the space dimension. Let $\partial\Omega$ denote the boundary of

Ω. Ω_f, Ω_s and Ω_{fsi} be respectively the fluid domain, the solid domain and the interface. They verify:

$$\Omega_f \cup \Omega_s = \Omega \quad \text{and} \quad \Omega_f \cap \Omega_s = \Omega_{fsi}. \tag{A.9}$$

The dynamic of the flow is given by the classical incompressible Navier-Stokes equations:

$$\rho_f \ (\partial_t \mathbf{v} + \mathbf{v} \cdot \boldsymbol{\nabla} \mathbf{v}) - \boldsymbol{\nabla} \cdot \boldsymbol{\sigma} = \mathbf{f} \quad \text{in } \Omega_f \tag{A.10}$$

$$\boldsymbol{\nabla} \cdot \mathbf{v} = 0 \quad \text{in } \Omega_f \tag{A.11}$$

$$\mathbf{v} = \mathbf{v}_\Gamma \quad \text{on } \Gamma \tag{A.12}$$

$$\mathbf{v} = \mathbf{v_i} \quad \text{on } \Omega_{fsi} \tag{A.13}$$

$$\boldsymbol{\sigma} \cdot \mathbf{n} = \mathbf{d} \quad \text{on } \Omega_{fsi} \tag{A.14}$$

$$\mathbf{v}(\mathbf{x}, \mathbf{0}) = \mathbf{v_0}(\mathbf{x}) \quad \text{in } \Omega_f \tag{A.15}$$

where $\mathbf{v}$ is the velocity vector, ρ_f is the fluid density, $\mathbf{n}$ is the outward normal on the solid surface, $\mathbf{v_i}$ is the velocity at fluid-solid interface Ω_{fsi} and $\mathbf{f}$ is an applied force vector. For incompressible flows the divergence-free constraint (A.11) gives rise to the pressure in the fluid. The stress tensor for a Newtonian fluid is then given by:

$$\boldsymbol{\sigma} = 2\eta_f \varepsilon(\mathbf{v}) - p \ \mathbf{I_d}, \tag{A.16}$$

where p is the pressure, $\mathbf{I_d}$ is the identity tensor, $\varepsilon(\mathbf{v}) = (\boldsymbol{\nabla} \mathbf{v} +^T \boldsymbol{\nabla} \mathbf{v})/2$ the deformation-rate tensor and η_f is the dynamic viscosity.

In the present formulation we treat the rigid body as a continuous domain subjected to an additional rigidity constraint. First, we present the governing equations for solids motion given by:

$$\rho_s \ (\partial_t \mathbf{v} + \mathbf{v} \cdot \boldsymbol{\nabla} \mathbf{v}) - \boldsymbol{\nabla} \cdot \sigma = \mathbf{f} \quad \text{in } \Omega_s \tag{A.17}$$

$$\boldsymbol{\nabla} \cdot \mathbf{v} = 0 \quad \text{in } \Omega_s \tag{A.18}$$

$$\varepsilon(\mathbf{v}) = 0 \quad \text{in } \Omega_s \tag{A.19}$$

$$\mathbf{v} = \mathbf{v_i} \quad \text{on } \Omega_{fsi} \tag{A.20}$$

$$\boldsymbol{\sigma} \cdot \mathbf{n} = -\mathbf{d} \quad \text{on } \Omega_{fsi} \tag{A.21}$$

$$\mathbf{v}(\mathbf{x}, \mathbf{0}) = \mathbf{v_0}(\mathbf{x}) \quad \text{in } \Omega_s \tag{A.22}$$

where ρ_s the solid density. In a rigid body there is no deformation $\varepsilon(\mathbf{v}) = 0$. These two equations imply a null value of the deformation-rate tensor (A.19). Note also that the rigidity constraint (A.19) ensures that the velocity field is divergence-free. Hence, equation (A.18) is a redundant equation. Nevertheless we choose to keep it to account for the pressure term. As noted earlier equation (A.18) gives rise to a pressure fluid. Similarly, equation (A.19) gives rise to a stress field $\boldsymbol{\tau}$. The stress tensor is then given by:

$$\boldsymbol{\sigma} = -p \ \mathbf{I_d} + \boldsymbol{\tau}_s \tag{A.23}$$

Mixing both systems, the strong form for the whole domain reads:

$$\begin{cases} \rho\ (\partial_t \mathbf{v} + \mathbf{v}\cdot\boldsymbol{\nabla}\mathbf{v}) - \boldsymbol{\nabla}\cdot(2\eta\varepsilon(\mathbf{v}) + \boldsymbol{\tau} - p\ \mathbf{I_d}) = \mathbf{f} \\ \boldsymbol{\nabla}\cdot\mathbf{v} = 0 \\ \varepsilon_s(\mathbf{v}) = 0 \\ \mathbf{v} = \mathbf{v_b} \qquad\qquad \text{on } \partial\Omega \\ \mathbf{v}(\mathbf{x},\mathbf{0}) = \mathbf{v_0}(\mathbf{x}) \end{cases} \tag{A.24}$$

where $\varepsilon_s(\mathbf{v}) = H(\alpha)\varepsilon(\mathbf{v})$, $\eta = (1-H(\alpha))\eta_f$, $\rho = \rho_s H(\alpha) + \rho_f(1-H(\alpha))$ and $\boldsymbol{\tau} = H(\alpha)\boldsymbol{\tau}_s$. The boundary conditions (A.13-A.14) and (A.20-A.21) are no longer needed.

Multiplying by the test functions and integrating by parts, the associated standard weak form of system (A.24), can be stated as:
Find $\mathbf{v} \in V = \left(H_0^1(\Omega)\right)^n$, $p \in Q = L^2(\Omega)$ and $\tau \in \mathcal{T} = L^2(\Omega)^{n\times n}$ such that:

$$\begin{cases} \rho(\partial_t\mathbf{v},\mathbf{w}) + \rho(\mathbf{v}\cdot(\boldsymbol{\nabla}\mathbf{v},\mathbf{w}) - (p\,\boldsymbol{\nabla}\cdot\mathbf{w}) + (2\eta\varepsilon(\mathbf{v}) : \varepsilon(\mathbf{w})) + (\boldsymbol{\tau} : \varepsilon(\mathbf{w})) = (\mathbf{f},\mathbf{w}) \\ (\boldsymbol{\nabla}\mathbf{v}, q) = 0 \\ (\varepsilon_s(\mathbf{v}) : \boldsymbol{\tau}^*) = 0 \end{cases} \tag{A.25}$$

Note that the problem is not well posed without an additional condition on $\boldsymbol{\tau}$. A possible way to choose $\boldsymbol{\tau}$ is to take it as a symmetric gradient of a vector field. Therefore, we choose not to add an additional variable and to use a modified symmetric gradient operator that would be computed by an Uzawa iteration. Solving iteratively the last equation of system (A.25) reads:

$$(\varepsilon_s(\mathbf{v^k}) : \varepsilon_s(\mu*)) - \frac{1}{\eta_s}(\underbrace{\varepsilon_s(\mu^k)}_{\boldsymbol{\tau}^k} : \varepsilon_s(\mu*)) + \frac{1}{\eta_s}(\underbrace{\varepsilon_s(\mu^{k-1})}_{\boldsymbol{\tau}^{k-1}} : \varepsilon_s(\mu*)) = 0. \tag{A.26}$$

Thus, $\boldsymbol{\tau}^k = \boldsymbol{\tau}^{k-1} + \eta_s\varepsilon_s(\mathbf{v}^{k-1})$ where $2\eta_u > 1$ is a given penalty parameter and $\eta_s = H(\alpha)\eta_u$. Using the augmented Lagrangian and Uzawa's algorithm, an extra term will be added to the first equation of system (A.25). Consequently, we modify the viscosity into $\eta = H(\alpha)\eta_u + (1-H(\alpha))\eta_f$ and we insert the extra term as $(2\eta_s\varepsilon(\mathbf{v}) : \varepsilon(\mathbf{w}))$. More details about the algorithm and the corresponding stabilized finite element formulation which is based on the Variational MultiScale Methods can be found in [122].

A.6 Numerical experiments

In this section, we present several numerical simulations, which were carried out using the C++ CimLib finite element library (see [46, 69]). We will apply two approaches: the classical one with boundary conditions and the monolithic approach with immersed

cylinders. The obtained results are then compared to solutions taken from the literature [156, 158, 159, 160, 161].

Figure A.4 shows the computational rectangular domain with a cylinder of diameter d located initially at $[12.5d, 5d]$. The lengths and heights of the computational domain are $32.5d$ and $10d$. The number of elements is fixed to 30000 as suggested in [156]. The inlet velocity U_∞ and the density of flow are constant. The Reynolds number is $Re = U_\infty d/\nu$, where ν is the cinematic viscosity of the fluid.

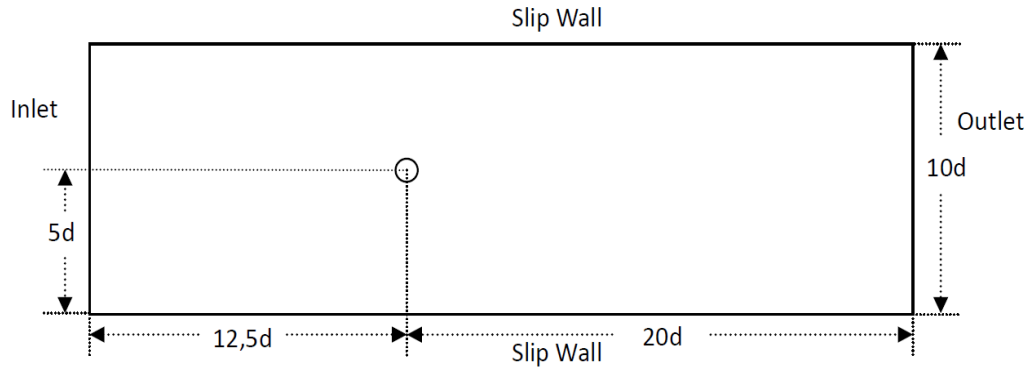


Figure A.4: Size and geometric disposition of the computational domain

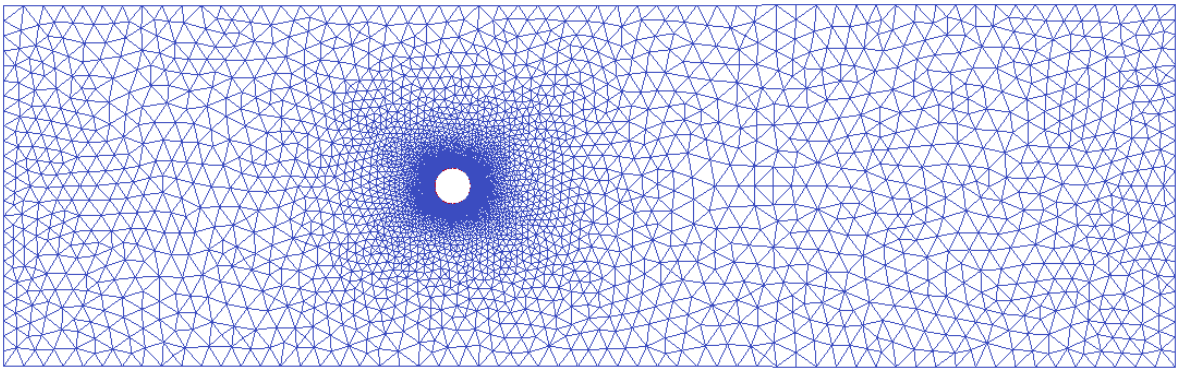
A.6.1 Flow around a 2D immersed fixed cylinder

We investigate first the fixed cylinder for four particular Reynolds numbers in permanent regimes ($5 \leq \text{Re} \leq 49$) and four others in the periodic regime ($49 \leq \text{Re} \leq 190$). Two groups of simulations were carried out: in the first group we used the classical approach whereas in the second we apply the monolithic approach. Figure A.5 shows the corresponding meshes having approximately the same number of elements and referenced as Mesh2. Moreover, in order to check the proposed number of elements by the literature (30000) and thus the influence of the mesh, we have provided additional simulations using 5000 elements referenced as Mesh1.

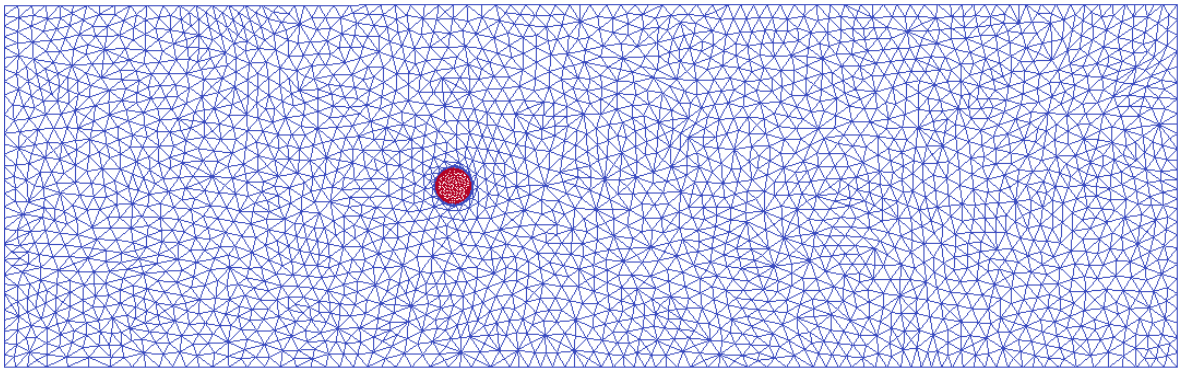
A.6.1.1 Permanent regime ($5 \leq \text{Re} \leq 49$)

The investigated Reynolds numbers are 10, 20, 30 and 40, all below Hopf bifurcation between the permanent and the periodic regimes. The vortex shedding is characterized then by two recirculation zones attached to the rear cylinder wall.

The first analysed parameter is the length L_r of the recirculation zone which is defined by the downstream distance on the central line of the vortex shedding where the velocity is null. The second parameter is the value of the separation angle θ_s, which is obtained by plotting the vortices at the cylinder wall against the angular position and corresponds to the angle where the vortices becomes null. Tables A.1 and A.2 present all the obtained



(a) Mesh for Classical approach



(b) Mesh for Monolithic approach

Figure A.5: Mesh comparison for classical and monolithic approach

results using both approaches which compares very well to the values obtained from Placzek [156].

Table A.1: Comparison of L_r

L_r	$Re = 10$	$Re = 20$	$Re = 30$	$Re = 40$
Cimlib Classical Mesh 1	0.35	0.73	1.2	1.36
Cimlib Classical Mesh 2	0.35	1.04	1.8	2.44
Cimlib Monolithic Mesh 1	0.36	0.95	1.71	2.35
Placzek et al. (2008)	0.25	0.9	1.6	2.2

Table A.2: Comparison of θ_s

θ_s	$Re = 10$	$Re = 20$	$Re = 30$	$Re = 40$
Cimlib Classical Mesh 1	29	42	45	50
Cimlib Classical Mesh 2	30	42.5	50	55
Cimlib Monolithic Mesh 1	30	43	50	53
Placzek et al. (2008)	28	46	49	53

The evolution of these two parameters in function of the Reynolds number is plotted in Figure A.6. The relative errors remain very small demonstrating the efficiency of the proposed approaches.

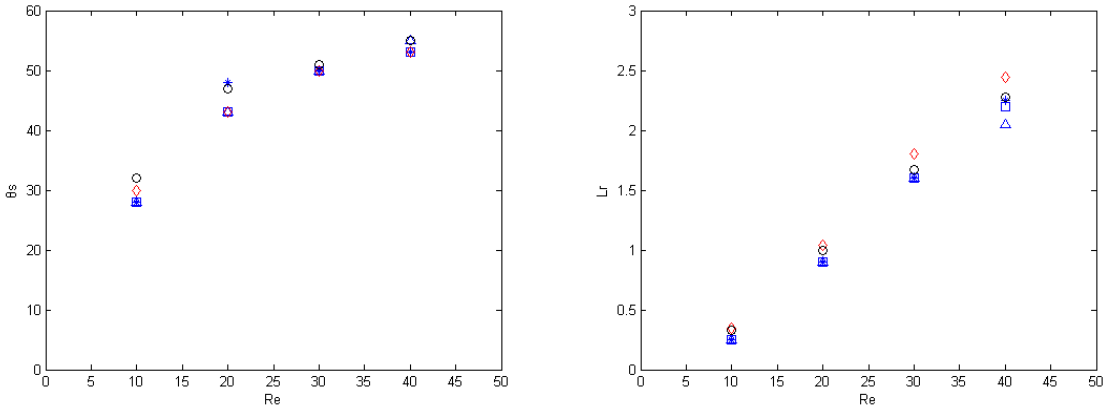


Figure A.6: Comparison of geometric vortex shedding characteristics for permanent regime $Re < 49$,(○)Monolithic simulations, (◇)Classical simulations,(⋆)Placzek[156], (□)Gerouache[158], (Δ)Baraz[159]

The third studied parameter is the drag coefficients C_D. The lift coefficient C_L remains null because of the perfect symmetry of the flow field. The expressions of these aerodynamic coefficients are given by:

$$C_D = \frac{F_D}{1/2\rho U_\infty^2 d} \quad \text{and} C_L = \frac{F_L}{1/2\rho U_\infty^2 d} \tag{A.27}$$

where F_D and F_L are the drag and lift forces by length unit. Again, values of the drag coefficient are close to those of Placzek[156], Gerouache[158], Lange[160]. The agreement becomes better when Re increases.

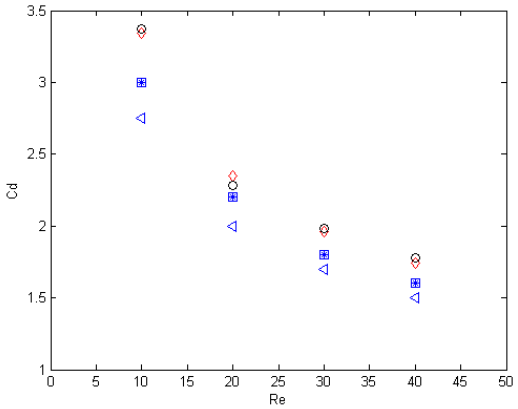


Figure A.7: Comparison of drag coefficients for permanent regime $Re < 49$,(○)Monolithic simulations, (◇)Classical simulations,(⋆)Placzek[156],(□)Gerouache[158], (◁)Lange[160]

A.6.1.2 Periodic vortex shedding regime ($49 \leq$ Re ≤ 190)

In this section, we investigate the Reynolds numbers of 60, 80, 100 and 120. We can find that the vortex shedding of two staggered rows of vortices being shed alternately from either side of the cylinder. The fluctuating values and mean values of the aerodynamic coefficients of the periodicity of shedding are noted by C_D', C_L' and $\overline{C_D'}$, $\overline{C_L'}$. The latters are evaluated as the average value of the fluctuating coefficients over several periodics chosen after the transient regime. The convergence of the coefficients is shown in Figure A.8. In the first part of time series, it exhibits the transient phase during which the perturbation initially introduced arrives on the cylinder and causes the shedding. When the periodic state is reached, the vortex shedding is characterized by the oscillation of the drag coefficient at twice the lift frequents.

In the periodic regime, a new parameter is introduced and analysed: the Strouhal frequency f_s defined also as the lift coefficient frequency:

$$S_t = f_s \frac{d}{U_\infty} \tag{A.28}$$

The values of Strouhal number obtained from the classical and monolithic approaches are presented in Table A.3. By comparing our results to the analytical expressions found

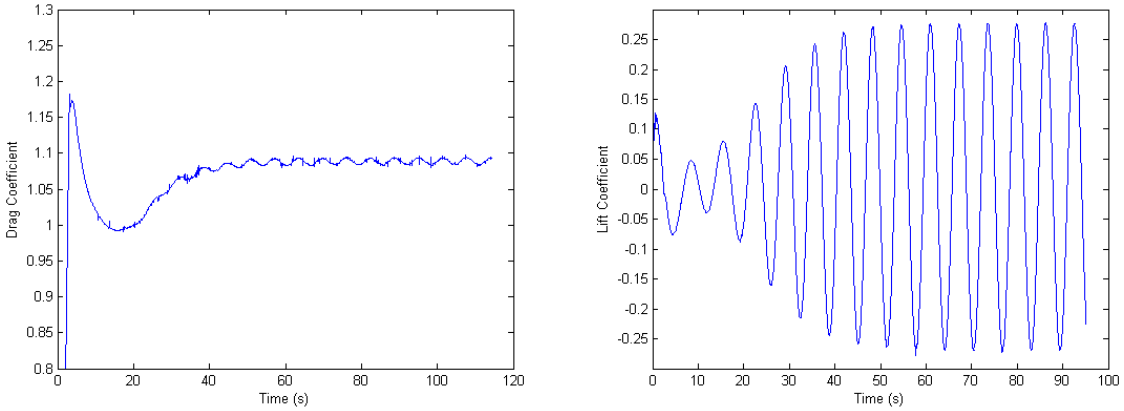


Figure A.8: Convergence of the aerodynamic fluctuating coefficients at $Re = 100$. Drag coefficient $C_D^{'}$, Lift coefficient $C_L^{'}$

in Placzek [156], Gerouache [158] and Henderson[161], we noticed that the relative error does not exceed 6% which confirms also the potential of the proposed stabilized finite element approach.

Table A.3: Comparison of S_t

S_t	$Re = 60$	$Re = 80$	$Re = 100$	$Re = 120$
Cimlib Classical Mesh 1	0.140	0.153	0.162	0.169
Cimlib Classical Mesh 2	0.139	0.157	0.167	0.174
Cimlib Monolithic Mesh 1	0.137	0.155	0.158	0.164
Placzek et al. (2008)	0.141	0.157	0.168	0.176

Since the mean values of the lift coefficient is null, we compare instead the maximal reached value noted by $C_{L,max}^{'}$. Figure A.9 shows the obtained values of the Strouhal number and the maximal lift coefficient $C_{L,max}^{'}$ compared to the values of the literature.

Table A.4: Comparison of Maximal lift Coefficient

Maximal lift coefficient $C_{L,max}^{'}$	$Re = 60$	$Re = 80$	$Re = 100$	$Re = 120$
Cimlib Classical Mesh 1	0.154	0.283	0.392	0.483
Cimlib Classical Mesh 2	0.143	0.267	0.364	0.448
Cimlib Monolithic Mesh 1	0.09	0.2	0.29	0.395
Placzek et al. (2008)	0.125	0.25	0.325	0.38

The comparisons show that the relative errors of the maximal lift coefficient decrease when the Reynolds number increases. It shows also that results obtained by the monolithic approach slightly differ from other values. This can be explained due to the fact that we transform the surface integral into a volume integral over a certain thickness when

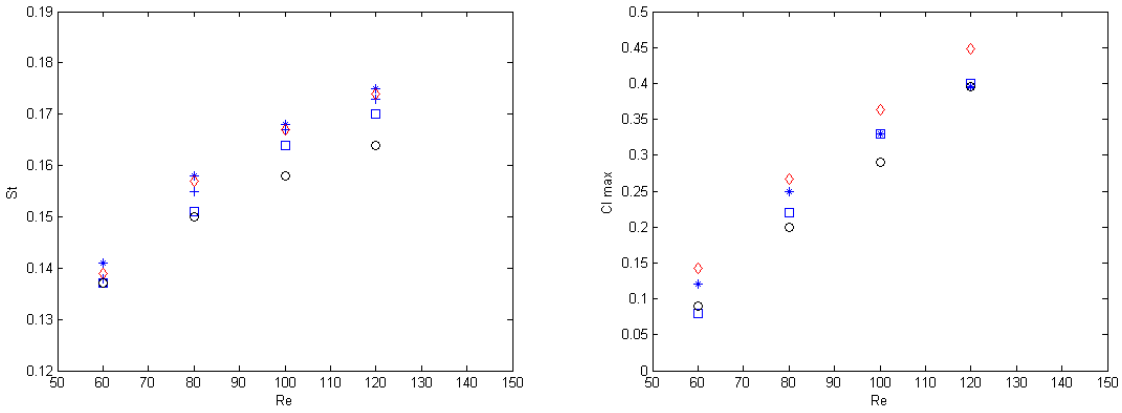


Figure A.9: Comparison of aerodynamic force coefficients for permanent regime $49 < Re < 190$,(∘)Monolithic simulations, (◇)Classical simulations,(⋆)Placzek[156],(□)Gerouache[158], (+)Henderson[161]

computing the aerodynamic coefficients. However, the overall accuracy of the results is very satisfactory, especially when it concerns the values of the Strouhal number and the lift coefficients since it will play a major role in the vertical oscillating regimes as described in the following sections.

A.6.2 Flow around a 2D immersed forced oscillating cylinder

To simulate the forced oscillatory motion, we update the coordinates of the center of the cylinder using a predefined motion: $x = constant, y = Asin(2\pi f_0 t)$, where A is the maximal amplitude of the oscillation. Therefore, rather than moving the nodes of the mesh as in the classical approaches, only the position of the distance function of the cylinder is easily updated and recomputed. The mesh adaptation follows also the fluid-solid interface and the material properties are reassigned accordingly.

These new simulations are made using a fixed Reynolds number equal to 100 as suggested in [156]. We note the frequency ratio by $F = f_0/f_s$, where f_0 is the obtained frequency of the forced oscillation cylinder and f_s is the Srouhal frequency. The lock-in zone is defined by the domain where the vortex shedding frequency diverges from the value expected at the considered Reynolds number and locks on the frequency of the forced oscillations: this zone is represented in the plane (A, F) in figure A.10 according to the limits established by Koopmann [162]. The lock-in zone is comprised between two limits almost symmetrical with respect to the axis $F = 1.0$. In order to highlight the different response regimes of the cylinder, the amplitude A is kept constant at a certain level and F varies over a range wide enough so that the lock-in zone should be crossed.

According to the frontiers established by Koopmann, the upper and lower limits are approximately located at $F = 0.75$ and $F = 1.25$. Therefore, we run several numerical tests for different values of F taken between 0.5 and 1.5 which corresponds well to both

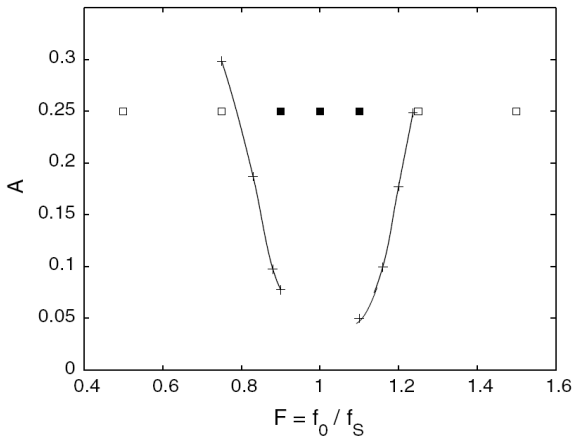


Figure A.10: Representation of the lock-in zone in the plane (A, F) for forced transverse oscillations. The solid lines represent the frontiers of the lock-in zone according to the data points (+) of Koopmann[162]. The simulations performed here are represented with squares: filled squares (■) correspond to locked configurations whereas empty squares (□) indicate unlocked ones.

the inside and the outside lock-in zones. The amplitude A is kept constant and equal to 0.25.

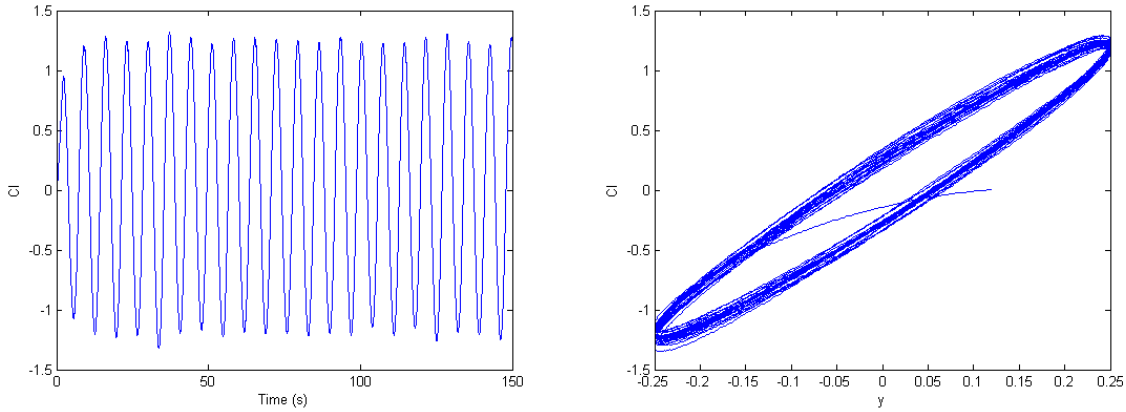
A.6.2.1 Locked configurations

We present in this section results for two cases of the locked configurations: $F = 0.90$ and $F = 1.10$. Figure A.11 presents the times series of the aerodynamic coefficients which are clearly characterized by a pure sinusoidal response and show an increase in the aerodynamic coefficients. Indeed, the mean drag coefficient was $\overline{C'_D} = 1.370$ for the fixed cylinder whereas it increases now to $\overline{C'_D} = 1.417$ for $F = 0.90$ and to $\overline{C'_D} = 1.380$ for $F = 1.10$. Similar behaviour is noticed for the the maximal lift coefficient: $C'_{L,max} = 0.29$ (fixed cylinder), $C'_{L,max} = 0.940$ ($F = 0.90$) and $\overline{C'_D} = 1.380$ ($F = 1.10$).

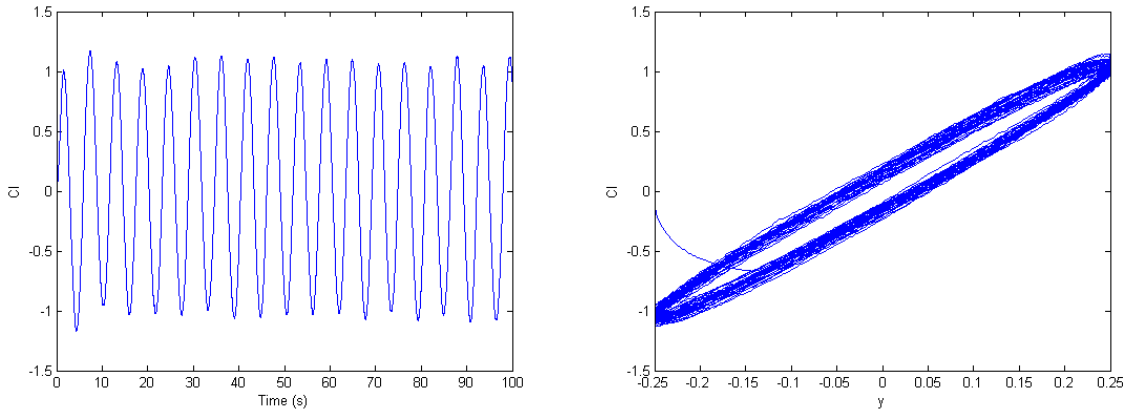
The phase portraits of the system are also a very practical tool to analyse the response. They represent the energy transfer which produces the fluctuating lift force characterized by the fluctuating lift coefficient C'_L and the adimensional cylinder displacement $y^* = y(t)/d$ between the motion of the cylinder and the fluid. They provide an interesting description of how the system behaves. The existence of a unique limit cycle is the result of the perfect undamped sinusoidal response and the inclination of the cycle gives an estimation of the phase angle between the imposed displacement and the lift.

A.6.2.2 Unlocked configurations

In this section, we present the results using two new frequency ratios: $F = 0.50$ and $F = 1.50$. As mentioned before, these values will lead to an unlocked vortex shedding. As



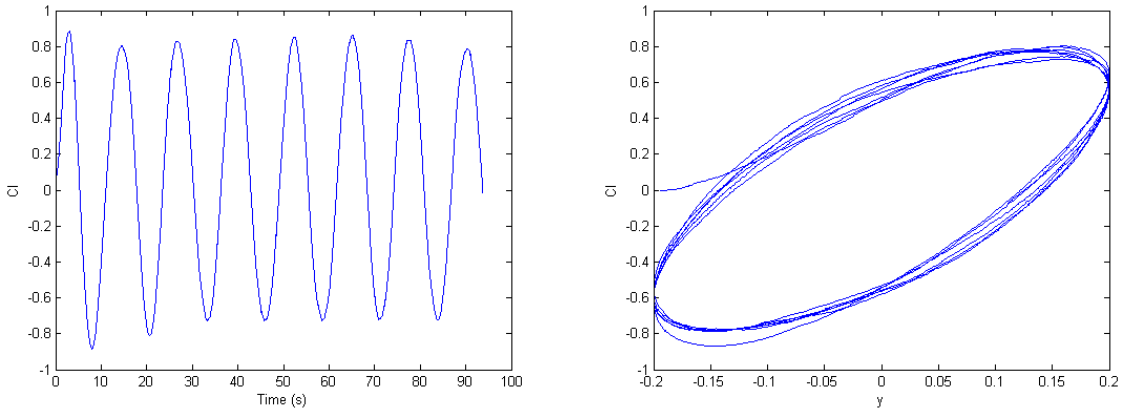
(a) F=0.90



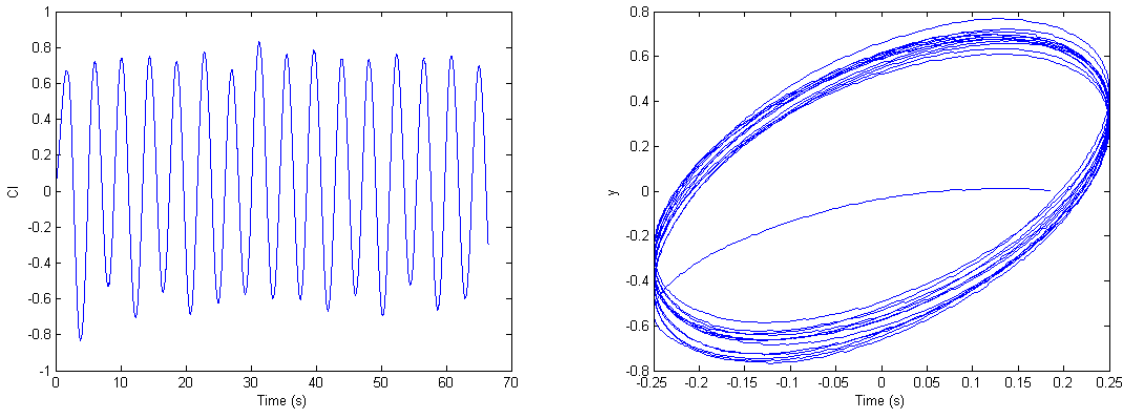
(b) F=1.10

Figure A.11: Time series of the fluctuation lift coefficient C_L' and the phase portraits at $F = 0.90 and\ F = 1.10$

expected, figure A.12 shows that the time series of the lift coefficients are no longer purely sinusoidal and a beating behavior is obtained. The beating behavior has been observed numerically by Anagnostopoulos [150] who noted that, when the frequency ratio F was outside the lock-in zone, the flow was not absolutely periodic at subsequent cycles but a quasi-periodic flow pattern occurred.



(a) F=0.50



(b) F=1.50

Figure A.12: Time series of fluctuation lift coefficient C_L', and phase portraits at $F = 0.50$ $F = 1.50$

In order to highlight the increase in the aerodynamic coefficients, we plot in figure A.13 their evolution in respect to the frequency ratio F compared to different reference values. We notice that the maximum values are inside the lock-in zone and near $F = 1$.

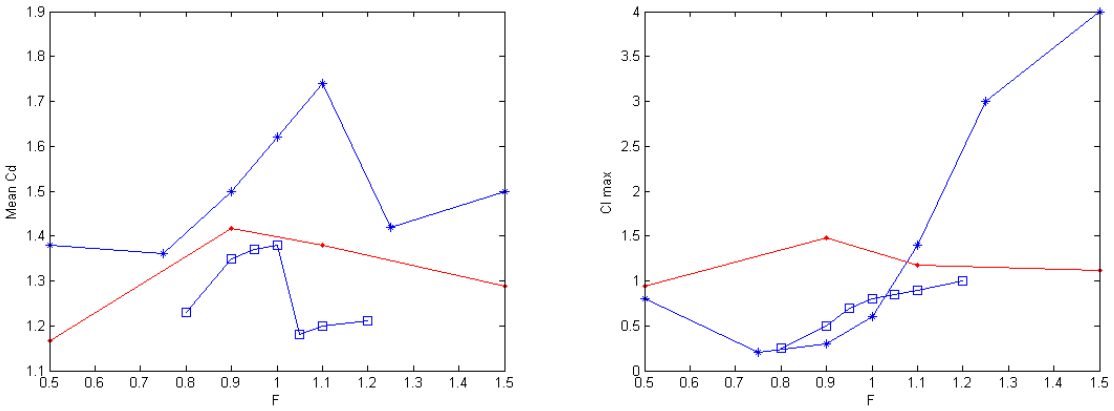


Figure A.13: Evolution of the mean drag and maximal lift coefficients with the frequency ratio F. The results are compared to those of (•)Monolithic simulations, (⋆)Placzek[156] and (□)Anagnostopoulos[150]

A.6.3 Flow around a 2D immersed flexible cylinder

The changes of the flow influence the response of the structure and in return the vibration of the structure will influence the flow around the cylinder, thus a two-way fluid-structure interaction is formed. Indeed, in two-dimensions, the cylinder flexibility can be modelled by a mass-spring system excited naturally by the fluid forces. The vertical cylinder motion $y(t)$ is then governed by the following equation:

$$m\ddot{y} + c\dot{y} + ky = F_y \tag{A.29}$$

where $\dot{y}$ and y are the velocity and the position of the cylinder respectively, m is the cylinder mass, c is the structural damping, k is the rigidity and F_y is the resultant of the lift force. We present here briefly the steps of the coupling algorithm:

1. Initialization for the first iteration (x_0, v_0, a_0 and F_0 are the initial displacement, velocity, acceleration and force respectively):

$$y(0) = 0, \quad \dot{y} = 0, \tag{A.30}$$

$$y^n = x_0, \quad \dot{y}^n = v_0, \quad \ddot{y}^n = a_0, \quad F_y^n = F_0. \tag{A.31}$$

2. Explicit prediction of the cylinder acceleration for the time step t_{n+1} using (A.29):

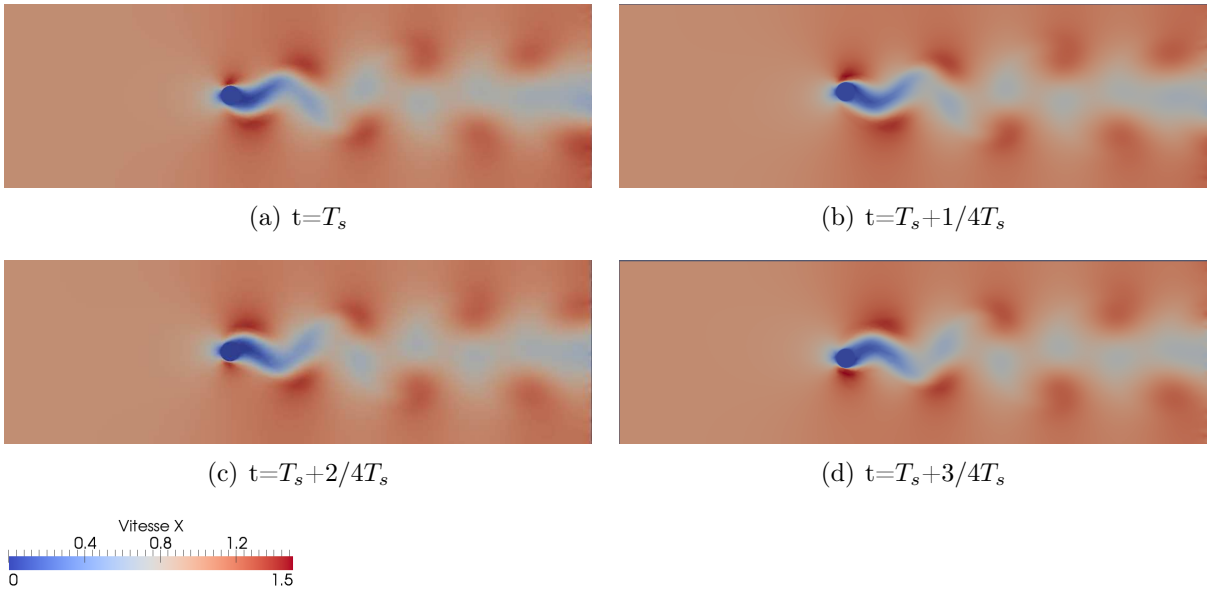
$$\ddot{y}^{n+1} = \frac{F_y^n}{m} - \frac{k}{m}y^n - \frac{c}{m}\dot{y}^n. \tag{A.32}$$

3. Evaluation of the cylinder velocity and displacement using linear approximations (Δt is the fluid time step, and θ is the blending factor):

$$\dot{y}^{n+1} = \dot{y}^n + \Delta t\ddot{y}^n, \tag{A.33}$$

$$y^{n+1} = y^n + \Delta t[(1-\theta)\dot{y}^n + \theta\dot{y}^{n+1}]. \tag{A.34}$$

4. Mesh update: computation of the new mesh configuration at the fluid-solid interface
5. Resolution of the Navier-Stokes equations on the new mesh configuration to obtain F_y^{n+1}.
6. Return to step 2 for the next time step.



(a) t=T_s (b) t=T_s+1/4T_s

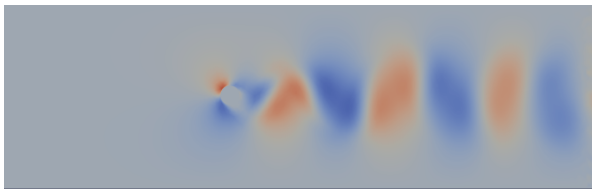
(c) t=T_s+2/4T_s (d) t=T_s+3/4T_s

(e) Velocity x scale

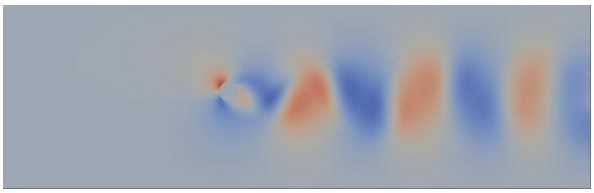
Figure A.14: Velocity in the x direction over one given period $F = 0.9$ at $Re = 100$

A first attempt using this algorithm provides a good potential for the developed formulations. Note that only arbitrary values for k, c and m are used in here to test if the natural interactions can be really obtained. Further investigation on these values will be the subject of a future work.

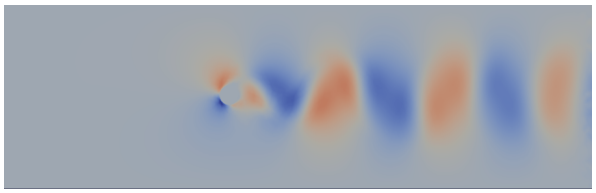
The profiles of the velocity and the pressure in figures A.14, A.15 and A.16 seem very encouraging since they reflect well the periodic behaviour and the corresponding natural fluid-structure interactions. These figures show the expected free oscillations of the cylinder. It is worth mentioning, at this stage, that the solutions do not suffer from spurious oscillations (undershoots or overshoots) which are frequently observed at the interface or in convection dominated problems across the water channel. This can be attributed to the stabilization finite element discretization applied on the system of equations. Summing up, the combination of the dynamic mesh adaptation and the use of iterative solvers together with the smoothed distribution of the physical properties across the interface overcome the numerical instabilities and lead to good numerical behaviour. Future investigations will be concerned with more comparisons between the free and forced oscillations cylinder.



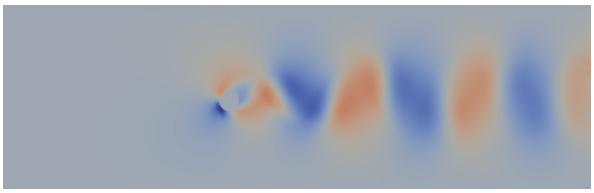
(a) t=T_s



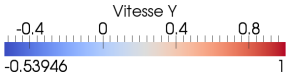
(b) t=T_s+1/4T_s



(c) t=T_s+2/4T_s

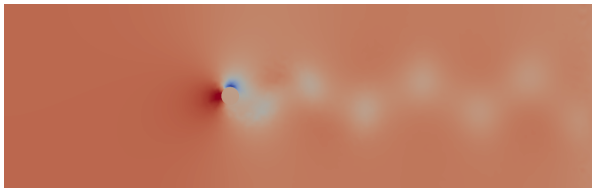


(d) t=T_s+3/4T_s

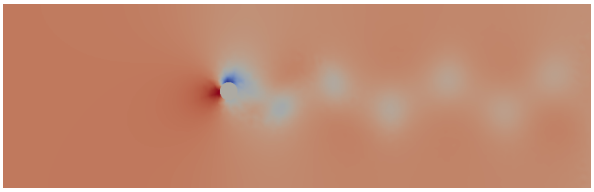


(e) Velocity y scale

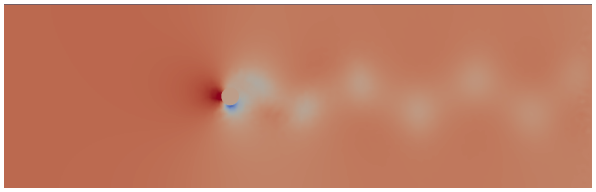
Figure A.15: Velocity in the y direction over one given period $F = 0.9$ at $Re = 100$



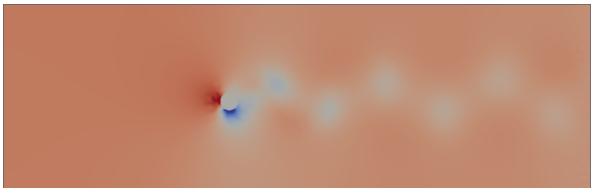
(a) t=T_s



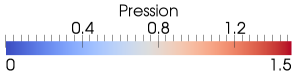
(b) t=T_s+1/4T_s



(c) t=T_s+2/4T_s

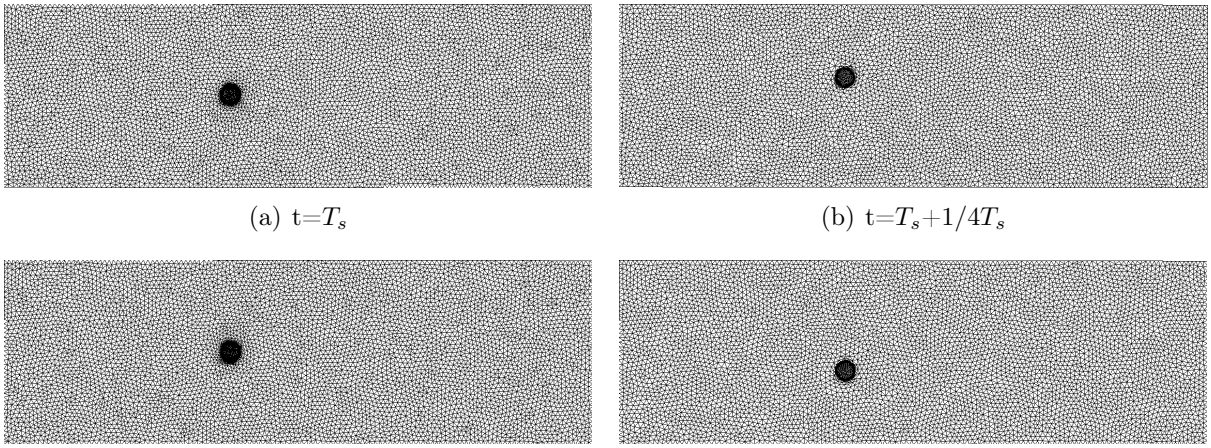


(d) t=T_s+3/4T_s



(e) Pressure scale

Figure A.16: Pressure over one given period $F = 0.9$ at $Re = 100$



(a) t=T_s (b) t=T_s+1/4T_s

(c) t=T_s+2/4T_s (d) t=T_s+3/4T_s

Figure A.17: Mesh variation over one given period $F = 0.9$ at $Re = 100$

A.7 Conclusion

In this paper, fixed, forced and free oscillating cylinders in a cross-flow water channel are studied and analysed. A monolithic approach was used to treat easily the induced fluid-structure interactions. It is combined with a dynamic anisotropic mesh adaptation applied at the fluid-solid interface rendering an accurate representation of the cylinder. An extended Variational MultiScale method was used to solve the Navier-Stokes equations in a stabilized finite element framework insuring a stable solution. The presence of the solid is taken into account as an extra-stress tensor in the Navier-Stokes equations.

The combination of all these techniques from CimLib demonstrates the capability and the potential of the proposed approach to deal with fluid-cylinder interactions. Several numerical tests were presented and analysed. Comparisons with the literature show that the method can be used in a wide range of fluid-cylinder applications needed for the safety and the design of a variety of reactor structures.

Further investigations will be focused on (i) simulating the global experimental setup by taking together in the same simulation the rigid and flexible cylinders, (ii) on continuing the assessment of the free oscillating cylinder and on characterizing all the used parameters in the mass-spring model, (iii) on studying the influence of the mesh at the fluid-solid interface and the integral computations since it plays an important role for the computation of the aerodynamic coefficients, (iv) on learning the EDF code needed for future comparisons with CimLib.

References

[1] F. Hamdan and P. Dowling, "Fluid-structure interaction: application to structures in an acoustic fluid medium, part 1: an introduction to numerical treatment," *Engineering Computations*, vol. 12, no. 8, pp. 749–758, 1995.

[2] D. Hartwanger and A. Horvat, "3D modeling of a wind turbine using CFD," 2008 NAFEMS Conference.

[3] D. Trimarchi, D. Turnock, S.R.and Chapelle, and D. Taunton, "Fluid-structure interactions of anisotropic thin composite materials for application to sail aerodynamics of a yacht in waves," *In, 12th Numerical Towing Tank Symposium*, pp. 173–178, 2009.

[4] H. Zhao and S. Pierson, "Simulation of automotive exhaust noise using fluid structure interaction, altair engineering„" *CAE Technnology conference 2009*.

[5] J. Leung, A. Wright, N. Cheshire, J. Crane, S. Thom, A. Hughes, and Y. Xu, "Fluid structure interaction of patient specific abdominal aortic aneurysms: a comparison with solid stress models," *BioMedical Engineering OnLine*, vol. 5, no. 1, p. 33, 2006.

[6] S. Deparis, M. A. Fernandez, and L. Formaggia, "Acceleration of a fixed point algorithm for fluid-structure interaction using transpiration conditions," *Mathematical Modelling and Numerical Analysis*, vol. 37, no. 4, pp. 601–616, 2003.

[7] F. Chouly, A. Van Hirtum, P.-Y. Lagrée, J.-R. Paoli, X. Pelorson, and Y. Payan, "Simulation of the retroglossal fluid-structure interaction during obstructive sleep apnea," *Lecture notes in computer science*, vol. 4072, pp. 48–57, 2006.

[8] M. Souli, A. Ouahsine, and L. Lewin, "ALE formulation for fluid-structure interaction problems," *Computer Methods in Applied Mechanics and Engineering*, vol. 190, no. 5-7, pp. 659–675, 2000.

[9] G.-H. Cottet, E. Maitre, and T. Milcent, "Eulerian formulation and level set models for incompressible fluid-structure interaction," *ESAIM: Mathematical Modelling and Numerical Analysis*, vol. 42, no. 3, pp. 471–492, 2008.

[10] P.-O. Persson and J. Peraire, "Curved mesh generation and mesh refinement using lagrangian solid mechanics," *Lawrence Berkeley National Laboratory*, 2009.

[11] C. W. Hirt, A. A. Amsden, and J. L. Cook, "An Arbitrary Lagrangian-Eulerian computing method for all speeds," *Journal of Computational Physics*, vol. 14, pp. 227–253, 1974.

[12] T. J. R. Hughes, W. K. Liu, and T. Zimmerman, "Lagrangian-Eulerian finite element formulation for incompressible viscous flow," *Computer Methods in Applied Mechanics and Engineering*, vol. 29, pp. 239–249, 1981.

[13] J. Donea, S. Giuliani, and J. P. Halleux, "An Arbitrary Lagrangian-Eulerian finite element method for transient dynamic fluid-structure interactions," *Computer Methods in Applied Mechanics and Engineering*, vol. 33, pp. 689–723, 1982.

[14] L. Ait Moudid, *Couplage Fluide-Structure pour la simulation numérique des écoulements fluides dans une conduite à parois rigides ou élastiques, en présence d'obstacle ou non.* PhD thesis, Faculté des Sciences Jean Perrin, Université, 2008.

[15] D. Benson, "An efficient, accurate, simple ALE method for non linear finite element programs," *Computer Methods in Applied Mechanics and Engineering*, vol. 72, pp. 305–350, 1989.

[16] M. Souli, A. Ouahsine, and L. Lewin, "Ale formulation for fluid structure interaction problems," *Computer Methods in Applied Mechanics and Engineering*, vol. 190, pp. 659–675, 2000.

[17] R. van Loon, P. D. Anderson, F. N. van de Vosse, and S. J. Sherwin, "Comparison of various fluid-structure interaction methods for deformable bodies," *Computers and Structures*, vol. 85, pp. 833–843, 2007.

[18] A. Legay and T. Chessa, J.and Belytschko, "An Eulerian-Lagrangian method for fluid-structure interaction based on level sets," *Computer Methods in Applied Mechanics and Engineering*, vol. 75, pp. 305–334, 2008.

[19] P. H. Saksono, W. G. Dettmer, and D. Perić, "An adaptive remeshing strategy for flows with moving boundaries and fluid-structure interaction," *International Journal for Numerical Methods in Engineering*, vol. 71, pp. 1009–1050, 2007.

[20] A. Gerstenberger and W. A. Wall, "An extended finite element method/lagrange multiplier based approach for fluid-structure interaction," *Computer Methods in Applied Mechanics and Engineering*, vol. 197, no. 19-20, pp. 1699–1714, 2008.

[21] W. A. Wall, A. Gerstenberger, P. Gamnitzer, and U. Mayer, "Advances in fixed-grid fluid structure interaction," *Computational methods in applied sciences*, vol. 14, pp. 235–249, 2009.

[22] W. A. Wall, A. Gerstenberger, P. Gamnitzer, C. Förster, and E. Ramm, "Large deformation fluid-structure interaction - advances in ALE methods and new fixed

grid approaches," *Lecture Notes in Computational Science and Engineering*, vol. 53, pp. 195–232, 2006.

[23] D. Sternel, M. Schäfer, M. Heck, and S. Yigit, "Efficiency and accuracy of fluid-structure interaction simulations using an implicit partitioned approach," *Computational mechanics*, vol. 13, no. 1, pp. 103–113, 2008.

[24] R. Garg, N. C., and S. S., "A numerically convergent Lagrangian-Eulerian simulation method for dispersed two-phase flows," *International Journal of Multiphase Flow*, vol. 35, no. 4, pp. 376–388, 2009.

[25] A. Legay and A. Tralli, "An Euler-Lagrange enriched finite element approach for fluid-structure interaction," *European Journal of Computational Mechanics*, vol. 16, no. 2, pp. 145–160, 2007.

[26] A. Zilian and A. Legay, "The enriched space-time finite element method (EST) for simultaneous solution of fluid-structure interaction," *International Journal for Numerical Methods in Engineering*, vol. 75, pp. 305–334, 2008.

[27] C. S. Peskin, "The immersed boundary method," *Acta Numerica*, vol. 11, pp. 479–517, 2002.

[28] R. Glowinski, T.-W. Pan, T.-I. Helsa, and D. D. Joseph, "A distributed lagrange multiplier/fictious domain methods for particulate flows," *International Journal of Multiphase Flow*, vol. 25, no. 5, pp. 755–794, 1999.

[29] R. Glowinski, T.-W. Pan, T. I. Helsa, D. D. Joseph, and J. Periaux, "A fictitious domain approach to the direct numerical simulation of incompressible viscous flow past moving rigid bodies: application to particulate flow," *Journal of Computational Physics*, vol. 169, pp. 363–426, 2001.

[30] J. De Hart, G. Peters, P. Schreurs, and F. Baaijens, "A three dimensional computational analysis of fluid-structure interaction in the aortic valve," *Journal of biomechanics*, vol. 36, no. 1, pp. 103–112, 2003.

[31] Z. Yu, "A DLM/FD methods for fluid/flexible-body interaction," *Journal of computational physics*, vol. 207, pp. 1–27, 2005.

[32] R. Van Lon, P. Anderson, and F. Van de Vosse, "A fluid-structure interaction method with solid-rigid contact for heart valve dynamics," *Journal of computational physics*, vol. 217, pp. 806–823, 2006.

[33] R. Van Lon, P. Anderson, J. Hart, and F. Baaijens, "CAE technnology conference 2009," *Journal of computational physics*, vol. 46, pp. 533–544, 2004.

[34] B. Hübner, E. Walhorn, and D. Dinkler, "A monolithic approach to fluid-structure interaction using space-time finite elements," *Computer Methods in Applied Mechanics and Engineering*, vol. 193, no. 23–26, pp. 2087–2104, 2004.

[35] E. Walhorn, A. Kölke, B. Hübner, and D. Dinkler, "Fluid-structure coupling within a monolithic model involving free surface flows," *Computers and structures*, vol. 83, pp. 2100–2111, 2005.

[36] J.-F. Gerbeau and M. Vidrascu, "A quasi-newton algorithm based on a reduced model for fluid structure interaction problems in blood flow," *Mathematical Modelling and Numerical Analysis*, vol. 37, pp. 631–647, 2003.

[37] C. Michler, E. H. van Brummelen, and R. de Borst, "An interface newton-krylov solver for fluid-structure interaction," *International Journal for Numerical Methods in Fluids*, vol. 47, no. 10-11, pp. 1189–1195, 2005.

[38] M. A. Fernández and M. Moubachir, "A newton method using exact jacobians for solving fluid-structure coupling," *Computers and Structure*, vol. 83, no. 2-3, pp. 127–142, 2005.

[39] W. A. Wall, S. Genkinger, and E. Ramm, "A strong coupling partitioned approach for fluid-structure interaction with free surfaces," *Computers & Fluids*, vol. 36, pp. 139–183, 2007.

[40] P. Caussin, J.-F. Gerbeau, and F. Nobile, "Added-mass effect in the design of partioned algorithms for fluid-structure problems," *Computer Methods in Applied Mechanics and Engineering*, vol. 194, pp. 4506–4527, 2005.

[41] C. Förster, W. A. Wall, and E. Ramm, "Artificial added mass instabilities in sequential staggered coupling of nonlinear structures and incompressible viscous flows," *Computer Methods in Applied Mechanics and Engineering*, vol. 196, no. 7, pp. 1278–1293, 2007.

[42] M. Razzaq, *Finite Element Simulation Techniques for Incompressible Fluid-structure Interaction with Applications to Bio-engineering and Optimization.* PhD thesis, Der fakultät für mathematik der technischen universität, 2011.

[43] S. R. Idelsohn, J. Marti, A. Limache, and E. Onate, "Unified lagrangian formulation for elastic solids and incompressible fluids : Appliction to fluid-structure interaction problems via the PFEM," *Computer Methods in Applied Mechanics and Engineering*, vol. 197, pp. 1762–1776, 2008.

[44] C. Förster, *Robust methods for fluid-structure interaction with stabiliseed finite elements.* PhD thesis, Institut für Baustatik, Universität Stuttgart, 2007.

[45] H. Digonnet, L. Silva, and T. Coupez, "Cimlib: a fully parallel application for numerical simulations based on components assembly," in *Materials Processing and Design; Modeling, Simulation and Applications; NUMIFORM '07; Proceedings of the 9th International Conference on Numerical Methods in Industrial*, 2007.

[46] H. Digonnet and T. Coupez, "Object-oriented programming for fast and easy development of parallel applications in forming processes simulation," in *K.J. Bathe, (ed)., Second MIT Conference on Computational Fluid and Solid Mechanics*, pp. 1922–1924, 2003.

[47] E. Hachem, T. Kloczko, H. Digonnet, and T. Coupez, "Stabilized finite element solution to handle complex heat and fluid flows in industrial furnace using the immersed volume method," *International Journal for Numerical Methods in Fluids*, vol. 68, no. 1, pp. 99–121, 2012.

[48] E. Hachem, H. Digonnet, N. Kosseifi, M. Massoni, and T. Coupez, "Immersed volume method for solving natural convection, conduction and radiation of a hat-shaped disk inside a 3d enclosure," *International Journal of Numerical Methods for Heat and Fluid Flow*, vol. 22, no. 6, pp. 22–59, 2012.

[49] M. Bernacki, Y. Chastel, and T. Coupez, "Level set method for the numerical modelling of primary recrystallization in the polycrystalline materials," *Scripta Materialia*, vol. 58, no. 12, pp. 1129–1132, 2008.

[50] J. Bruchon, H. Digonnet, and T. Coupez, "Using a signed distance function for the simulation of metal forming processes: Formulation of the contact condition and mesh adaptation. from a lagrangian approach to an eulerian approach," *International Journal for Numerical Methods in Engineering*, vol. 78, pp. 980–1008, 2009.

[51] T. Coupez, "Génération de maillage et adaptation de maillage par optimisation locale," *Revue européenne des éléments finis*, vol. 9, pp. 403–423, 2000.

[52] C. Gruau and T. Coupez, "3D tetrahedral unstructured and anisotropic mesh generation with adaptation to natural and multidomain metric," *Computer Methods in Applied Mechanics and Engineering*, vol. 194, pp. 4951–4976, 2006.

[53] R. Boussetta, T. Coupez, and L. Fourment, "Adaptative remeshing based on a posteriori error estimation for forging simulation," *Computer Methods in Applied Mechanics and Engineering*, vol. 195, pp. 6626–6645, 2006.

[54] T. Coupez, "Metric construction by length distribution tensor and edge based error for anisotropic adaptive meshing," *Journal of Computational Physics*, vol. 230, pp. 2391–2405, 2011.

[55] M. Cervera, M. Chiumenti, and R. Codina, "Mixed stabilized finite element methods in nonlinear solid mechanics: Part i: Formulation," *Computer Methods in Applied Mechanics and Engineering*, vol. 199, no. 37–40, pp. 2559–2570, 2010.

[56] T. Coupez, E. Hachem, and H. Digonnet, "Stabilized finite element method for heat transfer and fluid flow inside industrial furnaces," in *15th International Conference on Finite Elements in Flow Problems*, (Tokyo), 2009.

[57] R. Valette, J. Bruchon, H. Digonnet, P. Laure, M. Leboeuf, L. Silva, B. Vergnes, and T. Coupez, "Méthodes d'interaction fluide-structure pour la simulation multi-échelles des procédés de mélange," *Mécanique et Industries*, vol. 8, no. 3, pp. 251–258, 2007.

[58] P. Laure, G. Beaume, O. Basset, L. Silva, and T. Coupez, "Les méthodes numériques pour les écoulements de fluides chargés," in *1er colloque du GDR interactions fluide-structure*, September 2005.

[59] T. Coupez, D. Hugues, E. Hachem, P. Laure, L. Silva, and R. Valette, *Multidomain Finite Element Computations: Application to Multiphasic Problems. In:Arbitrary Lagrangian-Eulerian and Fluid-Structure Interaction. Numerical Simulation Edited by: M. Souli, D.J. Benson.* No. 221-289, 2010, Wiley.

[60] J. B. Ritz and J. P. Caltagirone, "A numerical continuous model for the hydrodynamics of fluid particle systems," *International Journal for Numerical Methods in Fluids*, vol. 30, pp. 1067–1090, 1999.

[61] E. Hachem, *Stabilized Finite Element Method for Heat Transfer and Turbulent Flows inside Industrial Furnaces.* PhD thesis, Ecole Nationale Supérieure des Mines de Paris, 2009.

[62] M. Coquerelle and G.-H. Cottet, "A vortex level set moethod for the two-way coupling of an incompressible fluid with colliding rigid bodies," *Journal of Computational Physics*, vol. 227, pp. 9121–9137, 2008.

[63] J. Janela, A. Lefebvre, and B. Maury, "A penalty method for the simulation of fluid-rigid body interaction," *ESAIM Proceedings*, vol. 14, pp. 115–123, 2005.

[64] L. P. Franca and T. J. R. Hughes, "Two classes of mixed finite element methods," *Computer Methods in Applied Mechanics and Engineering*, vol. 69, pp. 89–129, 1988.

[65] R. Codina, J. M. González-Ondina, G. Díaz-Hernández, and J. Principe, "Finite element approximation of the modified boussinesq equations using a stabilized formulation," *International Journal for Numerical Methods in Fluids*, vol. 57, pp. 1249–1268, 2008.

[66] R. Codina, "Pressure stability in fractional step finite element methods for incompressible flows," *Journal of Computational Physics*, vol. 170, pp. 112–140, 2001.

[67] E. Hachem, B. Rivaux, T. Kloczko, H. Digonnet, and T. Coupez, "Stabilized finite element method for incompressible flows with high reynolds number," *Journal of Computational Physics*, vol. 229, no. 23, pp. 8643–8665, 2010.

[68] R. Codina, "Stabilization of incompressibility and convection through orthogonal sub-scales in finite element methods," *Computer Methods in Applied Mechanics and Engineering*, vol. 190, pp. 1579–1599, 2000.

[69] Y. Mesri, H. Digonnet, and T. Coupez, "Advanced parallel computing in material forming with cimlib," *European Journal of Computational Mechnanics*, vol. 18, pp. 669–694, 2009.

[70] T. Coupez, "Metric construction by length distribution tensor and edge based error for anisotropic adaptive meshing," *Journal of Computational Physics*, vol. 230, no. 7, pp. 2391–2405, 2011.

[71] D. Rixen and P. Gosselet, "Domain decomposition methods applied to challenging engineering problems," in *16th International Conference on Domain Decomposition Method*, pp. 564–581, 2005.

[72] J. Bruchon, H. Digonnet, and T. Coupez, "Using a signed distance function for the simulation of metal forming processes: Formulation of the contact condition and mesh adaptation," *International Journal for Numerical Methods in Engineering*, vol. 78, no. 8, pp. 980–1008, 2009.

[73] S. van der Pijl, A. Segal, C. Vuik, and P. Wesseling, "A mass-conserving level-set method for modelling of multi-phase flows," *International Journal for Numerical Methods in Fluids*, vol. 47, pp. 339–361, 2005.

[74] T. Coupez, H. Digonnet, and R. Ducloux, "Parallel meshing and remeshing," *Appl. Math. Modelling*, vol. 25, no. 2, pp. 83–98, 2000.

[75] C. Gruau, *Génération de métriques pour adaptation anisotrope de maillages, applications à la mise en forme des matériaux*. PhD thesis, Ecole Nationale Supérieure des Mines de Paris, 2004.

[76] Y. Mesri, W. Zerguine, H. Digonnet, L. Silva, and T. Coupez, "Dynamic parallel adaption for three dimensional unstructured meshes: Application to interface tracking," in *Proceedings of the 17th International Meshing Roundtable*, pp. 195–212, 2008.

[77] F. M., "Estimation d'erreur a posteriori et adaptation de maillages," *Revue Européenne des éléments finis*, vol. 9, no. 4, pp. 467–486, 2000.

[78] T. Coupez, "Convection of local level set function for moving surfaces and interfaces in forming flow," in *NUMIFORM '07: Materials Processing and Design: Modeling, Simulation and Applications, Pts I and II*, (New-York, USA), pp. 61–66, January 2007.

[79] T. Coupez, "Réinitialisation convective et locale des fonctions level set pour le mouvement de surfaces et d'interfaces," Journées Activités Universitaires de Mécanique, 2006.

[80] L. Ville, L. Silva, and T. Coupez, "Convected level set method for the numerical simulation of fluid buckling," *International Journal for Numerical Methods in Fluids*, vol. on line, 2010.

[81] A. Brooks and T. Hughes, "Streamline upwind /petrov-galerkin formulations for convection dominated flows with particular emphasis on the incompressible navierstokes equations," *Computer Methods In Applied Mechanics And Engineering*, vol. 32, pp. 199–259, 1982.

[82] R. N. Elias and A. L. Coutinho, "Stabilized edge-based finite element simulation of free-surface flows," *International Journal for Numerical Methods in Fluids*, vol. 54, pp. 965–993, 2007.

[83] A. Johnson and T. Tezduyar, "3D simulation of fluid-particle interactions with the number of particles reaching 100," *Computer Methods in Applied Mechanics and Engineering*, vol. 145, pp. 301–321, 1997.

[84] H. Hu, "Direct simulation of flows of solid-liquid mixtures," *International Journal of Multiphase Flow*, vol. 22, no. 2, pp. 335–352, 1996.

[85] W. G. Dettmer and D. Perić, "A computational framework for fluid-rigid body interaction: Finite element formulation and applications," *Computer Methods in Applied Mechanics and Engineering*, vol. 195, no. 13–16, pp. 1633–1666, 2006.

[86] R. Glowinski, T.-W. Pan, and J. Periaux, "A fictitious domain method for external incompressible viscous flow modeled by navier-stokes equations," *Computing Methods in Applied Mechanical Engineering*, vol. 112, pp. 133–148, 1994.

[87] K. Khadraa, P. Angot, S. Parneixc, and J.-P. Caltagirone, "Fictitious domain approach for numerical modelling of navier-stokes equation," *International Journal for Numerical Methods in Fluids*, vol. 34, pp. 651–684, 2000.

[88] G. J. Wagner, N. Moës, W. Liu, and T. Belytschko, "The extended finite element method for rigid particles in stokes flow," *International Journal of Multiphase flow*, vol. 51, no. 3, pp. 293–313, 2001.

[89] N. Pantankar, P. Singh, D. Joseph, P. Glowinki, and T.-W. Pan, "A new formulation of the distributed lagrange multiplier/fictitious domain method for particulate flows," *International Journal of Multiphase flow*, vol. 26, pp. 1509–1524, 2000.

[90] N. Sharma and N. Patankar, "A fast computation technique for the direct numerical simulation of rigid particulate flows," *Journal of Computational Physics*, vol. 205, no. 2, pp. 439–457, 2005.

[91] S. Aptea, M. M., and N. Patankar, "A numerical method for fully resolved simulation (frs) of rigid particle-flow interactions in complex flows," *Journal of Computational Physics*, vol. 228, no. 8, pp. 2712–2738, 2009.

[92] D. V. Le, B. C. Khoo, and J. Peraire, "An immersed interface method for viscous incompressible flows involving rigid and flexible boundaries," *Journal of Computational Physics*, vol. 220, no. 1, pp. 109–138, 2006.

[93] D. Le, *An immersed interface method for solving viscous incompressible flows involving rigid and flexible boundaries*. PhD thesis, Singapore-MIT Alliance, 2005.

[94] E. Lima, A. Silva, A. Silveira-Neto, and J. Damasceno, "Numerical simulation of two-dimensional flows over a circular cylinder using the immersed boundary method," *Journal of Computational Physics*, vol. 189, pp. 351–370, 2003.

[95] M. C. Lai and C. Peskin, "An immersed boundary method with formal second order accuracy and reduced numerical viscosity," *Journal of Computational Physics*, vol. 160, pp. 707–719, 2000.

[96] P. Le Tallec and J. Mouro, "Fluid structure interaction with large structural displacements," *Computer Methods in Applied Mechanics and Engineering*, vol. 190, no. 24-25, pp. 3039–3067, 2001.

[97] C. Michler, E. E.H. van Brummelen, and R. de Borst, "An interface newtonŰkrylov solver for fluid-structure interaction," *International Journal for Numerical Methods in Fluids*, vol. 47, no. 10–11, pp. 1189–1195, 2005.

[98] J.-F. Gerbeau, M. Vidrascu, and P. Frey, "Fluid structure interaction in blood flows on geometries coming from medical imaging," *Computers and Structure*, vol. 83, no. 2-3, pp. 155–165, 2005.

[99] U. Küttler and A. W. Wall, "Fixed-point fluid-structure interaction solvers with dynamic relaxation," *Computational Mechanics*, vol. 43, pp. 61–72, 2008.

[100] P. Laure, G. Beaume, O. Basset, L. Silva, and T. Coupez, "Numerical methods for solid particles in particulate flow simulations," *European Journal of Computational Mechanics*, vol. Fluid structure interaction, pp. 365–383, 2007.

[101] S. Badia and R. Codina, "Stabilized continuous and discontinuous galerkin techniques for darcy flow," *Computer Methods in Applied Mechanics and Engineering*, vol. 199, pp. 1654–1667, 2010.

[102] M. Cereva, M. Chinumenti, and R. Codina, "Mixed stabilized finite element methods in nonlinear solid mechanics: Parti: Formulation," *Computer Methods in Applied Mechanics and Engineering*, vol. 199, pp. 2559–2570, 2010.

[103] W. R. Hwang, M. A. Hulsen, and H. E. H. Meijer, "Direct simulations of particule suspensions in a viscoelastic fluid in sliding bi-periodic frames," *Journal Non-Newtonian Fluid Mechanics*, vol. 121, pp. 15–33, 2004.

[104] R. Codina, "Stabilized finite element approximation of transient incompressible flows using orthogonal subscales," *Computer Methods in Applied Mechanics and Engineering*, vol. 191, pp. 4295–4321, 2002.

[105] J. Volker, "Reference values for drag and lift of a two-dimensional time-dependent flow around a cylinder," *International Journal for Numerical Methods in Fluids*, vol. 44, no. 7, pp. 777–788, 2004.

[106] D. P. Mok and W. A. Wall, "Partitioned analysis schemes for the transient interactions in incompressible flows and non linear flexible structures," in *Trends in computational structural mechanics, CIMNE*, (Barcelona), 2001.

[107] W. A. Wall, D. P. Mok, and E. Ramm, "Partitioned analysis approach for the transient coupled response of viscous fluids and flexible structures," in *ECCM'99*, European conference on computational mechanics, August 31 - September 3 1999.

[108] R. Codina, J. Houzeaux, H. Coppola-Owen, and J. Baiges, "The fixed-mesh ALE approach for the numerical approximation of flows in moving domains," *Journal of Computational Physics*, vol. 228, pp. 1591–1611, 2009.

[109] J. Baiges and R. Codina, "The Fixed-Mesh ALE approach applied to solid mechanics and fluid-structure interaction problems," *International Journal for Numerical Methods in Engineering*, vol. 81, pp. 1529–1557, 2010.

[110] J. Baiges, R. Codina, and H. Coppola-Owen, "The Fixed-Mesh ALE approach for the numerical simulation of floating solids," *International Journal for Numerical Methods in Fluids*, vol. 67, pp. 1004–1023, 2011.

[111] S. Feghali, E. Hachem, and T. Coupez, "Monolithic stabilized finite element method for rigid body motions in the incompressible navier-stokes flow," *European Journal of Computational Mechanics*, vol. 19, no. 5–7, pp. 547–573, 2010.

[112] R. Codina and O. Soto, "A numerical model to track two-fluid interfaces based on a stabilized finite element method and the level set technique," *International Journal for Numerical Methods in Fluids*, vol. 40, pp. 293–301, 2002.

[113] T. R. J. Hughes, "Multiscale phenomena: Green's functions, the Dirichlet-to-Neumann formulation, subgrid scale models, bubbles and the origin of stabilized methods," *Computer Methods in Applied Mechanics and Engineering*, vol. 127, pp. 387–401, 1995.

[114] R. Codina, "Finite element approximation of the three field formulation of the Stokes problem using arbitrary interpolations," *SIAM Journal on Numerical Analysis*, vol. 47, pp. 699–718, 2009.

[115] C. Codina, P. Principe, O. Guasch, and S. Badia, "Time dependent subscales in the stabilized finite element approximation of incompressible flow problems," *Computer Methods in Applied Mechanics and Engineering*, vol. 196, pp. 2413–2430, 2007.

[116] S. Badia and R. Codina, "On a multiscale approach to the transient Stokes problem. Transient subscales and anisotropic space-time discretization," *Applied Mathematics and Computation*, vol. 207, pp. 415–433, 2009.

[117] M. Schäfer and S. Turek, "The benchmark problem 'flow around a cylinder'. in flow simulation with high- performance computers ii.," *Notes on Numerical Fluid Mechanics*, vol. 52, pp. 547–566, 1996.

[118] J. Volker and M. Gunar, "Higher order finite element discretizations in a benchmark problem for incompressible flows," *Internat. J. Numer. Methods Fluids*, vol. 37, pp. 885–903., 2001.

[119] J. Frochte and W. Heinrichs, "A splitting technique of higher order for the navier-stokes equations," *Journal of Computational and Applied Mathematics*, vol. 228, no. 1, pp. 373 – 390, 2009.

[120] D. Wan and S. Turek, "Fictitious boundary and moving mesh methods for the numerical simulation of rigid particulate flows," *Journal of Computational Physics*, vol. 222, pp. 28ï£¡–56, 2007.

[121] T. Rabczuk, R. Gracie, J.-H. Song, and T. Belytschko, "Immersed particle method for fluidŰstructure interaction," *International Journal for Numerical Methods in Fluids*, vol. 81, pp. 48–71, 2010.

[122] E. Hachem, S. Feghali, R. Codina, and T. Coupez, "Immersed stress method for fluid structure interaction using anisotropic mesh adaptation, submitted (2012)," *International Journal for Numerical Methods in Engineering*.

[123] F. Alauzet, P. Frey, P.-L. George, and B. Mohammadi, "3d transient fixed point mesh adaptation for time-dependent problems: Application to cfd simulations," *Journal of Computational Physics*, vol. 222, pp. 592–623, 2007.

[124] A. Robinson, C. Schroeder, and R. Fedkiw, "A symmetric positive definite formulation for monolithic fluid structure interaction," *Journal of Computational Physics*, vol. 230, no. 4, pp. 1547–1566, 2010.

[125] D. Pagnutti and C. Olivier-Gooch, "two-dimensional delaunay-based anisotropic mesh adaptation doug pagnutti," *engineering with computers*, vol. 4, pp. 407–418, 2010.

[126] T. Richter and T. Wick, "Finite elements for fluid-structure interaction in ALE and fully eulerian coordinates," *comput. Meth. Appl. Mech. Engrg.*, pp. 2633–2642, 2010.

[127] J. Hron and S. Turek, "A monolithic FEM/multigrid solver for ALE formulation of fluid structure interaction with application in biomechanics," *Fluid-Structure Interaction Modelling, Simulation, Optimization*, pp. 146–170, 2006.

[128] T. Wick, "Solving monolithic fluid-structure interaction problems in arbitrary lagrangian eulerian coordinates with the deal.II library," *Institute of Applied Mathematics University of Heidelberg,*, 2011.

[129] G.-H. Cottet, E. Maitre, and T. Milcent, "Eulerian formulation and level set models for incompressible fluid-structure interaction," *ESAIM-Math. Model. Numer. Anal.*, vol. 42, no. 3, pp. 471–492, 2008.

[130] S. Okazawa, K. Kashiyama, and Y. Kaneko, "Eulerian formulation using stabilized finite element methods for large deformation solid dynamics," *Int. J. Numer. Math. Fluids.*, vol. 72, pp. 1544–1559, 2007.

[131] P. He and R. Qiao, "A full-eulerian solid level set method for simulation of fluid-structure interactions," *Micro fluid and Nano fluid*, vol. 11, pp. 557–567, 2011.

[132] T. Dunne, "An eulerian approach to fluid-structure interaction and goal- oriented mesh refinement," *Int. J. Numer. Math. Fluids.*, vol. 51, pp. 1017–1039, 2006.

[133] M. Rappaz, M. Bellet, and M. Deville, *Numerical Modeling in Materials Science and Engineering*. Springer Series in Computational Mathematics,, 2003.

[134] D. Clamond, *Mécanique des Milieux Continus*. Université de Nice, Sophia-Antipolis, 2011.

[135] P. Wriggers, *Nichtlineare Finite-Element-Methoden*. Springer DE, 2001.

[136] T. Dunne, *Adaptive Finite Element Approximation of Fluid-Structure Interaction Based on Eulerian and Arbitrary Lagrangian-Eulerian Variational Formulations*. PhD thesis, University of Heidelberg, 2007.

[137] R. Duddu, L. L. Lavier, T. J. R. Hughes, and V. Calo, "A finite strain eulerian formulation for compressible and nearly incompressible hyperelasticity using high-order b-spline finite elements," *International Journal for Numerical Methods in Engineering*, vol. 89, no. 6, pp. 762–785, 2012.

[138] S. Bünisch, T. F. Dunne, and R. Rannacher, *Numerics of Fluid-Structure Interaction*, vol. 37. Birkhäuser Basel, 2008.

[139] C. Bost, *Méthodes Level-Set et pénalisation pour le calcul d'interaction fluide-structure*. PhD thesis, Université Joseph Fourrier- Grenoble I, 2008.

[140] Z.-Q. Zhang, G. R. Liu, and B. C. Khoo, "Immersed smoothed finite element method for two dimensional fluid-structure interaction problems," *International Journal for Numerical Methods in Engineering*, vol. 90, no. 10, pp. 1097–0207, 2012.

[141] B. Griffith, "Immersed boundary model of aortic heart valve dynamics with physiological driving and loading conditions," *International Journal for Numerical Methods in Biomedical Engineering*, pp. 317–345, 2012.

[142] T. Shinar, C. Schroeder, and R. Fedkiw, "Two-way coupling of rigid and deformable bodies," *In SCA'08: Proceedings of the 2008 ACM SIGGRAPH/Eurographics symposium on Computer animation*, pp. 95–103, 2008.

[143] H. Zhao, J. Freunda, and R. Moser, "A fixed-mesh method for incompressible flow-structure systems with finite solid deformations," *Journal of Computational Physics*, vol. 227, no. 6, pp. 3114–3140, 2008.

[144] G. Xia and C.-L. Lin, "An unstructured finite volume approach for structural dynamics in response to fluid motions," *Computers and Structures*, vol. 86, pp. 684–701, 2008.

[145] J. Caltagirone, "Sur l'interaction fluide-milieu poreux: application au calcul des efforts exercés sur un obstacle par un fluide visqueux," *Comptes rendus de l'Académie des sciences. Série II, Mécanique, physique, chimie, astronomie*, vol. 318, no. 5, pp. 571–577, 1994.

[146] P. Angot, C.-H. Bruneau, and P. Fabrie, "A penalization method to take into account obstacles in incompressible viscous flows," *Numerische Mathematik*, vol. 81, pp. 497–520, 1999.

[147] S. Chan, K. Lam, R. So, and R. Leung, "Numerical study of flow around circular cylinder," *Flow-Induced Vibration, Poceedings of the 7th International Conference on Flow Induced Vibrations FIV*, pp. 249–255, 2000.

[148] S. Mittal and V. Kumar, "Flow-induced oscillations of two cylinders in tandem and staggered arrangements," *Journal of fluid and Structures*, vol. 15, pp. 717–736, 2001.

[149] A. Huerta and W. Liu, "Viscous flow structure interaction," *Journal of Pressure Vessel Technology*, vol. 110, pp. 15–21, 1988.

[150] P. Anagnostopoulos and P. Berman, "Reponse characteristics of a vortex-excited cylinder at low reynolds number," *Journal of Fluids and Structures*, vol. 6, pp. 39–50, 1992.

[151] A. Khalak and C. Williamson, "Investigation of the relative effects of mass and damping in vortex-induced vibration of a circular cylinder," *Journal wind engineering industrial aerodynamics*, vol. 69–71, pp. 341–350, 1997.

[152] D. Brika and A. Laneville, "Vortex-induced vibrations of a long flexible circular cylinder," *Journal fluid mechanics*, vol. 250, pp. 481–508, 1993.

[153] E. Guilmineau and P. Queutey, "Numerical simulation of vortex-induced vibration of a circular cylinder with low mass-damping in a turbulent flow," *Journal of Fluids and Structures*, vol. 19, pp. 449–466, 2004.

[154] S. Dong and G. Lesoinne, "Dns of flow past a stationary and oscillating cylinder at re=10000," *Journal of Fluids and Structures*, vol. 20, pp. 519–531, 2005.

[155] H. Al-Jamal and C. Dalton, "Vortex induced vibrations using large eddy simulation at a moderate reynolds number," *Journal of Fluids and Structures*, vol. 19, pp. 73–92, 2004.

[156] A. Placzek, J. Sigrist, and A. Hamdouni, "Numerical simulation of an oscillating cylinder in a cross-flow at low reynolds number: Forced and free oscillations," *Computer and Fluids*, vol. 38, pp. 80–100, 2008.

[157] C. Zhou, C. Sorm, and K. Lam, "Vortex induced vibrations of an elastic circular cylinder," *Journal fluid mechanics*, vol. 13, pp. 165–189, 1999.

[158] M.-S. Gerouache, "Etude numérique de l'instabilité de bénard-karman derrière un cylindre fix ou en mouvement pérodique. dynamique de l'écoulement et advection chaotique," *Ph.D.thesis, Ecole Polytechnique de l'Université de Nantes*, 2000.

[159] M. Braza, P. Chassaing, and H. Ha Minh, "Numerical study and physical analysis of the pressure and velocity fields in the near wake of circular cylinder," *Journal Fluid Mechanics*, vol. 165, pp. 79–130, 1986.

[160] C. Lange, F. Durst, and M. Breuer, "Momentum and heat transfer from cylinder in laminar crossflow at $10^{-4} \leq re \leq 200$," *International Journal of Heat and Mass Transfer*, vol. 41, no. 22, pp. 3409–3430, 1998.

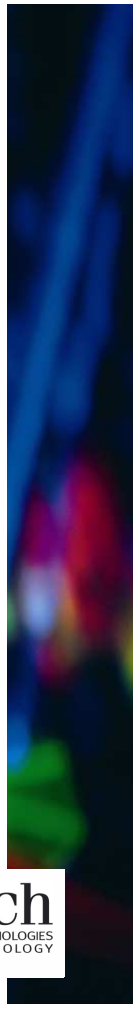
[161] R. Henderson, "Detail of the drag curve near the onset of vortex shedding," *Physics of Fluids*, vol. 7, no. 9, p. 2102, 1995.

[162] G. Koopmann, "The vortex wakes of vibrating cylinders at low reynolds numbers," *Journal of Fluid Mechanics*, vol. 28, no. 3, pp. 501–512, 1967.

Nouvelle formulation monolithique en éléments finis stabilisés pour L'Interaction Fluide-Structure

RESUME : L'Interaction Fluide-Structure (IFS) décrit une classe très générale de problème physique, ce qui explique la nécessité de développer une méthode numérique capable de simuler le problème FSI. Pour cette raison, un solveur IFS est développé qui peut traiter un écoulement de fluide incompressible en interaction avec des structures différente: élastique ou rigide. Dans cet aspect, le solveur peut couvrir une large gamme d'applications. La méthode proposée est développée dans le cadre d'une formulation monolithique dans un contexte Eulérien. Cette méthode consiste à considérer un seul maillage et résoudre un seul système d'équations avec des propriétés matérielles différentes. La fonction distance permet de définir la position et l'interface de tous les objets à l'intérieur du domaine et de fournir les propriétés physiques pour chaque sous domaine. L'adaptation de maillage anisotrope basé sur la variation de la fonction distance est ensuite appliquée pour assurer une capture précise des discontinuités à l'interface fluide-solide. La formulation monolithique est assurée par l'ajout d'un tenseur supplémentaire dans les équations de Navier-Stokes. Ce tenseur provient de la présence de la structure dans le fluide. Le système est résolu en utilisant une méthode élément fini et stabilisé suivant la formulation variationnelle multiéchelle. Cette formulation consiste à décomposer les champs de vitesse et pression en grande et petite échelles. La particularité de l'approche proposée réside dans l'enrichissement du tenseur de l'extra contraint. La première application est la simulation IFS avec un corps rigide. Le corps rigide est décrit en imposant une valeur nul du tenseur des déformations, et le mouvement est obtenu par la résolution du mouvement de corps rigide. Nous évaluons le comportement et la précision de la formulation proposée dans la simulation des exemples 2D et 3D. Les résultats sont comparés avec la littérature et montrent que la méthode développée est stable et précise. La seconde application est la simulation IFS avec un corps élastique. Dans ce cas, une équation supplémentaire est ajoutée au système précédent qui permet de résoudre le champ de déplacement. Et la contrainte de rigidité est remplacée par la loi de comportement du corps élastique. La déformation et le mouvement du corps élastique sont réalisés en résolvant l'équation de convection de la Level-Set. Nous illustrons la flexibilité de la formulation proposée par des exemples 2D.

Mots clés : Interaction Fluide-Structure, Formulation monolithique, Elément Finis Stabilisés, remaillage anisotrope, écoulement incompressible, mouvements de corps rigide, comportement élastique.



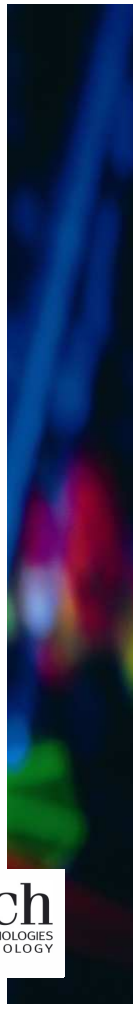
MINES ParisTech

ParisTech
INSTITUT DES SCIENCES ET TECHNOLOGIES
PARIS INSTITUTE OF TECHNOLOGY

Novel monolithic stabilized finite element method for Fluid-Structure Interaction

ABSTRACT Numerical simulations of fluid-structure interaction (FSI) are of first interest in numerous industrial problems: aeronautics, heat treatments, aerodynamic, bioengineering.... Because of the high complexity of such problems, analytical study is in general not sufficient to understand and solve them. FSI simulations are then nowadays the focus of numerous investigations, and various approaches are proposed to treat them. We propose in this thesis a novel monolithic approach to deal with the interaction between an incompressible fluid flow and rigid/ elastic material. This method consists in considering a single grid and solving one set of equations with different material properties. A distance function enables to define the position and the interface of any objects with complex shapes inside the volume and to provide heterogeneous physical properties for each subdomain. Different anisotropic mesh adaptation algorithms based on the variations of the distance function or on using error estimators are used to ensure an accurate capture of the discontinuities at the fluid-solid interface. The monolithic formulation is insured by adding an extra-stress tensor in the Navier-Stokes equations coming from the presence of the structure in the fluid. The system is then solved using a finite element Variational MultiScale (VMS) method, which consists of decomposition, for both the velocity and the pressure fields, into coarse/resolved scales and fine/unresolved scales. The distinctive feature of the proposed approach resides in the efficient enrichment of the extra constraint. In the first part of the thesis, we use the proposed approach to assess its accuracy and ability to deal with fluid-rigid interaction. The rigid body is prescribed under the constraint of imposing the nullity of the strain tensor, and its movement is achieved by solving the rigid body motion. Several test case, in 2D and 3D with simple and complex geometries are presented. Results are compared with existing ones in the literature showing good stability and accuracy on unstructured and adapted meshes. In the second, we present different routes and an extension of the approach to deal with elastic body. In this case, an additional equation is added to the previous system to solve the displacement field. And the rigidity constraint is replaced with a corresponding behaviour law of the material. The elastic deformation and motion are captured using a convected level-set method. We present several 2D numerical tests, which is considered as classical benchmarks in the literature, and discuss their results

Keywords : Fluid-Structure Interaction, Monolithic Formulation, Stabilized Finite Element Method, Anisotropic Mesh Adaptation, incompressible flow, rigid body motion, elastic behaviour.



MINES ParisTech

ParisTech
INSTITUT DES SCIENCES ET TECHNOLOGIES
PARIS INSTITUTE OF TECHNOLOGY